# *Faults, fractures and fluids in mudstones during Cenozoic extension in the Cleveland Basin*

LEE, JACK,KIERAN

# Abstract

Fractures and faults may act as important fluid-flow pathways through low permeability mudstone sequences; understanding their occurrence and properties is thus important when considering the risks of leakage of petroleum from underlying reservoirs, or $CO_2$ from storage sites. Fluid-flow is also an important in radioactive waste storage sites during construction or operation of the sites. This project studies calcite-filled fractures and faults developed within the exhumed, early-mature, Jurassic mudstone succession of the Cleveland Basin, NE England, combining structural geology with isotope geochemistry and geochronology. The abundance of well-exposed, natural fractures with different orientations and failure modes provides an opportunity to investigate the properties of these fractures and provides a basin-wide temporal and spatial framework of evolving deformation.

Calcite veins and fault fills are present in N-S to NNW-SSE trending normal faults and associated fractures in the north of the Cleveland Basin. U-Pb calcite geochronology has yielded ages in the range 45-20Ma for sampled calcite. This describes a previously unrecognised phase of Cenozoic faulting. I propose that this deformation relates salt-related deformation following regional tilting, uplift and eastwards gravity sliding related to Atlantic opening and the development of the proto-Icelandic plume to the NW of Britain.

Structural and petrographic observations suggest that N-S trending faults have complex kinematic and fluid-flow histories. Faults are characterised by damage zones with widespread calcite mineralisation, extensional jog structures and fracture reactivation. Stable isotope and clumped isotope analyses suggest that the regional fracture-controlled fluid-flow during the Cenozoic deformation involved post-exhumation mixing of cool meteoric waters (20°C) with warmer (80°C) basinal fluids. I hypothesise that fluid is driven by gravity-driven regional extension. Whilst fault-related displacements are modest, meaning that the structures are unlikely to be widely resolved in offshore seismic reflection profiles, they are widespread and therefore are inferred to represent highly effective fluid-flow pathways. Our findings place new important constraints on the poorly constrained Cenozoic tectonic history of the Cleveland Basin and northeast Britain.

DEPARTMENT OF EARTH SCIENCE, DURHAM UNIVERSITY

# Faults, fractures and fluids in mudstones during Cenozoic extension in the Cleveland Basin

A thesis submitted for the degree of Doctor of Philosophy (PhD)

Jack Kieran Lee

March 2022

# Declaration

No part of this thesis has previously been submitted for a degree at this or any other university. The work described in this thesis is entirely that of the author. Where appropriate, work in this thesis which has already been published is clearly indicated. Work for this thesis was conducted from October 2017 to March 2022 under the primary supervision of Prof. Robert Holdsworth at Durham University and secondary supervision of Dr Nick Roberts at the British Geological Survey and Prof. Andrew Aplin at Durham University.

# Statement of Copyright

# Acknowledgements

Laura Scott, who was always there for me during the tough times and the good and without whom I almost certain would not have rabbits.

Bob Holdsworth, who can read drafts quicker then I can write them (and I can touch type). Never judged me for losing car keys in a forest in Great Ayton.

Nick Roberts, whose great idea along with Jonny Imber this thesis was. Without Nick's support and guidance I would probably still be figuring out where I was going although we never did find that shortcut down to Runswick Bay headland.

Jonny Imber, without whom I probably would never have chosen this project and for whom the Cleveland Basin was never work but a labour of love. Also thanks for always being there to help even when you probably had many more important things to do after you left the department. Jonny also proofread this entire document, which takes some doing.

Andy Aplin, who worked to keep me sane and always was the voice of reason even when I flustered to hear his sage advice.

Ria, Bob, Marty, Inge, Saidhbhín and Fiach, my family, who were always there for support and to ask me how things were going…I frequently responded monosyllabically.

Chris, Sarah, Miles, Tim, Emma, Madeleine, Katharine, Bob, Claudia, Pavlos and everyone else in the postgraduate community at Durham University, Department of Earth Sciences; without you all these last 4 ½ years would have been a lot less fun.

Cornelia, Tom and Benji (my rabbits), always willing to provide a distraction by chewing or eating something they shouldn't.

Sam, Kitty, Chris (Dixon), Alice, Andrew, Charlotte, whose company always provided an escape from reality for a time.

Yorkshire Geological Society for providing a grant for the work at Cliff Rigg Quarry, Great Ayton.

NERC Oil and Gas CDT whose funded this project and provided support and training throughout.

Anyone I have forgotten who should be on the list but left out because I am so very tired.

# List of Tables

*– the minimum period the structures are indicated to be active i.e. the minimum difference between the maximum age and minimum age including uncertainty. In some cases there will not be separation between a set of ages for a structure in which case the overlap in ages is also stated.*

# Table of Contents

## Table of Contents

# Chapter 1 – Introduction and Geological History of the Cleveland Basin

## 1.1 Introduction

Mudrocks form important low permeability seals for hydrocarbons, $CO_2$ storage and radioactive waste (Bourg, 2015; Roberts et al., 2017; Douma, 2020). Jurassic mudstones form important hydrocarbon seals as well as source rock intervals in the Central and North Sea (Ziegler, 1980; Barnard & Cooper, 1981; Cooper & Barnard; 1984). The Lower Jurassic (Lias) mudrocks of the uplifted, onshore Cleveland Basin in North Yorkshire form a ~105m thick sequence of predominantly mudrocks with Total Organic Carbon values up to a maximum of 18.2% (Barnard & Cooper, 1984). The Lower Jurassic of the Cleveland Basin forms an excellent setting for analysing fracturing and related fluid-flow in an exhumed sedimentary basin.

In contrast to other sedimentary rocks, mudrocks have a special set of mechanical properties related to their compaction and composition that effect the manner the way in which they deform (Hooker et al., 2019). Shallow-buried mudrocks typically undergo ductile deformation, while deeper burial leads to compaction and diagenetic strengthening. This means that uplifted mudrocks are overconsolidated and undergo brittle deformation (Ingram & Urai, 1999). Brittle deformation results in dilation and the development of fractures (Urai & Wong, 1994; Urai, 1995). Fracture permeability influences pathways and can lead to cross-stratal fluid movement and decreased sealing capacity for hydrocarbon or $CO_2$ storage (Hooker et al., 2019).

Mudstones can fracture in a number of ways dependent on the stress state with brittle mudstones more likely to deform through tensile opening mode fractures forming where the minimum stress is tensile, or effectively tensile, and overcomes the tensile strength of the rock at low differential stress (i.e. shallow burial) and/or high fluid pressures (Sibson, 2000). Weaker, more ductile mudstones, however are more likely to deform through compactional shear with tensile fracture dominant only in the shallow surface. Laterally extensive subvertical tensile fractures are typically termed joints and occur in a wide range of rocks and tectonic settings (Pollard & Aydin, 1988). Joints can form highly effectively fluid-flow pathways in the subsurface (Taylor et al., 1999). Joint spacing is dependent on the layer thickness, joint spacing tending to increase due to drops in stress around existing joints (Narr & Suppe, 1991; Silliphant et al., 2002). Hybrid and shear fractures form at higher differential stress and in stronger rocks with a high angle of friction (Ingram & Urai, 1999). In contrast to joints, shear fractures tend to cluster, forming distinct fault zones. Faults are typically associated with distinct damage zones related to initiation, propagation and subsequent slip along the fault (McGrath and Davison, 1995; Kim et al., 2004). A number of different fault rocks (i.e. fault breccia, fault gouge, etc.) can be associated with faulting and are summarised in detail in Sibson (1977). Faults are commonly associated with areas of increased fracture permeability (Sibson, 1996) and along with joints may form important pathways for fluids through low permeability mudstones.

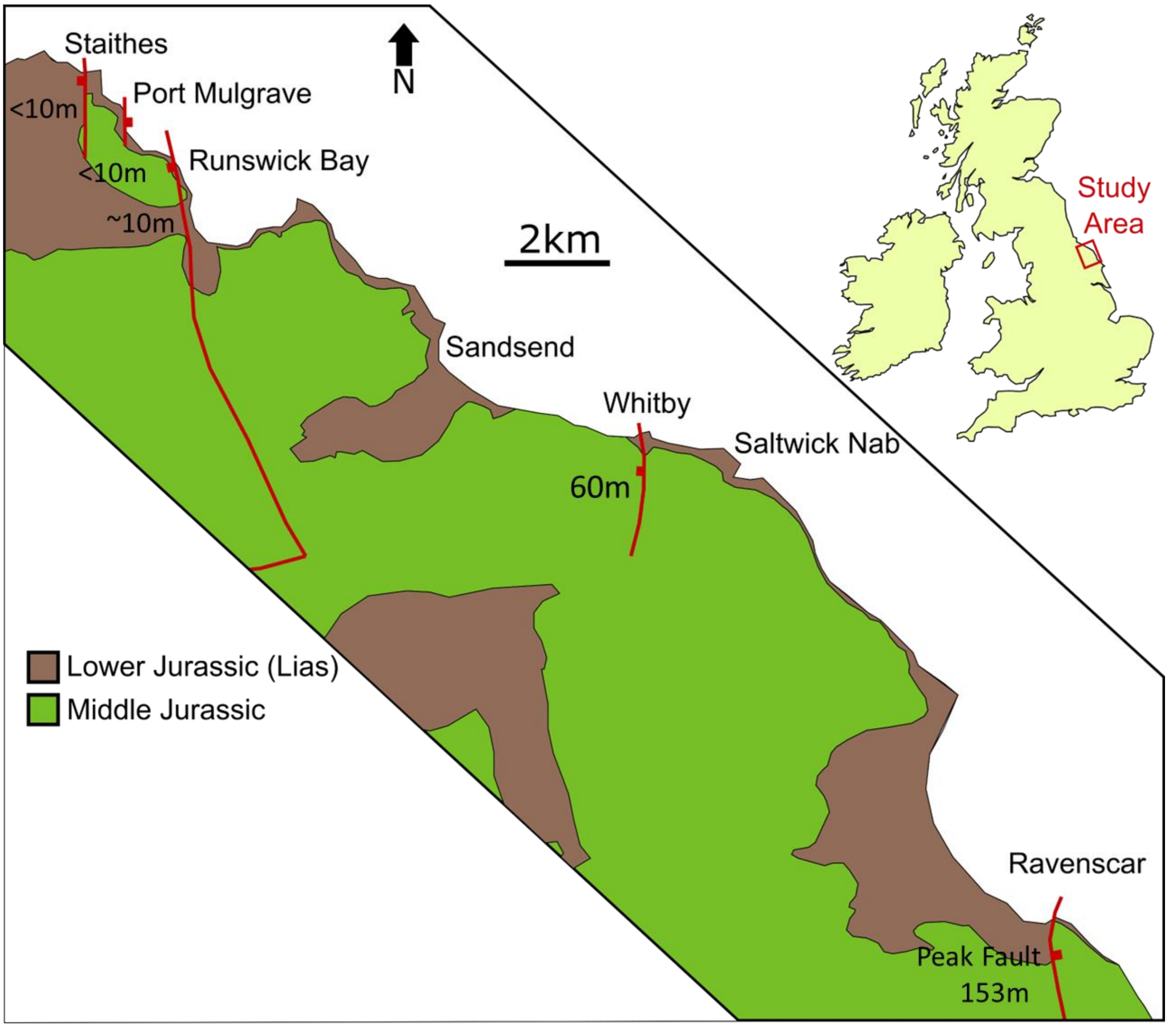


*Fig 1.1. Geological structure map of the Cleveland Basin showing the location of the main study area. The named locations will compose the main field locations in this research.*

Uplift and tilting can also lead to post-tectonic subsidence with post-uplift and orogenic extension previously documented as being associated with extensional deformation due to gravitational collapse accommodated along basal detachments (Fossen, 1992). The presence of salt or other evaporites similar to the Zechstein Evaporites in the Cleveland Basin (Woods, 1979; Talbot et al., 1982) can facilitate thin-skinned extension and gravitational sliding through gravity driven extension (Duval et al., 1991). The effects and timing of uplift and tilting could therefore form an important influence on the Cenozoic history of the Cleveland with possible halokinetic effects of the underlying Zechstein Evaporites adding extra complexity.

In exhumed basins, such as the Cleveland Basin, petroleum prospectivity is largely dependent on the ability of pre-existing traps to retain hydrocarbons during and post-exhumation (English et al., 2017). Thick mudstones form excellent seals for natural $CO_2$ storage sites, but the seal integrity of mudstones in these systems can be compromised by the presence of overpressure and proximity to modern extensional faults (Roberts et al., 2017). Therefore, understanding the stress state of the normal faults developed in the Cleveland Basin onshore could provide important implications for potential $CO_2$ storage and petroleum prospectivity in the offshore parts of this and other analogous offshore basins, including those in the Southern North Sea (Imber et al., 2014).

### 1.1.1 Aims and Rationale

The broad aim of this research is to present evidence to describe a previously unconstrained period of deformation and associated fluid-flow in the exhumed Cleveland Basin, North Yorkshire (Fig 1.1). A combination of structural, U-Pb calcite geochronology, microstructural and isotopic analysis were used as a toolbox for systematically interrogating and characterising deformation and fluid-flow associated with calcite-mineralised structures in exhumed sedimentary basins.

The research builds on previous work by Imber et al. (2014), who documented the presence of calcite mineralisation associated with fault zones in the Cleveland Basin, together with bedding-parallel and subvertical fractures. In this work, detailed, field-based, structural and microstructural analysis will be combined with U-Pb calcite geochronology to put absolute constraints on the timing of the deformation and potentially related fluid-flow described by Imber et al. (2014). A combination of conventional stable carbon and oxygen isotopes and clumped isotopes (Bergman et al., 2013) will be utilised to interrogate and analyse the fluid-flow regime associated with calcite mineralisation. These approaches will allow an improved understanding of the tectonic history of the Cleveland Basin and provide constraints on under-described deformation processes and associated fluid-flow at a scale that is generally not resolvable from seismic reflection data in sub-surface settings.

The focus of the work is the organic-rich mudstones of the Lower Jurassic (Lias), that are excellent analogues for hydrocarbon source rocks and seals in many sedimentary basins.

The Lias is approximately 100m thick at maximum thickness (Powell, 2010) but varies throughout the basin. The Whitby Mudstone Formation having matrix permeabilities in the range of $10^{-18}$ $m^2$ to $10^{-21}$ $m^2$ (Houben et al., 2017) which would inhibit vertical fluid-flow. Fractures and faults observable in outcrops along the North Yorkshire coast, therefore, are analogous to fluid conduits in the subsurface and could have facilitated fluid-flow under burial. The timing of deformation and related fluid-flow have important implications for our understanding of fluid movement in the onshore Cleveland Basin, and for hydrocarbon exploration and $CO_2$ storage in analogous basins.

## 1.2 Thesis Structure

The structure of the thesis will be focussed on exploring the objectives laid out in Section 1.1.2 and building a narrative of evidence-based research into the Cenozoic deformation history of the Cleveland Basin.

Chapter 1 introduces the aim, rationale and objectives of the thesis before describing previous literature on the tectonic and sedimentological history of the Cleveland Basin and its importance as a westward extension of the Southern North Sea (Fig 1.2).

Chapter 2 outlines the key methodologies utilised in this research including field observation and analysis, sampling and sample preparation, microscopy, U-Pb calcite geochronology and stable C-O and clumped isotopic analyses.

Chapter 3 describes field observations with specific focus on the structural elements analysed and sampled for further analyses. Kinematic evidence is collected and analysed to determine – where possible - the local and regional stress regimes associated with deformation. Field relationships are also utilised to determine a high level sequence of deformation for the Cleveland Basin.

Chapter 4 focuses on the calcite samples described in Chapter 3 and assesses the samples microstructurally to identify locally syn- and post-kinematic calcite precipitation associated with faulting. U-Pb calcite geochronology results are presented to ascribe absolute ages to the faulting, fracturing and associated mineralization.

Chapter 5 presents the isotopic results with stable and clumped isotope used to group and make correlations between samples based on their isotopic properties. Carbon and oxygen stable isotope results when combined with temperature constraints from clumped isotopic analyses allows predictions and deduction of the fluid-flow regimes to be made.

Chapter 6 synthesises and discusses the key findings across the Cleveland Basin as a whole in light of the pre-existing literature. The aim of the synthesis is to build on the narrative developed in the previous chapters into a regional model for deformation in the Cleveland Basin. The chapter will then proceed to focus on the key outcomes and implications of this research before suggesting future work to build on the research presented herein.

## 1.3 Geological History of the Cleveland Basin

The Cleveland Basin is a Mesozoic depocenter that formed due to differential subsidence of the Southern North Sea. The basin forms a part of a series of small extensional tectonic basins in a shallow marine environment from the Permian to the Cretaceous in the Southern North Sea (Rawson & Wright, 1992; Powell, 2010). These basins include the Sole Pit Basin, the Central Graben and the East Midlands Shelf (Fig 1.2; Dixon, 1989; Powell, 2010). The Cleveland Basin is bounded to the northeast by the Mid-North Sea High, the Market Weighton High to the south and the Pennine High to the west (Powell, 2010) and was linked through to the central part of the North Sea Basin via the Sole Pit Basin (also termed the Sole Pit Trough: Fig 1.2 – Kent, 1974; Kent 1980; Glennie & Boegner, 1981; Ziegler, 1982; Van Hoorn, 1987; Powell, 2010).

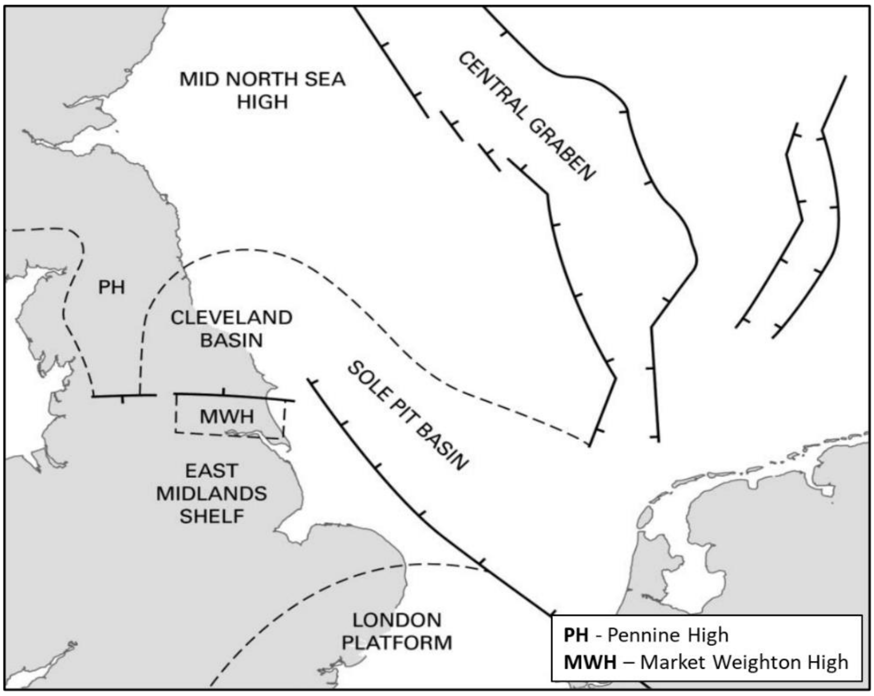


*Fig 1.2. Schematic diagram after Powell (2010) which shows the location of the Cleveland Basin and the bounding highs. The Cleveland Basin extends into the Southern North Sea via the Sole Pit Basin.*

### 1.3.1 Tectonic History

The local Carboniferous depocentre has been identified from boreholes and seismic reflection data. These have suggested that the basin may have been inverted during the Late Carboniferous and uplifted prior to the Permian, with removal of the Westphalian and Namurian sediment fills (Van Hoorn, 1987; Dixon, 1989). The Cleveland Basin was created during the Late Permian to Early Triassic (Sclater and Christie, 1980; Glennie, 1984; Van Hoorn, 1987) due to the breakup of Pangaea, and resulted in the opening of the Neotethys Ocean (Fig 1.3). Models of tectonic subsidence by Dixon (1989) indicate that the Cleveland Basin experienced rapid pulses of Late Permian to Early Triassic tectonic subsidence punctuated by periods of thermal subsidence. Offshore seismic interpretation of the Flamborough Head Fault Zone by McKeen (2019) indicates that the Zechstein Evaporites form an important detachment between the whole of the Cleveland Basin and underlying Palaeozoic stratigraphy.

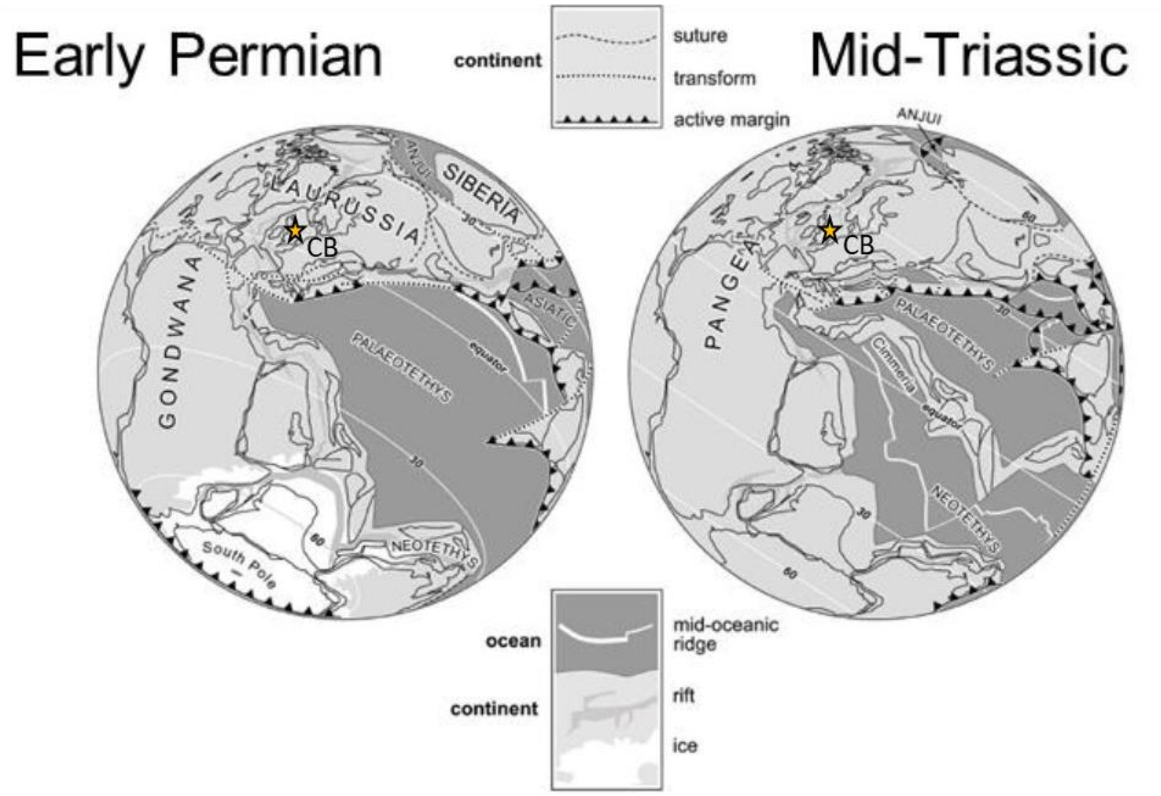


*Fig 1.3. Tectonic reconstruction modified after Woodcock & Strachan (2012) demonstrating global reconstructions for the Early Permian and Mid Triassic. CB indicates the location of the Cleveland Basin.*

Modelling of tectonic subsidence by Dixon (1989) indicates that the Jurassic-Cretaceous of the Cleveland Basin was dominated by thermal subsidence punctuated by short-lived rift phases in the Early Jurassic, Late Jurassic and Late Cretaceous (Fig 1.4 & 1.5; Imber et al., 2014). Periods of inversion have been invoked during the Early Jurassic to Middle Jurassic

(Black, 1929; Rawson & Wright, 1992; Hesselbo & Jenkyns, 1998; Powell, 2010). The Middle Jurassic saw the tilting of the Mid North Sea High in response to the Forties-Piper Volcanic Centre in the central North Sea Basin (Sellwood & Hallam, 1974; Ziegler, 1982; Underhill & Partington, 1993; Powell, 2010) and is thought to have resulted in a change from marine to predominantly non-marine deposition in the Cleveland Basin. The Late Jurassic saw a return to marine conditions in the Cleveland Basin with tectonic subsidence (Imber et al., 2014).

Opening of the North Atlantic during the Late Cretaceous to Cenozoic and initiation of the Iceland hot-spot (Fig 1.4) is widely thought to have led to regional uplift and tilting of Britain to the southeast (Cope, 1994; Gale & Lovell, 2018). Widespread basaltic dyke intrusion, including the Cleveland Dyke is thought to be associated with the development of the Mull igneous centre in NW Scotland. The Cleveland Dyke has been dated using K/Ar dating at 55.8 ±0.3Ma by Fitch et al. (1978). The regional uplift is at least in part concurrent with inversion and exhumation of the Cleveland Basin based on estimates from Apatite Fission Track Analysis (AFTA) modelling, structural interpretation and other methods (Hurford, 1977; Green, 1986; Bray et al., 1992; Lewis et al, 1992; Japsen, 1997; Rawson & Wright, 1992; Green et al., 2012; McKeen, 2019; Roberts et al. 2020). Interpreted seismic lines running E-W displayed by McKeen (2019) illustrate the effects of this tilting with a steady SE dip in the pre-Permian strata offshore from Flamborough Head.

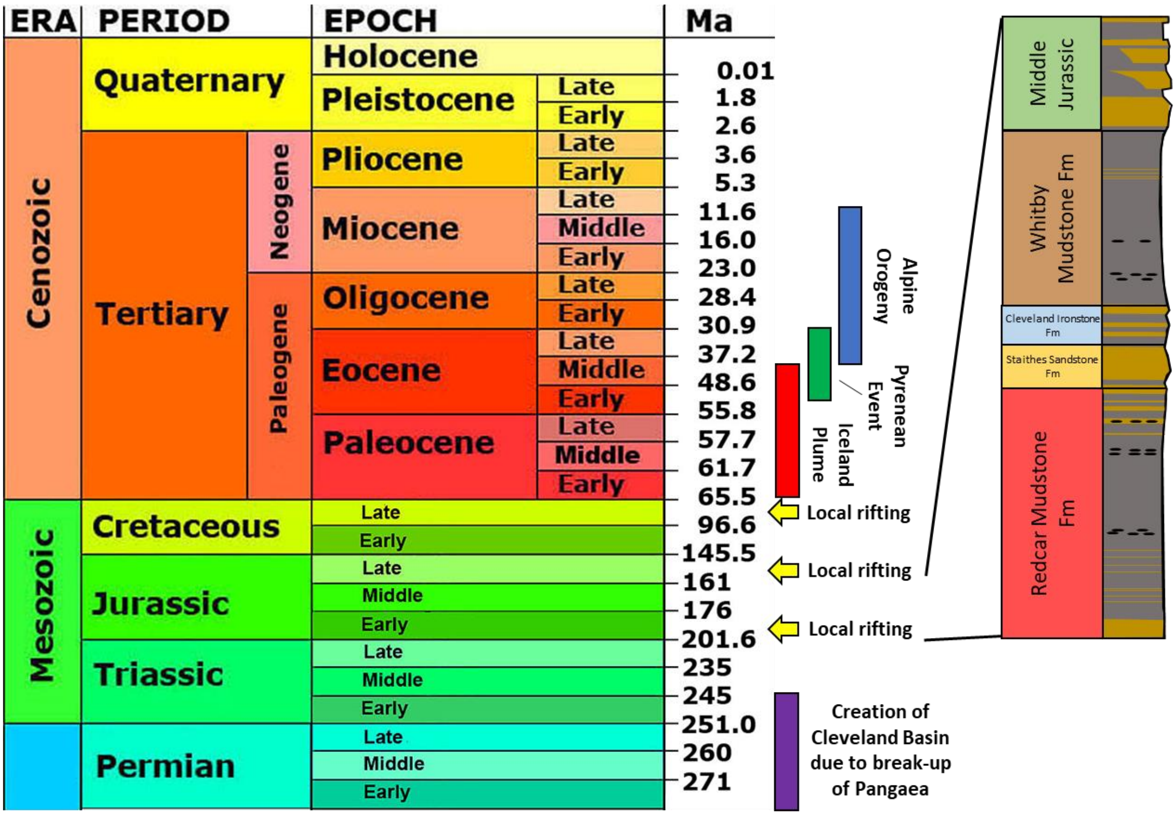


*Fig 1.4. Tectonostratigraphic representation of the Cleveland Basin showing the main tectonic events in the development of the Cleveland Basin and NW Europe with an inset of the Early to Middle Jurassic stratigraphy of the Cleveland Basin based on Hesselbo & King (2019).*

The Cenozoic was an important period of plate reconfiguration in Western Europe with the Pyrenean (Sibuet et al., 2004) and Alpine Orogenic episodes (Ziegler, 1987; Mortimore, 2019). Rotation of the Iberian microcontinent and docking with the Eurasian continent led to the Pyrenean Orogeny (50-28Ma; Fig 1.4), which was followed by the main collision of the African continent with Eurasia leading to the complex, multiphase Alpine Orogeny (35-10Ma; Fig 1.3). Ziegler (1989), Starmer (1995), Mortimore (2019) and McKeen (2019) specifically associate folding and dextral reactivation of the Flamborough Fault Zone and inversion of the Cleveland Basin with regional NW-SE oriented Pyrenean-Alpine compression (Fig 1.4 & 1.5). This event is also widely believed to be associated with development of regional inversion structures such as the onshore E-W trending Cleveland Anticline and offshore Scarborough Dome (Fig 1.10; Rawson & Wright, 1992). These orogenic events are traditionally viewed as post-dating tilting and uplift of Britain related to the proto-Iceland plume (Parrish et al., 2018).

Estimations of cumulative uplift and erosion in the Cleveland Basin vary significantly between 1.5km (Holliday, 1999) and 4.0km (Kemp et al., 2005). However, 2-3km is a reasonable value suggested by the following authors based on AFTA methods (Green, 1986; Bray et al., 1992) and estimates of basin uplift and erosion (Hemingway & Riddler, 1982).

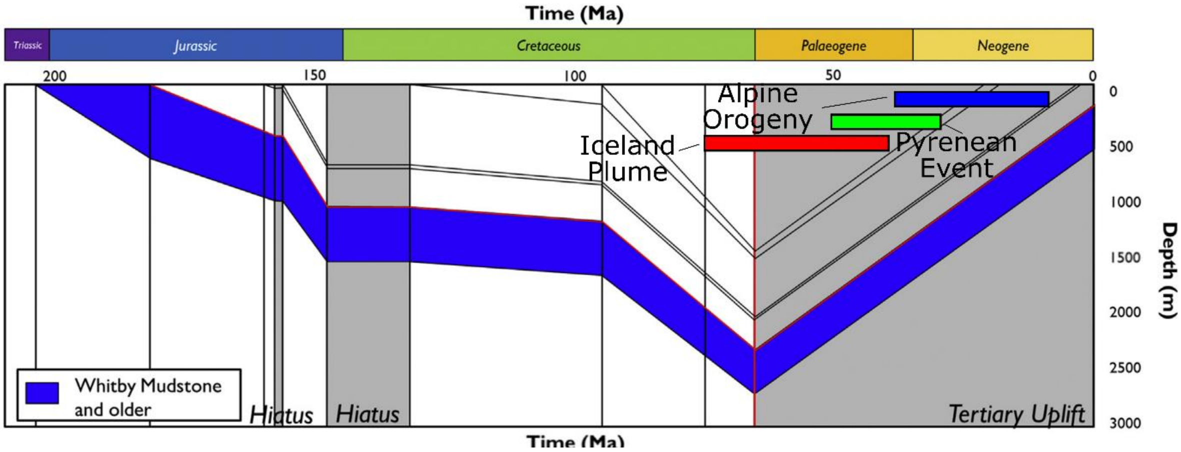


*Fig 1.5. Summary burial history plot modified after Emery (2016) with a summary of the Cenozoic NE Europe tectonic events. Subsidence is shown throughout the Jurassic and Cretaceous before uplift during the Palaeogene and Neogene. This model assumes that the basin sat at high burial of ~2km at 60 Ma before uplift and inversion.*

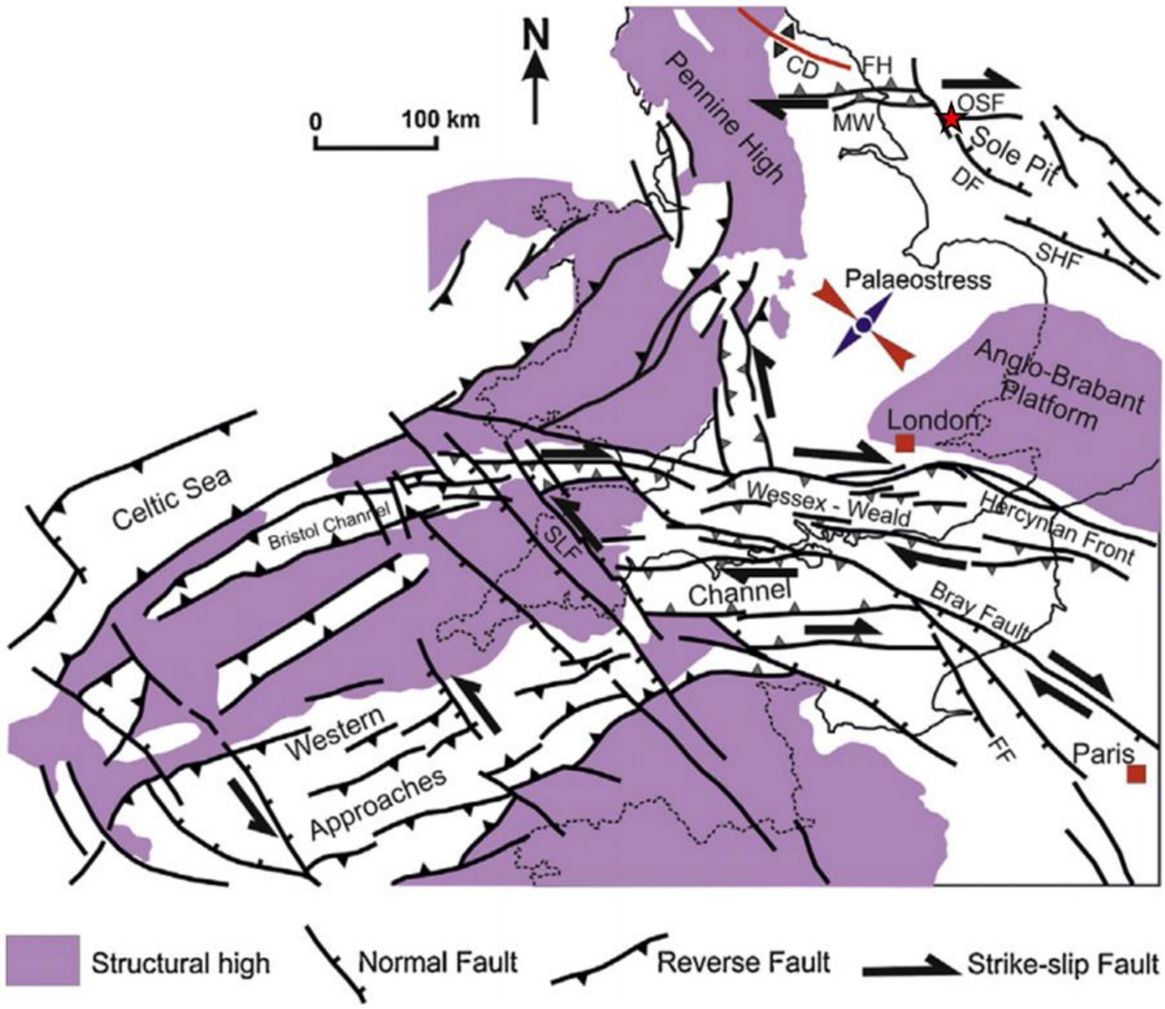


*Fig 1.6. Structural map of palaeostress conditions in onshore and offshore Britain during the Late Cretaceous from Mortimore (2019) and based on palaeostress studies by Hibsch et al. (1995) and tectonic studies by Lake and Karner (1987), Ziegler (1990) and Hibsch et al. (1995). NW-SE compression is indicated with dextral reactivation and reverse motion of the Flamborough Head Fault Zone (FH). The location of a preserved outlier of Cenozoic sediments called the Flamborough Tertiary Outlier (Stewart & Bailey, 1996) is indicated by a red star. The Cleveland Dyke is denoted by CD, Dowsing Fault by DF and The Market Weighton Block by MW.*

### 1.3.2 Stratigraphy

The Cleveland Basin is a Mesozoic basin primarily composed of Jurassic mudrocks with Cretaceous chalk preserved at the southern margins (Powell, 2010). The Mesozoic basin overlies an earlier Carboniferous basin. Permian evaporites and Triassic mudrocks formed on the western margins of the Southern North Sea Basin act as a decollement that effectively decouples the overlying Mesozoic basin from its deeper basement (Fraser & Gawthorpe, 2003).

#### 1.3.2.1 Permian to Triassic

The Early Permian saw subsidence due to intermontane collapse following the Variscan Orogeny, which led to the formation of a series of E-W trending sedimentary basins (Kent,

1980) in what is now NW Europe. The Cleveland Basin formed part of the Southern Permian Basin in an arid, continental setting characterised by deposition of aeolian, sabkha and fluvial deposits of the Rotliegend Group (Underhill, 2009). In the Late Permian, the tropical desert basin was flooded by the Zechstein Sea with fluctuating relative sea-levels, in addition to, short lived differential subsidence leading to the deposition of repeating cycles of carbonate platform deposits (highstand) and the thick evaporites (lowstand) of the Zechstein (Smith & Taylor, 1989; Tucker, 1991). Seven cycles of carbonate and evaporite deposition have been identified by Tucker (1991) in north-eastern England in the Durham and Yorkshire provinces. The Zechstein Evaporites are shown to thin westwards onto the high that the now Cleveland Basin formed at the time (Fig 1.7; Talbot et al., 1982).

During the Middle Triassic, the Cleveland Basin lay near the western margin of an extensive lowland typified by seasonal playa lakes in which reddish marls were deposited (Keuper Marl/Mercia Mudstone groups – Cope et al., 1992; Rawson & Wright, 1992). In the Late Triassic (Rhaetian), a marine transgression (Rawson & Wright, 1992) led to the deposition of the mudstones and intercalated thin limestone beds of the Penarth Group (Ivimey-Cook & Powell, 1991).

#### 1.3.2.2 Lower Jurassic (Lias)

The Lias (Fig 1.7 & 1.8) has a maximum thickness of 454m (Powell, 2010) and lies conformably on the Penarth Group (Powell, 1992). The currently accepted nomenclature for the Jurassic of the Cleveland Basin is set out in Powell (2010) and is summarised below.

The latest Triassic to Lower Pliensbachian Redcar Mudstone Formation (c. 283m thick; Fig 1.7; Powell, 2010) overlies the Penarth Group and represents the continuity of marine conditions, which persisted into the Early Jurassic. The Redcar Mudstone Formation forms the greater section of the Lias and is composed of marine siltstones and mudstones interbedded with carbonate-rich shell beds, concretion beds and fine to medium grained sandstones (Fox-Strangways & Barrow, 1915; Powell, 2010). The Redcar Mudstone is sub-divided into five distinct members: Calcareous Shales, Siliceous Shales, Pyritous Shales, Banded Shales and Ironstones Shales (Tate & Blake, 1876; Fox-Strangways, 1892; Fox-Strangways & Barrow, 1915; Buckman, 1915; Hemingway, 1974; Knox et al., 1991; van Buchem & McCave, 1989; Hesselbo & Jenkyns, 1998; van Buchem & Knox, 1999). The Redcar Mudstone Formation records a change in environment from the shallow marine-dominated tempestites of the Hettangian to Sinemurian, to the hemi-pelagic, deeper water sediments of the lower Pliensbachian followed by shallower marine deposition of the

Lower to Middle Pliensbachian and then transition to pro-delta/shallow marine deposits of the Upper Pliensbachian (Powell, 2010).

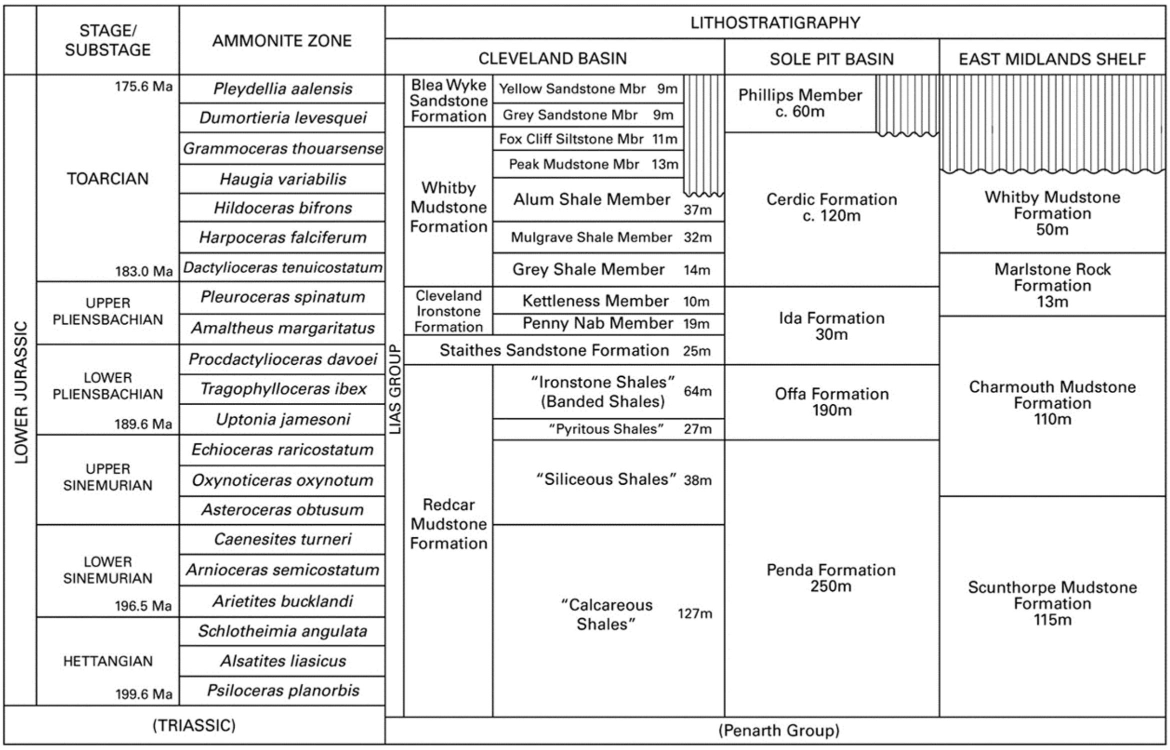


*Fig 1.7. Formalised lithostratigraphic framework for the Lower Jurassic of the onshore Cleveland Basin, East Midlands Shelf and offshore Sole Pit Basin (modified from Powell, 2010).*

The Staithes Sandstone Formation (c. 30m thick; Fig 1.8) overlies the Redcar Mudstone Formation and documents basin shallowing and a change to the deposition of storm-controlled shallow marine sandstones (Howard, 1985; Powell, 2010). The Staithes Sandstone Formation is typified by tempestite deposits of grey, yellow weathering, fine- to medium-grained Upper Pliensbachian age sandstones and siltstones (Howarth, 1955; Hemingway, 1974; Howard, 1985; Powell, 2010).

The Staithes Sandstone Formation passes conformably upwards into the Cleveland Ironstone Formation (c. 28m thick; Fig 1.8). The Cleveland Ironstone is characterised by the deposition of 5-6 cycles of berthierine ooid and siderite mud-rich ironstone seams punctuating a sequence of silty mudstones deposited in laterally extensive lagoons and shallow seas with reduced siliclastic input (Fox-Strangways & Barrow 1915; Hemingway, 1951; Chowns, 1968; Catts et al., 1971; Howard, 1985 Hesselbo & Jenkyns, 1998; Powell, 2010).

The Toarcian, in contrast, represents a coarsening upwards sequence driven by deep open water conditions with occasional bottom-water anoxia due to rapid basin subsidence and increase in clastic influx (Powell, 2010). The Whitby Mudstone Formation (c. 105 m; Fig 1.8;

Rastall, 1905; Fox-Strangways & Barrow 1915; Dean, 1954; Powell, 1984; Knox, 1984; Powell, 2010) is composed of dark grey mudstones and siltstones with shelly fossil beds. The sub-divisions of the Whitby Mudstone Formation have been formalised by Powell (2010): Mulgrave Shale Member (Rawson & Wright, 1992; Hemingway, 1974) and Alum Shale Member (Hemingway, 1974) except in the Peak Trough where the Peak Shale Member (Knox, 1984) and Fox Cliff Siltstone Member are present. The Blea Wyke Sandstones Formation (c. 18m thick) is comprised of grey, mud-rich sandstone (Grey Sandstone Member) which passes upwards into the yellow, well sorted sandstones of the Yellow Sandstone Member (Powell, 2010). The Blea Wyke Sandstone Formation is only present in the Peak Trough due to increase tectonic subsidence.

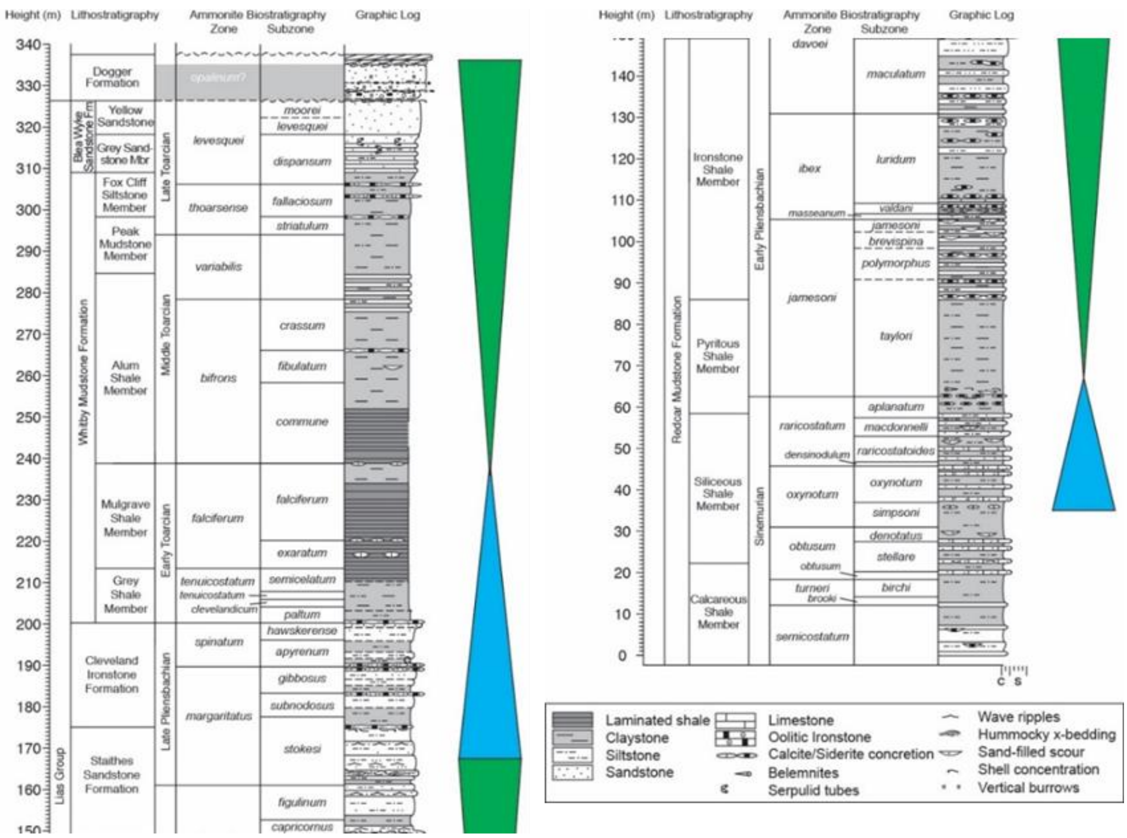


*Fig 1.8. Stratigraphic log of the Lower Jurassic succession of the Cleveland Basin (Hesselbo & King, 2019). Transgressive (blue triangles) and regressive (green triangles) cycles are shown on the right of the diagram.*

### 1.3.2.3 Middle Jurassic

Basinal inversion and gentle folding in the late Toarcian to Aalenian (Black, 1934a; Hemingway, 1974; Hesselbo & Jenkyns, 1998) means that the Dogger Formation rests unconformably on an erosional surface on the Lower Jurassic (Fig 1.8; Powell, 2010). The Aalenian Dogger Formation (0-12m thick) is a complex, condensed shallow water heterolithic unit of predominantly ferruginous sandstone (Rastall & Hemingway, 1943; Dean, 1954; Hemingway & Knox, 1973; Powell, 2010). Later Middle Jurassic deposition was typified by stacked deltaic and fluvial units of the Saltwick Formation (c. 37m thick; Fig 1.9; Hemingway & Knox, 1973; Hesselbo & Jenkyns, 1998) with marine incursions leading to highly variable development of lithofacies (Powell, 2010). These include lime mudstones and ooidal limestones (Eller Beck Formation; c. 2m thick), ooid and peloid carbonates of the Lebberston Member in the marine limestones/sandstones of the Cloughton Formation (c. 85m thick), tidal dependent sand bar deposits, peloidal limestones and marine mudstones (Fig 1.9; Scarborough Formation; c. 30m thick).

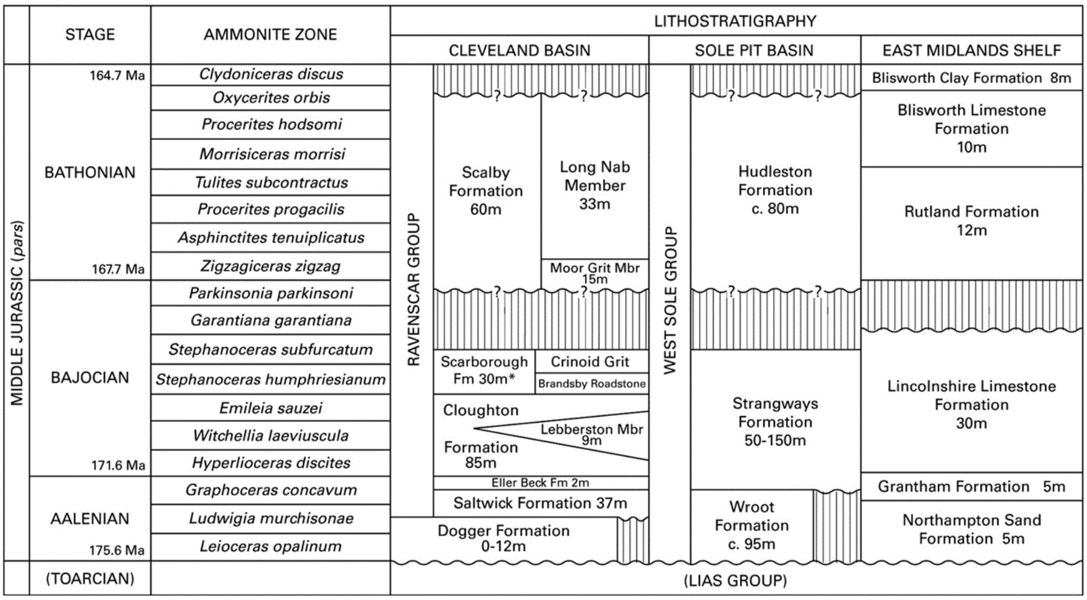


*Fig 1.9. Formalised lithostratigraphic framework for the Middle Jurassic (cont. on Fig 1.6) of the onshore Cleveland Basin, East Midlands Shelf and offshore Sole Pit Basin (Powell, 2010).*

The Scalby Formation (c. 60m thick) represents a return to fluvio-deltaic and paralic deposits (Fig 1.9; Black, 1928; Leeder & Nami, 1979; Powell, 2010). The overlying Cornbrash Formation (c. 1m thick; Fig 1.9) represents a basin wide marine transgression caused by rapid global sea-level rise leading to deposition within a shallow marine environment during the Callovian. The marine clays of the Cayton Clay Formation (c. 4m thick; Fig 1.10; Rawson & Wright, 1992; Powell, 2010) overly the Cornbrash Formation and were followed by siliclastic siltstones and sandstones of the Osgodby Formation (c. 28m thick; Fig 1.10; Wright, 1978).

#### 1.3.2.4 Upper Jurassic

The Osgodby Formation is followed by a transition into the deeper water environment with the deposition of mudstones of the Oxford Clay Formation (0-44m thick) in the Oxfordian. The Oxfordian is followed by further basin shallowing typified by the establishment of carbonate platform units (Corallian Group; c. 121m thick; Fig 1.10) represented by coral patch reefs, ooidal shoals and marine muds. Powell (2010) suggests a complex interaction existing between sedimentation and intra-Oxfordian tectonics due to undefined movement along of the Howardian-Flamborough Fault Zone. Global sea-level rise subsequently led to a shallow marine environment with deposition of the hemi-pelagic marine mudstones of the Ampthill Clay (c. 48m thick; Fig 1.10; Cope, 1974) and Kimmeridge Clay (c. 300m thick) formations. The Kimmeridge Clay Formation is the youngest Jurassic stratigraphy preserved in the Cleveland Basin and is represented by a succession of fossiliferous mudstones interbedded with bituminous mudstones (Powell 2010). The Kimmeridge Clay Formation is followed by a significant period of non-deposition (Rawson & Wright, 1992) caused by tectonic uplift (Powell, 2010).

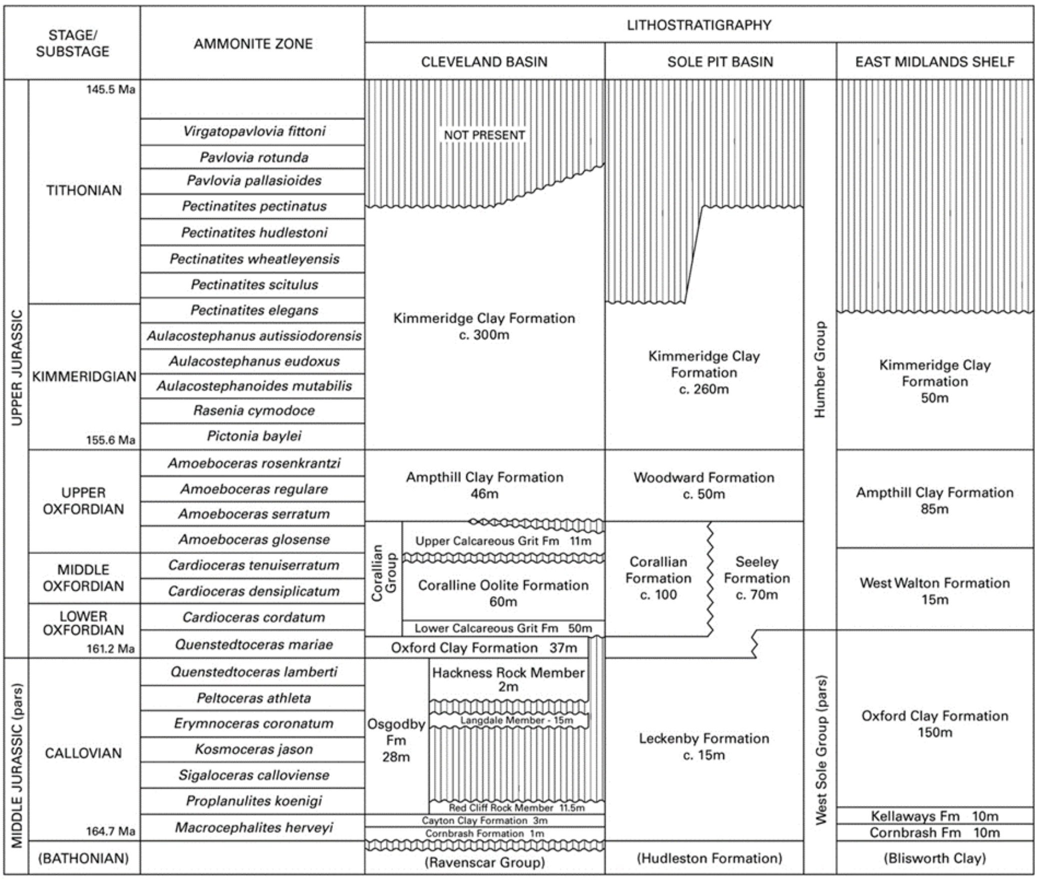


*Fig 1.10. Formalised lithostratigraphic framework for the Middle Jurassic and Upper Jurassic of the onshore Cleveland Basin, East Midlands Shelf and offshore Sole Pit Basin (Powell, 2010).*

### 1.3.2.5 Cretaceous

Tectonic uplift and basin shallowing (Powell, 2010) means that the Kimmeridge Clay Formation is unconformably overlain on the south-eastern coastline of the current coastline Cleveland Basin by the Lower Cretaceous Speeton Clay Formation (c. 102m thick; Rawson & Wright, 1992). The Speeton Clay Formation is made up of dark grey, laminated mudstones (Rawson & Wright, 1992; Powell, 2010) and passes upwards into the base of the Chalk Group (Rawson & Wright, 1992). The stratigraphy of the Cretaceous Chalk Group (c. 485m thick) of Yorkshire and Lincolnshire is summarised by Sumbler (1999) and Mortimore et al. (2001). Sumbler (1999) sub-divided the chalk of the southern Cleveland Basin and East Midlands Shelf into six sub-divisions: The Haunstanton, Ferriby, Welton, Burnham, Flamborough (c. 215m thick; Mitchell, 1994; Whitham, 1993) and Rowe formations. The Chalk Group of northern England is indicated as comprising of thin beds of hard chalks (Jeans, 1980; Sumbler, 1999). No post-Cretaceous stratigraphy is preserved in the onshore Cleveland Basin (Powell, 2010) although it is unclear whether this is due to erosion or non-deposition. Cenozoic sediments are preserved in the offshore area and are discussed below.

#### 1.3.2.3 Offshore Stratigraphy

Powell (2010) indicates a good correlation between the onshore Cleveland Basin and the offshore Sole Pit Basin based on stratigraphical subdivision by Lott & Knox (1994), although there is little literature describing direct comparisons of the onshore Cleveland Basin to the immediate offshore area. As the research here focuses on the onshore basin a full description of the offshore stratigraphy is not necessary; however a brief description is included on the sparse offshore stratigraphy focussed on the Jurassic and Cenozoic stratigraphy.

Dingle (1971) suggests little difference between the onshore Lower Lias and its offshore equivalents based on core samples. The Middle Lias ironstones are absent offshore and suggested by Dunham (1960) to be limited to the current onshore outcropping basin. Offshore the thickness of Lias in the Sole Pit Trough locally is greater than 4000ft/1219.2m (Brunstrom & Walmsley, 1969) although the actual preserved thickness varies significantly due to uplift, halokinesis and associated erosion (Dingle, 1971).

Dingle (1971) suggests that the deltaic/marine facies of the Middle Jurassic extended into the offshore Cleveland Basin but thins to the south towards the Market Weighton Block. Discovery of the Gristhorpe Bed facies a few miles to the north-west of the Sole Pit Basin indicates that the Middle Jurassic deltaic facies likely extended to the margin of the English Zechstein Basin.

Dingle (1971) indicates that knowledge about the development of Callovian to Oxfordian strata offshore is unknown with only Corallian-type oolites proven offshore Filey. The Kimmerdigian strata is indicated to continue offshore and no Jurassic strata younger then

Kimmeridgian are indicated offshore (Dingle, 1971). Offshore, Lower and Upper Cretaceous strata are deposited on an erosional unconformity onto the Jurassic, similar to onshore.

No post-Cretaceous stratigraphy is preserved in the onshore Cleveland Basin, but Stewart and Bailey (1996) describe the Paleogene sequence preserved in the Flamborough Tertiary outlier in the UK Southern North Sea. 184m of Eocene and Palaeocene sediments were analysed from the 47/4b-6 well. The contact between the Palaeocene and the underlying Upper Cretaceous (Late Maastrichtian age) strata is indicated as unconformable or representing a normal fault (Stewart & Bailey, 1996). The Paleogene stratigraphy is split into three units with lateral equivalents of the Horda, Balder-Sele and Lista formations (Cameron et al., 1993). The Eocene interval consists of silty mudstones which grade up to micromicaceous siltstones. The youngest beds are Middle Eocene in age. These sediments indicate that Cenozoic sedimentation occurred in parts of the Southern North Sea. It is unclear whether similar sedimentation occurred in the onshore Cleveland Basin with subsequent erosion during exhumation or whether earlier exhumation and tilting prevented the deposition of similar stratigraphy in the already uplifted Cleveland Basin.

### 1.3.3 Onshore Basin Structures

The next section will discuss the major structures that make up the onshore Cleveland Basin and will form the main focus of this research. Dominant basin-scale structures in the onshore Cleveland Basin can be split into four distinct categories (Fig 1.11): the E-W-trending Vale of Pickering and Flamborough fault zones (Fig 1.11-1.13), N-S to NNW-SSE-trending normal faults (Fig 1.1), including those bounding the Peak Trough, the E-W trending Cleveland Anticline (Fig 1.9) and associated N-S trending inversion structures, and the WNW-ESE trending Cleveland Dyke.

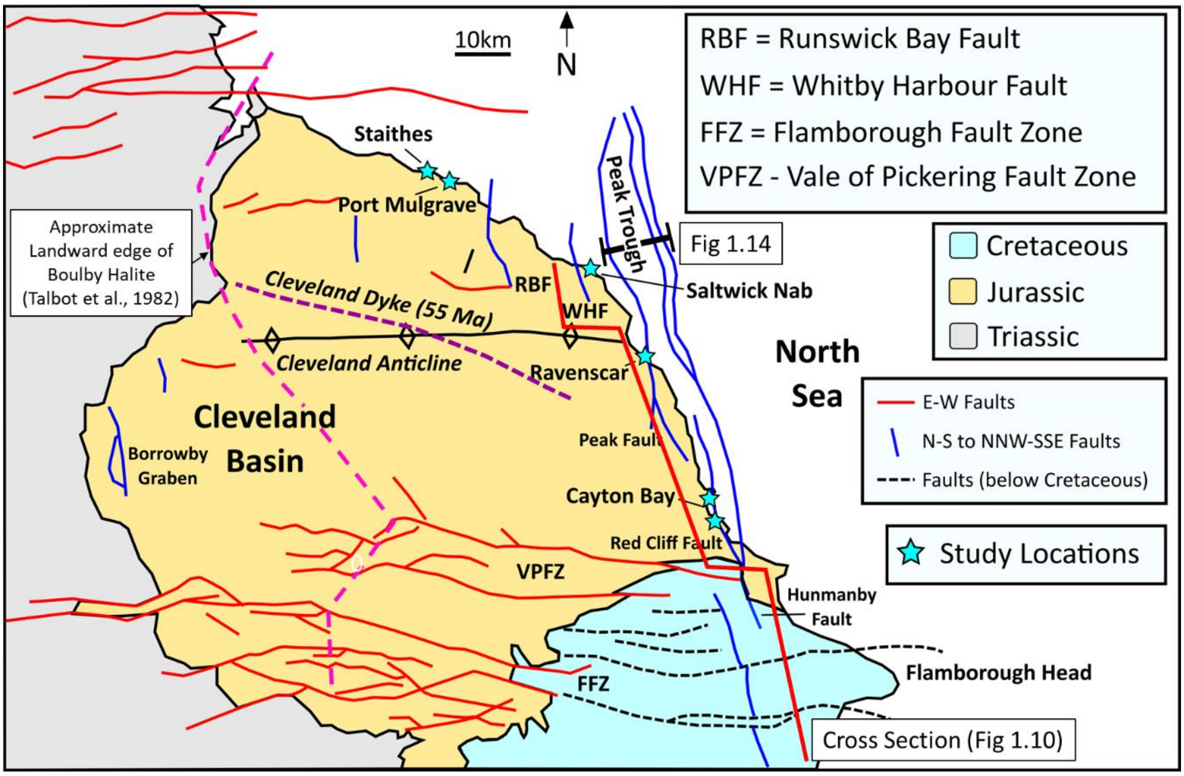


*Fig 1.11. Structural Map of the Cleveland Basin showing the major basin structures and Mesozoic outcrop (redrawn after Imber et al., 2014). N-S to NNW-SSE trending faults (blue), Flamborough and Vale of Pickering fault zones (red), Cleveland Anticline (black) and the Cleveland Dyke (purple). The Triassic outcrops to the west of the basin (grey), the Jurassic in the main basin (yellow) and Cretaceous chalk to the southeast (light blue).*

#### 1.3.3.1 N-S trending normal Faults

The eastern margin of the Cleveland Basin is cut by numerous N-S to NNW-SSE-striking normal faults that include the Runswick Bay Fault, the Whitby Harbour Fault and the Peak Trough faults including the Peak Fault, Cayton Bay Fault and Red Cliff Fault (Fig 1.17; Hemingway & Riddler, 1982; Milsom & Rawson, 1989; Rawson & Wright, 1992). Fault movement is thought to have occurred during Early, Middle and Late Jurassic to Early Cretaceous times (Milsom & Rawson, 1989). Interpretation of seismic reflection profiles (Milsom & Rawson, 1989) and field relationships (Howarth, 1962; Alexander, 1986; Powell, 1992; Alexander & Gawthorpe, 1993) have been used to document synsedimentary movement of the Runswick Bay, Whitby Harbour and Peak faults with across-fault thickening or facies changes in the Lower Jurassic Whitby Mudstone Fm and the Middle Jurassic Saltwick Fm. McKeen (2019) suggests that Middle Jurassic reactivation of the Peak Fault is linked to a process analogous to radial expansion faults around a salt diapir caused by the rise of the Central North Sea Dome (Underhill & Partington, 1993). The western margin of the present basin is thought to correspond in part to the north-south trending Borrowby Graben which is suggested to display synsedimentary movement in the Middle Jurassic similar to the Peak Trough (Powell, 1992; Powell, 2010).

Interpretation of 2D seismic cross sections by Milsom & Rawson (1989) suggested that the Peak Trough faults are listric in nature and detach at multiple levels down into the underlying Triassic mudstones and Zechstein evaporites at depth. McKeen (2019) suggests that the Zechstein evaporites exerted a control on the development of the Peak Trough faults with marginal facies in the footwall pinning the faults and mobile evaporites in the hanging wall facilitating listric detachment development.

The Early Jurassic Blea Wyke Sandstone Formation is only preserved in the Peak Trough and indicates synsedimentary thickening of the Toarcian into the regional scale trough (Milsom & Rawson, 1989; Powell, 2010). Hemingway & Riddle (1982) suggest that the Peak Fault has undergone 8km of sinistral movement during the Cenozoic due to variations in Upper Lias and Middle Jurassic strata and offsets of what they term the “pre-Dogger structural basin”. Facies changes, however, could be explained through syn-sedimentary thickening and facies changes in the fault hanging wall according to Milsom & Rawson (1989).

The Hunmanby Fault marks the southern extension of the eastern margin of the Peak Trough and extends southwards towards the Flamborough Head Fault Zone (McKeen, 2019). The Hunmanby Fault is indicated from seismic interpretation to display synsedimentary thickening of the Middle, Late Jurassic and Early Cretaceous (Milsom & Rawson, 1989; McKeen, 2019). Juxtaposition of the Upper Cretaceous Chalk against the Lower Cretaceous Cromer Knoll by the Hunmanby Fault is suggested by Milsom & Rawson to represent Cenozoic inversion in the Cleveland Basin. Detailed mapping outlined by Vernon et al. (2020) documents the southern extension of the Peak Trough which they term the Hunmanby Trough where it intersects the Flamborough Fault Zone (Fig 1.14). The normal faults of the Hunmanby Trough are demonstrated to offset the E-W Langtoft and

Bempton Faults and are suggested to have been reactivated under dextral transpression during Late Cretaceous to Early Cenozoic inversion.

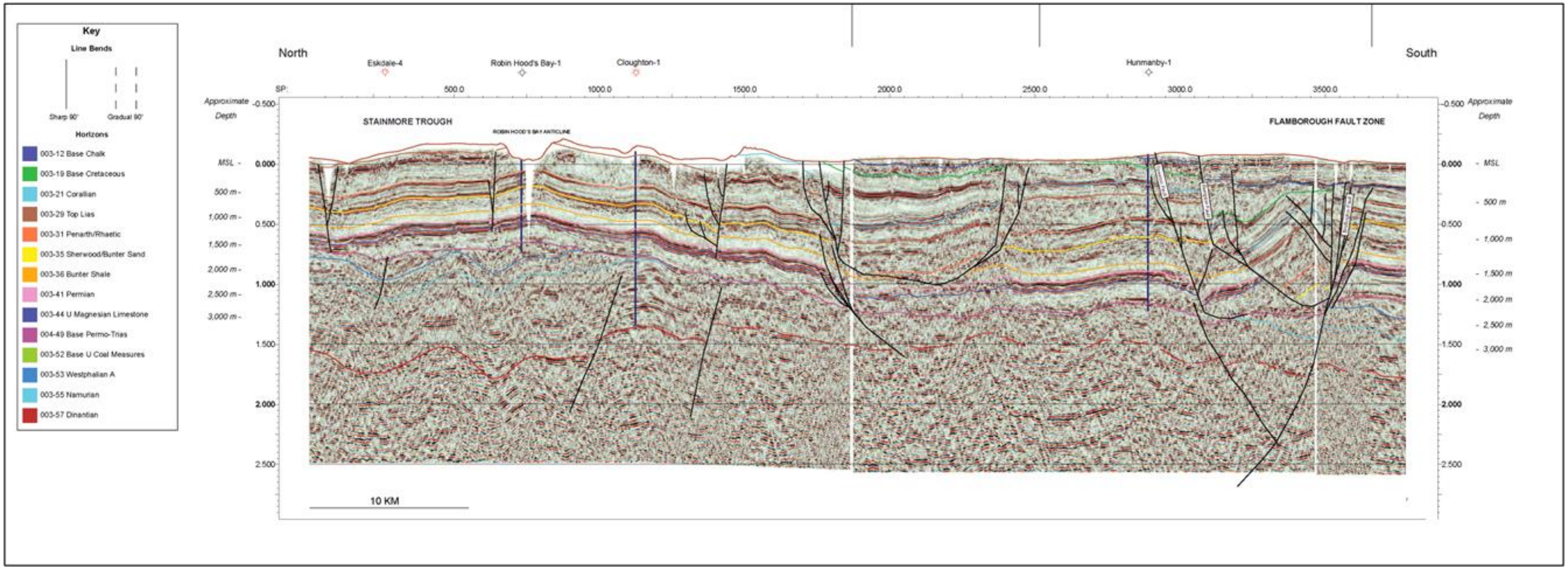


*Fig 1.12. Interpreted seismic cross section of the Cleveland Basin from the UK Onshore Geophysical Library (UKOGL). E-W trending faults are shown to detach on the underlying Permian. The cross section shows distinct faulting patterns between the Mesozoic Cleveland Basin and the underlying Carboniferous basin with thin-skinned detachment of the Flamborough Fault Zone over an older, underlying E-W striking fault zone. The Mesozoic basin shows structural inheritance of faults from the underlying Carboniferous basin. The Cleveland Anticline is visible on the left hand margin of the cross section with low amplitude folding of the Mesozoic section. The focus of this study will be the Jurassic stratigraphy, which is shown to outcrop at the surface at the northern margin of the cross section and is cut by a number of fault structures that are interpreted to terminate or sole out on the underlying Permian-Triassic stratigraphy.*

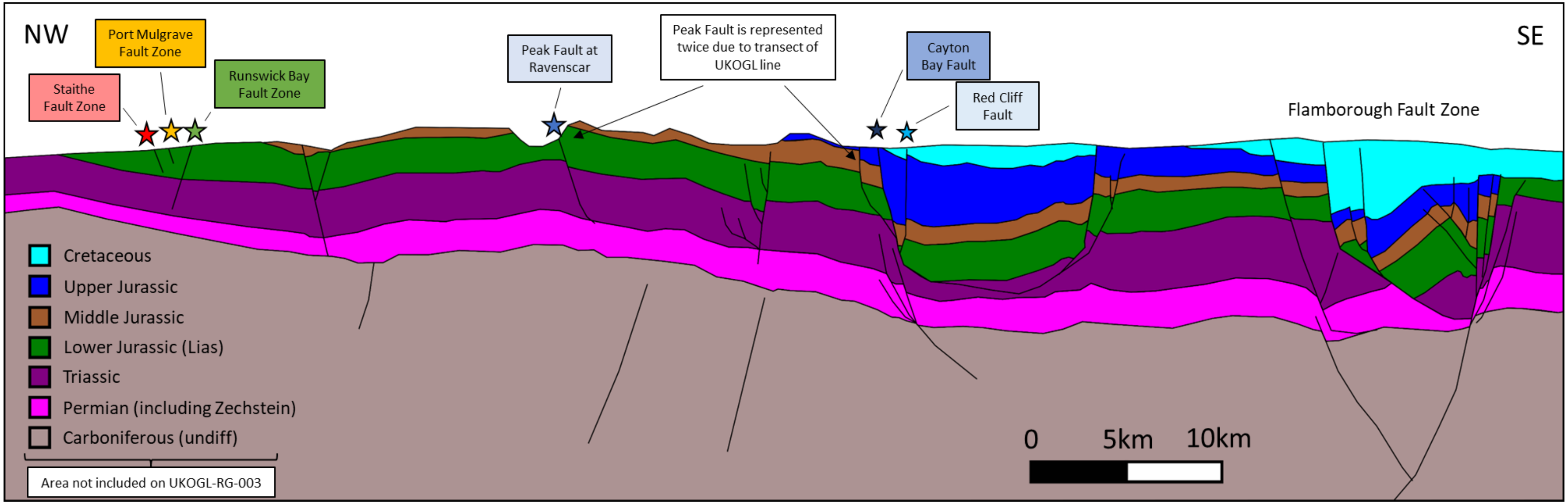


*Fig 1.3. Schematic cross section of the Cleveland Basin showing the an approximate NW-SE transect through the Cleveland Basin based on and following the same transect line as the UKOGL seismic line in Fig 1.10.*

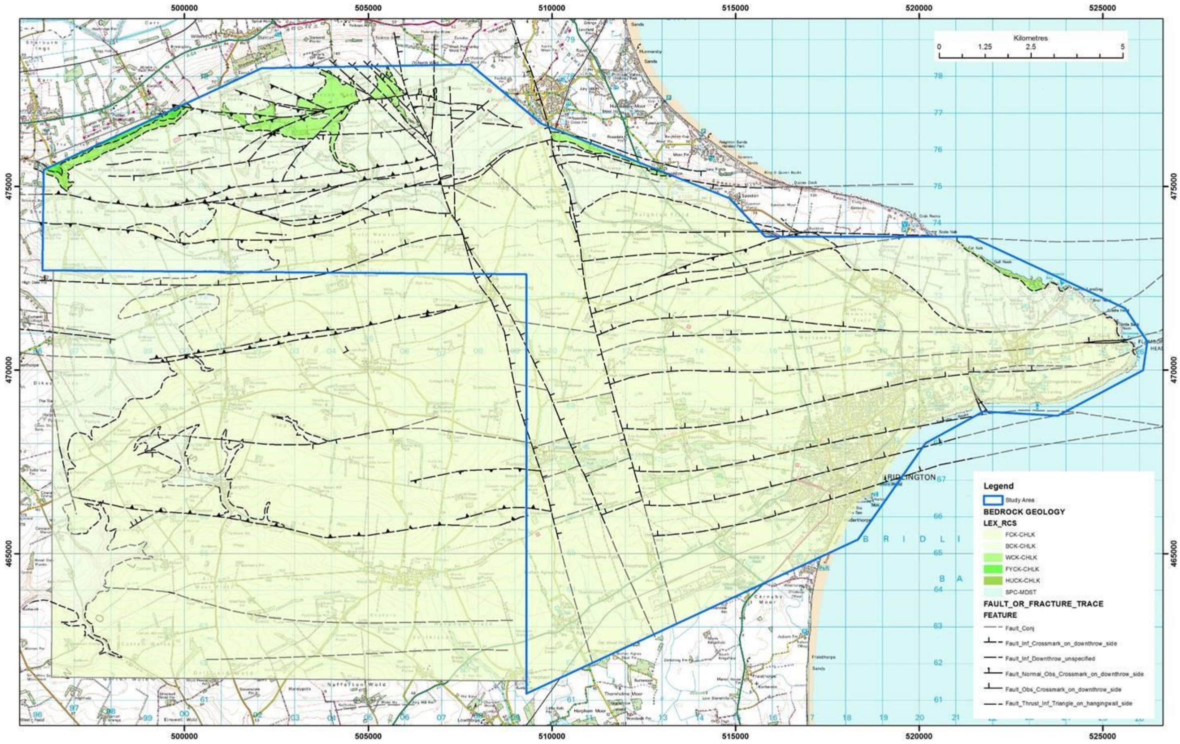


*Fig 1.14. Mapping of the onshore Flamborough Fault Zone (Vernon et al., 2020) demonstrates abutment and partitioning of the Flamborough Fault Zone across the southern continuation of Peak Trough (Hunmanby Fault). Contains Ordnance Data © Crown Copyright and database rights 2020 Ordnance Survey Licence no 100021290 Geological data British Geological Survey © UKRI 2020.*

Imber et al. (2014), Imber (Pers. Comm.) and De Paola (Pers. Comm.) have observed the presence of N-S striking predominantly normal faults at Staithes and Port Mulgrave with Imber (Pers. Comm.) also highlighting the presence of localised strike-slip fault movements at Port Mulgrave. These structures will be described in detail in Section 3.2.3 and shown to be related to a previously unconstrained period of faulting and reactivation of existing structures.

### 1.3.3.2 Flamborough and Vale of Pickering Fault Zones

The Flamborough Fault Zone (also termed the Howardian-Flamborough Fault Belt) (Fig 1.15) is a zone of E-W trending faults extending inland for 50-60km and is linked to the E-W Vale of Pickering Fault Zone which lies to the north (Kirby & Swallow, 1987). The Flamborough Fault Zone is hypothesised to have formed during the Late Jurassic to Early Cretaceous as a set normal faults due to differential movements of the Cleveland Basin and the Market Weighton High to the south (Wright, 2009; Powell, 2010; Sagi et al., 2016). Many authors suggest that it experienced later reverse reactivation during the Late Cretaceous to Early Cenozoic (Kirby & Swallow, 1987; Starmer, 1995). The deformation structures seen onshore have been documented in detail by Starmer (1995; 2008; 2013), Sagi et al. (2016) and Roberts et al. (2020). The fault zone downthrows to the north and is suggested by Kent (1974, 1980)to mark the onshore extension of the Dowsing Fault Zone, however, Kirby & Swallow (1987) contradicts this indicating that the offshore Flamborough Fault terminates at an arcuate junction with the Dowsing Fault Zone.

Seismic interpretation by Kirby & Swallow (1987) suggest a combined faulting style along the FHFZ, in which, steeply dipping faults cut the underlying Permian and Carboniferous strata, whilst shallower listric faults detach along on a Zechstein decollement. McKeen (2019) describes deep faulting at the Rotliegend and deeper levels and suggests post-Permian dip-slip movement. McKeen (2019) proposes that active extensional faulting occurred during the Rotliegend creating a palaeo-low in the Flamborough Fault Zone hanging wall leading to the establishment of a desert lake environment influencing deposition of the Silverpit Claystone Formation (Capitanian-Wuchiapingian).

Jeans (1973) and Kirby & Swallow (1987) suggest Early Cretaceous movements in the Chalk of Flamborough Head with a phase of subvertical normal faulting forming a graben structure followed by the development of listric normal faults with Late Cretaceous uplift of the Cleveland Basin leading to inversion of the previously extensional structures.

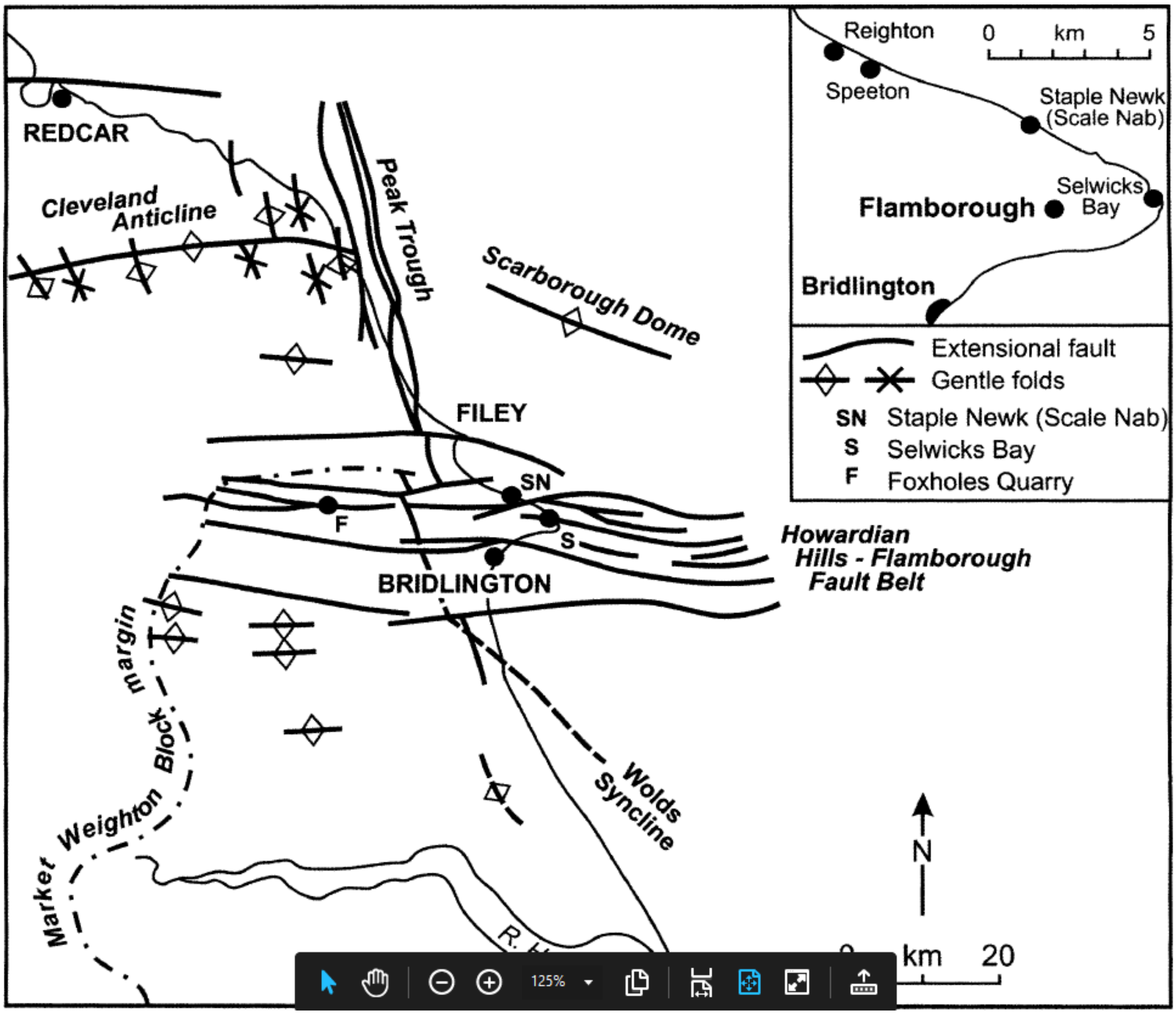

*Fig 1.15. Regional structure map from Starmer (2008) showing the Howardian-Flamborough Fault Zone, Cleveland Anticline (and subsidiary N-S trending folds), Scarborough Dome, Peak Trough and an inset map of the key locations at Flamborough Head.*

McKeen (2019) documents a general west to east movement of salt in the vicinity of the Flamborough Head Fault Zone with the zone of Z2 salt withdrawal trending parallel to the underlying Carboniferous to Rotliegend structures with the base of the Zechstein displaced upwards. McKeen (2019) uses this displacement of the base Zechstein up to Z2 Strassfurt halite level to suggest a possible tectonic control on the initiation of halokinesis and demonstrates a distinct detachment between the basement faults (in the Palaeozoic) and younger faults, which detach on the Zechstein evaporites in the Flamborough Head Fault Zone.

Vernon et al. (2020) split the Flamborough Fault Zone into western and eastern portions on either side of the NNW-SSE trending Hunmanby Trough. The Western Flamborough Fault Zone is characterised by three graben structures which are each associated to a deep-seated faults whilst the Eastern Flamborough Fault Zone is characterised by steep, north-dipping faults which terminate at depth against the listric Bempton Fault. Vernon et al. (2020) suggest that the complex interactions between the Hunmanby Trough and the Flamborough Fault Zone are indicative of a history of reactivation of both fault zones with normal faults of the Flamborough Fault Zone undergoing reactivation as reverse faults during Late Cretaceous to Early Cenozoic inversion to accommodate uplift.

Sagi et al. (2016) suggested Late Jurassic to Early Jurassic N-S extension followed by Cenozoic E-W compression for the Flamborough Fault Zone based on structural analyses of outcrops at Selwicks Bay. Roberts et al. (2020) demonstrate through new field and microstructural observations coupled with the use of U-Pb calcite geochronology on extensional faults and tensile veins at Selwicks Bay that a phase of Early Paleocene to Early Eocene (63-55 Ma) extensional faulting along the Frontal Fault Zone at Flamborough Head. This phase of extensional faulting was associated with an episode of prolonged voluminous fluid-flow and the development of a fissure open to the surface. This period of Paleogene extension is indicated to postdate any contractional/transpressional deformation (Roberts et al., 2020) and a model is proposed by which the majority of deformation at Selwicks Bay can be explained through overlapping strike-slip and extensional deformation with no evidence of Alpine or Pyrenean inversion.

#### 1.3.3.3 Cleveland Anticline and fold structures

The main inversion structure in the Cleveland Basin is believed to be the E-W trending Cleveland Anticline that passes eastwards offshore into the Scarborough Dome (Fig 1.14; Dingle, 1971; Hemingway & Riddler, 1982; Starmer, 2008). The Cleveland Anticline is flanked to the north and east by a series of N-S and E-W trending subsidiary anticline and synclines (Hemingway & Riddler, 1982; Fig 1.15). The main axis of the Cleveland Anticline is shown on Figure 1.16 and detailed by Hemingway & Riddler to pass offshore at Robin Hood's Bay. The Cleveland Anticline and subsidiary folds have been linked to Late Cretaceous to Early Cenozoic inversion and tilting of eastern England (Kent 1980) or to Oligocene to Miocene inversion (Hemingway & Riddler, 1982). The latter timing is problematic considering the dates obtained from the FHFZ by Roberts et al. (2020), which suggests that the main phase of compression pre-dates Palaeocene mineralisation. Folding and the timing of inversion will be discussed in detail in Chapter 6 in relation to the findings of research.

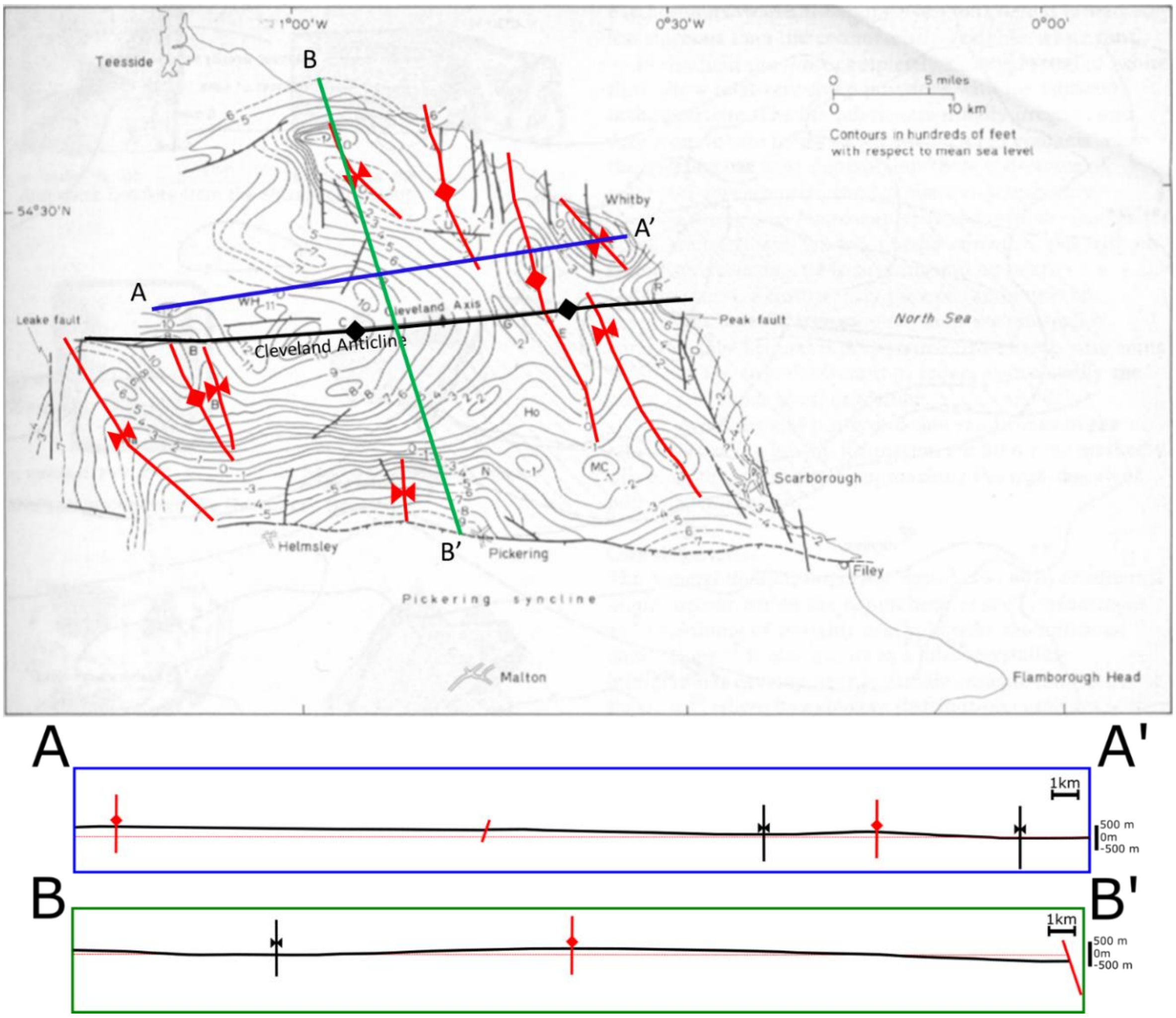


*Fig 1.16. Generalised structural map of the northern Cleveland Basin projected on to the Dogger Formation modified from Hemingway & Riddler, (1982). B – Bilsdale syncline, C - Cleveland dome, E – Eskdale anticline, F – Fylingdales syncline, G – Goathland syncline, H – Hackness basin, Ha – Hambleton syncline, Ho – Horcum syncline, MC – Moor Cock dome, N – Newton Dale syncline, R – Robin Hood's Bay dome, S – Skelton basin, U – Ugthorpe basin, W – Whitby basin, WH – Westerdale horst. The Cleveland Anticline axis is shown trending E-W and passing offshore at Robin Hood's Bay just north of the onshore limits of the Peak Fault. Two clear trends of folding exist with NNW-SSE trending folds annotated on in red and the E-W trending Cleveland Anticline in black. The black line shows the Top Dogger Formation with the red line denoting a 0m reference frame. Two cross-sections are shown A to A' (E-W) and B to B' (N-S). These show that folding is very gentle with interlimb angles of 1-2°.*

#### 1.3.3.4 Cleveland Dyke

The Cleveland Dyke (Fig 1.11) is a 55.8 ±0.3Ma (Fitch et al., 1978) NW-SE trending dyke which extends 430km from Mull in northwest Scotland through the Scottish Midland Valley to the coast of the Cleveland Basin, Yorkshire (MacDonald et al., 1988). Dewey & Windley (1988) suggested that the propagation of Cleveland Dyke south-eastwards joined into northward propagating fractures from the Rhine Graben in the Sole Pit Basin. Versey (1937) remarks that the Cleveland Dyke follows the northern flank of the Cleveland Anticline and seems to postdate this folding and therefore uplift and inversion of the Cleveland Basin.

#### 1.3.3.5 Summary

A series of N-S and E-W oriented fault and fold structures have been described. N-S fault structures will be analysed intensely during this research and along with E-W faults such as the Flamborough Head Fault Zone were formed initially as synsedimentary fault structures. Whether calcite mineralisation relates to this initial movement or to a later phase of reactivation will be examined during this research. The Cleveland Dyke is a useful structure as it can be linked directly to the development of the North Atlantic Igneous Province and development of the proto-Iceland plume.

### 1.3.4 Offshore Basin Structures

While offshore fault structures are not the main focus of this research an introduction to the offshore structures is important to provide context for the tectonic history of the Cleveland Basin as a part of the larger Southern North Sea.

The evolution of the North Sea in the Cenozoic was dominated by thermal subsidence (Stewart & Bailey, 1996). Most extensional faults in the Cenozoic and Mesozoic strata mapped between the Central Graben and the UK coastline detach down into the Zechstein evaporites (Stewart & Bailey, 1996). This was expressed by large-scale normal fault inversion, uplift and erosion in the Sole Pit Basin. Shortening in the basement outside of the Sole Pit Trough is indicated and led to further amplification of salt-cored structures (Stewart & Bailey, 1996). Mobile evaporites in the SNS have in general led to decoupling of the underlying Palaeozoic structures from the overlying Mesozoic and Cenozoic structures (Van Hoorn, 1987; Stewart & Bailey, 1996; Underhill, 2009; McKeen, 2019).

The immediate offshore area of the Cleveland basin is poorly constrained with little well constraint and few seismic lines of which a few are reinterpreted in Grant et al. (2020), although their focus was predominantly on the eastern margin of the Dowsing Fault Zone.

The Peak Trough has been imaged by Milsom & Rawson (1989) with thickening of reflectors shown in Figure 1.17 interpreted to represent Jurassic growth faulting. Milsom & Rawson (1989) show detachment of the Peak Trough onto the underlying Zechstein Evaporite sequence.

#### 1.3.4.1 Peak Trough

The offshore Peak Trough (Fig 1.13) is a zone of complex normal faulting trending 330° subparallel to the coast coming onshore at Ravenscar (Milsom & Rawson, 1989). Milsom & Rawson (1989) have interpreted the western margin of the Peak Trough to be the continuation of the onshore Peak Fault, while the eastern margin is inferred to represent the onshore Red Cliff Fault at Cayton Bay. The exact architecture of internal faults such as the Cayton Bay Fault and Scarborough Castle Hill Fault requires three-dimensional imaging (Milsom & Rawson, 1989). Similar to onshore, the Zechstein Evaporites are shown to have acted as a decollement zone into which the faults of Peak Trough detach (Milsom & Rawson, 1989).

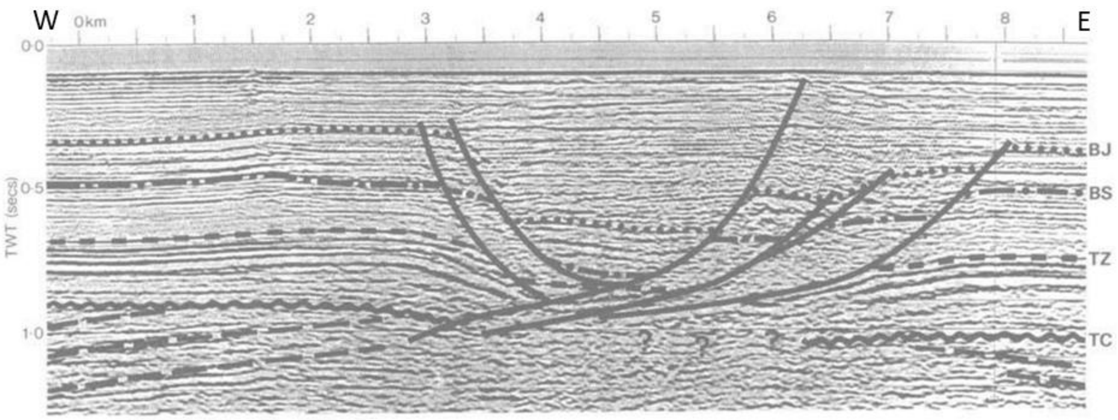


*Fig 1.17. Interpretation of a migrated seismic section across the Peak Trough, offshore Whitby (Milsom & Rawson, 1989). TC is Top Carboniferous, TZ is Top Zechstein, BS is Bunter Shales and BJ is Base Jurassic. The location of this section is shown on Figure 1.11.*

#### 1.3.4.2 Flamborough Fault Zone

The Flamborough Fault Zone passes offshore at Flamborough Head and is suggested by Kirby & Swallow (1987) to terminate against the Dowsing Fault Zone. The termination is deflected northwards which is inferred to reflect Late Cretaceous sinistral movements along the Dowsing Fault Zone (Kirby & Swallow, 1987). Offshore seismic interpretations by Stewart & Bailey (1996) and McKeen (2019) indicate full detachment of the Flamborough Fault Zone from the underlying Permian and Carboniferous basement with rotation of an N-S oriented graben during inversion above salt cored buckle folds. An N-S oriented seismic line interpretation (Fig 1.15, Stewart & Bailey, 1996) shows domino-style faulting of Triassic and Jurassic units that detach onto the Zechstein evaporites (Fig 1.18) with thickening of Liassic sediments in the hanging wall. The Cleveland Basin (northern footwall) margin of the Flamborough Fault Zone in Fig 1.15. is noticeably uplifted and tilted relative to the southern margin (Stewart & Bailey, 1996). This uplift could reflect regional tilting of the onshore Britain during the Late Cretaceous to Early Paleogene described previously.

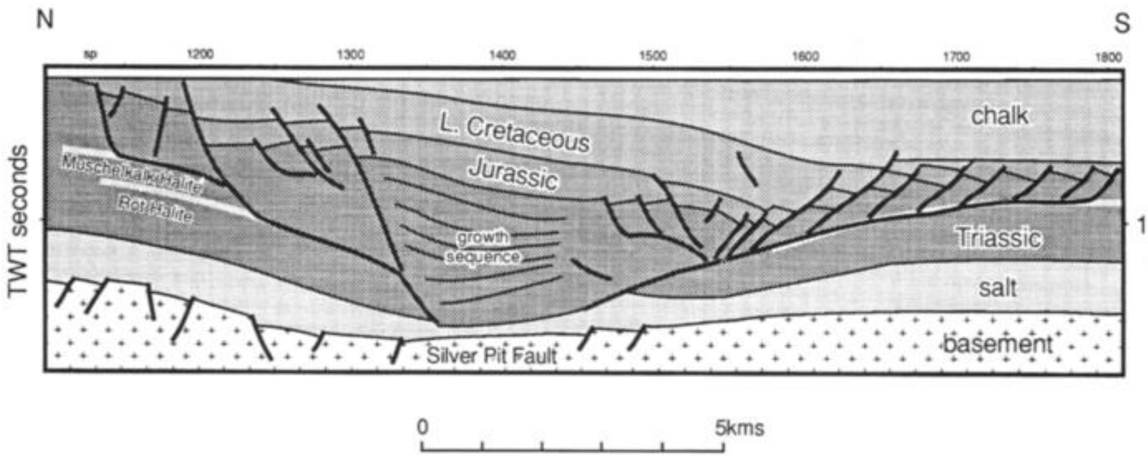


*Fig 1.18. Interpretation from a seismic profile of the offshore Flamborough Fault Zone (Stewart & Bailey, 1996). Domino-style fault blocks are shown to be rotating into the graben structure with uplift of the northern section.*

### 1.3.4.3 Dowsing Fault Zone

The Dowsing Fault Zone forms the western boundary fault of the Sole Pit Basin (Fig 1.6) and is indicated by Kirby & Swallow (1987) to have geometries indicative of transcurrent motion in proximity to the Flamborough Fault Zone. Further south, at the margin of the Sole Pit Basin, the Dowsing Fault Zone is indicated as having dextral movement during the early Permian to early Cretaceous times, followed by sinistral motion during the Late Cretaceous (Glennie & Boegner, 1981). Kirby & Swallow (1987) suggest that dextral motion was generated during E-W extension during the Permian-Triassic opening of the Southern North Sea with later dextral reactivation due to N-S oriented compression during the Late Cretaceous.

### 1.3.4.4 Sole Pit Basin

The offshore Sole Pit Basin formed in the latter part of the Triassic and is indicated by Stewart & Bailey (1996) to be the deepest part of the Mesozoic Southern North Sea Basin. Late Triassic extension was synchronous with initiation of Late Triassic salt tectonics, with salt swells forming in the Sole Pit Trough (Stewart & Coward, 1995). Reactivation of Variscan basement faults led to enhanced Late Triassic to Early Jurassic subsidence in the

Sole Pit Basin attributed to mid-Triassic salt movement of the Upper Permian evaporites (Balson et al., 2001).

The Sole Pit Basin is indicated to have undergone Late Cretaceous inversion (Glennie & Boegner, 1981) with an additional inversion phase in the Oligocene with total uplift of 1500m (Van Hoorn, 1987). Alternatively Ziegler (1989) suggested that the main phase of inversion occurred during the Eocene to Oligocene. Kley (2018) discusses the relative timings of Cretaceous and Cenozoic inversion events in the Southern Permian Basin and attributes Late Cretaceous uplift to the Subhercynian orogeny and Late Eocene to Late Oligocene/Early Miocene to the Pyrenean/Savian orogeny. Kley (2018) suggests that Late Cretaceous inversion was related to horizontal shortening with thrusting and folding accounting for much of the uplift. Inversion is suggested to have terminated during the latest Cretaceous with only minor shortening continuing into the early Paleogene (Kley, 2018).

Late Eocene to Late Oligocene/Early Miocene (Pyrenean/Savian) N-S shortening is not very different from the NNE-SSW shortening direction during the Cretaceous event (Kley, 2018). The two inversion events are isolated temporally and spatially, with spatial overlap only indicated in the southwestern-most Sole Pit Basin and Southern North Sea.

#### 1.3.4.5 Flamborough Tertiary Outlier

The Flamborough Tertiary Outlier is significant as a preserved outlier of Cenozoic sediments in blocks 42/29 and 474b in the NE corner of the East Midlands Shelf in the Southern North Sea (Stewart & Bailey, 1996). The outlier is split into two structural compartments with an unfaulted western portion adjoined to a NW-SE trending graben possibly reflecting underlying halokinetic controls related to basinward sliding caused by Cenozoic inversion of the Dowsing Fault Zone (Stewart & Bailey, 1996). Stewart and Bailey (op. cit.) have used seismic reflection and biostratigraphic data across the Flamborough Tertiary Outlier to suggest that inversion events occurred during the Campanian, late Maastrichtian and intra-Miocene. The preserved Palaeogene sediments are interpreted to represent the eroded cover of the East Midlands Shelf (Stewart & Bailey, 1996).

#### 1.3.4.6 Summary

Whilst the early Mesozoic history of the Cleveland Basin and southern North Sea is generally agreed upon, its later tectonic history is complicated with many different inversion events suggested. The recent findings by Roberts et al. (2020) imply a total absence of significant onshore inversion after the Late Cretaceous to Palaeocene. This appears to be in contrast to the offshore Sole Pit Basin and Flamborough Tertiary Outlier, which have been indicated to have undergone significant intra-Cenozoic inversion. A focus of this research is made to analyse onshore fault structures for evidence of Cenozoic deformation to better constrain the Cenozoic history of the onshore Cleveland Basin.

## 1.4 Objectives

1. Describe and sample calcite mineralisation along faults and fractures that crop out in coastal exposures in the Cleveland Basin.

2. Identify locally syn-kinematic and post-kinematic calcite veins and use U-Pb calcite geochronology to constrain the timing of deformation and fluid-flow.

3. Use C-O stable and clumped carbonate isotopic analyses of calcite fills to identify spatial and temporal patterns of fluid-flow.

4. Interrogate the results in the context of the regional tectonic history of onshore Britain and the Southern North Sea to propose a regional model for calcite associated deformation and fluid-flow in the Cleveland Basin.

5. Identify and analyse the implications for wider tectonics of the Southern North Sea and western Europe.

# Chapter 2- Methodology

## 2.1 Introduction

The aim of this chapter is to introduce and describe the various method utilise to collect data and analyse outcrops and samples as part of this thesis. This PhD project has been designed so that the methods used build a narrative from initial large-scale structure mapping and field and structural analysis down to small-scale geochemical and U-Pb calcite geochronology (Figure 2.1). Detailed sample imaging and detailed structural analysis provides a link between to larger outcrop and regional scale observations and small centimetre-scale to millimetre-scale analyses.

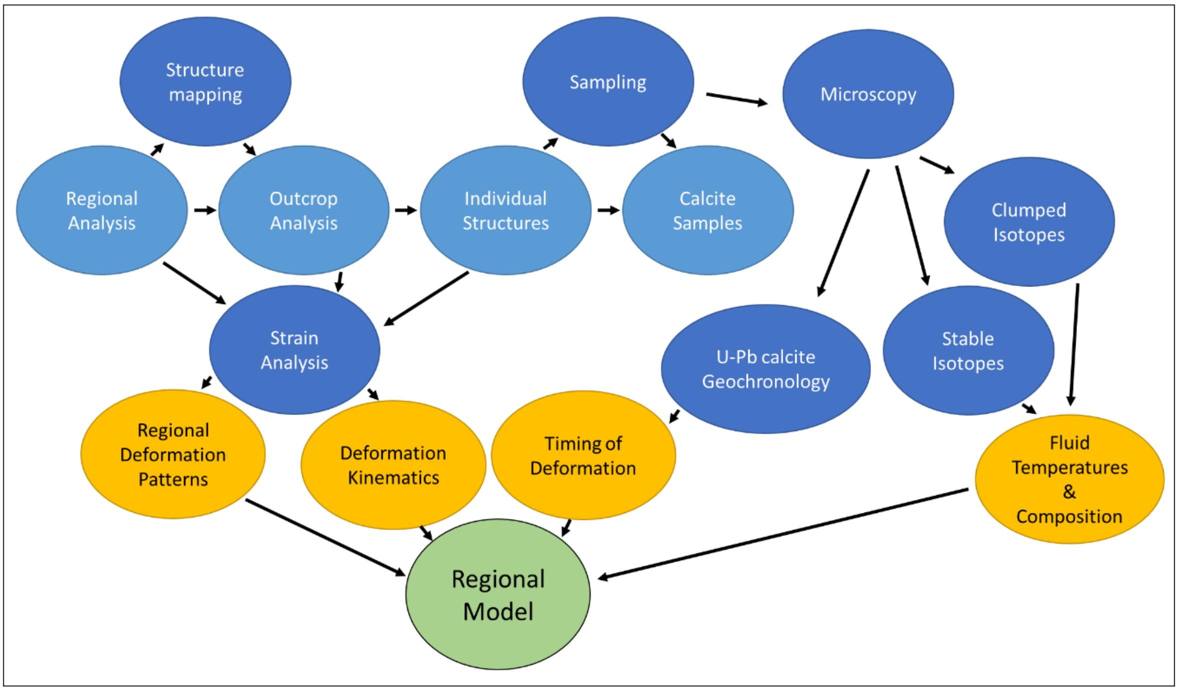


*Fig 2.1. Mindmap of the different analyses (blue and light blue) used in this project and their relations to each other and to the main objectives and outcomes (yellow). These will all then feed into a regional model (green).*

### 2.2 Field and Structural data

To build a regional and local picture of the structures and tectonics by analysing key locations and sampling a wide range of calcite-mineralised structures.

### 2.3 Petrography

Petrographical analysis utilises microscopic and Scanning Electron Microscopy (SEM) to image key samples and identifying and document structures detailing the relationship of calcite mineralisation to deformation.

### 2.4 U-Pb Geochronology - Carbonate LA-ICP-MS

Calcite U-Pb geochronology builds on previous analysis to provide absolute age constraints on the timing of calcite mineralisation.

2.5 Trace Elements Carbonate LA-ICP-MS

Trace elements analysis map has been utilised to map the relative distribution of key element concentrations.

2.6 Stable Isotopes

Stable isotopes are a key analysis that have been used to build an picture of the sourcing of oxygen and carbon isotopes in calcite in the key samples.

2.7 Clumped Isotopes

Clumped isotopes builds on the stable isotope work to identify distinct trends in the grouping of oxygen and carbon isotopes providing important information on the temperature and isotopic composition of fluids.

## 2.2 Field and Structural data

### 2.2.1 Field and structural characterisation

The overarching aims of fieldwork were to structurally characterise key locations and sample a diverse range of calcite-bearing structures. Fieldwork was conducted over the space of three years between June 2018 and September 2020, with multiple trips lasting between a day and two weeks in length. The fieldwork and sample locations are outlined in detail in Chapter 3. Preparation included compilation of existing 1:25,000 OS maps, published geology maps and aerial photographic images. These datasets were also used to assess access and potential escape routes as the coastal sections are tidal.

Fieldwork studied brittle deformation structures cross-cutting predominantly Jurassic sedimentary rocks of the Cleveland coastline (Fig 1.9). The relative ages of calcite-bearing faults and fractures were constrained through their cross-cutting relationships (e.g. Potts & Reddy, 2000). Field measurements were focused on brittle deformation structures of varying size (hand specimen to regional scale). Orientation measurements were collected using a combination of standard compass-bearing system and the Fieldmove$^{TM}$ software on an iPad. Planar measurement data were taken using the British Right Hand Rule (RHR) with an additional dip direction included to minimise error. Lineation measurements have been taken as a combination of plunge and azimuth and rake upon the plane (pitch).

In addition to measurements taken conventional use of a compass clinometer, Fieldmove™ was utilised on a 6th generation iPad to acquire a large dataset of joint and fault measurements to build up a comprehensive and statistically viable data population that could be digitised and analysed concurrent with fieldwork. Recent work by Hama et al. (2014), Allmendinger et al. (2017) and Novakova & Pavlis (2017) has assessed the reliability of android sensors for digitial data acquisition. Hama et al. (2014) concluded that iOS devices and iPad tablets were the most suitable. In addition, regular compass measurements were taken to bracket the digital measurements (approximately every 1-2 every 20 measurements) to assess the accuracy of digital measurements. In general, a close correlation was found between conventional compass and digital measurements.

### 2.2.2 Sampling

Locations were scouted for suitable sampling locations. Once the structures were identified and relative chronology established, the structures were photographed and measured prior to sampling. The sampling location was documented and eight figure grid reference (UTM 30) taken. Calcite veins in joints and fault rocks were oriented (McClay, 1991) with dip/strike symbol on the top surface where possible. The primary, larger sample pieces were wrapped in cellophane and then placed in named ziplock sandwich bags before being placed into a plastic box for extra protection. Smaller additional pieces were placed into protective plastic 1.5 ml Eppendorf tubes. A subset of samples (to avoid unnecessary repetition) were then identified, and either mounted by hand in epoxy resin (Buehler Epofix) or sent to Durham University Rock Sectioning laboratory for thin sections, thick sections and/or polished blocks to be prepared (Section 2.2.2).

### 2.2.3 Stress Analysis

The stress conditions that existed at the time of the observed brittle deformation can be inferred through use of palaeostress inversion analyses, which consist of combined numerical and stereographic projection techniques. These techniques use fault and fracture slip vector data to provide an approximation of the stress conditions related to a set of fault and fracture data related to a single deformation event (Angelier, 1990). The main assumption involved is that the slip vector data seen along a fault are assumed to lie parallel to the ideal shear component of the resolved stress tensor (Wallace, 1951; Bott, 1959).

Analyses were undertaken on high-confidence slickenline data and minor fault intersections from a series of locations and also on a regional scale. These data were compared to mineral fibre and fracture pull-apart lineations where possible. Tilting and folding prior to and during exhumation may have induced an amount of rotation, but since it is impossible to constrain the relative timing of this deformation and the low degrees of bed dip (typically <5 degrees) no correction was applied in the current study.

Stress inversion was conducted using the Win_Tensor software (Delvaux & Sperner, 2003) with the Mohr Diagram for resolved stress with the Composite Min optimisation (Delvaux, 2010). The outputs were compared with the Improved Right Dihedron method (Angelier & Mechler, 1977) and almost always yielded highly comparable results.

## 2.3 Petrography

### 2.3.1 Introduction

Imaging and microscopy are an integral aspect of the project and are essential in order to correctly relate dates from U-Pb calcite geochronology to the deformation seen in outcrops and on regional-scale structures, i.e. which geological event is being dated? Microscopy, therefore, forms the bridge between the structural aspects of the project and the lab-based dating and isotope work. Petrography focused on imaging microstructures indicative of pre-, syn- or post-kinematic calcite precipitation and identifying distinct phases of calcite growth. Indicators of later reworking and alteration were important as these processes could have a significant impact on the validity and interpretation of geochronological ages and isotope geochemical results.

### 2.3.2 Sample Preparation

#### 2.3.2.1 Resin Mounted Blocks

Chips and veins of calcite with flat edges were mounted in circular 25mm diameter blocks of epoxy resin (Buehler Epofix). Resin mounts cannot be analysed under transmitted light but can be further polished to remove ablated or micro drilled areas for further analysis. "Key" samples with unique structures or which held important information about the relative sequence of deformation were later sent to the Durham University Rock Sectioning laboratory to produce standard size thin sections. These were selected to cover a range of vein textures, from a range of fault structures, and in general related to later field sampling trips.

#### 2.3.2.2 Thick Sections

Polished thick sections, 48 × 28mm in size and ca. 100µm thick, were prepared at the Durham University Rock Sectioning Laboratory for analysis of certain samples that were either deemed too difficult or too large to mount by hand in resin, or where transmitted microscopy was deemed important for understanding and relating microstructures to the deformation history of the sampled structure. These sections, while compatible with further microscopy, could not be repolished to remove ablation or drilling damage and ablation parameters needed to be carefully monitored to prevent ablation of the underlying glass base.

### 2.3.3 Hand Specimen/Optical

Microstructures can be analysed in the field to aid sampling of primary calcite in veins or prior to ablation to guide ablation and/or further analyses. Millimetre-scale microstructures could be analysed using the naked eye in mounts, thick section or hand specimen.

### 2.3.4 Microscopy

Reflected light, transmitted light and cathodoluminescence microscopy techniques were utilised to image sub-millimetre to micron-scale vein fabrics and microstructures.

#### 2.3.4.1 Optical Microscopy

Microscopy was conducted using a range of techniques at the Department of Earth Sciences, Durham University, UK and the British Geological Survey, Nottingham, UK.

Imaging was conducted using standard reflected and transmitted (plane- and cross-polarised) microscopy techniques with images montaged using Microsoft Image Composite Editor software.

#### 2.3.4.2 Cathodoluminescence

Cathodoluminescence is a technique in which luminescence is induced in carbonates and other minerals through the application of an electron beam to the sample surface (Sippel, 1965; Sippel & Glover, 1965). Cathodoluminescence can be carried out through the affixation of a “cold cathode” or “hot cathode” system to an optical microscope (Sippel, 1965) or SEM device (e.g. Götze, 2002; Passchier & Trouw, 2005). In carbonate minerals the colour intensity of cathodoluminescence is typically controlled by the concentrations of trace elements, although it also reflects structural defects (Machel, 1985). The brightness of cathodoluminescence in calcite and dolomite was typically believed to be linked to the presence of $Mn^{2+}$ as the primary activator and $Fe^{2+}$ the primary inhibitor (Machel, 1985; Savard et al., 1995; Cazenave et al., 2003; Richter, 2003). However, the exact concentrations needed to cause activation and inhibition are still debated (Sippel & Glover, 1965; Machel, 1985, 2000; Savard et al., 1995; Habermann et al., 1998). Rare Earth Elements such as $Eu^{2+}$, $Eu^{3+}$, $Dy^{3+}$, $Sm^{3+}$, $Tb^{3+}$ and $Pb^{2+}$ have been suggested as other causes of cathodoluminescence activation (Richter et al., 2003; Passchier & Trouw, 2005) while Machel (1985) lists $Ni^{2+}$ and $Co^{2+}$ as additional inhibitors.

Cathodoluminescence images were taken at the BGS using a Technosyn 8200 MkII cold-cathode luminoscope stage attached to a Nikon optical microscope with long working distances lenses equipped with a Zeiss AxioXam MRc5 digital camera. The vacuum and electron beam voltage and current were continuously adjusted to generate optimal sample luminescence.

### 2.3.5 Scanning Electron Microscope

Back-scattered electron (BSE) and charge contrast (CCI) imaging was undertaken at the British Geological Survey (BGS, Nottingham, UK) utilising a FEI Quanta 600 environmental scanning electron microscope (ESEM). Samples were resin-impregnated 25mm diameter circular mounts, which were imaged without coating under low-vacuum conditions (130Pa) with variable working distance of 10-15 mm.

#### 2.3.5.1 Back-scattered Electron (BSE)

Back-scattered electron imaging is a standard SEM technique that utilises the induced emission of back-scattered electrons from a sample under bombardment of an electron beam with the emission of electrons being correlative to the atomic number of the elemental atom excited (i.e. mineral composition). Larger elements with higher atomic number will appear brighter than lighter elements. The lack of a conductive coating (necessary for CCI) in the present study will have caused some attenuation of BSE image quality, but images were still of sufficient standard to interrogate the necessary structural variations.

BSE imaging was conducted using a solid-state (dual-diode) electron detector with beam currents of 0.1-0.3 nA and an electron beam accelerating voltage of 20kV.

#### 2.3.5.2 Charge Contrast Imagine (CCI)

Charge Contrast Imaging (CCI) is not a fully understood method (Doehne & Carson, 2001), but is thought to be equivalent to and linked with cathodoluminescence (CL - Griffin, 2000;

Cuthbert & Buckman, 2005; Buckman et al., 2016) with small differences in the electron emissions and therefore variation in contrast (Doehne & Carson, 2001). CCI allows for imaging of microstructures in various non-conductive and semi-conductive materials (Robertson et al., 2005), and has been utilised for the imaging of sub-micron features in crystalline materials (Doehne & Carson, 2001). Features previously imaged include physical defects such as microstructures (Cuthbert & Buckman, 2005), crystal composition (Cuthbert & Buckman, 2005), crystal zoning (Doehne & Carson, 2001), areas of chemical alteration (Doehne & Carson, 2001), twinning planes (Watt et al., 2000), and cleavage structures (Buckman et al., 2016).

CCI reflects differences in a mineral's ability to accept, store and discharge ions from the electron beam with changes in composition and breaks or misorientations in crystal structures (Griffin, 1997). Calcite impurities create charge traps which are accentuated through the CCI phenomenon (Baroni et al., 2001). CCI is believed to be related to optimum charge compensation at the sample surface allowing areas of high-change density to be enhanced (Robertson et al., 2005). Griffin (2000) indicates a sensitivity of CCI to low levels of surface contaminants.

Charge Contrast Imaging is sensitive to small changes in operating conditions (Griffin, 1998; Watt et al., 2000) and the specific operating conditions reflect complex interactions between the electron beam, the positive ion flood generated, a bias detector and the sample (Griffin, 2000). CCI occurs most strongly under a high detector gain (detector bias or electron gain) and with a fast scan rate (Doehne & Carson, 2001), with Watt et al. (2000) highlighting the role of fast scans in limiting electron detrapping and limiting image degradation. A working distance of ~10mm is suggested by Doehne & Carson (2001) to minimise arcing from the detector to the sample that occurs at shorter working distances. Doehne & Carson (2001) indicated that the greatest CCI contrast occurs at high accelerating voltages (kV) with Buckman et al. (2016) suggesting a value of 20 kV with a spot size of 3.5-5.2.

Charge contrast imaging was recorded utilising an FEI large-field gaseous secondary electron (electron cascade) detector, with an electron beam accelerating voltage of 20kV and beam currents of 1.2-4.5 nA.

## 2.4 U-Pb Geochronology - Carbonate LA-ICP-MS

In situ U-Pb carbonate geochronology using Laser Ablation Inductively Coupled Mass Spectrometry (LA-ICP-MS) was performed at the Geochronology and Tracers Facility at the National Environmental Isotope Facility in Nottingham, UK. Samples were selected based on previous combined microstructural and field relationships. Selected samples were focussed on building a comprehensive and complete picture of the timings of deformation and associated fluid-flow. U-Pb dating was attempted on a comprehensive dataset covering all the structural features with the results produced representing successful analyses where a robust age was produced.

The analyses utilised a New Wave Research 193UC excimer laser ablation system fitted with a TV2 cell coupled to a Nu Instruments Attom single-collector sector-field ICP-MS. The methodology for carbonate geochronology was first outlined in a series of papers, Li et al. (2014), Coogan et al. (2019) and Roberts & Walker (2016), and is modified from the approach used for traditional minerals such as zircon (e.g. Spencer & Kim, 2015; Roberts et al., 2017). The key modification is that the carbonate reference material used for normalisation of isotope ratios is not homogeneous, but forms a mixing line between common and radiogenic lead isotope compositions. As such, a two step normalisation is utilised. First, normalisation of $^{207}Pb/^{206}Pb$ ratios uses standard sample bracketing with a silicate glass (NIST 614; ratios of Woodhead & Hergt, 2001). Then, also through standard sample bracketing, a carbonate reference material (WC-1; Roberts et al., 2017) is used to normalise the $^{206}Pb/^{238}U$ ratios. WC-1 is a carbonate matrix-matched reference material developed at the Geochronology & Tracers Facility and is described in detail by Roberts et al. (2017); the known age used of 254 ± 7Ma is derived from isotope dilution mass spectrometry. In addition to WC-1, two additional secondary reference materials have been run across the analytical sessions as a check on accuracy and precision, these are ASH15D (Nuriel et al., 2021) and Duff Brown Tank (Hill et al., 2016).

Inter-element fractionation (i.e. between U and Pb) is the greatest contributor to uncertainty of LA-ICP-MS U-Pb geochronology. In this study, the use of large spot sizes (typically 100 µm) limits the downhole fractionation of U-Pb ratios during ablation. No downhole fractionation correction is applied, instead the mean of each isotope ratio is used, with an ablation time of 30s; the first and last 2s of each ablation is discarded. The normalisation factors applied to the samples utilises a combination of the measured vs accepted ratio derived from a session calibrated drift-corrected mean of the WC-1 primary reference material (Roberts et al., 2017). No common lead correction is applied to the data, instead, ages are derived from lower intercepts with concordia in Tera-Wasserburg plots.

The validity and robustness of the data is dependent on multiple factors discussed in detail in Roberts et al. (2020). The most important of these are that the data population has a low Mean Squared Weighted Deviation (MSWD), preferably 2 or lower. The MSWD, also referred to as reduced chi-squared statistic, is discussed in detail by Spencer & Kim (2015) and is used to assess the degree to which the data represent a single population. When MSWD equals 1, the observed values and their uncertainties conform to a single (normally distributed) population. In contrast, a value of greater than 1 reflects either: 1) that the uncertainties have been underestimated; or 2) that the data represents natural variation outside of a normally distributed population. With carbonate geochronology, the MSWD is commonly >1, and thus the quoted ages for samples do not conform to the strict use of the MSWD criteria. However, most authors argue the data are still robust even when the MSWD is in the range of 1 to 3, with higher MSWDs reflecting natural variability in ablation behaviour, and small degrees of alteration of mobility of the parent or daughter U and Pb isotopes. An MSWD of less than 1 suggests that the uncertainties attributed to the data have been overestimated.

For carbonates, the measured U-Pb isotope data are plotted in Tera-Wasserburg space ($^{238}U/^{206}Pb$ vs. $^{207}Pb/^{206}Pb$), and define a mixing line between compositions dominated by common and radiogenic lead. Common (or 'initial') lead, is the lead incorporated in the mineral during formation, whereas radiogenic lead is that derived via radiogenic ingrowth from the parent uranium. The ratio of the parent and radiogenic daughter isotopes ($^{238}U/^{206}Pb$) lie on the x-axis. The composition of the common lead component determines the intercept on the x-axis ($^{207}Pb/^{206}Pb$). A sample devoid of common lead will sit along the concordia curve, while, conversely, a common lead-dominated sample will sit at high values of $^{207}Pb/^{206}Pb$ (typically ~0.8 to 0.9) and low $^{206}Pb/^{238}U$ values. Highly scattered samples, where the 2σ ellipse envelopes do not overlap with a regression line through the data (commonly referred to as the isochron), will lead to high MSWD values. In this situation, the relationship between parent and daughter isotopes has broken down, likely due to uranium or lead mobility and/or multiple generations of calcite being sampled. In addition, samples with very low counts at or near background levels (ca. 50 cps for Pb) will generally lead to erroneous/unsuccessful results.

The accuracy of the LA-ICP-MS method for carbonates has been tested in two studies, where samples were measured by both LA-ICP-MS and by isotope dilution methods (Li et al., 2014; Woodhead and Petrus, 2020). Both of these demonstrated that the LA-ICP-MS data overlapped within uncertainty with the data generated using isotope dilution. The latter is a more accurate technique, as it used gravimetrically calibrated isotope spike solutions.

The full analytical protocol is provided in Appendix 8.6. Laser parameters are typically set at 100µm static spots, with a repetition rate of 10Hz, a fluence of 6-8j.cm$^2$, for 30 seconds of ablation, with a washout time of 5 seconds. Material is cleaned using a 2 second pre-ablation with a 150 µm spot size. A typical run consists of 200-300 spots in total, with 16-25 spots on each reference material in batches of 4 to 5 spots, spread through the run approximately. Each run will take 1 to 2 hours, such that 2 or 3 runs can be measured each session (day). Each run is split into three sets with the main data bracketed by reference materials and NIST 614 glass is run at the start and end of each run.

Uncertainty propagation follows the principals outlined by Horstwood et al. (2016). The excess variance (a measure of over dispersion in the data) of WC-1 (for $^{206}Pb/^{238}U$ ratios) and NIST614 (for $^{207}Pb/^{206}Pb$ ratios) are calculated for each run, then propagated onto each sample and reference material value. This excess variance is typically 0.4-0.6% 2σ for $^{207}Pb/^{206}Pb$, and 2-3% 2σ for WC-1. The final age uncertainty uses the output derived from the IsoplotR software for the lower intercept age, and includes addition of systematic uncertainty components in quadrature. The systematic uncertainties are the decay constant uncertainty, reference material $^{206}Pb/^{238}U$ ratio uncertainty, and the long-term reproducibility of the method. These are estimated at ca. 0.1, 2.5 and 1 %, respectively.

Data reduction uses the Time Resolved Analysis function on the Nu Attolab software, this conducts a subtraction of the background values, and calculates the mean of each isotope ratio for each ablation. Normalisation to the reference materials, drift correction, and propagation of the uncertainties is achieved in an in-house Excel spreadsheet. Plotting and age calculation uses the IsoplotR software (Vermeesch, 2018).

## 2.5 Trace Element - Carbonate LA-ICP-MS

Trace element analysis was accomplished using the same instrumentation as the U-Pb geochronology on the resin mounted samples, generally after the dating in separate analytical sessions. The laser parameters are similar to those discussed in Section 2.3 with a beam size of 80 or 100 µm, and an ablation time of 20 seconds. Measurements were accomplished using the Linkscan mode on the Attom ICP-MS. In this mode, the magnet completes a full sweep of the periodic table in 0.2s, and automatically calculates the individual dwell times for each isotope of interest. The masses measured were $^{24}$Mg, $^{44}$Ca, $^{51}$V, $^{55}$Mn, $^{57}$Fe, $^{63}$Cu, $^{88}$Sr, $^{89}$Y, $^{95}$Mo, $^{137}$Ba, $^{139}$La, $^{140}$Ce, $^{141}$Pr, $^{146}$Nd, $^{147}$Sm, $^{153}$Eu, $^{157}$Gd, $^{163}$Dy, $^{165}$Ho, $^{167}$Er, $^{172}$Yb, $^{175}$Lu, $^{208}$Pb, $^{232}$Th, and $^{238}$U.

Samples were normalised to NIST614 (using values from Jochum et al., 2011), with $^{44}$Ca used as an internal standard under the assumption of 40wt% $CaCO_3$. NIST614 contains known quantities of uranium (0.823mg/kg) and lead (2.32mg/kg). Standard sample bracketing was applied with five NIST614 measurements taken between every 20-40 sample spots. No matrix-matched reference materials were analysed and therefore the trace element data are considered as semi-quantitative. Future work could use isotope dilution methodology to confirm measurements although this method lacks the spatial resolution and analytical speed benefits of LA-ICP-MS trace element analysis.

## 2.6 Stable Isotopes

### 2.6.1 Calcite stable and clumped isotope preparation

Calcite-bearing resin mounts were prepared for stable isotope analysis at both the Geochronology Tracers Facility and the Department of Earth Sciences, Durham University, UK. A single zone of interest was identified from prior petrographic analysis. This approach was focussed on minimising the chance of separate phases of fluid-flow being averaged by singling out distinct zones and carefully sampling with an appropriate tool.

Time constraints due to the Covid-19 pandemic meant that samples had to be drilled separately at the Geochronology Tracers Facility, BGS and at the Department of Earth Science, Durham University. At the Geochronology Tracers Facility, samples were drilled using a Dremel hand tool, with various size burred bits. This was conducted under an optical microscope, to ensure the accuracy of the drilling, but was only utilised for coarser >2mm domains. In contrast at the Department of Earth Sciences, Durham, samples were mounted in a Proxxon MF 70 micro mill, and drilled with a burred #107 (0.0483 mm) or #105 (0.0686 mm) size bit depending on the width of calcite zone targeted. Samples were drilled slowly (5000 rpm) and with a shallow penetration of < 1mm to preserve bit integrity. Sample powders were weighed using a Mettler Toledo XS3DU microbalance and stored in 1.5ml

Eppendorf/microtubes. Greater than 1 mg was considered optimal to counter static dispersion of the carbonate powder in the microtube, but this was not possible where thin fibrous veins were being sampled.

### 2.6.2 BGS C-O Stable Isotopic Procedure

Bulk carbon and oxygen stable isotope analyses were performed at the National Environmental Isotope Facility, British Geological Survey, Nottingham, by trained staff; this was due to laboratory limitations imposed by the Covid-19 pandemic. Each carbonate sample is weighed into a glass vial and placed into a reaction vessel containing anhydrous phosphoric acid ($H_3PO_4$), which is then attached to the glass vacuum line and evacuated. Once a sufficient vacuum pressure had been achieved (< $8x10^{-5}$ mbar), the vessels are sealed and transferred to a water bath at 25°C to equilibrate for at least 15 minutes. The vessels are then overturned and the sample reacted with the phosphoric acid:

$3CaCO_3[s] + 2H_3PO_4[aq] = Ca_3(PO_4)2[aq] + 3CO_2[g] + 3H_2O[l]$

The vessels are then returned to the water bath and left to react for at least 16 hours at a constant 25°C (McCrea, 1950; Craig, 1957; Swart et al., 1991). After allowing enough time for a complete reaction, any remaining water vapour is removed from the liberated $CO_2$ by passing the gas through a cold trap held at –90°C on the vacuum extraction line. The purified $CO_2$ is subsequently transferred and frozen into collection vessels submerged in liquid nitrogen and evacuated to < 2x10-5 mbar to remove any other gaseous fractions.

The evolved $CO_2$ is analysed using a VG Optima or Thermo MAT 253 dual inlet mass spectrometer relative to a reference $CO_2$, where stable isotope measurements are made on $CO_2$ from the both the sample and within-run carbonate standards (internal standards are MCS and CCS). The mass spectrometer measures three mass fractions (44, 45, 46) and these correspond primarily to 44 = $^{12}C^{16}O_2$, 45 = $^{13}C^{16}O_2$, and 46 = $^{12}C^{16}O^{18}O$. Individual $\delta^{13}C$ and $\delta^{18}O$ are calculated from the mass ratios 45/44 and 46/44, respectively, relative to the Vienna Pee Dee Belemnite (VPDB) scale using a single-point anchoring procedure based on calibrated $\delta^{13}$CMCS-VPDB and $\delta^{18}$OMCS-VPDB values (via NBS and IAEA international reference materials). A correction is applied to the 45/44 and 46/44 ratios for the minor contribution from $^{17}O$ on the 45 ($^{12}C^{17}O^{16}O$) and 46 ($^{13}C^{17}O^{16}O$) ion beams (Craig, 1957). A fractionation factor is also applied to $\delta^{18}O$ as although all carbon is transferred to the evolved $CO_2$ during reaction with phosphoric acid, only two-thirds of the oxygen is collected

(Sharp, 2017). The acid fractionation factor is constant in this case as the oxygen isotope fractionation between the evolved $CO_2$ and original mineral is temperature-dependent and the reaction is controlled at 25°C using the water bath. The fractionation factor (α) between $CO_2$ and calcite during reaction with phosphoric acid at 25°C is 1.01025 (Friedman and O'Neil, 1977). Using $\alpha CO_2\text{–}calcite$ the $\delta^{18}$O of the original calcite is then calculated using 1.01025 = [1000 + $\delta CO_2$] / [1000 + $\delta$calcite] (Sharp, 2017).

The analytical reproducibility calculated from the standard deviation ($1\sigma$) of the within-run laboratory standards is typically <0.1‰ for both $\delta^{18}$O and $\delta^{13}$C.

## 2.7 Clumped Isotopes

10 samples, described in Chapter 5, were analysed at the Clumped Isotope facilities at Imperial College London. The methodology for the clumped isotope analysis is outlined in Adlan et al. (2020). Clumped Isotope values are reported with respect to ETH carbonate standards with an acidification temperature of 90°C. The method of date reporting is termed as the 'Intercarb Carbon Dioxide Reference Frame' or 'I-CDES'. A complete explanation of reference frames is provided in Bernasconi et al. (2021). Temperature calculations from clumped isotopes utilise a community calibration curve described by Anderson et al. (2021). This temperature calibration curve utilises the I-CDES reference frame and high temperature standards using the equation below from Anderson (2021).

$$\Delta_{47(I-CDES90°C)} = 0.0390 \pm 0.0004 \times \frac{10^6}{T^2} + 0.153 \pm 0.004$$

# Chapter 3 – Structural Characterisation of the Cleveland Basin

## 3.1 Introduction

The aim of this chapter is to detail the regional- to outcrop-scale structural setting of the previously poorly documented calcite-bearing faults and fractures from the Cleveland Basin, which are herein dated using U-Pb calcite geochronology (Chapter 4) and isotopically characterised (Chapter 5).

By documenting and characterising the structural elements of the Cleveland Basin, this enhances our knowledge of the basin's deformational history, and provides crucial context and relative age relationships for subsequent microscopy, U-Pb calcite geochronology and isotopic analyses. Key localities and samples (Fig 3.1) have been grouped based on their dominant structural components and are arranged based on whether they are associated with regional structures (Peak Trough Faults), local fault structures (e.g. Runswick Bay, Staithes and Port Mulgrave faults) or are background fracture fills (subvertical and bedding-parallel veins).

The key locations discussed were chosen to represent calcite mineralised structures varying from regional (Peak Trough faults) down to local faults and fractures with cm to mm wide calcite fills. Analysis and sample locations are geographically spread out along the coastline of the Cleveland Basin (Fig 3.1) where structures are well exposed. With the exception of the High Red Cliff and Osgodby Nab locations, all sampling locations were targeted at analysing calcite mineralisation in the mud-rich, low permeability lithologies of the Lower Jurassic (Lias). Locations were chosen to fully represent the structural affinity (i.e. normal, strike-slip etc.) of all structures in the Cleveland Basin.

Forty-eight samples of calcite-bearing structures were taken from exposures at nine main localities and from cores related to the Elm Tree Farm Borehole (Fig 3.1). These localities were chosen to build on previous work by Imber et al. (2014) and Emery (2016) analysing the nature and timing of deformation in the Cleveland Basin. An overarching aim here was to describe and sample all major calcite mineralised structures, in addition to a representative selection of structures taken from within key intervening fault blocks. A number of samples (denoted with prefix NR) were collected prior to this study by Nick Roberts (British Geological Survey). All the localities related to prior sampling by Nick Roberts have been revisited, resampled and appraised as part of the current field campaign, excluding the Runswick Bay Fault Zone locality where safety issues prevented a revisit to the original outcrops.

Slickenlines associated with faults are categorised and analysed using WinTensor software to characterise the palaeostress conditions of the main fault systems (i.e. Peak Fault and local fault structures) with comparison to other palaeostress/strain indicators from vein fills (e.g. fibre opening directions). An understanding of local and basin-scale palaeostresses can be developed via stress inversion analysis (Section 2.1.3), as well as comparison between different localities and structures. In addition, knowledge of the palaeostress environment combined with U-Pb calcite dating will enable the development of the stress regime over time to be tracked, alongside providing a comprehensive model for deformation and associated fluid-flow (Chapter 6 - Synthesis).

## 3.2 Structural Domains

Fieldwork localities (Fig 3.1) are subdivided based on scale of structure from pervasive joint trends and the Peak Trough faults to local and outcrop scale faults and fractures.

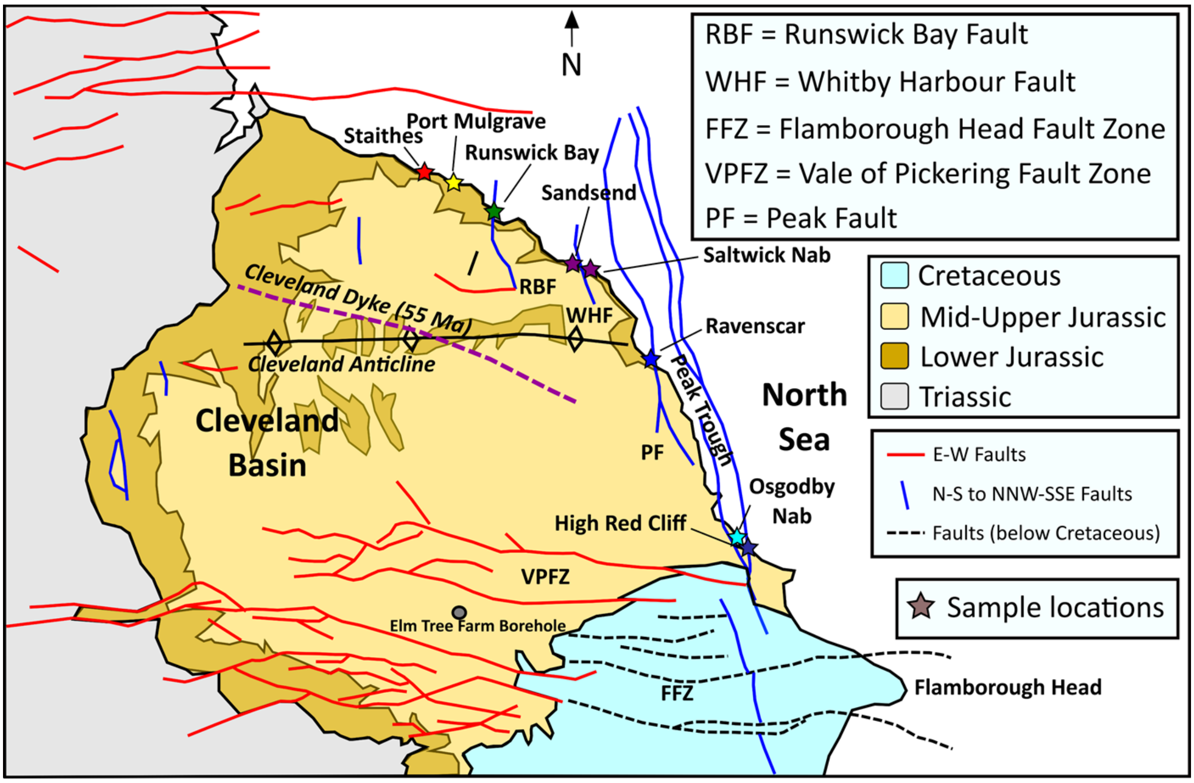


*Fig 3.1. Regional map of the Cleveland Basin documenting the primary field and sampling localities in this study. Sampling locations are indicated by stars and with each structural location coloured separately. Colours are kept consistent with tables and other future images.*

### 3.2.1 Pervasive Joint Sets

The joint systems in the Cleveland Basin have received relatively little attention, although Attewell & Taylor (1971), Rives et al. (1992), Rawnsley et al (1992), Imber et al. (2014) and Emery (2016) all refer to the presence of two approximately orthogonal joints at Whitby, Saltwick Nab, Jet Wyke and Robin Hood's Bay. Stereonets of joints have been recorded at multiple locations around the Cleveland Basin are shown in Figure 3.4. Figure 3.2 shows a rose diagram in with a main distinct joint sets described: $J_1$ - N-S to NW-SE trending with two additional trends: $J_2$ – E-W to NE-SW trending and $J_3$, which trends WNW-ESE.

These joints are important as they provide potential fluid pathways in the subsurface and understanding their relative timing and relationship to calcite minerlisation is crucial to understanding the story of deformation and fluid-flow in the Cleveland Basin.

Documentation of the joint sets in the literature is mainly limited to the Early Jurassic strata (highlighted on Figure 3.1). However, observations made by Imber et al. (2014) from the cliffs near Whitby east pier and by author at Cayton Bay (see Section 3.2.2.2) suggest that similar joints also cut Middle Jurassic stratigraphy. Imber et al. (2014) indicate that that at cliff exposures near Whitby, joints are seen crossing the unconformity that separates Early Jurassic and Middle Jurassic strata. Furthermore, the Middle Jurassic of Osgodby Nab at Cayton Bay (Section 3.2.2.2) exhibits a similar jointing pattern to the underlying Lias, although further fieldwork is required to statistically document the trends, joint sets and genetic relationships (Fig 3.5).

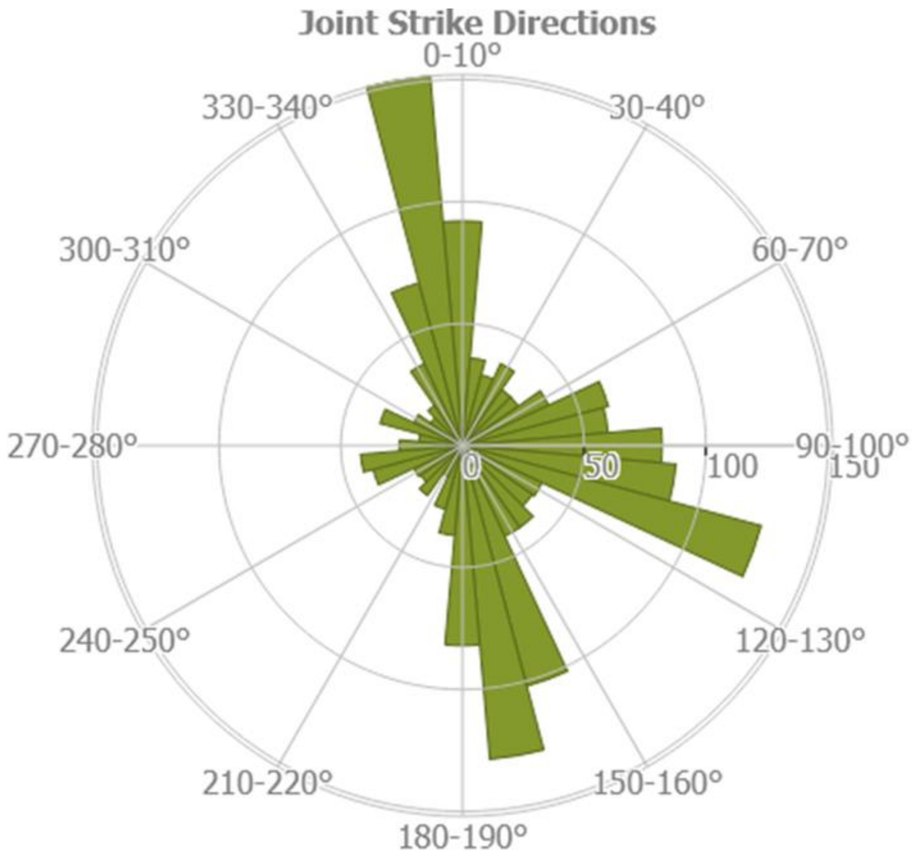


Fig 3.2. Rose diagram of the strike directions of the pervasive joints using British Right Hand Rule. This indicates that the joints have a mean strike directions of 170°-350° ($J_1$) with two additional joint trends centred on 075°-255° ($J_2$) and 110-290° ($J_3$).

The former alum quarry at Saltwick Nab (Fig 3.5) in the Lower Jurassic Whitby Mudstone Formation at the western margin of Saltwick Bay can be used as a representative case study due to the excellent 3D exposures of the joint sets, and previous fieldwork documented in Imber et al. (2014) and Emery (2016). Imber et al. (2014) utilised systematic cross-cutting relationships at Saltwick Nab to infer that of the pervasive joint sets the $J_1$ set formed prior to $J_2$ with counter-clockwise rotation of the minimum horizontal stress and other principal stresses. The identification of an additional, local joint set at this location during the present study ($J_3$) suggests a more complicated history than reported in Imber et al. (2014);

however, Emery (2016) refers to two dominant joint trends at Saltwick Nab corresponding well with $J_1$ and $J_3$ while alluding to two minor joint sets with short lengths of which one is likely to be $J_2$. Thus the presence of a third joint set at this locality could therefore reflect local deformation processes whilst the pervasive joint sets are more likely to reflect basin-scale deformation and stress conditions.

The presence of plumose marking and concentric arrest lines indicate tensile opening of the joints (Solomon & Hill, 1962; Imber et al., 2014). Opening mode (Mode I) veins require specific stress conditions with a low differential stress and low effective stress (normal stress $\sigma$ in Fig 3.3), which are typically associated with shallow subsurface and/or high pore pressure regimes since, during burial, the vertical stress increases making it impossible to open extensional fractures without elevated pore pressures. Emery (2016) further infers that plumose markings and arrest lines are representative of hydrofracturing with episodic recharge as per Engelder & Lacazette (1990) and Savalli & Engelder (2005). This is combined with interpretations from Imber et al. (2014) that both subvertical and bedding-parallel fractures (discussed later in Section 3.2.4.1) formed during burial and/or hydrocarbon generation with hydrofracturing occurring prior to uplift and exhumation of the basin.

It is interpreted that the joints formed due to tensile failure at low effective stress related to hydrofracturing (Fig 3.3; Engelder, 1999). Hydrofracturing occurs when low permeability units are unable to effectively dewater leading to the generation of overpressure which can overcome lead to tensile failure at even great depths of burial. The low differential stress likely facilitated switching of the minimum principle stress direction allowing conjugate sets to form at 90° to each other. The joints were then present as distinct planes of weakness for the later reactivation.

The $J_1$ joints at Saltwick Nab are rarely filled with thin (1-2mm thick) calcite fills, which are discussed further in Section 3.2.4.2. The uncommon nature of these fills is combined with observations concerning the relative timing of formation and U-Pb calcite geochronology in Chapter 4.

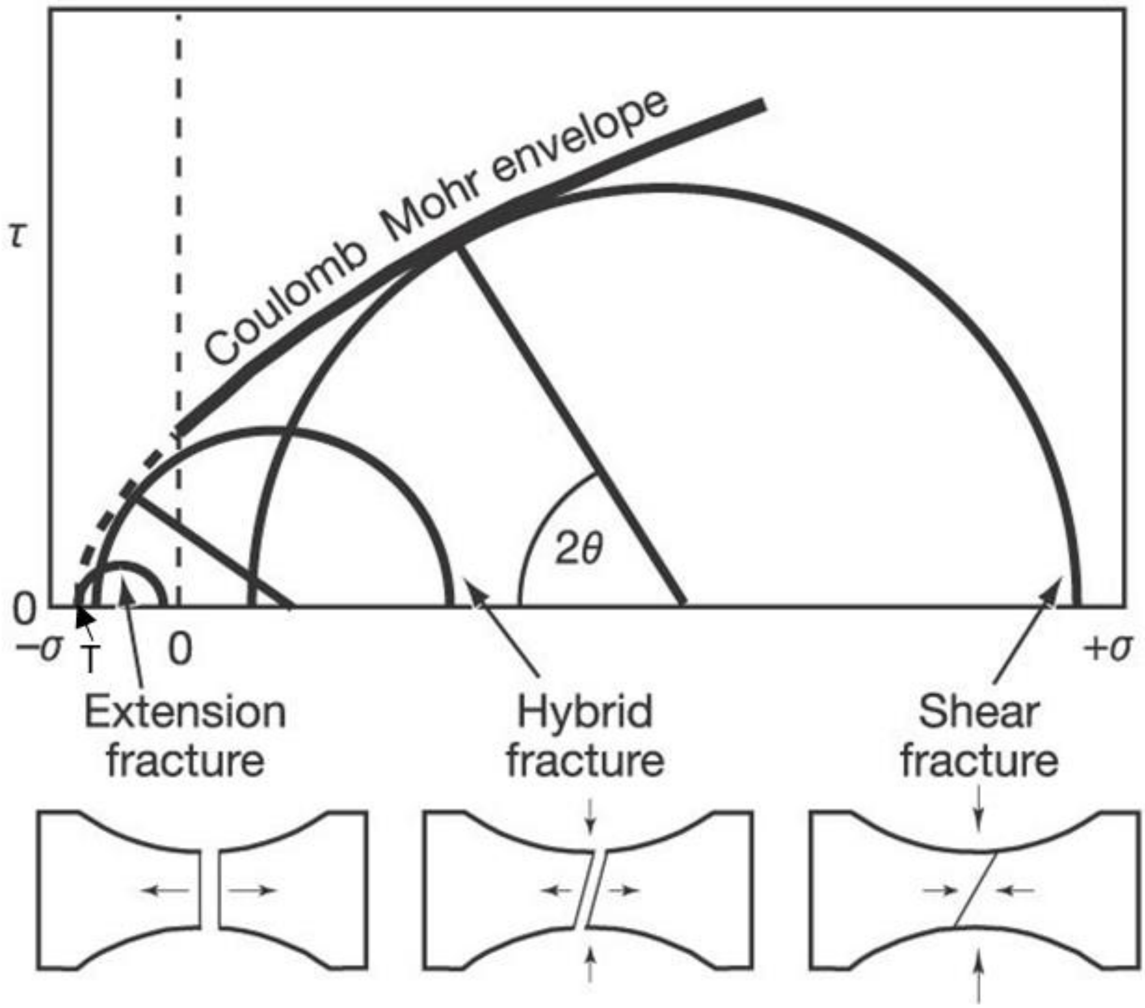


*Fig 3.3. Mohr diagram (Engelder, 1999) plotting shear stress (τ) against normal stress (σ) based on models of Mohr (1914) and Coulomb (1773). Schematic Mohr circles are shown for extension (Mode I), Hybrid (Mode II) and Shear (Mode III) fracture propagation. To initiate an opening mode extension fracture, the Mohr circle must encounter the Coulomb Mohr envelope at zero shear stress and effective normal stress equal to -T, where T is the tensile strength.*

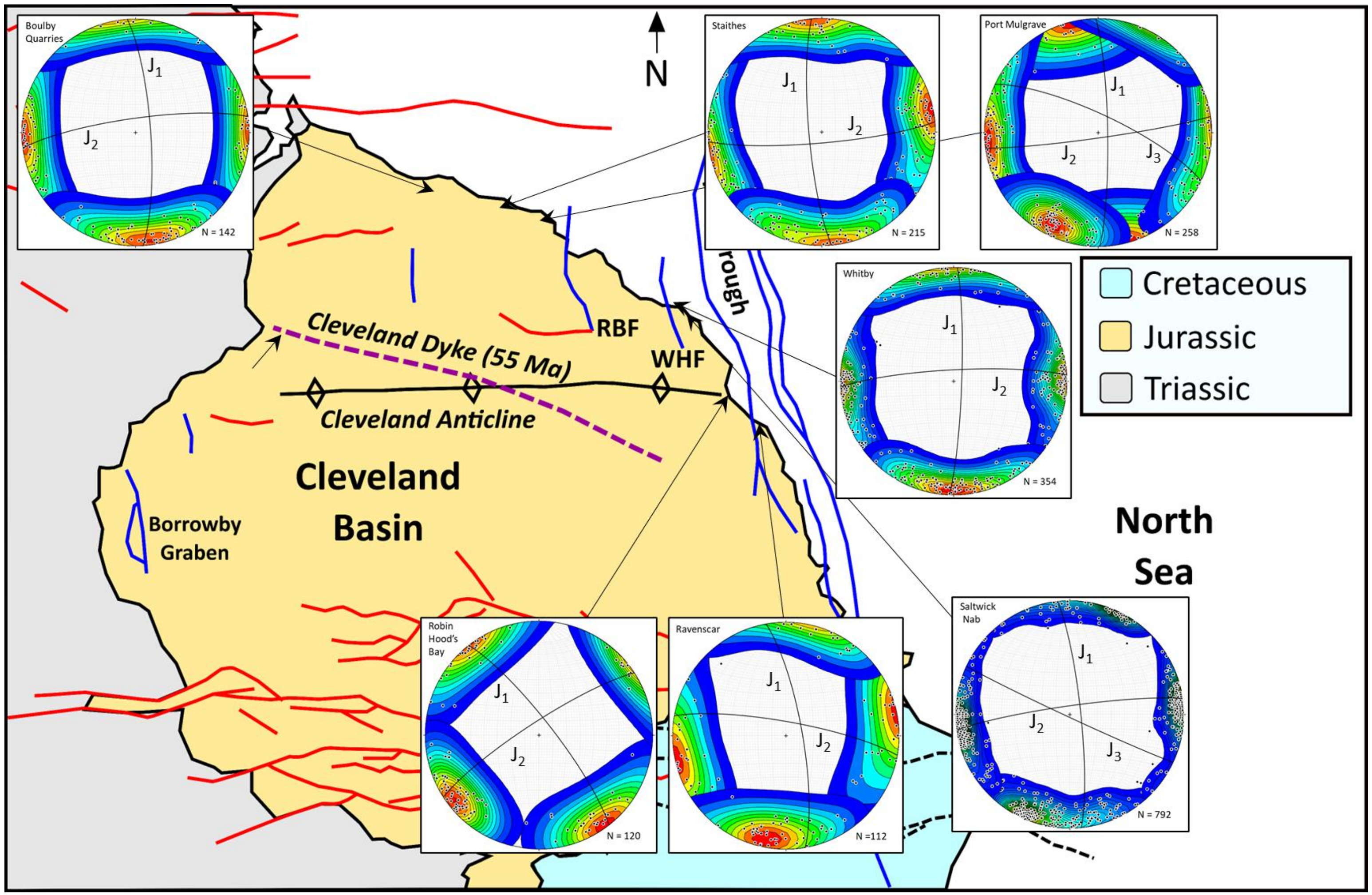


*Figure 3.4. Map* showing stereonets of *joint* orientations at the studied localities. *Stereonets with Kamb contouring (blue - low-density to red - high density) of poles to plane data and best-fit planes labelled $J_1$ to $J_3$. Each image shows at least two approximately orthogonal subvertical joint sets trending NW-SE to NNE-SSW and E-W to NE-SW with an additional joint set $J_3$ present at Saltwick Nab and Port Mulgrave with WNW-ESE trends. $J_1$ and $J_2$ trends at Robin Hood's Bay demonstrate clockwise rotation which could be consistent with the rotation towards the Peak Fault as documented by Rawnsley et al (1992).*

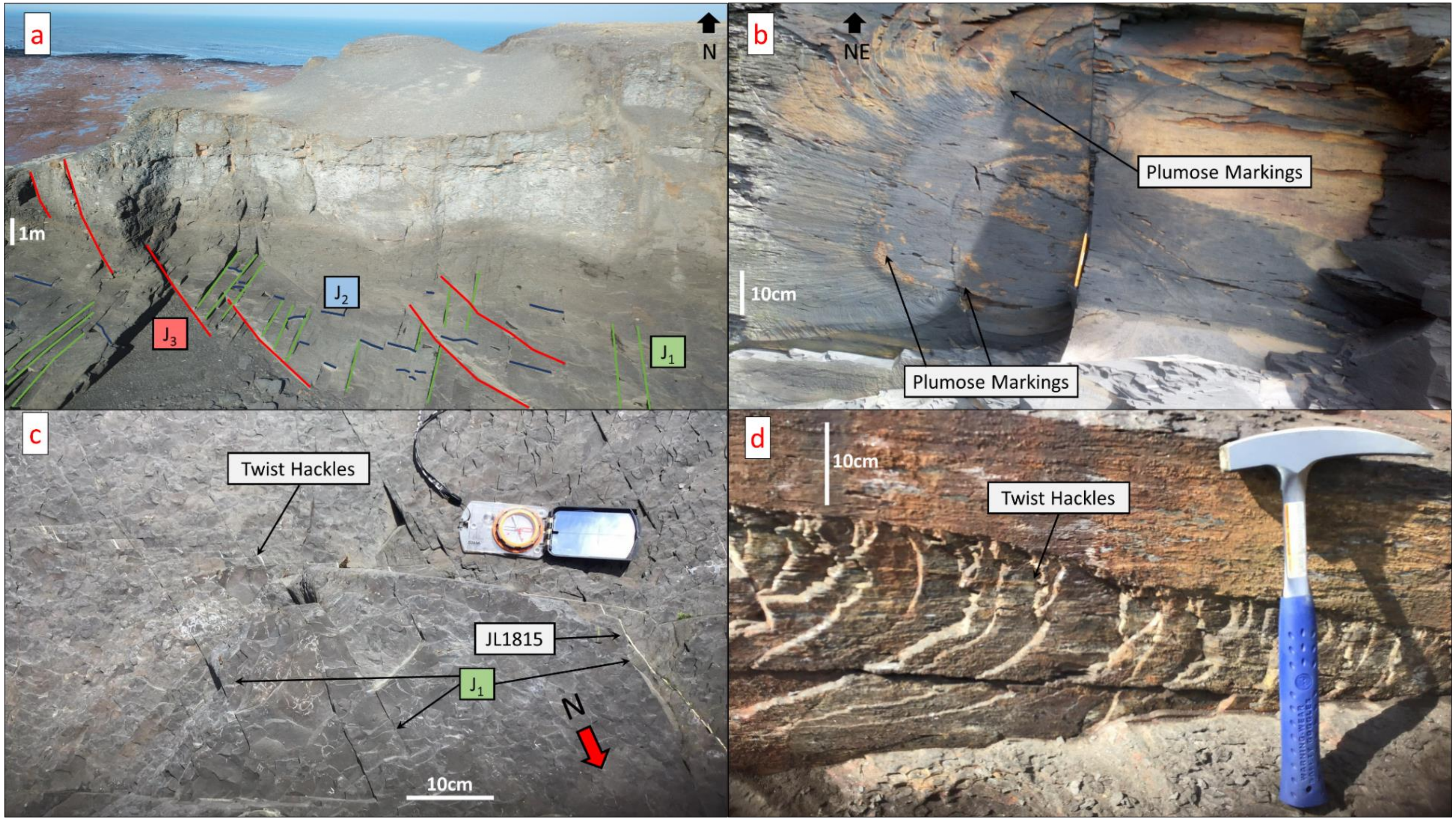


Fig 3.5. a) Oblique sectional view of Saltwick Nab from drone photography illustrating the various joint sets (J1-J3). J2 joints abut and curve into the plane of J1. J2 have short fracture lengths of ~1m compared to J1 and J3, which both have lengths of >5m. b) Sectional image of a J3 joint with plumose markings and concentric arrest lines indicative of opening mode propagation. c) A map view of the J1 joints in the wave cut platform with a thin fibrous calcite preferentially filling the N-S oriented J1 joints (Section 3.2.4.1). d) Abrupt twist hackles indicative of a stress regime not parallel or orthogonal to the tip line of the parent joints (see Kulander et al., 1979; Pollard et al., 1982; Bankwitz and Bankwitz, 1984; Younes & Engelder, 1999).

## 3.2.2 Peak Trough Faults

The Peak Trough is a basin-scale graben structure discussed in detail in Section 1.3.3. Three localities, shown in Figure 3.1 and 3.6, focus on detailing and analysing features associated with three sub-parallel structures collectively referred to here as the Peak Trough faults (ordered from North to South): Ravenscar (Peak Fault), Osgodby Nab (Cayton Bay Fault) and High Red Cliff (Red Cliff Fault).

The Peak Trough faults represent the largest calcite-mineralised structures exposed in the basin, with the Peak Fault at Ravenscar having high quality exposure of multiple fault structures. Additional attention is given to the exposures at Ravenscar to determine the importance regional structures have in controlling the deformational history and associated fluid-flow in the Cleveland Basin. The Cayton Bay and Red Cliff faults are poorly exposed with highly weathered, difficult to access cliff sections that are used to supplement and compare with the comprehensive appraisal of the Peak Fault at Ravenscar.

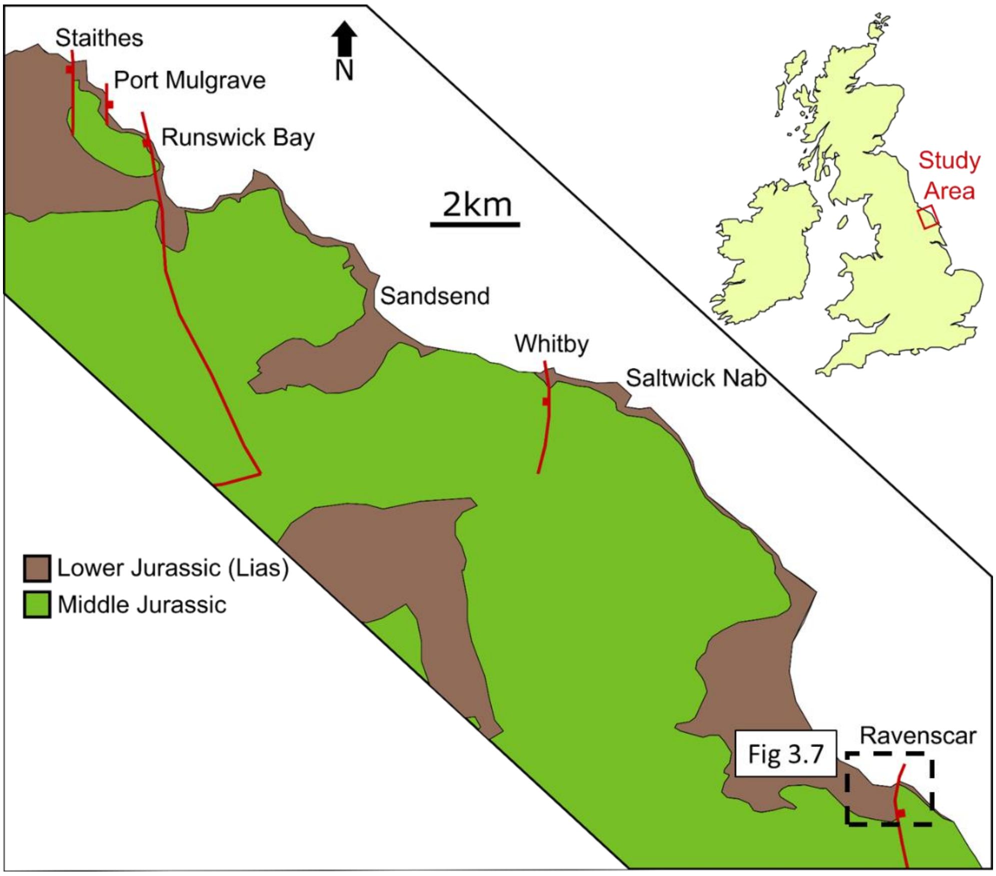


Fig 3.6. Geological map of the main area of interest highlighting the location of Figure 3.7.

### 3.2.2.1 Peak Fault (Ravenscar - NZ 979 024)

Exposures of the Peak Fault at the Ravenscar locality (Fig 3.7) are in the cliffs and wavecut platform 500m north of the village of Ravenscar. The main structures are summarised in

Figure 3.7. The *main fault plane* can be traced for >30m in the wavecut platform an trends NNE-SSW with a dip ~60° to the east, downthrowing and juxtaposing the Whitby Mudstone Formation to the east 153m based on measurements by Rawson & Wright (1992) against the Redcar Mudstone formation in the cliff to the west. A NNW-SSE trending *splay fault* downthrows the Staithes Sandstone Formation against the Redcar Mudstone Formation in the wavecut platform to the north. Minor faults (<10m in extent) are present in the damage zone of the Peak Fault. The faults show variable dip with individual faults dipping from 10° to 70°, but form distinct sets of apparently conjugate faults dipping east and west While these faults might not actually be true conjugate for simplicity sake they are referred to as the conjugate faults from hereon. *$J_1$ joints* are present at Ravenscar and strike N-S. Rawnsley et al. (1992) showed that the joints have undergone rotation into the trend of the Peak Fault. No evidence is seen of the same rotation in minor faults or the bulk rock mass. In addition, a top to the east bedding-parallel fault is present adjacent to the main fault plane in the cliff face of the hanging-wall. The bedding-parallel fault offsets the conjugate faults by 5cm top to the east. The bedding is mostly consistent across the outcrop and dips 2-15° to the east or southeast.

While it is impossible to quantify the total amount of displacement associated with mineralised faults and joints, the total displacement of the Dogger Formation across the Peak Fault is indicated by Rawson & Wright (1992) to be ~90m. Calcite mineralisation, however is associated with millimetre to centimetre-wide fills along the main, splay and conjugate sets of normal faults. It is suggested that the displacement related to reactivation of the Peak Fault, associated with calcite-veining, is low (metres) as field observation show that much of the total displacement is also associated with synsedimentary movement with thickening of strata in the fault hangingwall. In addition, apparently conjugate faults and veins demonstrate a low degree of strain (mm- to cm-scale) with little offset.

<u>Main Fault</u>

The Peak Fault plane (Fig 3.8a) is observable in the cliff as a 2m wide zone of brecciated mudstone that can be seen to bifurcate the wavecut platform and juxtapose the Whitby Mudstone with the Redcar Mudstone in the cliff wall. The fault plane can be traced onto the wavecut platform (Fig 3.7 & 3.8b) where a series of aligned four ~1m circumference mud mounds (Fig 3.8b) are present in the hangingwall of the main fault, within 10 metres of the main fault plane. One sample taken from the exposed main fault plane is characterised by the presence of a 0.5cm thick jog fill with blocky calcite fill (JL2021). The extensional jog structure has slickenlines plunging 48-109, which suggest mineralisation was synchronous with normal fault movements along the Peak Fault.

10cm above the extensional jog are a layer of cone-in-cone structures striking N-S (inset in Fig 3.7). The cone-in-cone structures form a distinct planar zone of uniform thickness (5cm) plunging at 10-15° and are situated below the main fault plane with the cones dipping 20° to the west. The mud mounds are inferred to reflect an early phase of pore fluid build-up and fault movement prior to lithification. Similarly cone-in-cone structures have been linked to overpressure (Cobbold & Rodriquez, 2007; Cobbold et al., 2013) and it is unclear whether the cone-in-cone structures observed here are related to early fluidisation similar to mud mounds, or later carbonate mineralisation along the fault plane gouge. The significance of cone-in-cone structures will be discussed in more detail in Section 6.3.3.

Splay Fault

The NNW-SSE trending trace of the splay fault (Fig 3.7a & 3.8b) is distinguished in the wavecut platform by a distinctive NNW-SSE trending rollover anticline in the hangingwall stratigraphy (Fig 3.8b). The exact displacement of the splay fault is ca. 100m. The anticline has an approximate interlimb angle of 160-170° with an axial plane dipping steeply (70-80°) to the west.

One calcite sample (NR1619) was taken from a 2-3cm extensional jog along the Splay Fault plane. NR1619 is composed of mm to cm-scale blocky calcite with cm-scale vugs (10-15%) indicative of crack-fill mineralization. In contrast to JL2021, taken from the main Peak Fault, the vuggy crack-fill of NR1619 does not unequivocally record evidence of syn-kinematic mineralisation with the fill either formed either during or after fault slip.

Apparently Conjugate Faults

The Peak Fault has a diffuse damage zone encompassing a zone ~20m thick, which surrounds the main fault core. The damage zone is characterised by N-S striking apparently conjugate faults, termed conjugate faults for simplicity, (Fig 3.9a) with thin calcite fills developed along the fault planes (0.5-2cm thick) and in dilational jogs (Fig 3.11a). The sets of conjugate faults appear well developed in both the hangingwall and footwall of the Peak. The faults are discrete, well-developed planes 1-10m long, dipping 20-60° typically to the E or W and consistently crosscut and reactivate pre-existing subvertical joints (Fig 3.9b). This indicates that this fault set formed after development of the joint sets at this locality, which were postulated to have formed at maximum burial (Section 3.2.1). Calcite mineralised slickenlines that plunge down-dip are widespread and, in combination with the systematic offset of distinctive bedding layers and extensional jog structures, are used to infer normal movements along the conjugate sets of E-W dipping faults.

Five samples of calcite from a breccia (NR1623), hybrid opening veins (NR1620, JL2022 & JL2024) and an extensional jog (JL2020) have been sampled from conjugate faults (Table 3.1). These samples vary from thin 1-2mm veins along the plane of the fault to extensional jog structures with crack-seal textures. Calcite fills are a mixture of blocky and fibrous textures. Fibrous fills suggest rapid calcite growth in the direction of local to regional tectonic extension (Means & Li, 2001; Passchier & Trouw, 2005). Some samples have apparent have apparent implosion breccia textures with mm to cm-scale clasts supported in a calcite matrix. These extensional jogs are interpreted to track hybrid shear opening, however mineralisation could also have post-dated jog opening in some cases. The relation of samples to kinematic movement will be discussed in more in detail in Chapter 4.

Subvertical Fractures Fills

The subvertical fracture fills are thin mm-scale calcite mineralisation along the previously mentioned joints at Ravenscar. Four calcite vein samples have been taken from subvertical fractures and are interpreted to represent syndeformational tensile fracture development related to the fault movement due to their close spatial association with conjugate shear fractures and a bedding-parallel fault zone (Fig 3.7 & 3.8). Fracture fills of this kind are thought to have occurred during local reactivation of the previous $J_1$ joint set due to local fault movement as shown in Fig 3.9. The subvertical fracture fills - as with other subvertical fills in fault damage zones elsewhere in the region - are interpreted to be unrelated to the isolated subvertical veins described in Section 3.2.4.2; U-Pb dating (Section 4.5.2) demonstrates that these veins are temporally distinct from other fault-related subvertical veins.

Bedding-parallel Fault

A bedding-parallel fault >10m in length is present in the Peak Fault hangingwall (Fig 3.10) and displays a well-defined slip plane with a clay gouge (1-5cm thick) of reworked mudstone. The total offset with the intersection of an inclined fault (Fig 3.10) indicates top to the east displacement of ~10cm. Lithified clasts of angular mudstone are present in the gouge indicating that the fault formed post-lithification. The aforementioned conjugate faults are seen to be offset by the bedding parallel fault (Fig 3.10 & 11b).

Figure 3.10c shows the intersection of an inclined (conjugate) fault and the bedding-parallel fault. Figure 3.11b shows a 1-2cm thick calcite vein is present in the inclined fault. The vein has slickenfibres with down plunge lineations, indicative of fault movement during emplacement. The vein can be traced between the now offset fault segments through the bedding-parallel faults. Since the vein connects the segments of the inclined fault and is present in a section of the bedding-parallel fault, it must post-date the top to the east offset of the bedding-parallel fault. This indicates movement along the inclined faults and the bedding-parallel fault were broadly contemporaneous.

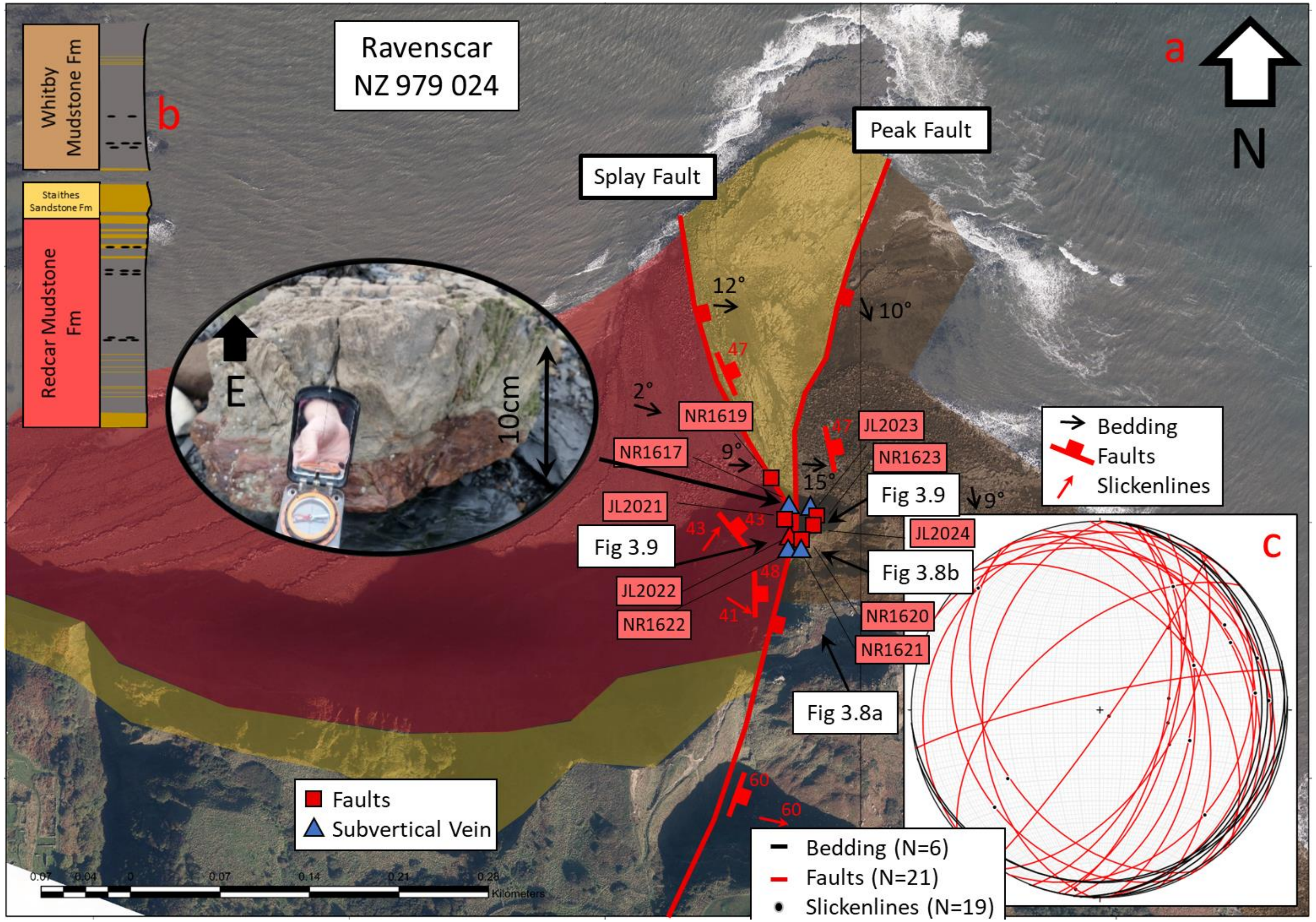


Fig 3.7. a) Aerial photography of the Peak Fault at Ravenscar, North Yorkshire with sample locations shown around the main and splay fault traces. A stratigraphic log (b) is included on the left with the Redcar Mudstone (red), Staithes Sandstone (yellow) and Whitby Mudstone formations (brown). A stereonet is included (c) showing faults (red) and bedding (black). Aerial photography is courtesy of the North East Coastal Observatory (NECO). The stratigraphic log is redrawn based on Hesselbo & King (2019). An inset is included of cone-in-cone structures located at the main fault plane in the wavecut platform.

Subvertical fractures commonly concentrate around the intersection of inclined faults and the bedding-parallel fault (Fig 3.10). The bedding-parallel fault can also be shown to offset top to the east subvertical fractures by ~3-4cm (Fig 3.11), whilst some subvertical joints show abutting relationships and curve into the bedding-parallel fault plane. These cross-cutting and abutting relationships suggest that the bedding-parallel fault represents a pre-existing mechanical boundary. This could suggest that a clay-rich bed acted mechanical boundary to fracture propagation prior to faulting and was later was reactivated as a bedding-parallel fault. The fault then utilised this weak bed to nucleate along, synchronous with the movement of the inclined faults.

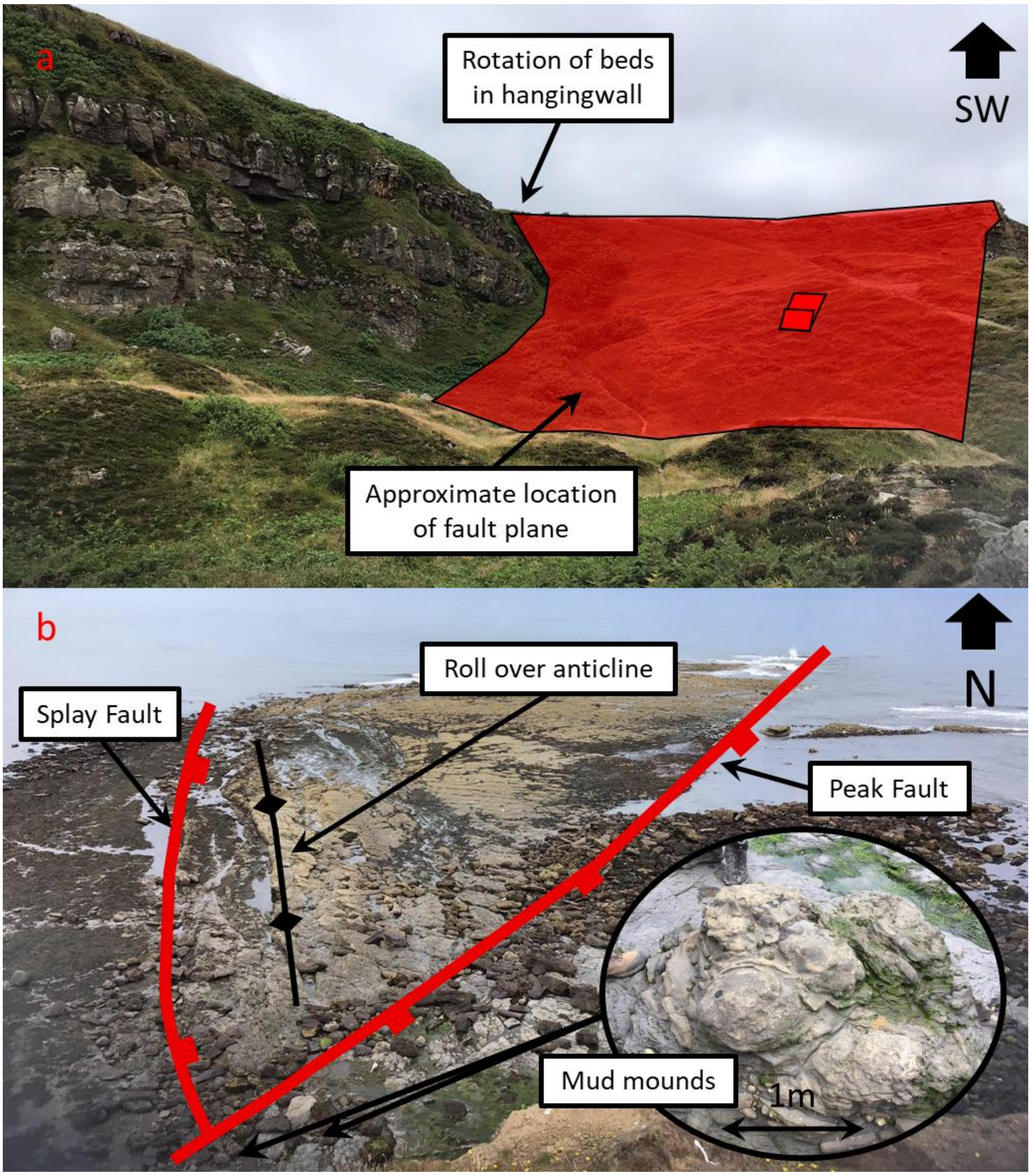


*Fig 3.8. a) Sectional image of the Peak Fault in the cliff. Stratigraphy in the hangingwall forms a NNW-SSE rollover anticline. b) An oblique overview image of the wavecut platform at Ravenscar with an inset of a mud mound. Other mud mounds not labelled are off to the south of the image. The splay fault terminates against*

*the main trend of the Peak Fault with folding of the Staithes Sandstone Formation in the hangingwall of the splay fault observable.*

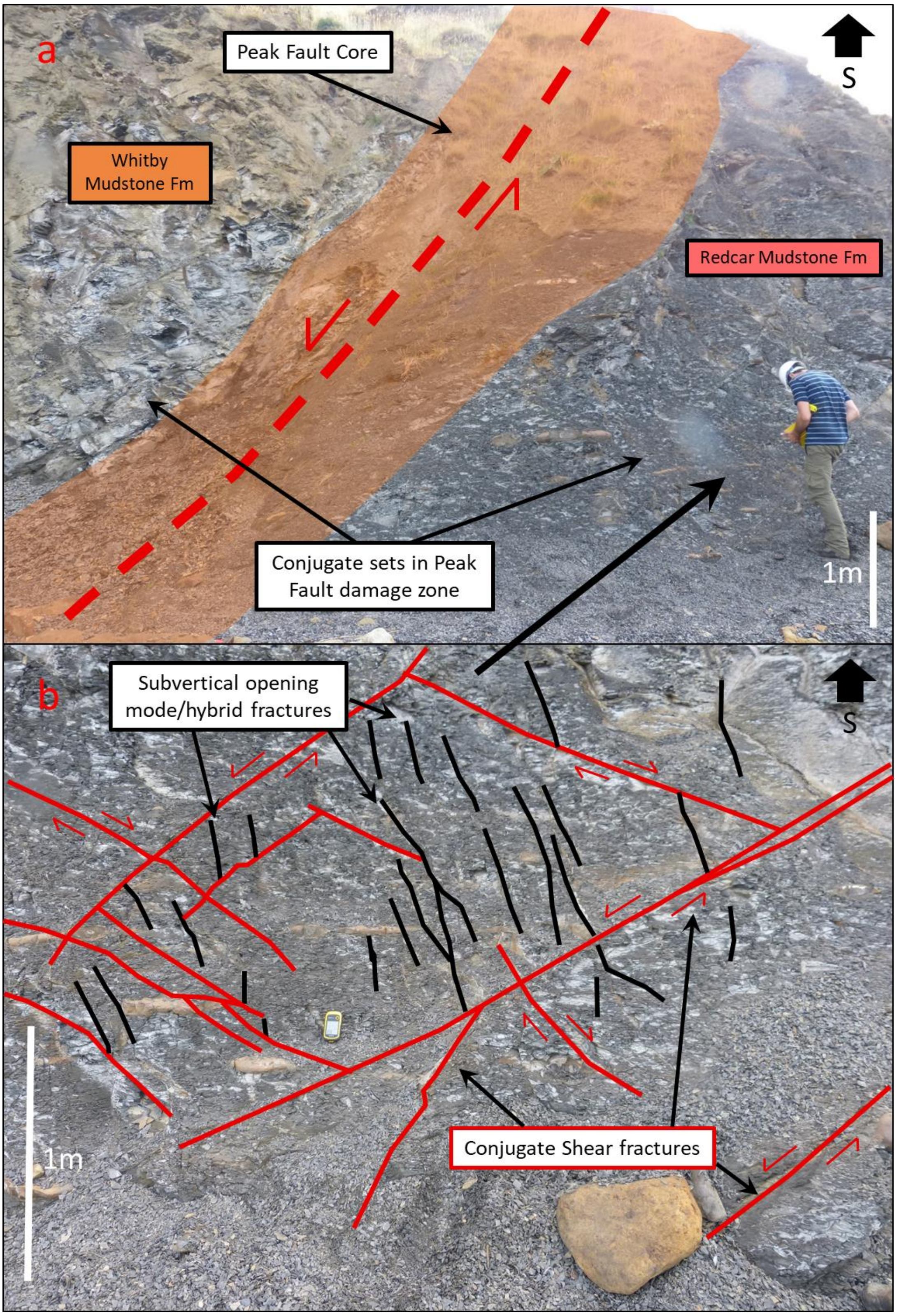


Fig 3.9. Field photos of the Peak Fault core (a) and conjugate shear fractures in the wider damage zone (b). a) A cross-section view of the Peak Fault as it intersects the cliff at Ravenscar with the lighter grey Whitby Mudstone Formation juxtaposed against the darker Redcar Mudstone Formation. The main fault plane is indicated in red with the wider fault core shaded in orange. b) A sectional image of conjugate shear fractures (red) and subvertical opening mode/hybrid fractures (black) with calcite fills from the location indicated in a).

Faults crosscut subvertical fractures and the subvertical fractures look to be widely reactivated during fault movement. Calcite filled extensional jog structures and slickenlines are common along the conjugate sets of normal faults as shown in Figure 3.11.

Sample data from the Peak Fault and related structures are summarised in Table 3.1. The samples span all the structures described and show a variety of different calcite fills and crystal textures. All 11 samples have been successfully dated and are discussed further in Chapter 4.

| Sample | Location | UTM N | UTM E | Peak Fault | Calcite Fill | Texture | Kinematics | Dating | C-O | Clumped |
|---|---|---|---|---|---|---|---|---|---|---|
| JL2021 | Ravenscar - PF | 662724 | 6031788 | Main Fault | Extensional Jog | Blocky | Synkinematic | Y | - | - |
| NR1619 | Ravenscar - PF | 662753 | 6031771 | Splay Fault | Extensional Jog | Blocky | Syn or post-kinematic | Y | Y | - |
| NR1620 | Ravenscar - PF | 662818 | 6031988 | Conjugate Normal Faults | 3-5mm thick vein | Fibrous | Synkinematic | Y | - | - |
| NR1623 | Ravenscar - PF | 662715 | 6031838 | Conjugate Normal Faults | Breccia (mosaic) | Blocky | Synkinematic | Y | - | Y |
| JL2020 | Ravenscar - PF | 662718 | 6031771 | Conjugate Normal Faults | Extensional Jog | Blocky | Syn or post-kinematic | Y | Y | - |
| JL2022 | Ravenscar - PF | 662729 | 6031771 | Conjugate Shear Fracture | 0.5mm thick Vein | Fibrous | Synkinematic | Y | - | - |
| JL2024 | Ravenscar - PF | 662749 | 6031781 | Conjugate Normal Faults | 2-4mm thick Fault Fill | Fibrous | Synkinematic | Y | - | Y |
| NR1617 | Ravenscar - PF | 662727 | 6031789 | Vein - Vertical | 1cm thick Vein | Blocky | Syn or post-kinematic | Y | - | - |
| NR1622 | Ravenscar - PF | 662715 | 6031838 | Vein - Vertical | Breccia | Blocky | Synkinematic | Y | - | - |
| NR1621 | Ravenscar - PF | 662715 | 6031838 | Vein - Vertical | 2-3cm thick Vein | Blocky | Syn or post E-W Opening | Y | - | - |
| JL2023 | Ravenscar - PF | 662749 | 6031785 | Vein - Vertical | 6-7mm thick Vein | Fibrous | Syn E-W Opening | Y | - | - |

Table 3.1. Summary of sample data from the Peak Fault (PF) at Ravenscar. The locations of samples are shown in Fig 3.7. The structure type, calcite fill structure and apparent texture in hand specimen are summarised.

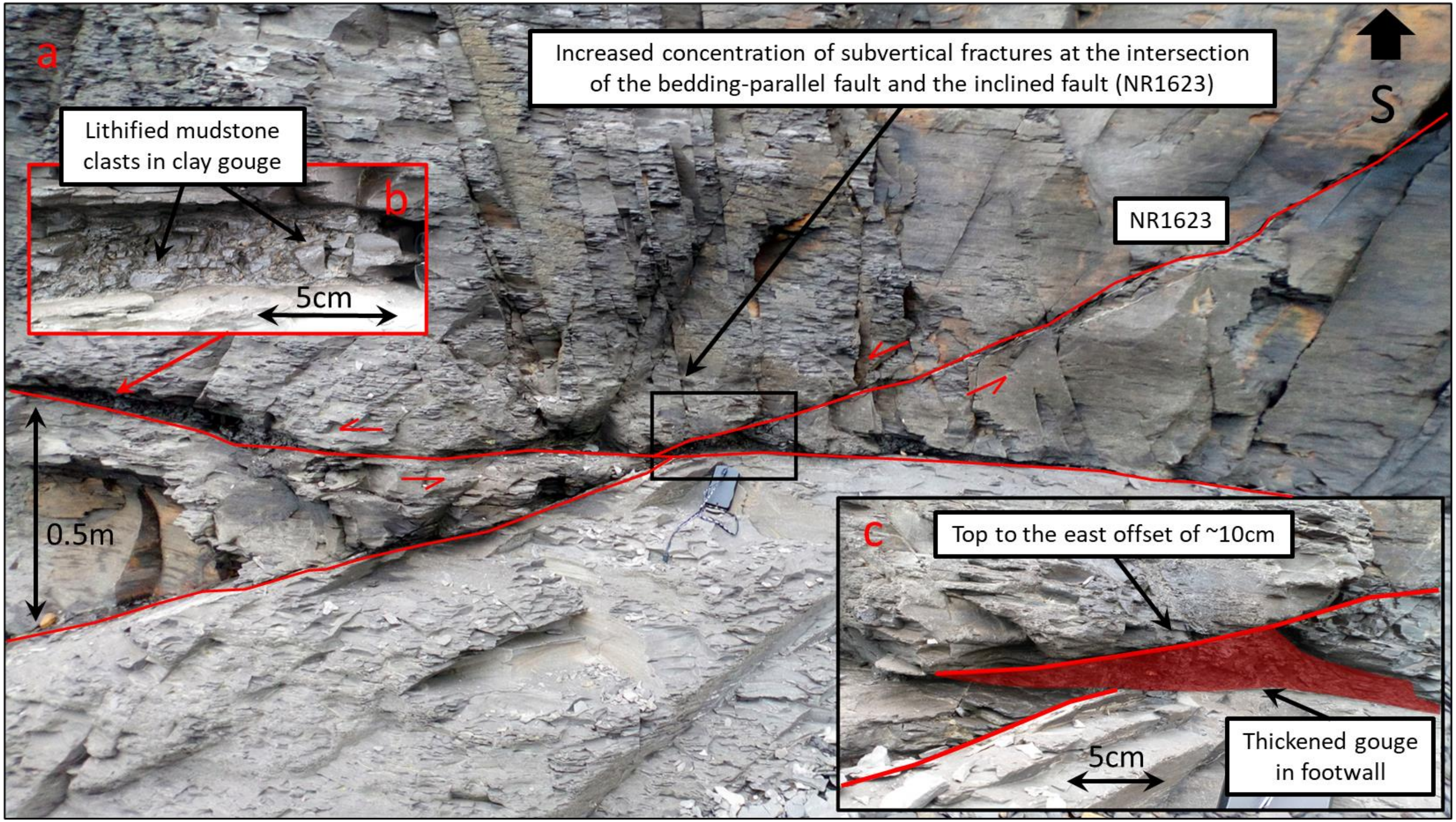


Fig 3.10. Sectional field photos of a bedding-parallel fault plane with mudstone breccia (b) and a minor westward dipping fault plane (NR1623), which is offset by a bedding-parallel fault (c). b) The mudstone gouge varies between 0.5-5cm thick with wall rock mudstone blocks set in a finer clay matrix of disaggregated mudstone. c) The bedding parallel fault is shown in c) to offset the bedding-parallel fault although a calcite vein along the inclined fault soles into the shear plane. The gouge is shown in c) to thicken into the fault footwall.

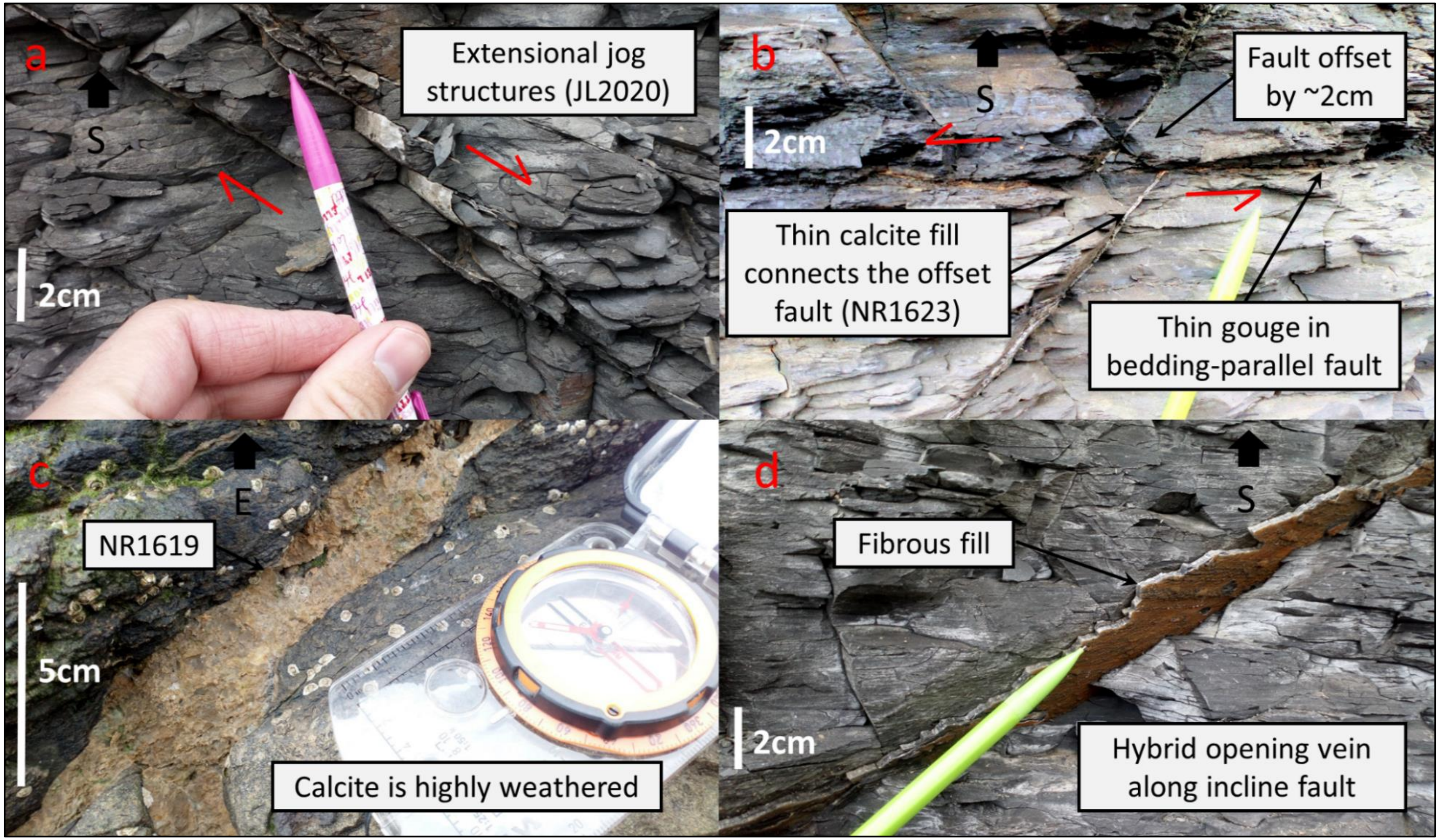


Fig 3.11. a) Dilational jog structures (JL2020) on an inclined fault (conjugate sets) with normal offset. b) An inclined fault (conjugate sets) with <1cm thick calcite fill is offset by the bedding-parallel fault. A thin veneer of calcite 1-2mm thick connects the offset fault segments indicating that calcite precipitation continued until after displacement on the bedding-parallel fault. c) A highly weathered calcite fill (2-4cm thick) in an extensional jog structure on the main fault plane. d) A 0.5mm thick fibrous calcite fill on an inclined fault (JL2024). Section 4.3.1.2 will demonstrate that opening was oblique to this fracture.

### 3.2.2.2 Osgodby Nab (Cayton Bay Fault - TA 065 854)

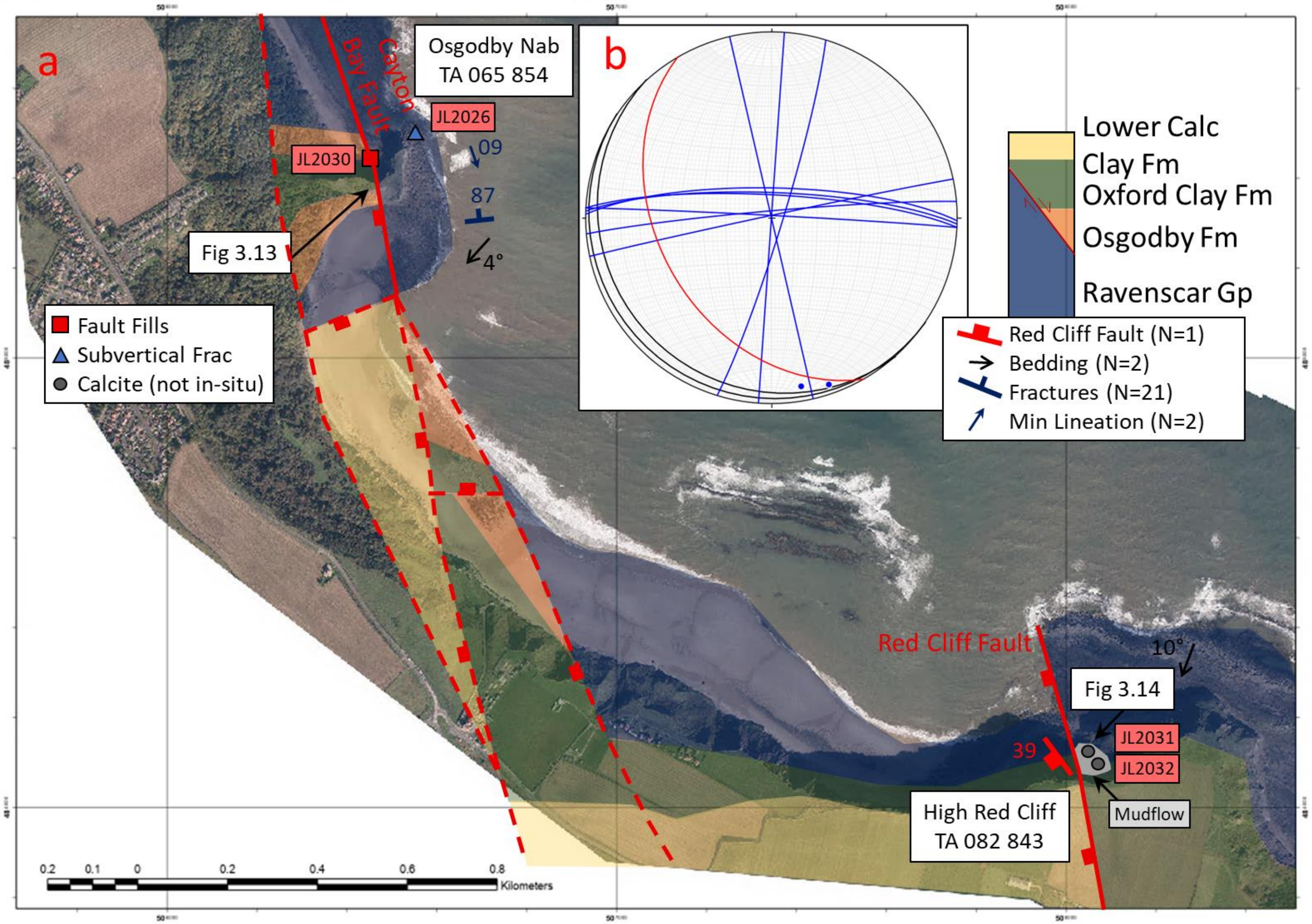


Fig 3.12. Aerial photography of Cayton Bay, North Yorkshire with fault traces plotted based on BGS 1:50,000 mapping. Osgodby Nab is shown at the northern side of the bay and High Red Cliff at the southeastern end. The Min Lineation is a mineral fibre lineation measured from calcite fibres in the calcite veins. A sketch lithological column is shown of the major geological relationships and a stereonet of the key structures: red - faults, black – bedding, blue – subvertical veins and mineral lineations. Aerial photography is courtesy of the North East Coastal Observatory (NECO). Geological interpretation is redrawn after Edina Digimap 1:25,000 geological map. The stratigraphic log is based on divisions outlined in Powell (2010).

Osgodby Nab lies at the northwestern end of Cayton Bay (Fig 3.12a). The westerly-dipping Cayton Bay Fault forms the main large-scale structure seen at this locality. The fault downthrows the sedimentary rocks of the Middle Jurassic Osgodby Formation and Upper Jurassic Oxford Clay Formation to the west 110m against the Middle Jurassic Ravenscar Group to the east (Fig 3.13; Rawson & Wright, 1992).

Cayton Bay Fault

The main fault plane (Fig 3.13) is poorly exposed, but a zone of anastomosing veinlets are present in a calcite cemented oolitic limestone (Ravenscar Group) along the fault trace at the high tide line. The N-S trending veinlets are filled with blocky centimetre-scale calcite crystals with 1-2cm wide vugs (which make up 5-10% of the vein fill volume; JL2030).

Subvertical Fractures

N-S and E-W trending joints, similar to the $J_1$ and $J_2$ joints described in Section 3.2.1, are present within the damage zone on the eastern side of the Cayton Bay Fault. E-W striking fractures are discontinuously filled with calcite fibre lineations oriented N-S (Fig 3.13). E-W striking fracture fills are locally dominant over N-S striking fracture fills with only one N-S striking fracture with E-W oriented calcite fibres identified compared to 10-20 observed E-W striking fracture fills over the space of 100m.

No clear crosscutting relationship is observable between the anastomosing veins in the main fault core and the subvertical fractures. Similarly to the Peak Fault (Section 3.2.2.1), joints are inferred to have formed first (Section 3.2.1) with later local reactivation and calcite mineralization during movement of the main Cayton Bay. This hypothesis will be tested later by seeing if dated calcite samples fit with ages from the Peak Fault.

| Sample | Location | UTM N | UTM E | Cayton Bay Fault | Calcite Fill | Texture | Kinematics | Dating | C-O | Clumped |
|---|---|---|---|---|---|---|---|---|---|---|
| JL2026 | Osgodby Nab | 671580 | 6014911 | Vein - Vertical | 2-3cm thick Vein | Blocky | Syn or post N-S Opening | Y | Y | Y |
| JL2027 | Osgodby Nab | 671564 | 6014970 | Vein - Vertical | 2-3cm thick Vein | Blocky | Syn or post N-S Opening | - | Y | - |
| JL2029 | Osgodby Nab | 671580 | 6014958 | Vein - Vertical | 2-3cm thick Vein | Blocky | Syn or post E-W Opening | - | Y | - |
| JL2030 | Osgodby Nab | 671537 | 6014841 | Cayton Bay Fault | Anastomosing Veins | Blocky | Syn or post-kinematic | Y | Y | - |

*Table 3.2. Summary of sample data from the Cayton Bay Fault and subvertical joint fills at Osgodby Nab, Cayton Bay. The locations of samples are shown in Fig 3.12. The structure type, calcite fill structure and apparent texture in hand specimen are summarised in addition to the successful analyses to be documented in Chapters 5 and 6.*

Key structures were sampled and analysed further via U-Pb dating, stable isotope and fluid inclusion analyses (Table 3.2); see Chapter 4 for further information.

### 3.2.2.3 High Red Cliff (Red Cliff Fault - TA 082 843)

High Red Cliff is transected by the westerly-dipping Red Cliff Fault (Fig 3.12a) which downthrows the Upper Jurassic Oxford Clay Formation and the Lower Calcareous Grit Formation by 37m against the Middle Jurassic Ravenscar Group (Fig 3.12b & 3.14; Rawson & Wright, 1992). A landslip obscures the fault plane except where it is accessible at the location of Fig 3.14b where a bifurcating fault plane juxtaposes mudstone units. 1cm thick dilational jog structures here (Fig 3.14b) filled with blocky calcite are present along the fault plane. Dating of a sample of blocky calcite (JL2033) via U-Pb geochronology was unsuccessful due to lack of uranium.

Two samples were taken from the landslip that covers the majority of the accessible fault exposure, both of which have been successfully dated (Table 3.3) The samples were located far above the tideline, have little to no chance of having been washed in, and lay along-strike from the main fault plane. Both samples have undergone further analysis through trace elements and stable isotopes, and JL2032 has been mapped for trace elements.

The timing of movement of the Red Cliff Fault cannot be inferred from field relations, but as samples JL2031 and JL2032 are assumed to have been transported downward from the main fault core they can used to give a low confidence approximation of fault movement associated with calcite mineralisation. The samples will be compared isotopically to results from Osgodby Nab and other localities in Chapter 5 & 6.

| Sample | Location | UTM N | UTM E | Red Cliff Fault | Calcite Fill | Texture | Kinematics | Dating | C-O | Clumped |
|---|---|---|---|---|---|---|---|---|---|---|
| JL2031 | High Red Cliff | 673110 | 6013607 | Unknown | Bladed calcite | - | Unknown | Y | Y | - |
| JL2032 | High Red Cliff | 673108 | 6013588 | Unknown | Blocky calcite | Blocky | Unknown | Y | Y | - |

Table 3.3. Summary of sample data from the Red Cliff Fault, Cayton Bay. The locations of samples are shown in Fig 3.12 & 3.14. The structure type, calcite fill structure and apparent texture in hand specimen are summarised in addition to the successful analyses to be documented in Chapters 5 and 6.

### 3.2.2.4 Summary

The structures observed at Ravenscar, Osgodby Nab and High Red Cliff are regional scale faults that likely underwent early syndepositional movement (Milsom & Rawson, 1989) which are recorded in the field by preserved mud mounds and possibly cone-in-cone structures located along the Peak Fault trace. The Peak Trough faults were then reactivated in extension post-burial and lithification. Conjugate sets of normal faults, and at least one bedding-parallel fault were also formed during reactivation. These structures, along with some subvertical joints with calcite fibres record mineralisation synchronous with E-W extension in many veins. Reactivated features are typically striking N-S, except at Osgodby

Nab where some E-W trending joints have been preferentially opened, with fracture dilation and normal fault movement. The implications of these findings are further discussed in Section 3.3.2 & 3.3.6.

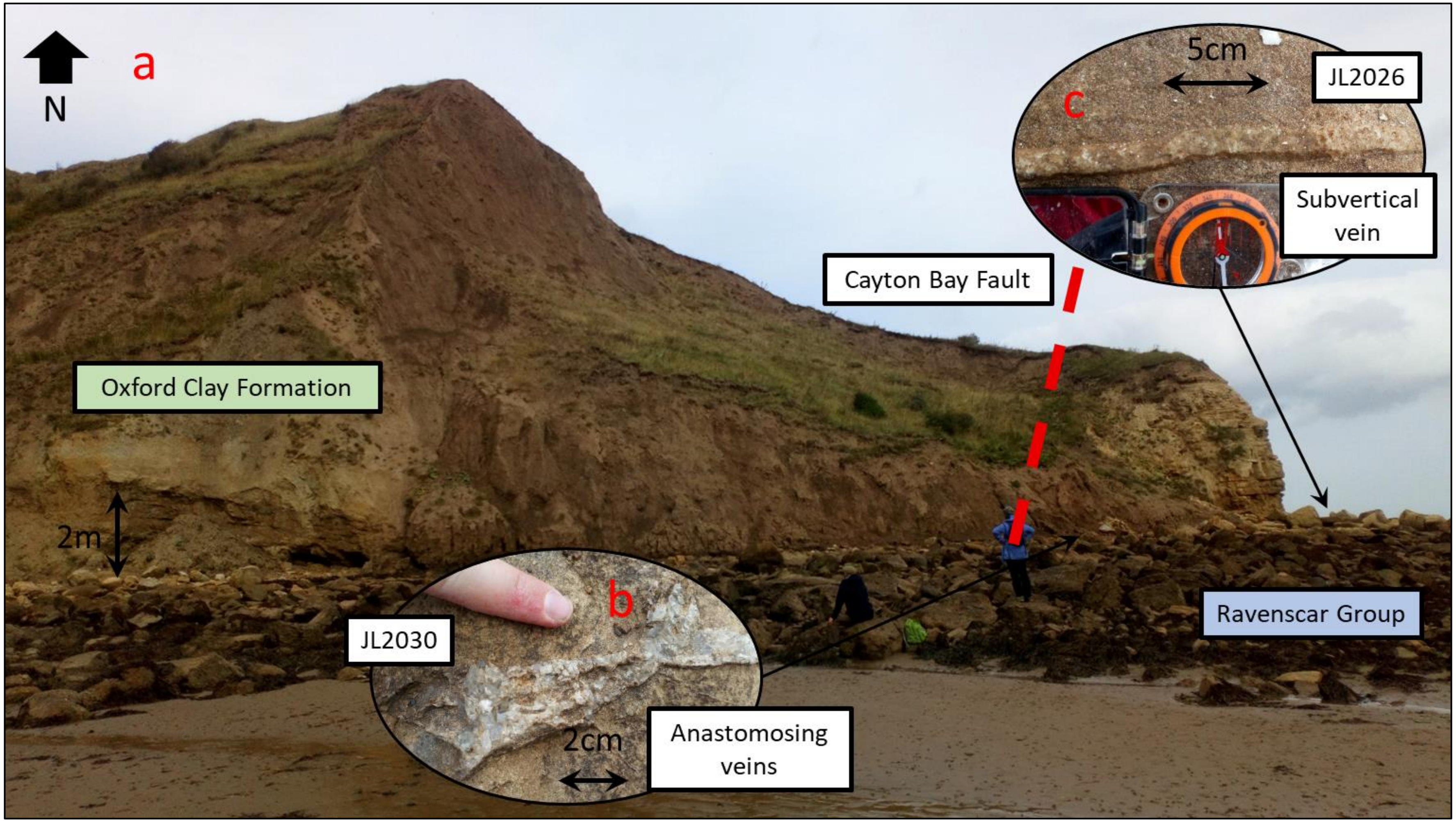


Fig 3.13. Field photographs of the Cayton Bay Fault intersecting Osgodby Nab at the northern margin of Cayton Bay. a) Sectional image of the Osgodby Nab locality with an inferred fault plane shown juxtaposing the Upper Jurassic Oxford Clay Formation against the Middle Jurassic Ravenscar Group. b) Plan view of anastomising E-W and N-S striking 1-5cm thick calcite veins (JL2030) at the inferred location of the fault plane shown in a). Calcite fills in JL2030 are blocky spar (1-2cm thick) with cm-scale vug with milky to optical clear calcite. c) Plan view image of an E-W striking fracture with a 2cm calcite fibrous calcite fill (JL2026).

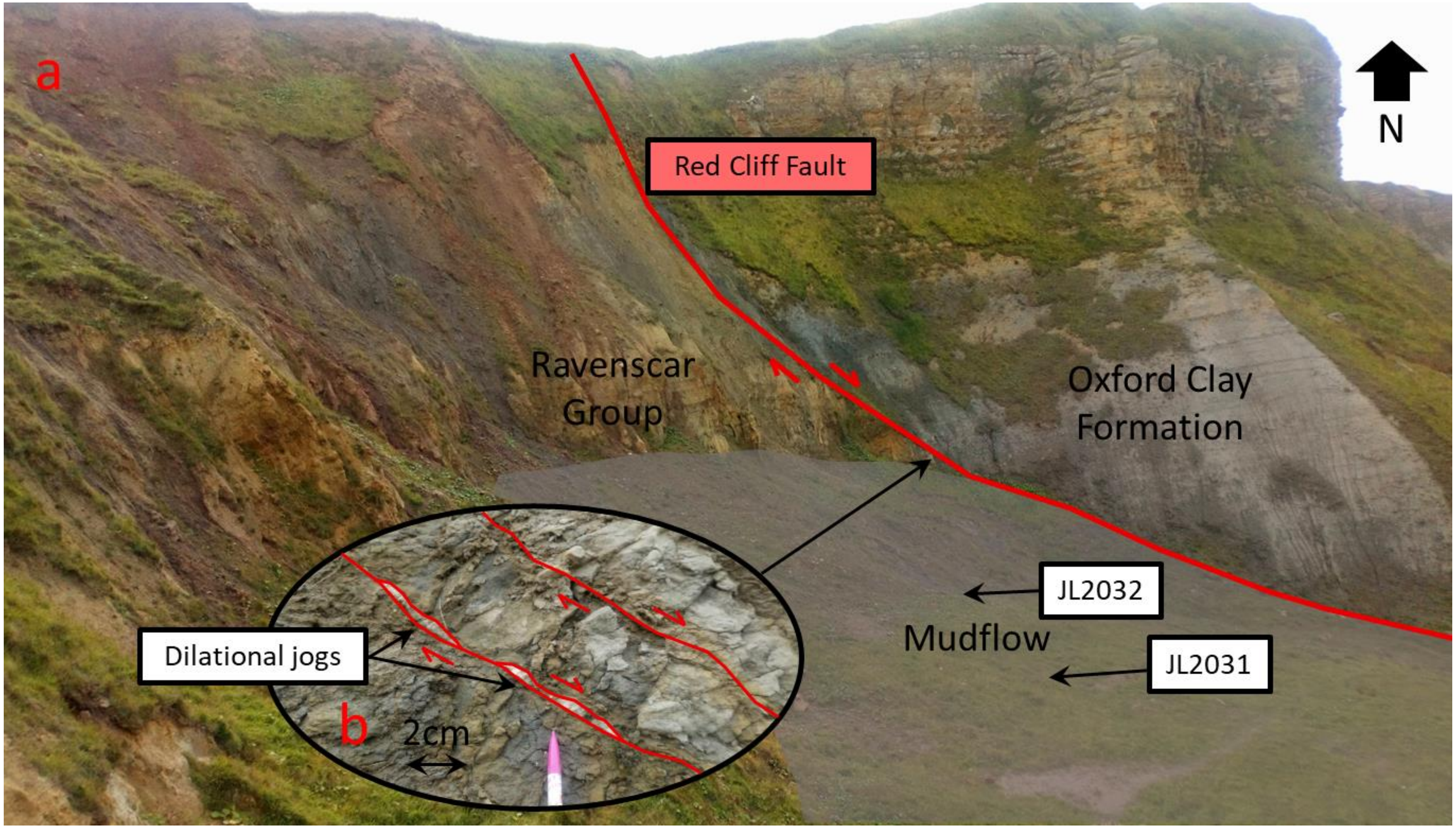


Fig 3.14. Field photographs from the High Red Cliff locality. a) Sectional overview image of the Red Cliff Fault with the inferred trace highlighted. The fault has normal offset with Oxford Clay Formation juxtaposed against the Scalby Formation. Samples JL2031 and JL2032 were taken from the zone of landslip/mudflow >20m above the high tide line. b) A sectional image of the Red Cliff Fault fault plane with the contact shown between the Ravenscar Group and the Oxford Clay Formation. The location of sample JL2033 is shown along the fault plane with 1-2cm thick blocky calcite fills along the bifurcating fault planes.

### 3.2.3 Meso-Scale Fault Structures

In contrast to the Peak Trough which forms a >50km long faulted graben structure, numerous smaller fault zones up to 10km in length cross-cut the Cleveland Basin. Of these fault zones, the Runswick Bay, Staithes and Port Mulgrave fault zones all have good coastal exposure and fault structures associated with calcite mineralisation. These fault zones are "meso-scale" structures, which will provide more localised information on variations in the stress state of the Cleveland Basin. Port Mulgrave in particular has a distinct pattern of localised mixed extensional and oblique-slip faulting, which will require careful analysis.

#### 3.2.3.1 Runswick Bay Fault Zone (Runswick Bay - NZ 811 165 & NZ 812 164)

The Runswick Bay Fault Zone (Fig 3.15 & Fig 3.16a) is a set of N-S to NNW-SSE trending faults that transect the headland for 0.6km north of the village of Runswick Bay, North Yorkshire. The fault zone has been analysed at two main sub localities, detailed below.

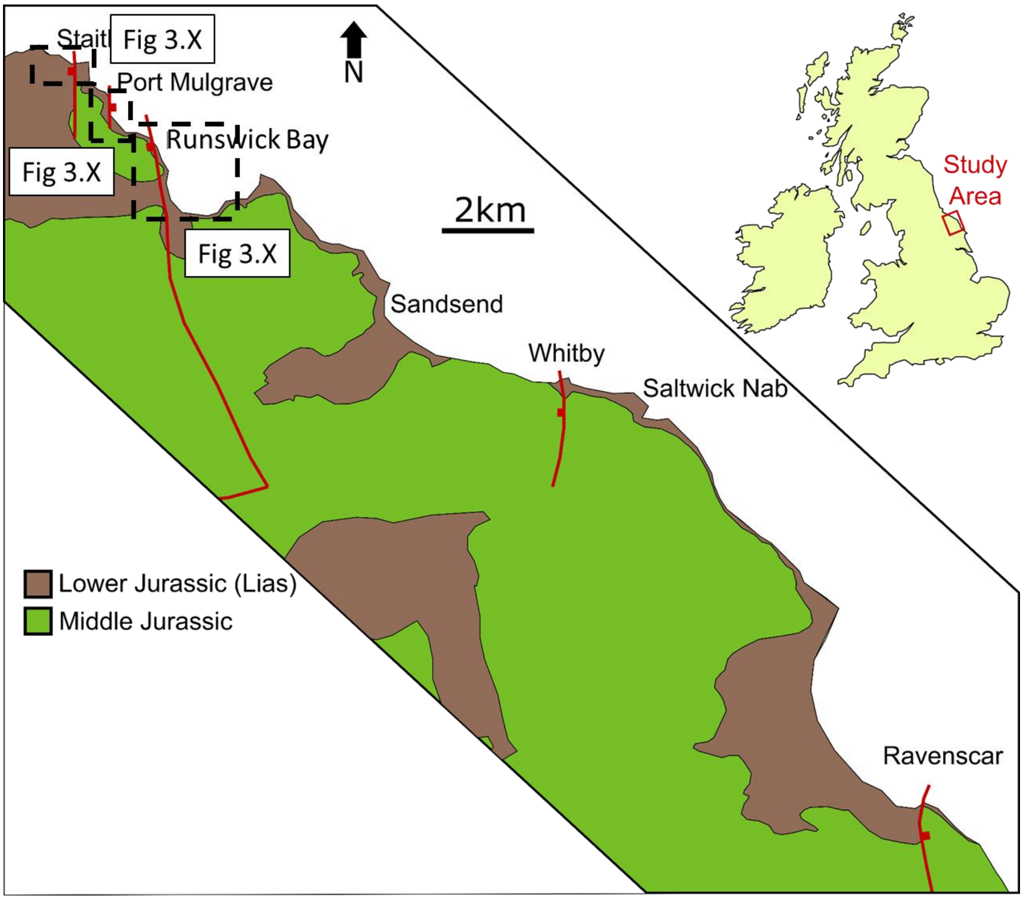


Fig 3.15. Geology map of the main area of interest highlighting the location of the Runswick Bay (Fig 3.16), Staithe (Fig 3.19) and Port Mulgrave Fault Zones (Fig 3.21 & 3.25).

<u>Locality A</u> is located at the northern end of the headland. Samples were taken here and further analysed by Roberts and Imber (Pers. Comm.), but the exact location of these samples could not be identified during the present study. Safe access along the wavecut

platform is hindered by the tidal nature of the outcrop and rubble covering the wavecut platform in numerous locations. Both of these factors restricted safe access meaning that the assessments herein are based on the photos and sampling notes made by Imber and Roberts. The Runswick Bay Fault Zone at Locality A is shown in Figure 3.17 and comprises of a series of west-dipping (30-70°; Fig 3.16b) anastomosing and coalescing ramp-flat geometry normal faults with common calcite mineralised extensional jog structures up to 5cm thick. The faults were interpreted by Roberts & Imber to have a normal displacement, which is supported by the preservation of extensional jogs and down-dip plunging slickenlines. A steep antithetic fault to the anastomosing set is shown in Figure 3.17b. The fault appears to have a 10-30cm thick clay-grade fault gouge with a cm-scale calcite vein running parallel to the gouge. The trace of this fault can be followed northwards into the wavecut platform.

Locality B is located 0.3km directly north of the village of Runswick Bay and is comprised of combined cliff and wavecut exposures. In both localities, the country rock is gently SW dipping (4-10°) organic-rich mudstones of the Mulgrave Shale Member (Whitby Mudstone Formation).

Locality B sits 100m from the unexposed inferred fault trace of the main Runswick Bay Fault Zone (Fig 3.16a). There is a similar faulting style present to Locality A with variably dipping faults with ramp-flat geometries (Fig 3.18). Similar to the faults at Locality A, the faults have cm-scale clay gouges with calcite mineralisation preserved in extensional jog structures typically 2-3cm thick. In addition to extensional jog structures, bedding-parallel veins (0.5-1cm thick; JL2010, Fig 3.18) are present on flat segments with large blocky calcite with common vugs (10-20%). Extensional jogs and cm-scale rollover anticlines formed in the gouge demonstrate normal fault offset. JL2012 is a thin (1-2mm thick) N-S subvertical vein that has been reactivated due to extension along the normal faults similar to joints described at Ravenscar in Section 3.2.2.

Both localities show deformation distributed along multiple minor fault structures with minimal displacement of less than two metres along individual minor faults associated with the larger fault zone. This is consistent with very low magnitudes of displacement. The total extension associated with the Runswick Bay Fault Zone is estimated at up to 10% in the fault zone but quickly dies away from the fault zone. The nearest fault zones are >1km away and therefore it is likely that the total magnitude of regional extensional is 1% or less.

Further transect work could be conducted at this location to better constrain the magnitude of extension although it is likely that poor access will hamper any such analysis.

The faults at this locality have a distinct ramp-flat geometry, which is commonly seen in fault structures in the more clay-rich lithologies and could be related to geomechanical properties of the clay-rich Whitby Mudstone Formation. In both localities at Runswick Bay, fluid-flow appears to be focused around the fault zone.

| Sample | Location | UTM N | UTM E | Runswick Bay Fault | Calcite Fill | Texture | Kinematics | Dating | C-O | Clumped |
|---|---|---|---|---|---|---|---|---|---|---|
| NR1615 | Runswick Bay | 645420 | 6046223 | Main Fault | Breccia + Jog | Blocky | Syn to post-kinematic | Y | Y | - |
| NR1612 | Runswick Bay | 645370 | 6046175 | Fault - Normal | Extensional Jog | Blocky | Synkinematic | Y | Y | Y |
| JL2010 | Runswick Bay | 645727 | 6045194 | Fault - Normal | Extensional Jog | Blocky | Synkinematic | - | Y | - |
| JL2012 | Runswick Bay | 645758 | 6045157 | Vein - Vertical | 0.5mm thick Vein | Fibrous | Syn E-W Opening | - | Y | - |

*Table 3.4. Summary of sample data from the Runswick Bay Fault Zone. The locations of samples are shown in Fig 3.16. The structure type, calcite fill structure and apparent texture in hand specimen are summarised in addition to the successful analyses to be documented in Chapters 5 and 6.*

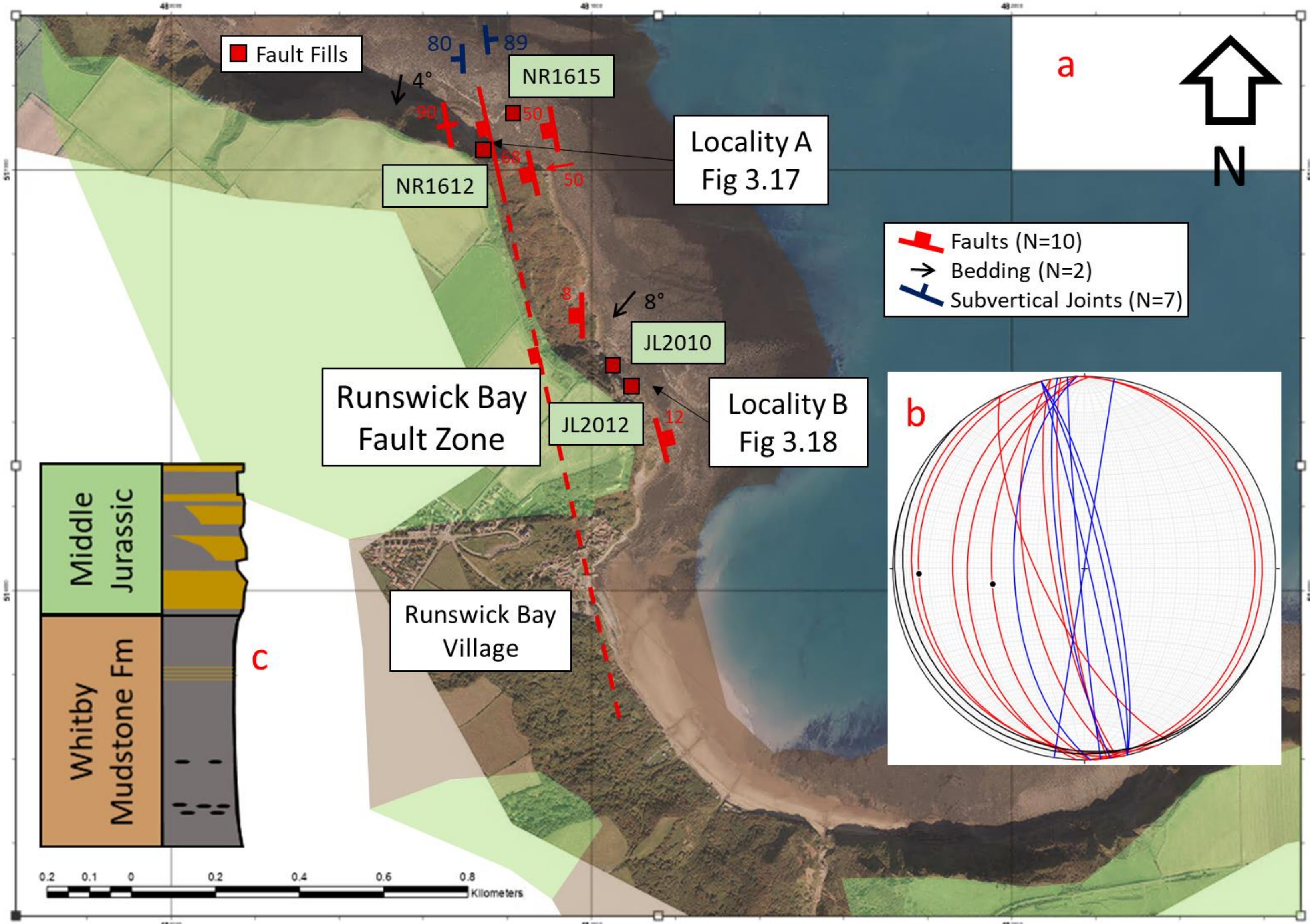


*Fig 3.16. a) Aerial photography demonstrating the locations of key samples at Runswick Bay. The inferred trend of the Runswick Bay Fault Zone is NNW-SSE and the fault crops out at the headland 0.6km north of the village of Runswick Bay. b) A stereonet is included showing faults (red), subvertical veins (blue) and bedding (black). Aerial photography is courtesy of the North East Coastal Observatory (NECO). c) The stratigraphic log is redrawn based on Hesselbo & King (2019).*

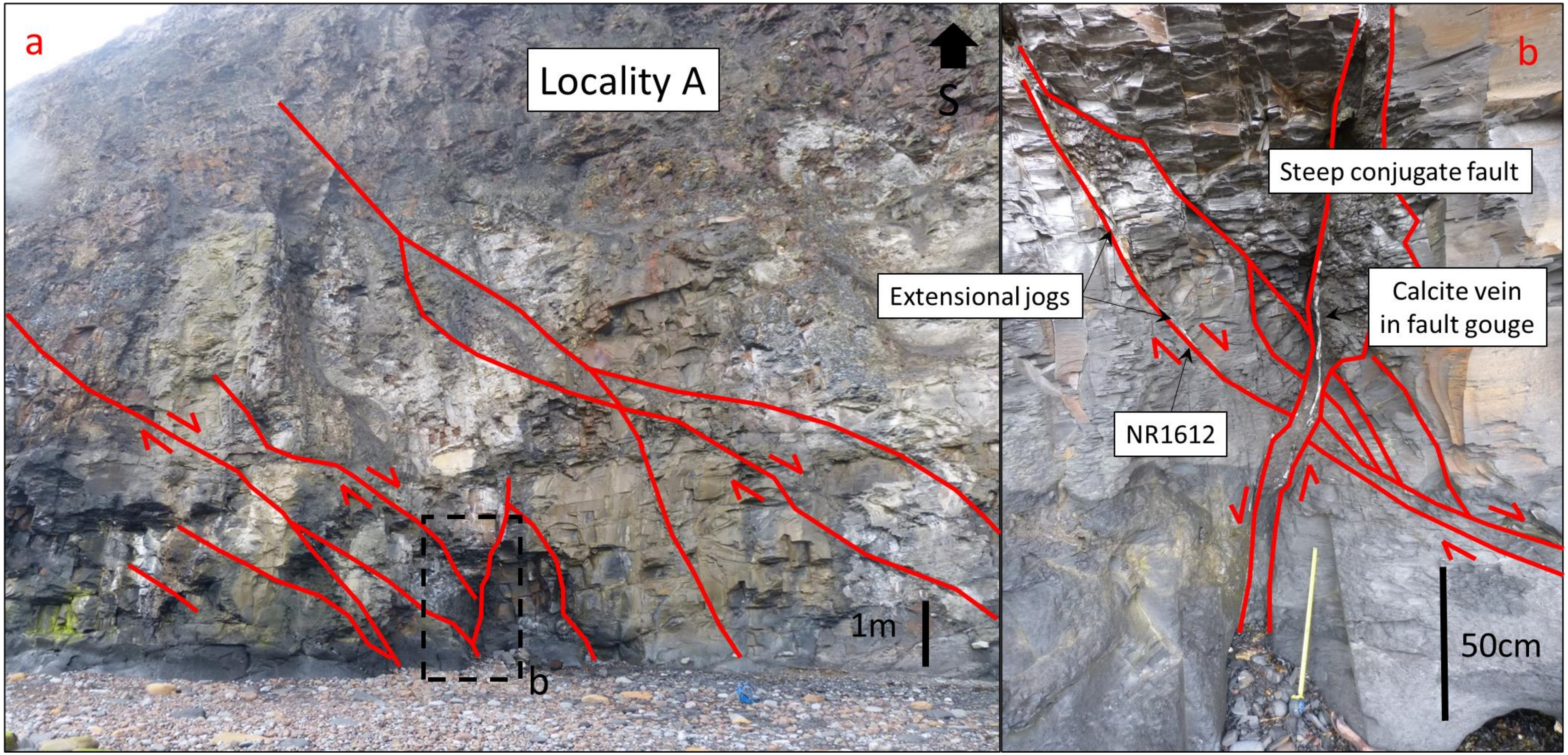


*Fig 3.17. Interpreted field photos from the Runswick Bay Fault Zone. a) Sectional image of the N-S striking fault zone sampled is formed of a series of anastomosing and coalescing westward dipping normal fault planes dipping between 30-60° with a steeper antithetic fault set shown in b) along with location of NR1612 a calcite filled extensional jog structure.*

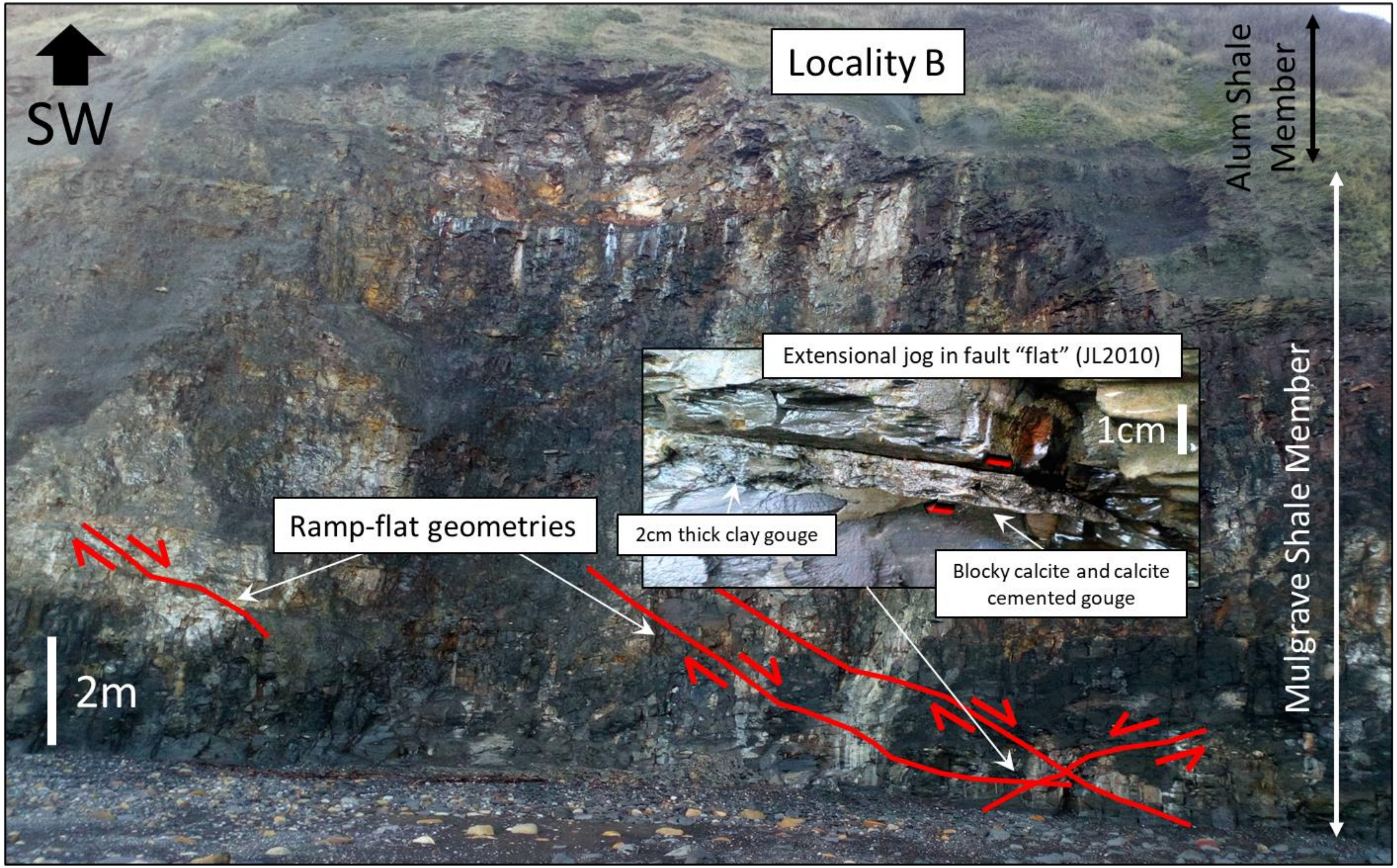


*Fig 3.18. Sectional image of the Runswick Bay fault Zone at locality B, 100m west of the main fault, with a sequence of ramp-flat NNW-SSE striking faults with an inset image of JL2010, an extensional jog structure on a fault “flat” section dipping 5° to the west.*

### 3.2.3.2 Staithes Fault Zone (Staithes - NZ 787 188)

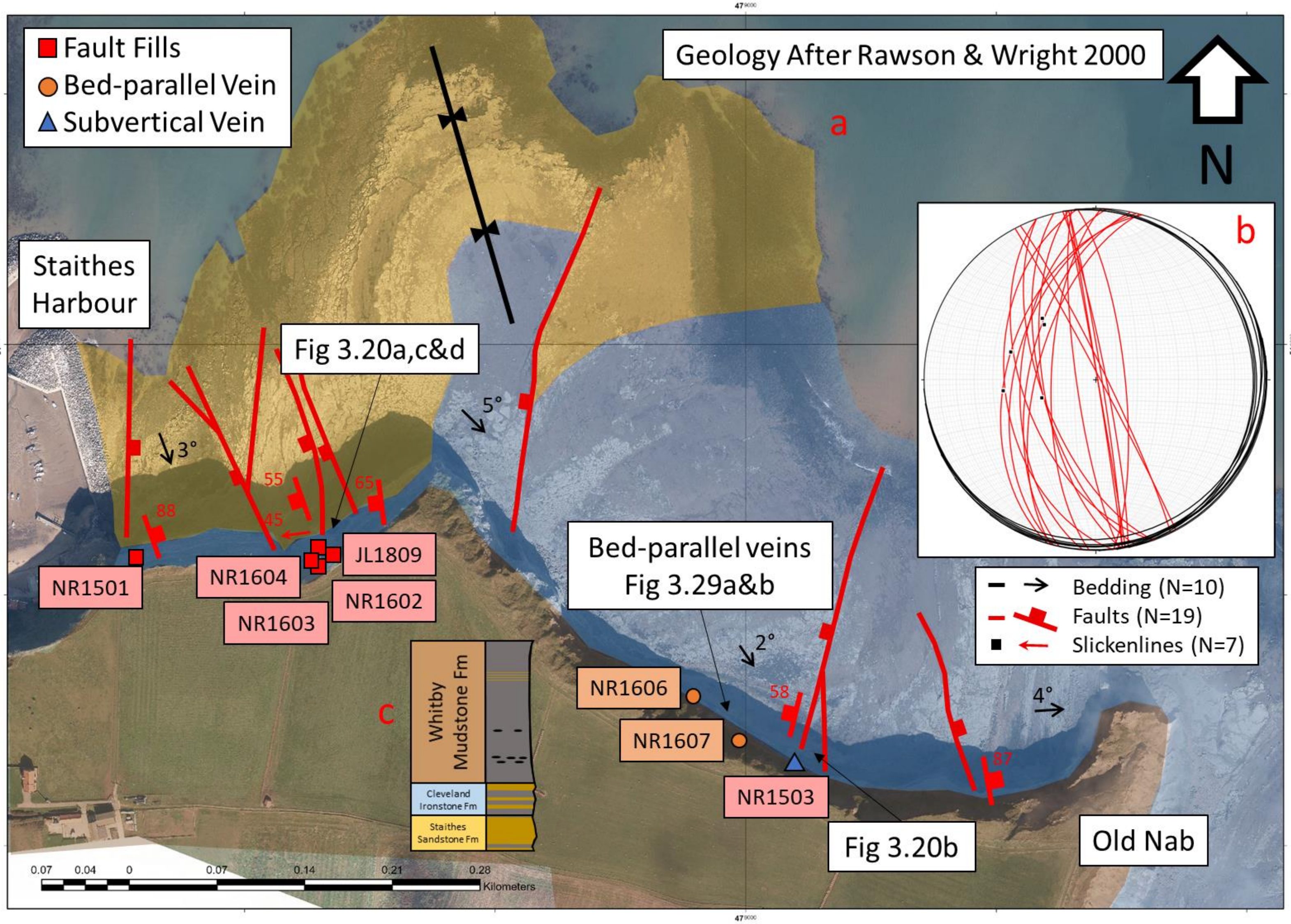


*Fig 3.19. a) Aerial photography of the fault structures at Staithes. b) A stereonet is inset with the fault planes (red) and bedding (black). Two bedding-parallel vein samples are present (NR1606 & NR1607) and will be discussed further in Section 3.2.4.1. Geology is based on work by Rawson & Wright, 1992). Aerial photography is courtesy of the North East Coastal Observatory (NECO). c) The stratigraphic log is redrawn based on Hesselbo & King (2019).*

The Staithes locality extends approximately 750m east of the village of Staithes, North Yorkshire (Fig 3.15). Mixed wavecut platforms and cliff exposures trend E-W, with exposures dominated by the shallow, easterly dipping upper Staithes Sandstone Formation (Lower Jurassic). This passes conformably up into the Cleveland Ironstone Formation as far as the Avicula Seam, outcropping at Old Nab (Fig 3.19a) and following the detailed stratigraphic divisions provided by Howarth (1955).

<u>Normal Faults</u>

A series of faults are exposed along the cliff between Staithes Harbour and Old Nab (Fig 3.20a & 21) as outlined by Imber et al. (2014) and are collectively termed here the "Staithes Fault Zone". Many fault planes are difficult to access due to dangerous cliff exposures. The faults can be grouped into two sets of conjugate normal faults occasionally forming ~20m wide graben structures. The faults systematically displace marker ironstone beds (Fig 3.20b) downwards in the hangingwall, diagnostic of normal motion. West dipping faults range in dip from 40° to 80° with eastward dipping conjugates having dips between 75 and 90° (Fig 3.19b). These faults individually show 0.5-2m displacement, with displacement observed to decrease upwards 20-30m in the cliff, as can be seen on Figure 3.20b. This appears to be true of all faults observed at this locality. The total magnitude of extension is anticipated to be low with faults widely spaced 20-300m apart and likely total offset of 10s of metres across the whole fault zone. This is supported by fracture traverse data collected by Ashman (2017), which found extension (including earlier joints) varied between <0.01 and 12% with local maximums near fault structures. It is therefore suggested that the actual magnitude of extension across the entire fault zone is likely low (1-5%) and consistent with low regional extension of <1%.

In addition to normal fault structures, the pervasive jointing sets ($J_1$ / N-S and $J_2$ / E-W) and bedding-parallel veins are present at this locality. Joints are rarely mineralised here and when calcite fills are present they are always associated with a larger fault structure (NR1503). Bedding-parallel veins show a degree of displacement (1-2cm) and gouge development with bedding-parallel calcite veins developed. These bedding-parallel veins will be discussed in more detail in Section 3.2.4.1.

The stereonet in Figure 3.19b shows that the faults strike between NNE-SSW and NNW-SSE and display slickenlines plunging down-dip as illustrated in Fig 3.19d and described by Imber et al. (2014). Where fault planes can be safely accessed, a fault core of brecciated mudstone wall rock clasts set in a clay gouge is bounded by two planar faults with frequent extensional jog structures present (Fig. 3.20c). Extensional jog structures are calcite mineralised with slickenfibre development indicating synkinematic calcite fills (Fig. 3.20d).

Samples taken are primarily from fault structures with a variety of different calcite fills, and are summarised in Table 3.5. Hand specimen calcite crystal textures are predominantly blocky at this locality with evidence for marginal slickenfibres.

| Sample | Location | UTM N | UTM E | Staithes Fault | Calcite Fill | Texture | Kinematics | Dating | C-O | Clumped |
|---|---|---|---|---|---|---|---|---|---|---|
| NR1501 | Staithes | 643061 | 6047936 | Fault - Normal | Calcite in Gouge | Blocky | Pre to Synkinematic | Y | Y | - |
| NR1602 | Staithes | 643296 | 6048179 | Fault - Normal | Calcite in Gouge | Blocky | Pre to Synkinematic | Y | - | - |
| NR1603 | Staithes | 643294 | 6048169 | Fault - Normal | -7mm vein along fau | Blocky | Synkinematic | Y | - | - |
| NR1604 | Staithes | 643294 | 6048169 | Fault - Normal | Thin vein/jog | Blocky | Synkinematic | Y | Y | Y |
| JL1809 | Staithes | 643209 | 6047954 | Fault - Normal | Extensional Jog | Blocky | Synkinematic | Y | Y | - |
| NR1503 | Staithes | 643565 | 6047800 | Vein - Vertical | 0.5cm thick vein | Blocky | Syn or post Opening | Y | Y | - |

Table 3.5. Summary of sample data from the Staithes faults. The locations of samples are shown in Fig 3.19. The structure type, calcite fill structure and apparent texture in hand specimen are summarised in addition to the successful analyses to be documented in Chapters 5 and 6.

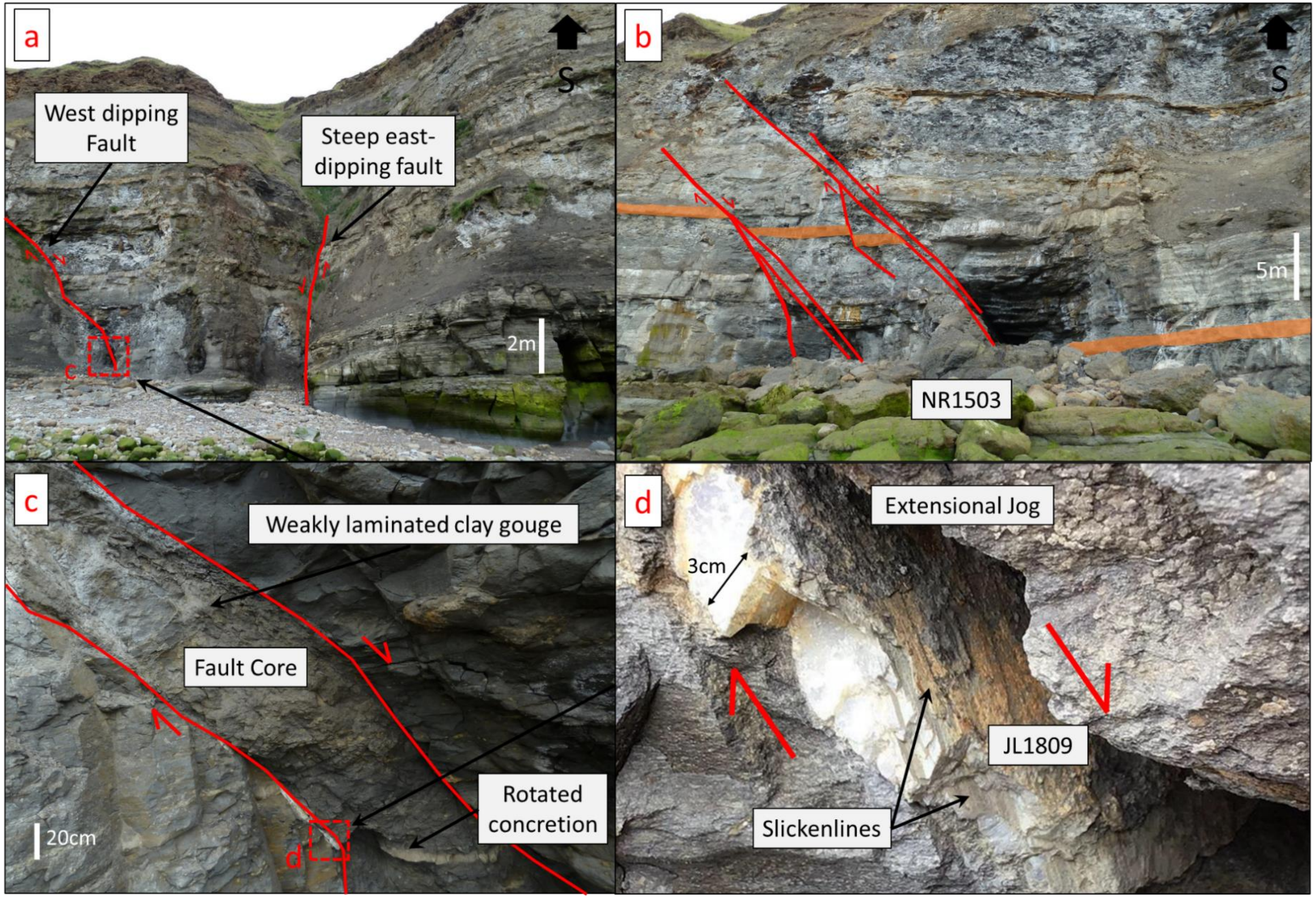


*Fig 3.20. a) Sectional photography of a horst structure with a steep east-dipping (~80°) fault and a shallower (30-50°) west-dipping conjugate fault. b) Sectional image of a sequence of planar west-dipping faults systematically offsetting the Two Foot Ironstone Seam (orange). c) Sectional image of the fault core from image a) with a well developed clay gouge (~0.5m thick) between two bounding faults. d) A sectional image of an extensional jog structure (3cm thick) in the lower bounding fault from c) with dip-slip slickenfibres, which have formed a veneer on the outer part of the vein.*

### 3.2.3.3 Port Mulgrave Fault Zone and associated structures (NZ 799 159 & NZ 798 175)

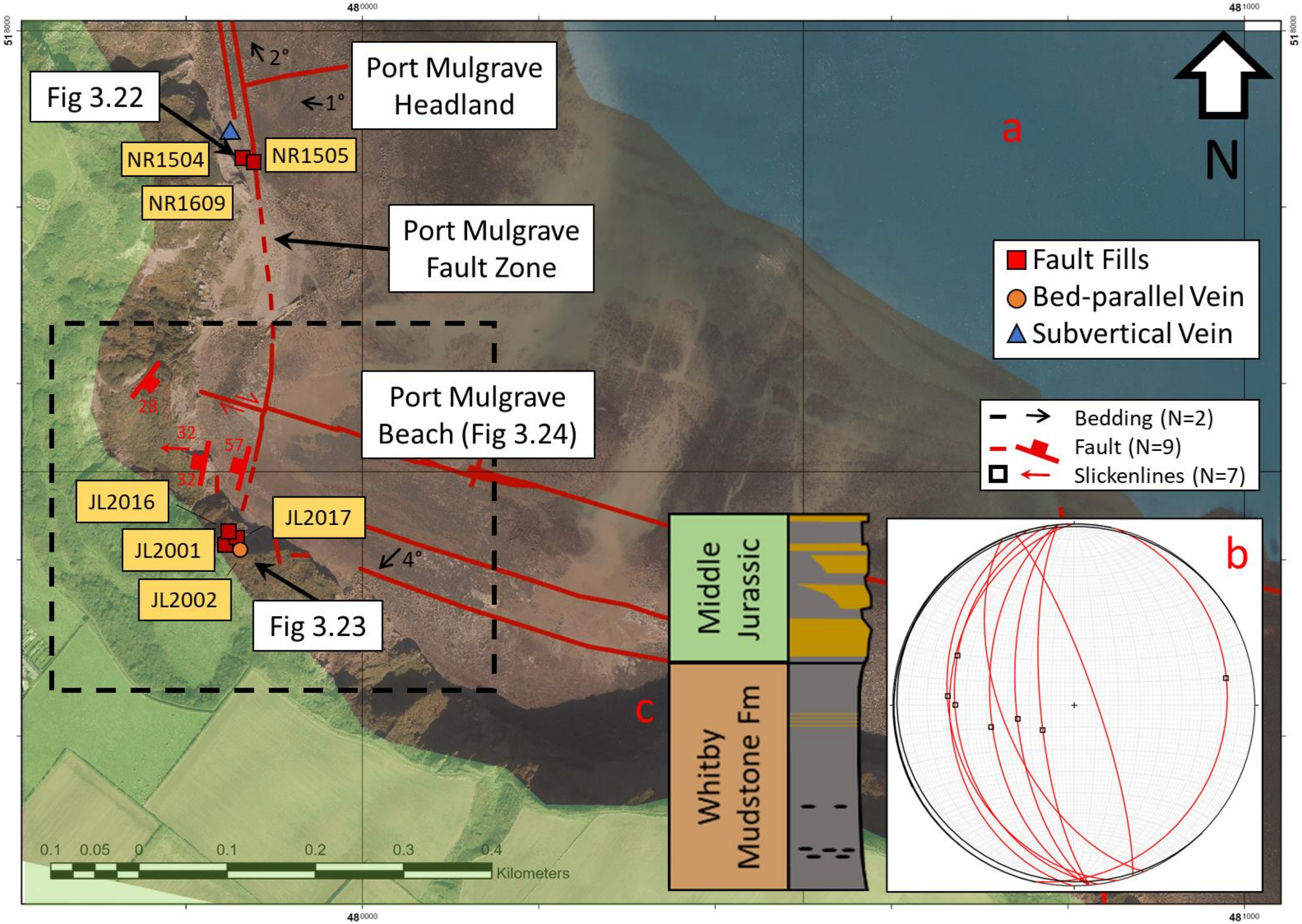


*Fig 3.21. a) Aerial photography of the Port Mulgrave Fault. The fault trends NNW-SSE at Port Mulgrave headland and is inferred to bend to a NNE-SSW trend at the beach locality. b) A stereonet (inset) showing measurements from the Port Mulgrave Fault (red) and bedding (black). Aerial photography is courtesy of the North East Coastal Observatory (NECO). c) The stratigraphic log is redrawn based on Hesselbo & King (2019) and Morgans et al. (1999).*

The Port Mulgrave field locality is exposed near the coastal village of Port Mulgrave, North Yorkshire (Fig. 3.15 & 3.21a). Port Mulgrave is split into two sub-localities: 'headland' (Locality A - NZ 799 159), 0.5km to the north of the village and 'beach' (Locality B - NZ 798 175), 0.3km to the northeast (Fig. 3.24). Both sub-localities are characterised by the presence of shallowly dipping mudstones of the Mulgrave Shale Member (Whitby Mudstone Formation; Fig 3.21c) which outcrop in the wavecut platforms and cliff sections.

The Port Mulgrave locality is unique in that - in addition to N-S extensional structures - oblique-slip faulting (N-S and NW-SE striking sets) is also present (Fig 3.21b). The structures at Port Mulgrave have therefore been sub-divided based on their dominant slip sense. The extensional structures can be further sub-divided into normal faults and extensional imbricate structures, whilst the oblique-slip structures are split into dextral and sinistral faults.

<u>Extensional Structures - *Normal Faults*</u>

The Port Mulgrave Fault Zone is highlighted on Figure 3.21a and transects the headland, with a SSE trace until the Port Mulgrave beach locality, where it swings in a clockwise direction to trend SSW.

A series of N-S striking faults make up the Port Mulgrave Fault Zone with offset marker layers, extensional jogs and down-dip plunging slickenlines (Fig 3.21b) are indicative of normal offset (up to 2m) with minor lateral offset (cm-scale). The faults analysed vary from stair-step and listric geometries. Fault fills include gouges, protocataclasites and calcite-mineralised breccias and are indicated by De Paola (Pers. Comm.) to vary from texturally immature to mature with variable thicknesses (mm to 10s of cm). In addition, oil filled extensional jogs are present along the normal faults associated with the Port Mulgrave Fault Zone (Imber, Pers. Comm.)

Two faults are discussed here from the Port Mulgrave Fault Zone. Fault 1 is a west-dipping fault with a stair-step geometry, with the steps forming extensional jog structures (Fig 3.22). Extensional jogs and field observations of offset marker layers indicate a down throw of 20-30cm, with (Per Comms.) suggesting a minor lateral offset. The presence of common down plunge slickenlines, however, support the interpretation that extension was dominant over any lateral movement in these faults.

The fault core is up to 40cm thick and consists of a slip zone gouge (clay grade grains) and calcite mineralised breccia fills in extensional jogs. The breccia is indicated by De Paola (De

Paola, Pers. Comm.) to be composed of 55-65% clasts and 45-35% calcite cement with sub-rounded mudstone clasts of 2-6mm in length forming a chaotic to mosaic texture, with iron-staining. Calcite mineralisation is shown in Figure 3.22c to be focused along the fault plane.

Fault 2 is an east-dipping conjugate to Fault 1 with predominantly normal movement (1-2m) with minor dextral movement. The fault has a stair-step geometry and is suggested to be texturally immature (De Paola, Per. Comms.). Extensional jogs are present and are represented by eroded voids. However, in one preserved fill, De Paola (Per. Comms.) identified a mosaic breccia with jigsaw textures, and clasts recording synkinematic movement of the fault structure This fill was not identified in this study, likely due to subsequent erosion of the cliffs.

Subvertical (NR1609) and bedding-parallel calcite veins (mm wide) are present within 10-20m of the fault zone. These veins grow increasingly infrequent away from discrete fault planes, which suggests that at this locality, fluid was focused primarily along the fault planes with only minor secondary fluid-flow along adjacent subvertical and bedding-parallel fractures.

The overall magnitude of normal fault extension is at a maximum at the Port Mulgrave Fault (5-10%) where metre-scale displacements are associated with the normal fault structures ; however, the number of faults and displacement dies away quickly away from the fault zone and is likely consistent with low magnitude regional extension of <1% (Ashman, 2017).

Bedding-parallel and extensional imbricate structures

Along the interpreted trace of the Port Mulgrave Fault Zone at the beach locality (Locality B; Fig 3.24a), bedding-parallel imbricate structures are present in addition to minor extensional dominated faults similar to those described at the headland locality. These imbricate structures have previously been described by Imber (Unpublished Work) with centimetre-scale extensional duplex structures and detachments described. The exact the relation of these structures to local faulting is unclear due to recent, to local landslips, which cover much of the exposure but these imbricate zones likely represent detachments layers of extensional faults or flats along ramp-flat faults.

Imbricate structures have been observed at a metre- and centimetre-scale. One such structure is shown in Figure 3.23. Duplex structures are composed of inclined fault planes linking into bedding parallel detachments. Both sets of structures have <2cm wide clay gouges developed along their fault planes with sigmoidal and planar calcite veins developed (JL2001 & JL2002).

Detachments are also described as having fibrous calcite fills (Imber, Pers. Comm.), but these have not been observed during the present study, likely due to recent landslides or beach movement, which covers a lot of the available outcrop at this location. Calcite filled pull-apart structures are indicated and have been documented in relationship to the bedding-parallel detachment zones and are used to infer top to the West displacement of these extensional imbricate structures. Some joint structures trending N-S or NW-SE are shown to curve to the plane of the imbricate structure (Fig 3.23). This could suggest the local presence of an additional later joint set ($J_3$) in Section 3.2.1. The implications of this will be discussed in the next section.

Minimal offset of joints is shown in Figure 3.20 and this included with millimetre to centimetre thickness extensional jogs associated with imbricate zones is used to infer very low magnitude extension <1%.

| Sample | Location | UTM N | UTM E | Port Mulgrave Fault | Calcite Fill | Texture | Kinematics | Dating | C-O | Clumped |
|---|---|---|---|---|---|---|---|---|---|---|
| JL2017 | Port Mulgrave | 644445 | 6046552 | Fault - Normal | Extensional Jog | Blocky | Synkinematic | Y | - | Y |
| NR1504 | Port Mulgrave | 644433 | 6046965 | Fault - Normal | Extensional Jog | Blocky | Syn to post-kinematic | Y | - | - |
| NR1505 | Port Mulgrave | 644433 | 6046965 | Fault - Normal | Extensional Jog | Blocky | Syn to post-kinematic | Y | Y | - |
| JL2016 | Port Mulgrave | 644448 | 6046559 | Fault - Normal | Extensional Jog | Blocky | Synkinematic | Y | - | - |
| JL2001 | Port Mulgrave | 644501 | 6046612 | Fault - Normal (Duplex) | Extensional Jog | Blocky | Syn to post-kinematic | Y | Y | - |
| JL2004 | Port Mulgrave | 644483 | 6046531 | Vein - Vertical | 0.5mm thick Vein | Fibrous | Syn E-W Opening | - | Y | - |
| NR1609 | Port Mulgrave | 644534 | 6047178 | Vein - Vertical | 1-2mm thick vein | Blocky | Syn or post E-W Opening | Y | Y | - |
| JL2002 | Port Mulgrave | 644501 | 6046612 | Vein - Bedding-parallel (Duplex) | 0.5-1mm thick vein | Blocky | Syn to post-kinematic | Y | Y | - |

*Table 3.6. Summary of sample data from the Port Mulgrave Fault and related structures. The locations of samples are shown in Fig 3.21 & 3.24. The structure type, calcite fill structure and apparent texture in hand specimen are summarised in addition to the successful analyses to be documented in Chapters 5 and 6.*

#### 3.2.3.4 Port Mulgrave Oblique-slip Faulting

Imber (Unpublished Work) has previously documented two sets of oblique-slip faults at the Port Mulgrave beach locality, with dextral and sinistral oblique-slip faults present in the wavecut platform and cliff exposures (Fig 3.24a). In contrast to the extension-dominated faults described with minor components of oblique movement, the oblique-slip faults are dominated by strike-slip movement with only minor amounts of extension. The oblique-slip faults form ~60° conjugate sets (Stereonet; Fig 3.24b).

<u>Dextral oblique-slip fault</u>

An E-W striking listric fault (Fig 3.24a & 3.25a) outcrops on Port Mulgrave beach. The fault dips to the south and shallows from 75° to 60°, with measurable offset of a distinctive marker bed showing an apparent downthrow of approximately 40-50cm. The extent amount of dextral offset is difficult to determine but is likely ~1-2m.

The fault bifurcates at beach level and splits into two planes marked by a fault plane with an extensional jog structure (Fig 3.25b) with oblique slickenlines (35-114; Fig 3.25c), and a fault plane with nested cone-in-cone (Fig 3.25d) structures (5cm thick). Cones are oriented normal to the fault plane and border a 5-10cm thick zone of laminated fault gouge (clay grade grains).

The extensional jog structure is up to 5cm thick and varies from a blocky textures with 1-2mm vugs (1-2% vugs; JL1812b) to a 2cm thick blocky calcite fill with inclusion bands of submillimetre thick mudstone clasts (JL1812a) that track oblique opening and suggest synkinematic fault movement while the blocky fill with open pores suggests subsequent crack-fill.

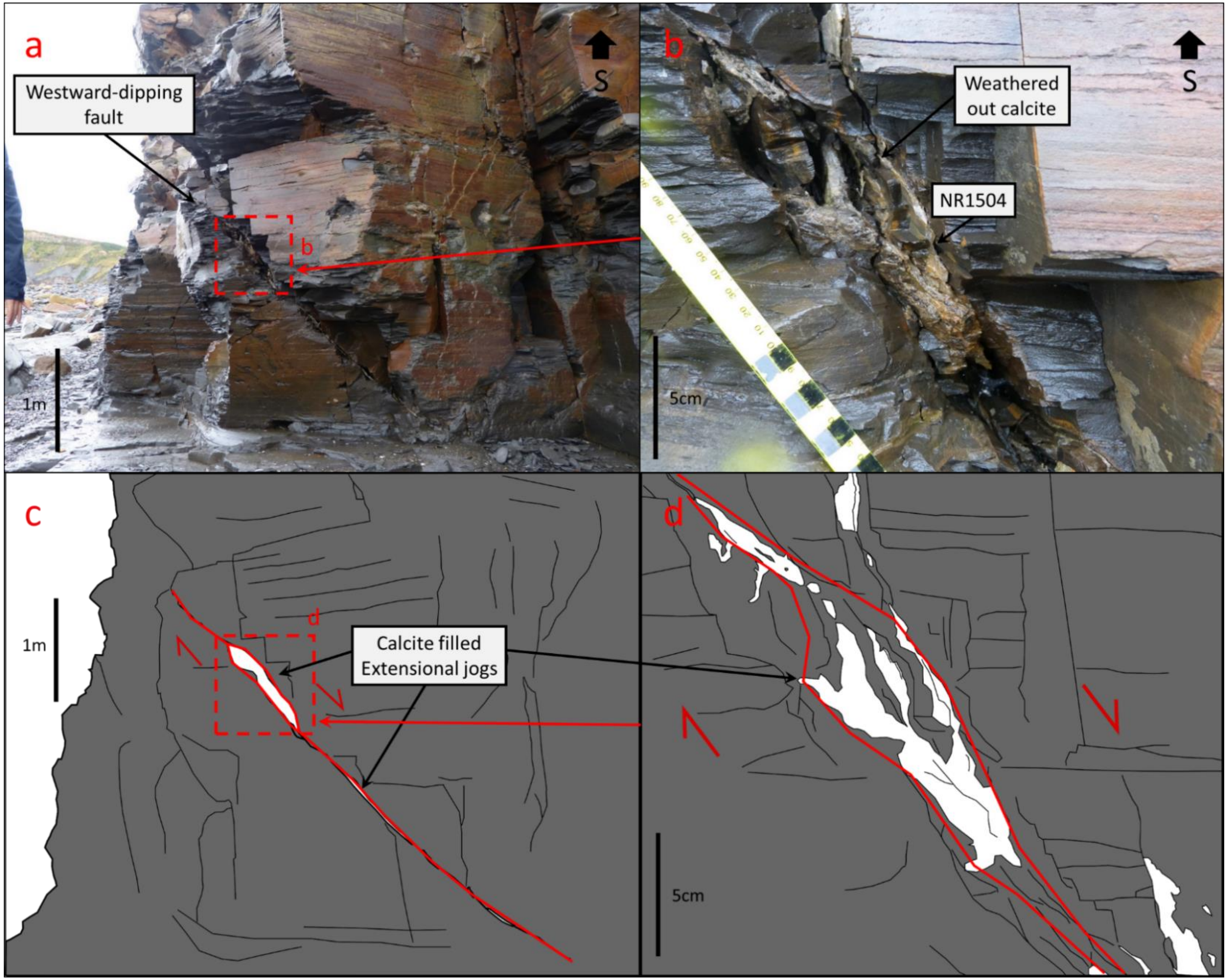


*Fig 3.22. Sectional images of a westward-dipping fault (Fault 1 in the Port Mulgrave Fault Zone. a) A westward-dipping fault is shown with white zones corresponding to 2-5cm wide calcite filled extensional jogs. b) A zoomed image of the largest extensional jog structure in a) and location of sample NR1504. Figures c) & d) are interpreted sketches of a) and b) respectively with the relative fault motion inferred from extensional jog offsets and the offset of identifiable bedding layers. A calcite infill (coloured white) is shown against grey Whitby Mudstone Formation.*

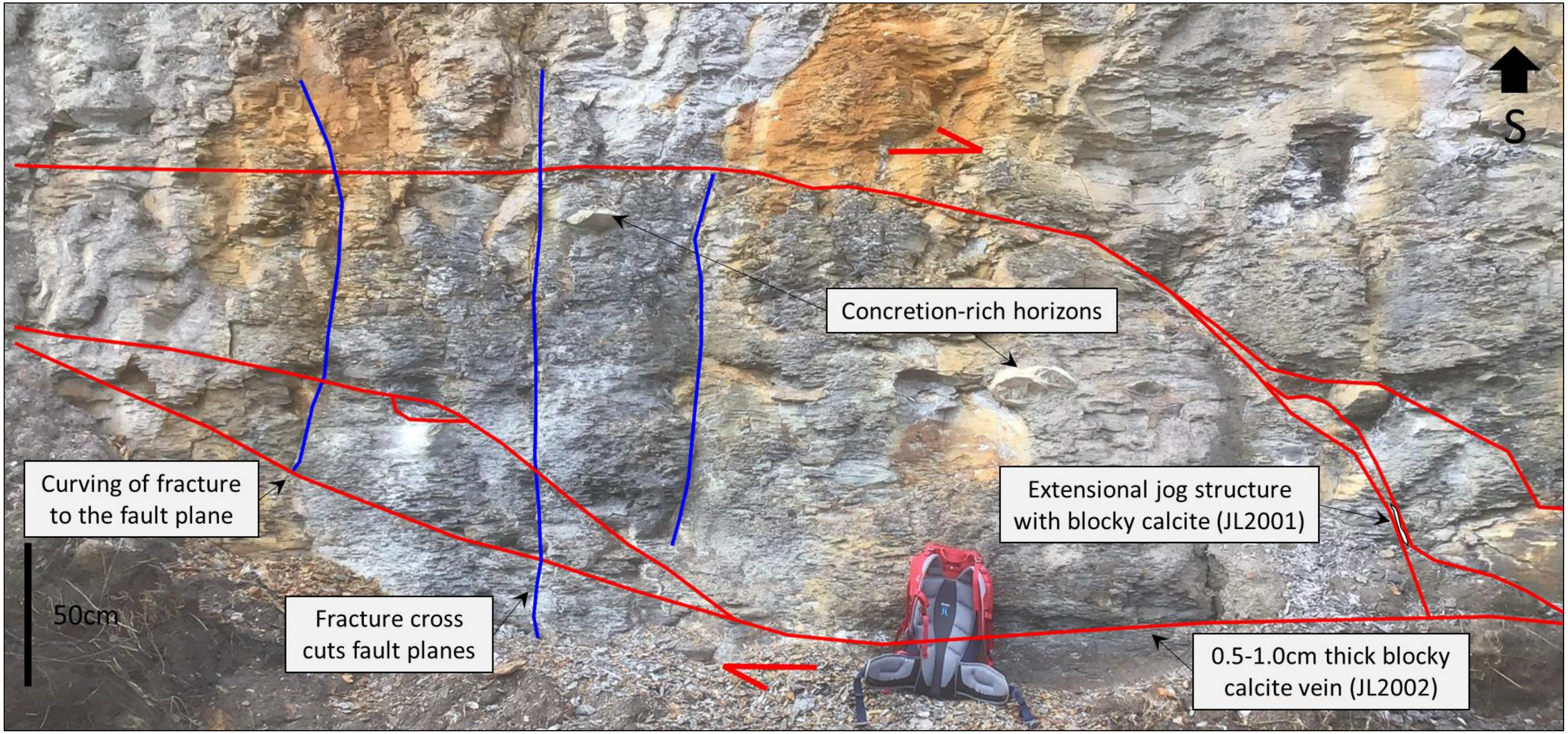


Figure 3.23. Duplex structure of bedding-parallel and linking curviplanar low-angle faults. The concretion horizons indicated show minimal (2-5cm) downward displacement in the hangingwall of the low-angle faults. Subvertical joints are highlighted in blue with individual fractures cross cut or curving to and abutting along the bedding parallel detachment. The duplex structure has a sigmoidal shape with top to the W displacement inferred.

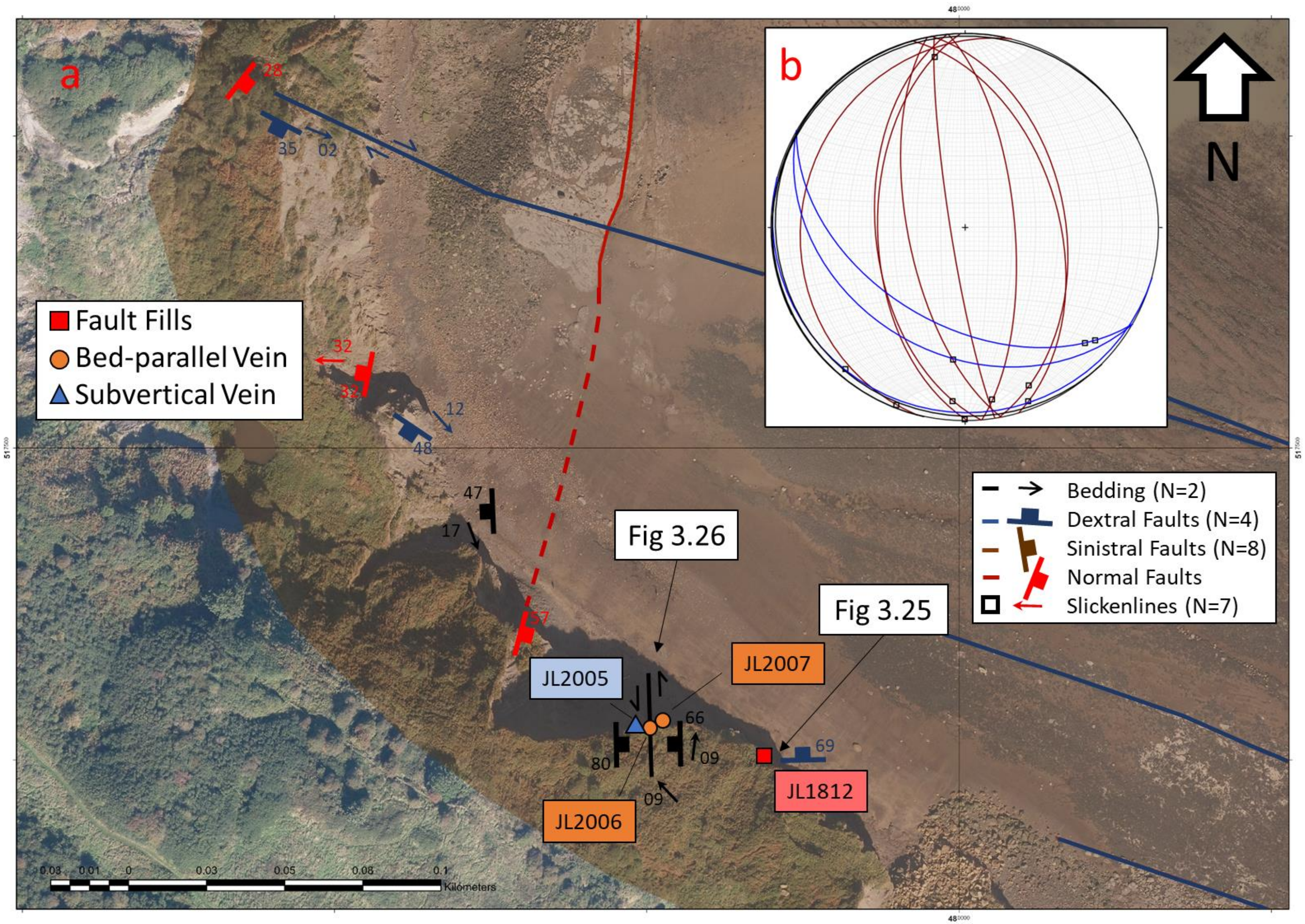


Fig 3.24. a) Aerial photography of oblique-slip faults at the Port Mulgrave Beach locality shown in Fig 3.21. b) A stereonet is inset-showing measurements from the sinistral oblique faults (brown), dextral oblique faults (blue) and bedding (black) Aerial photography is courtesy of the North East Coastal Observatory (NECO).

Sinistral oblique slip fault zone

N-S striking faults bound a mudstone block at the location shown in Figure 3.26a&b. The block is bounded to the west by a well-defined listric plane dipping 70-90° to the east and to the east by a scalloped/stair-step geometry fault with a 10-50cm thick clay gouge.

The bedding in the block shows rotation from dipping ~5-10° to the west in the wall rocks to ~30° to the west in the block (Fig3.26a) which is also cross cut by shallowly dipping (0-30°; Fig 2.26b) low-angle fault planes with 1-3cm thick sigmoidal calcite veins (JL2006 & JL2007) and horizontal E-W and N-S oriented slickenlines. This indicates that the block has been rotated down to the west and that the sigmoidal veins are syn-kinematic with fault movement, with top to the right offsets. The sigmoidal veins are shown on Figure 3.26c&d to bifurcate from the clay gouge

Top to the right shearing give the margins a domino block form (Fig 3.26d), indicative of an overall sense of sinistral shear across the rotated block.

Summary and Interpretation

The presence of localised oblique-slip faults is unique to Port Mulgrave with these oblique-slip faults potentially representing R and R' Riedel shears as described by Petit (1987) with $J_3$, NW-SE striking opening mode joints, locally present (Fig 3.3), potentially forming T fractures. This supports previous observations of a younger joint set at this location (Section 3.2.3.3). The presence of Riedel shearing is used to infer a zone of distributed dextral deformation possibly relating to a sub-surface pre-existing E-W fault as shown in Figure 3.27. A stress inversion analysis is presented in Section 3.3 to test this hypothesis.

Imber (Pers. Comm.) hypothesised that there were two generations of faults at Port Mulgrave with 1) vein-filled normal faults and bedding parallel detachments (duplex structures) which formed during dextral oblique extension, and 2) later gouge filled dip-slip extensional faults post-dating detachments. This hypothesis will be tested in Chapter 4 with U-Pb calcite geochronology.

| Sample | Location | UTM N | UTM E | Oblique-slip Faults | Calcite Fill | Texture | Kinematics | Dating | C-O | Clumped |
|---|---|---|---|---|---|---|---|---|---|---|
| JL1812 | Port Mulgrave | 644521 | 6046542 | ault - Dextral Oblique | Extensional Jog | Blocky | Synkinematic | Y | - | Y |
| JL2007b | Port Mulgrave | 644479 | 6046511 | Low angle fault | cm thick sigmoidal v | Blocky | Synkinematic | Y | Y | - |
| JL2006 | Port Mulgrave | 644479 | 6046511 | Low angle fault | cm thick sigmoidalv | Blocky | Synkinematic | Y | - | - |
| JL2005 | Port Mulgrave | 644479 | 6046511 | Vein - Vertical | 1-2mm thick vein | Blocky | Syn to post-kinematic | Y | - | - |

Table 3.7. Summary of sample data from the Port Mulgrave Fault and related structures. The locations of samples are shown in Fig 3.24. The structure type, calcite fill structure and apparent texture in hand specimen are summarised in addition to the successful analyses to be documented in Chapters 5 and 6.

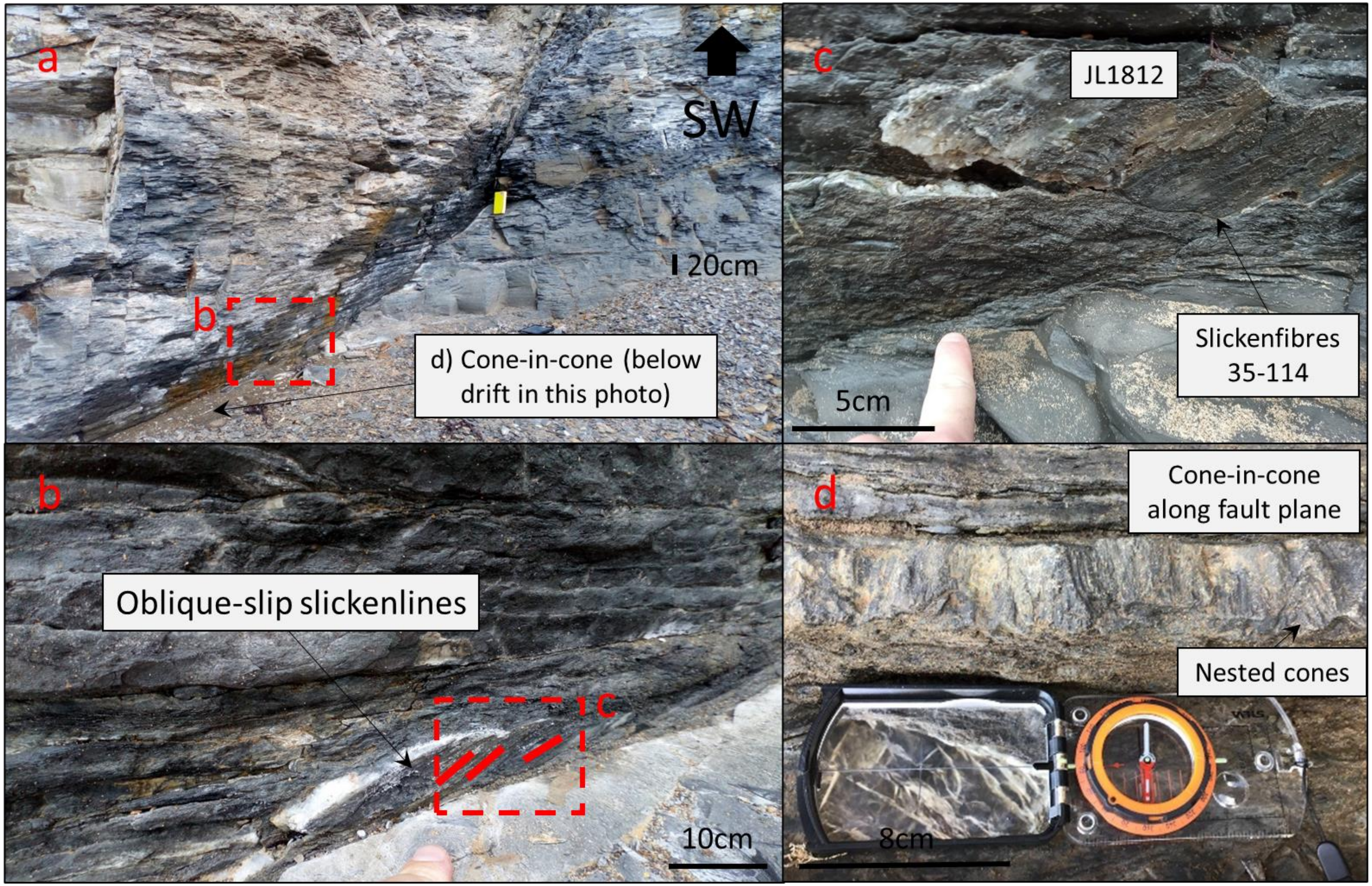


Fig 3.25. a) Sectional image of a dextral curviplanar fault at the Port Mulgrave beach locality. No marker beds were evident to constrain relative offset. b) A sectional zoomed in image of the fault plane with slickenlines on a dilational jog structures. The dilational jog appears to thicken from left to right of the image. c) Oblique slickenlines plunging at 35° to 114°. d) Oblique-view of nested cone-in-cone structures along the fault plane. Cone radiated away from the fault plane from south to north.

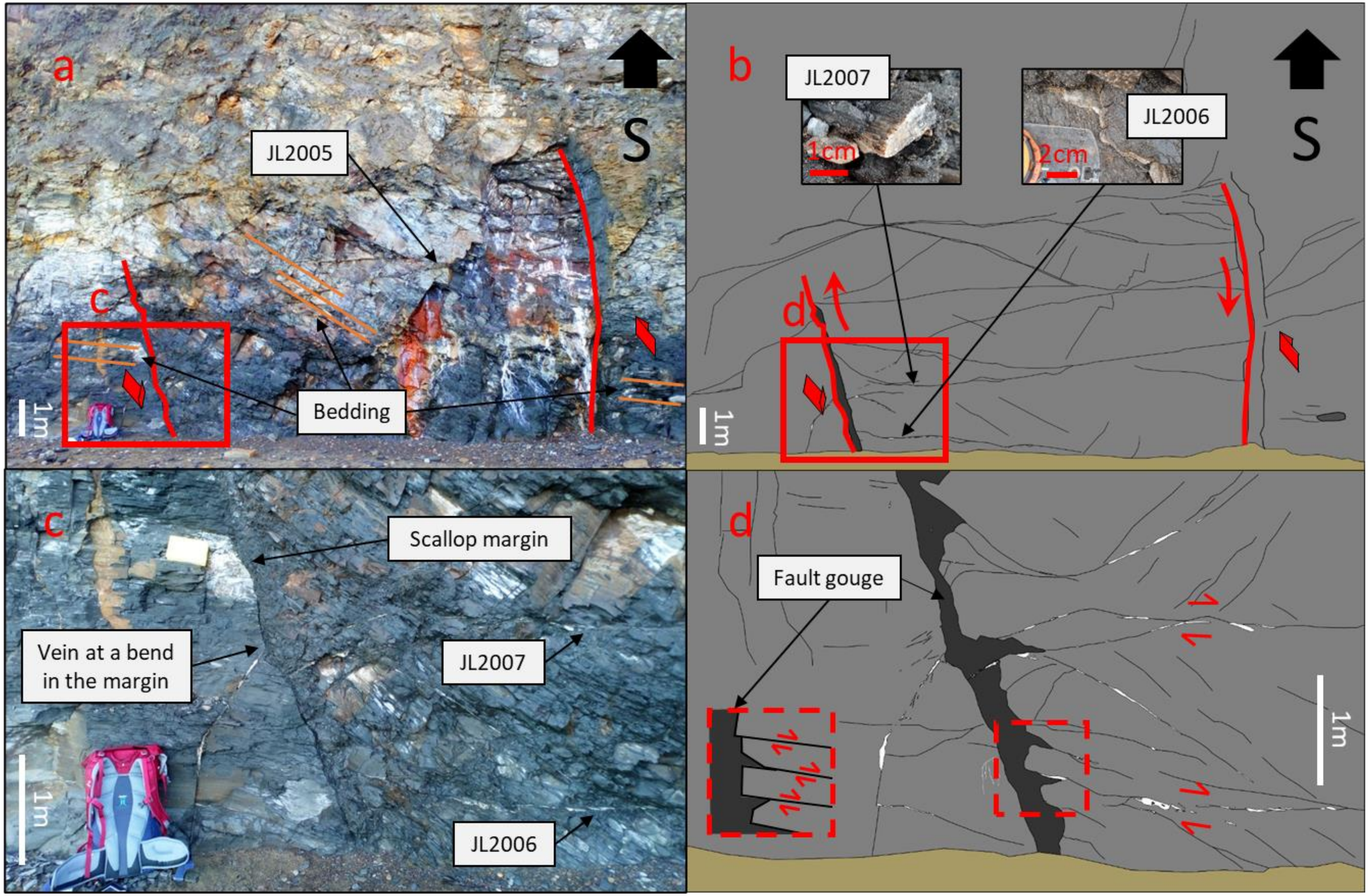


Fig 3.26. a & b) a sectional photograph and interpreted sketch of a rotated block structure at Port Mulgrave Beach. The western margin strikes N-S shows acute curvature while the eastern margin (c & d) has a scallop-shape with clay gouge. Coherent bedding blocks show a diagnostic domino-pattern offset into the margins. Veins in the country rock are associated with bends in the scallop margin and could be due to local stress state variations.

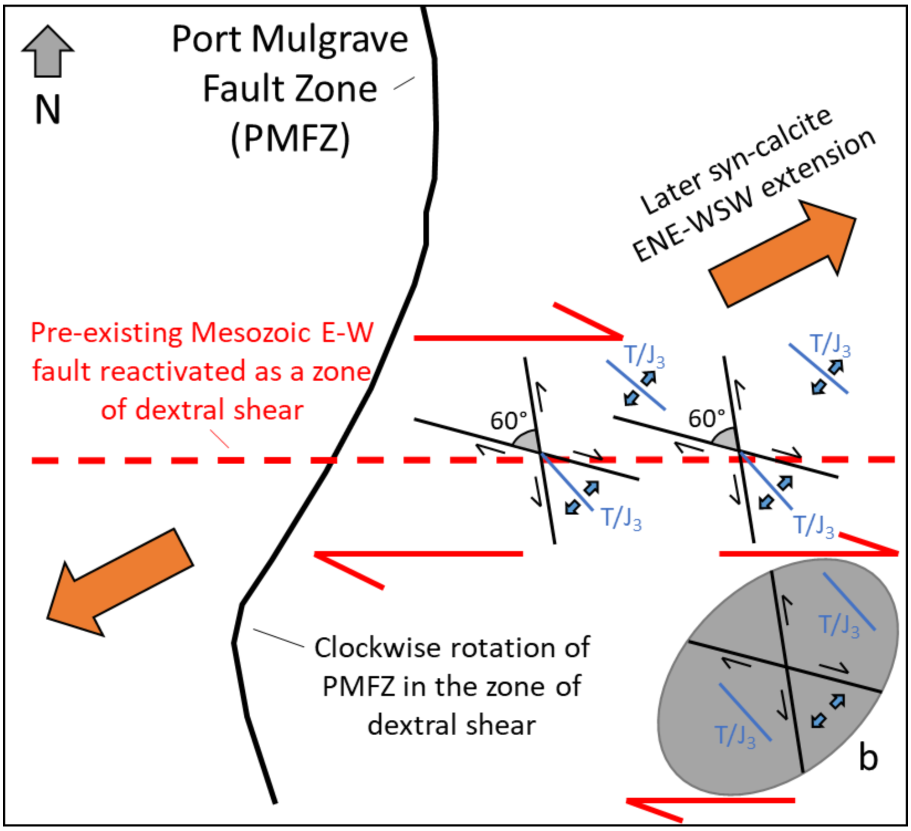


Fig 3.27. Sketch structural map of the Port Mulgrave Fault Zone with an inferred pre-existing E-W fault reactivated to cause a zone of distributed dextral shear with minor oblique-slip conjugate fault sets developed. A stress ellipsoid is shown to illustrate the relative shortening (NW-SE) and extension (NE-SW) axes.

### 3.2.3.5 Elm Tree Farm Borehole

Three boreholes were analysed and logged (Appendix 8.5) with samples of calcite taken for analysis of which only the Elm Tree Farm Borehole is discussed here. The Elm Tree Farm Borehole is focussed on, as it is the only borehole analysed to have yielded a successful age date from veins cutting the Mesozoic strata. In contrast to all outcrop exposures, which are coastal, the Elm Tree Farm Borehole is located near Kirby Misperton (Fig 3.1) and provides an important control point to analyse whether deformation documented along the coastline extends into the interior of the basin.

Elm Tree Farm borehole (Total Depth of 180m - Vertical Borehole) was drilled as part of the environmental monitoring program in the Vale of Pickering associated with the development of KM8 well by Third Energy (Smart, 2017) for shale gas exploration (Ward et al., 2020, Ward et al., 2019, Ward et al., 2018). The Elm Tree Farm borehole was one of two deep boreholes drilled in 2016 as part of the monitoring program (Smedley, 2015). The borehole remains confidential at present, but permission to sample for this project was kindly granted by BEIS and BGS. The borehole intersects the lower part of the Kimmeridge Clay correlating with *Eudoxus, Mutabilis* and *Cymodoce* zones (Mark Woods, Pers. Comm.).

There are numerous faults with associated calcite mineralisation cutting the core sample rocks from the borehole.

Three samples were taken from calcite mineralised fault structures in the Lower Kimmeridge Clay mudstones (summarised in Table 3.8): SSK110588 (35.16m MD), SSK110598b (40.95m MD) and SSK110588 (47.03m MD). The aim of sampling was to identify whether calcite mineralised faults in the core, which could be correlated temporally, structurally and/or isotopically with samples taken from local or regional fault structures.

The host stratigraphy sampled was dark grey weakly laminated mudstone with common fault zones shown in Fig 3.28. SSK110588 and SSK110596b both are calcite-mineralised faults (dipping between 10° and 40° to bedding respectively) as shown in Fig 3.28b with 2-3cm thick calcite fills. In the case of SSK110588, the base of the calcite fill is characterised by brecciated fragments of calcite reworked from the main vein in a 1.0-2.0cm thick clay gouge. SSK110596, in contrast is composed of a 2-3cm wide fault zone typified by clay gouge with fragments of reworked calcite aligned lengthways along the fault plane. This suggests that both fault fills likely formed with fault perpendicular opening or oblique opening with later cataclasis and reworking of the calcite fill. This suggests that calcite mineralisation was either synkinematic and/or pre-dated to fault movement.

Calcite mineralisation is widely distributed within the core with a variety of structures documented, including anastomosing ramp-flat thin (<1mm thick) calcite veins, cone-in-cone (Fig 3.28d) structures, mineralised fault planes (Fig 3.28e), and extensional jog structures. Dip-slip slickenlines (Fig 3.28c) are common and combined with systematic offset and extensional jogs indicate normal offset of faults.

The fault fills sampled appear to represent minor zones of centimetre-wide deformation and will be compared isotopically and geochronologically to other samples taken from coastal outcrops. As the core is unoriented, it is not clear from the fault fills their relation to coastal sampling. In addition, the width of the core is insufficient for the offsets of fault structures to be determined.

| Sample | Location | UTM N | UTM E | Structure | Calcite Fill | Texture | Kinematics | Age | C-O | Clumped |
|---|---|---|---|---|---|---|---|---|---|---|
| SSK110588 | Elm Tree Farm Borehole | 478910 | 478770 | Fault | Inclined fault | Blocky | Pre to Synkinematic | Y | - | - |
| SSK110596 | Elm Tree Farm Borehole | 478910 | 478770 | Fault | Calcite in gouge | Blocky | Pre to Synkinematic | - | Y | - |
| SSK110598 | Elm Tree Farm Borehole | 478910 | 478770 | Fault | Calcite in gouge | Blocky | Pre to Synkinematic | - | Y | - |

*Table 3.8. Summary of sample data from the Elm Tree Farm Borehole. Images of samples SSK110596 & SSK110598b are shown in Fig 3.28. The structure type, calcite fill structure and apparent texture in hand specimen are summarised in addition to the successful analyses to be documented in Chapters 5 and 6.*

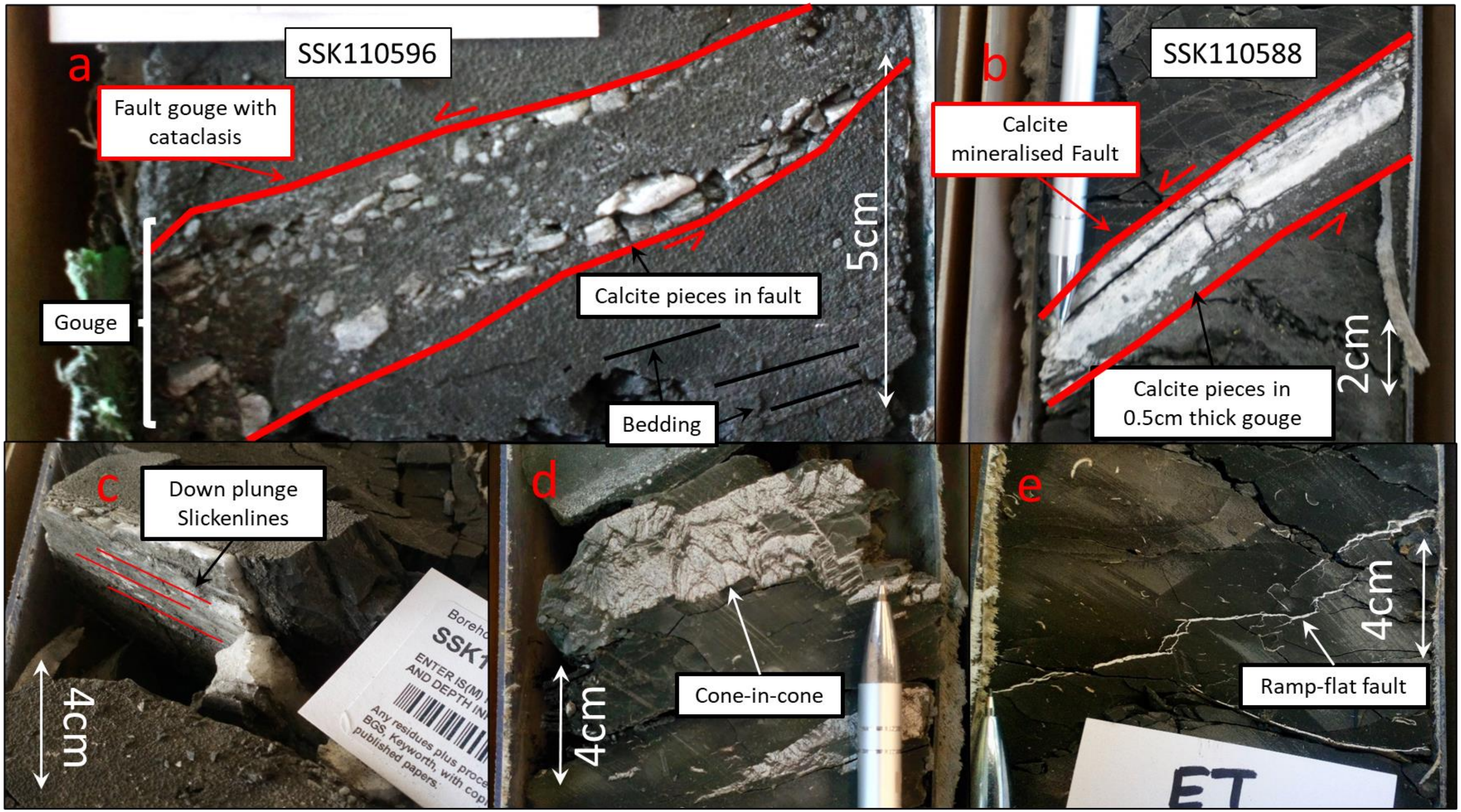


Fig 3.28. Core images of samples SSK110596 (a) and SSK110588 (b). a) Shallowly dipping shear plane (3-4cm wide) with 0.5-1.0cm thick calcite fragments in a mudstone gouge. Calcite pieces seem dislocated and broken up possibly due to reworking and brecciation. b) Steeper (~60°) dipping 2cm thick calcite fill with some minor fragments in the gouge. c) down plunge slickenlines along the base of calcite fill. d) cone-in-cone structures approximately parallel with bedding. e) ramp-flat geometry calcite filled fault with mm-wide calcite fill.

### 3.2.3.6 Summary of N-S Faults

The Runswick Bay, Staithes, and Port Mulgrave fault zones, as well as additional oblique-slip faults present at Port Mulgrave have been documented and sampled for U-Pb calcite geochronology and geochemical analyses. These fault zones represent important indicators of local stress conditions and localized fluid flow away from the major basin-scale faults such as the Peak Trough faults.

Systematic offset of marker beds, combined with the presence of extensional jog structures and down-plunge slickenlines indicate that the majority of faults analysed underwent normal movement with the exception of the localised oblique-slip faulting described at Port Mulgrave.

The normal faults typically strike NNW-SSE to NNE-SSW and have dips ranging from 20-90°. Faults are typically composed of two or more segments. Faults in the Staithes Sandstone and Cleveland Ironstone Formation consist of few segments compared to Runswick Bay and Port Mulgrave, where faults cross-cut the clay and organic rich Whitby Mudstone Formation. Therefore it may be possible that the nature of the host rock lithology has a significant influence on the fault network complexity and style. Several of these fault structures are spatially associated with bedding-parallel faults, extensional duplex structures or bedding-parallel veins.

Fault structures are commonly found spatially associated with bedding-parallel faults, imbricate structures or bedding-parallel veins. Normal faults and associated structures contain a variety of different calcite fills including breccias, extensional jogs, subvertical veins and thin hybrid opening mode veins along the fault planes.

Oblique-slip faults are only present as a zone of distributed strike-slip deformation at Port Mulgrave. Two conjugate fault sets have been determined from field relations illustrated here: dextral and sinistral oblique-slip. These conjugate faults are very similar to Riedel R and R' shears (Petit, 1987) with a localised T fractures also locally present. This supports an interpretation that formed in response to local stress conditions due to dextral reactivation of an underlying E-W fault, which formed a zone of distributed dextral transtension. That E-W fault is plausibly related to Mesozoic normal faulting related to the initial opening of the Cleveland Basin (see Chapter 6).

### 3.2.4 Small-fracture fills

This section will focus on the description of fractures with small-scale fracture fills. These fractures are either found far away from faults such as the subvertical calcite veins or record opening processes unrelated to fault movement such as the bedding-parallel fractures.

#### 3.2.4.1 Bedding-parallel veins (Staithes) (NZ 787 188)

Bedding-parallel fracture swarms

Bedding-parallel fracture swarms have been described by Imber et al. (2014) and Emery (2016) and form distinct weathered out notches (Fig 3.26a) in the cliff 400m east of Staithes. These bedding-parallel fractures are of much greater extent than other bedding-parallel structures previously described with blocky calcite fills recording bedding normal opening over the bedding-parallel fracture swarms. The locations of the bedding-parallel fractures are shown on Fig 3.16a. Individual bedding-parallel fractures can extend laterally up to 400m (Imber et al., 2014) and typically have blocky calcite fills 2-5mm thick (Fig 3.26b) with <1cm thick clay gouge locally (Imber et al., 2014). These long lateral extents and the presence of blocky calcite fills distinguish these veins from other smaller bedding-parallel veins described previously.

Bedding-parallel fractures are inferred by Imber et al. (2014) to be tensile opening mode in origin, with minor shear reactivation forming gouges and reflective of a time during which pore fluid pressure overcame the minimum principal stress which was oriented vertically. As stated in Section 3.2.1; Imber et al. (2014) and Emery (2016) have interpreted bedding-parallel fractures to have formed at maximum burial similar to the subvertical joints. U-Pb calcite geochronology and microstructural analysis presented in Chapter 4 suggests that it is unlikely that the bedding-parallel veins formed at the same time as the joint sets and are more likely synchronous with faulting.

Imber et al. (2014) suggested that the bedding-parallel veins described here could have formed due to dilational effects caused by movement along normal faults at Staithes that sole into the bedding-parallel veins. This inference is supported by presence of clay gouges at the vein margins, folding of the vein structures and truncating of calcite zones, which are discussed in Section 4.5.2. Here it is interpreted that bedding-parallel veins are related to pore fluid pressure overcoming the minimum principle stress, which must have been vertical and that temporally associated fault movement led to later re-shear and deformation of these veins.

| Sample | Location | UTM N | UTM E | Bed-parallel Veins | Calcite Fill | Texture | Kinematics | Dating | C-O | Clumped |
|---|---|---|---|---|---|---|---|---|---|---|
| NR1606 | Staithes | 643623 | 6047354 | Vein - Bedding -parallel | 3-4mm thick vein | Blocky | Synkinematic | Y | - | - |
| NR1607 | Staithes | 643676 | 6047326 | Vein - Bedding-parallel | 5mm thick vein | Blocky | Synkinematic | Y | - | - |

Table 3.9. Summary of sample data from the bedding-parallel veins at Staithes. The locations of samples are shown in Fig 3.19. The structure type, calcite fill structure and apparent texture in hand specimen are summarised in addition to the successful analyses to be documented in Chapters 5 and 6.

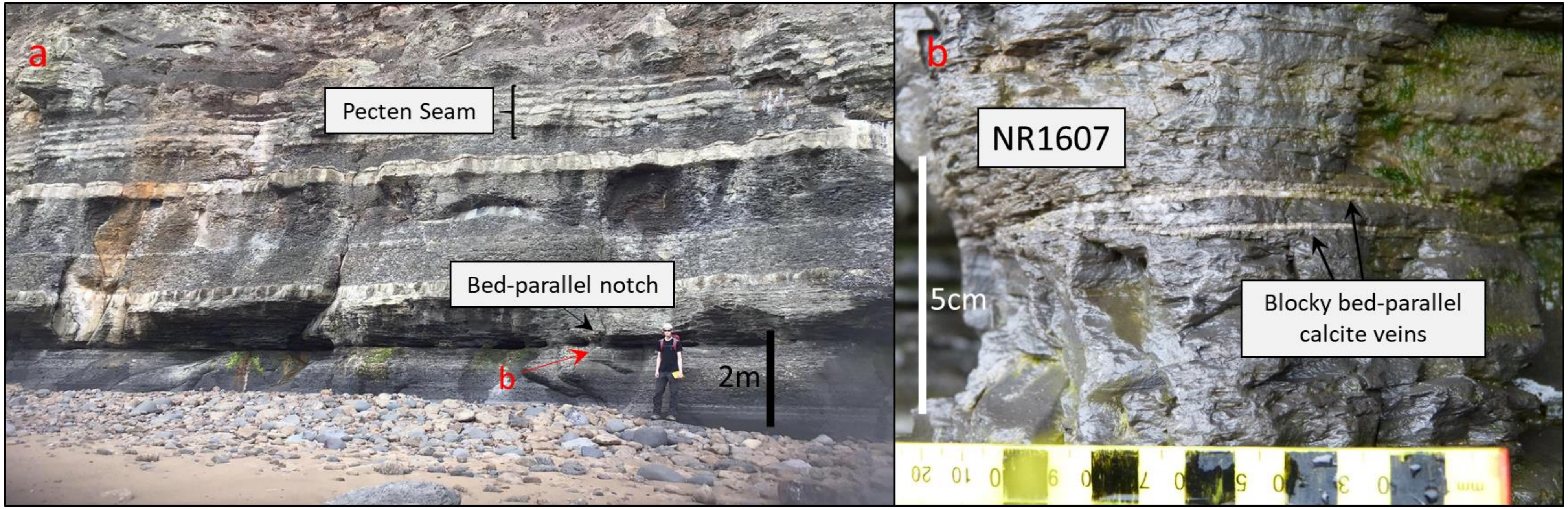


Fig 3.29. a) A sectional image of a distinct bedding-parallel notch in the Cleveland Ironstone Formation. The notch (~1m below the Raisdale Seam) is formed by eroded out layer of mudstone with 0.2 to 0.5cm thick bedding-parallel veins with blocky calcite (b).

### 3.2.4.2 Subvertical Calcite Veins

At the Saltwick Nab and Sandsend (Fig 3.30) localities, thin millimetre wide calcite veins are found in strata located well away (>1 km) from any known fault structure. These veins typically discontinuously fill the pre-existing N-S trending joint structures ($J_1$) discussed in Section 3.2.1.

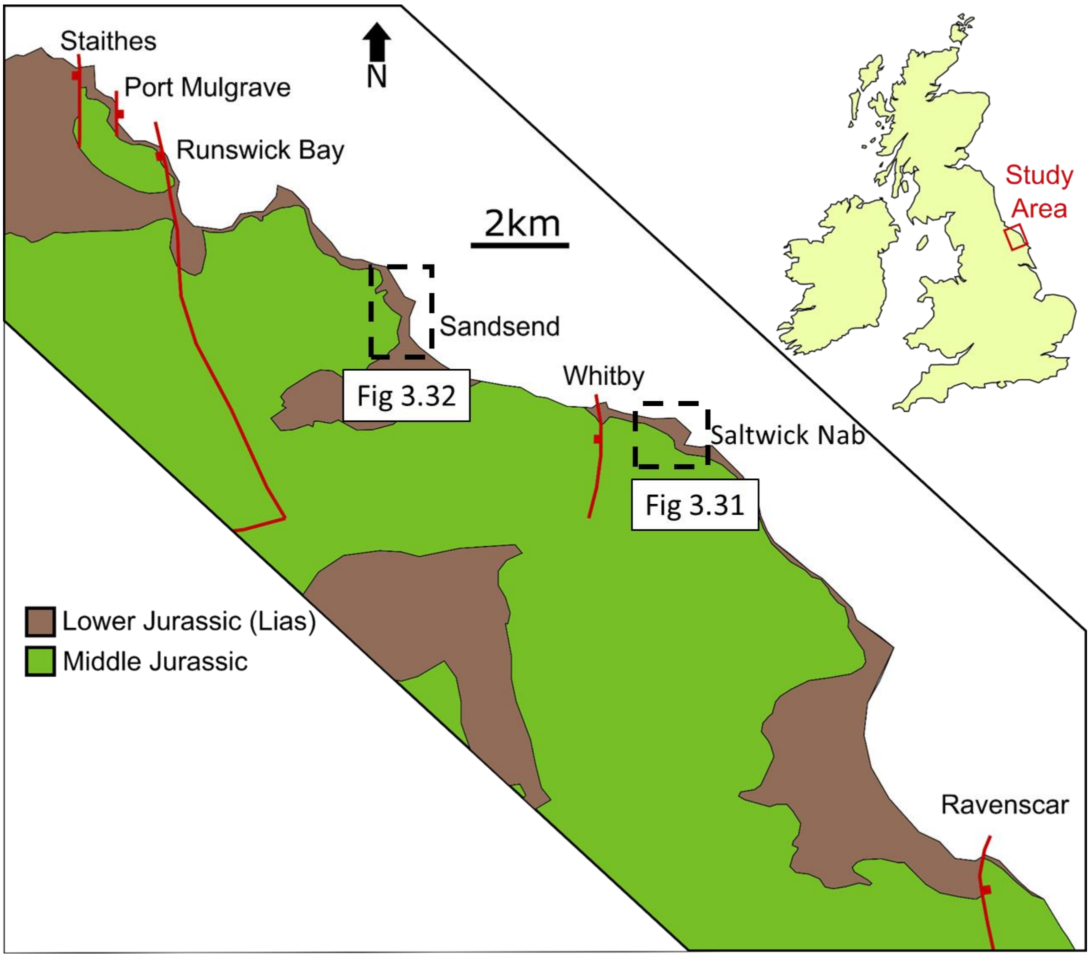


*Fig 3.30. Geological map of the main area of interest highlighting the location of subvertical calcite veins at Saltwick Nab (Fig 3.31) and Sandsend (Fig 3.32).*

<u>Saltwick Nab</u>

Saltwick Nab (Fig 3.30 & 3.31) is situated approximately 1km east of the Whitby's East Pier locality and forms a distinct promontory at the northwestern margin of Saltwick Bay. There is an extensive wave cut platform and cliff exposures in the rocks of the Mulgrave Shale Member (Whitby Mudstone Formation). Bedding dips gently 4-5° to the southwest.

A number of thin (1-2mm thick) calcite bearing joints ($J_1$) strike NNW-SSE to NNE-SSW with perpendicular oriented mineral fibres (1-2mm thick) that indicate opening directions oriented on average 175-265° (Fig 3.31b). A number of calcite vein samples were taken, but only one (JL1815; Fig 3.5a, c) was successfully dated (Chapter 4; Table 3.10).

| Sample | Location | UTM N | UTM E | Subvertical Veins | Calcite Fill | Texture | Kinematics | Dating | C-O | Clumped |
|---|---|---|---|---|---|---|---|---|---|---|
| JL1815 | Saltwick Nab | 656232 | 6040793 | Vein - Vertical | 1-2mm thick vein | Fibrous | Syn E-W Opening | Y | - | Y |
| JL1934 | Sandsend | 650693 | 6042954 | Vein - Vertical | 1-2mm thick vein | Fibrous | Syn E-W Opening | Y | - | - |
| JL1939 | Sandsend | 650778 | 6043115 | Vein - Vertical | 2-3mm thick vein | Fibrous | Syn E-W Opening | Y | - | - |
| JL1932 | Sandsend | 650684 | 6042769 | Vein - Bedding-parallel | 1-2mm thick vein | Fibrous | Syn E-W Opening | Y | - | - |

Table 3.10. Summary of sample data from the subvertical veins at Saltwick Nab and Sandsend. The locations of samples are shown in Fig 3.31 & 3.32. The structure type, calcite fill structure and apparent texture in hand specimen are summarised in addition to the successful analyses to be documented in Chapters 5 and 6.

Sandsend

The Sandsend locality (Fig 3.30 & 3.32) is located approximately 4km WNW of Whitby half a kilometre north of the small coastal village of Sandsend. The locality is composed of an 800m long cliff section and wavecut platform exposures of shallowly dipping (4-10° SE) mudstone of the Mulgrave Shale Member (Whitby Mudstone Formation).

Faulting is absent at the Sandsend locality and deformation is characterised by NNW-SSE ($J_1$) and NE-SW ($J_2$) sub-vertical joints present in cliff and wave cut platform exposures. JL1934 & JL1939 (Table 3.10) are millimetre thick fibrous calcite veins filling $J_1$ joints and tracking E-W opening veins similar to those at Saltwick Nab. In addition, millimetre thick bedding-parallel veins were identified (JL1932; Fig 3.33a), which strike between 016-044 with dips of 5-7°. One identified vein has down-dip slickenfibres plunging 06-098 on the top surface approximately perpendicular to the strike of the neighbouring subvertical veins (Fig 3.33a). The bedding-parallel veins are of short extent (<10cm) and appear to connect subvertical veins; this evidence combined with the plunge of the slickenlines suggest that these are accommodation structures facilitating fluid connection and small top-to-the-west shear displacements between otherwise unconnected joints.

Both the Saltwick Nab and Sandsend localities display predominantly subvertical veins in reactivated $J_1$ joints and, in the absence of any fault related deformation, appear to represent a somewhat different style of veining. In Chapter 4 U-Pb calcite geochronology will be utilised to demonstrate that these veins show a distinct age population separate from calcite fills associated with fault related deformation.

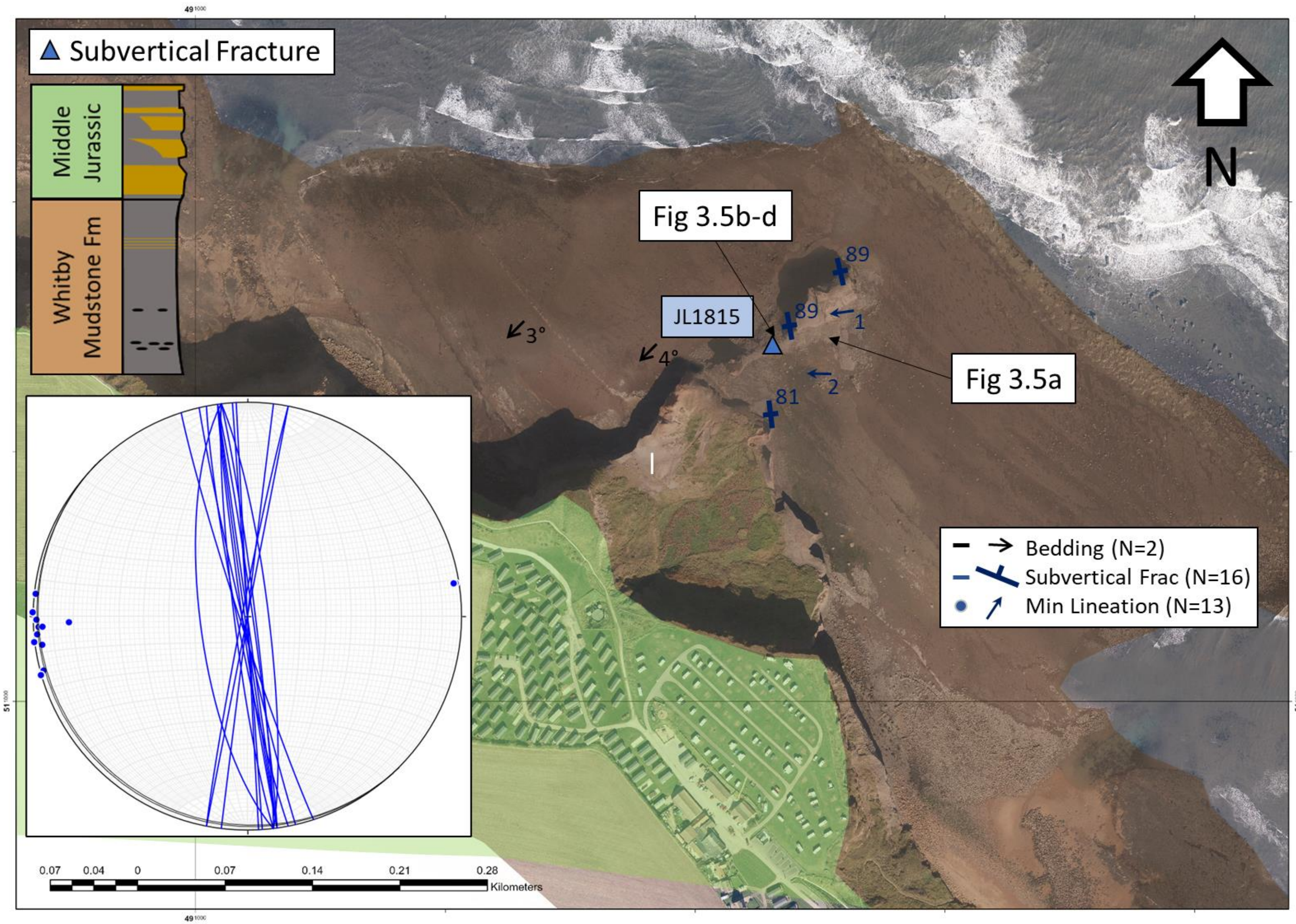


*Fig 3.31. Aerial photography of Saltwick Nab. A stereonet is inset-showing measurements for subvertical calcite veins (blue) with mineral fibre lineations and bedding (black) also shown. Aerial photography is courtesy of the North East Coastal Observatory (NECO).*

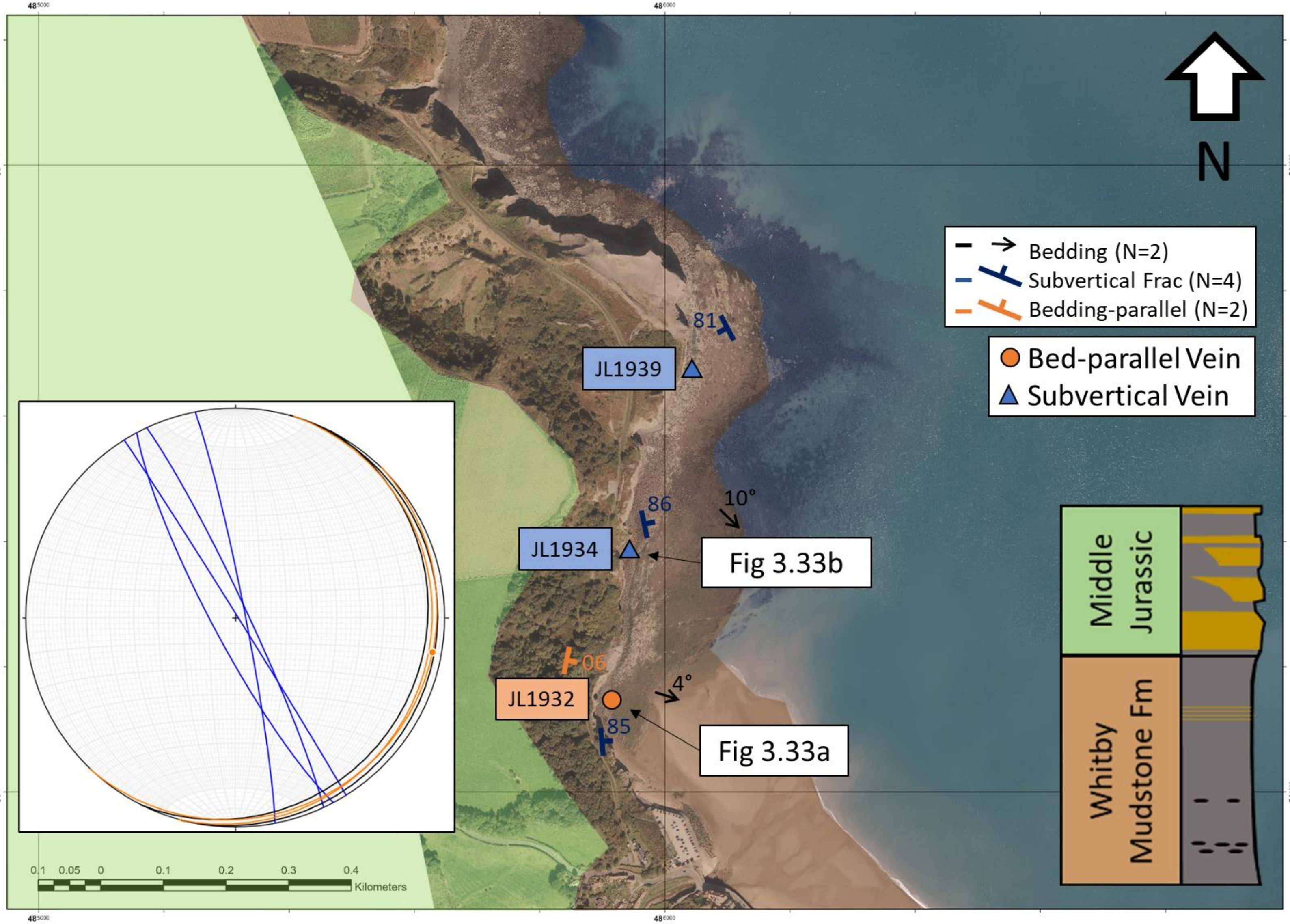


*Fig 3.32. Aerial photography of Sandsend. A stereonet is inset-showing measurements for subvertical calcite veins (blue), a bedding-parallel vein and bedding (black). Aerial photography is courtesy of the North East Coastal Observatory (NECO).*

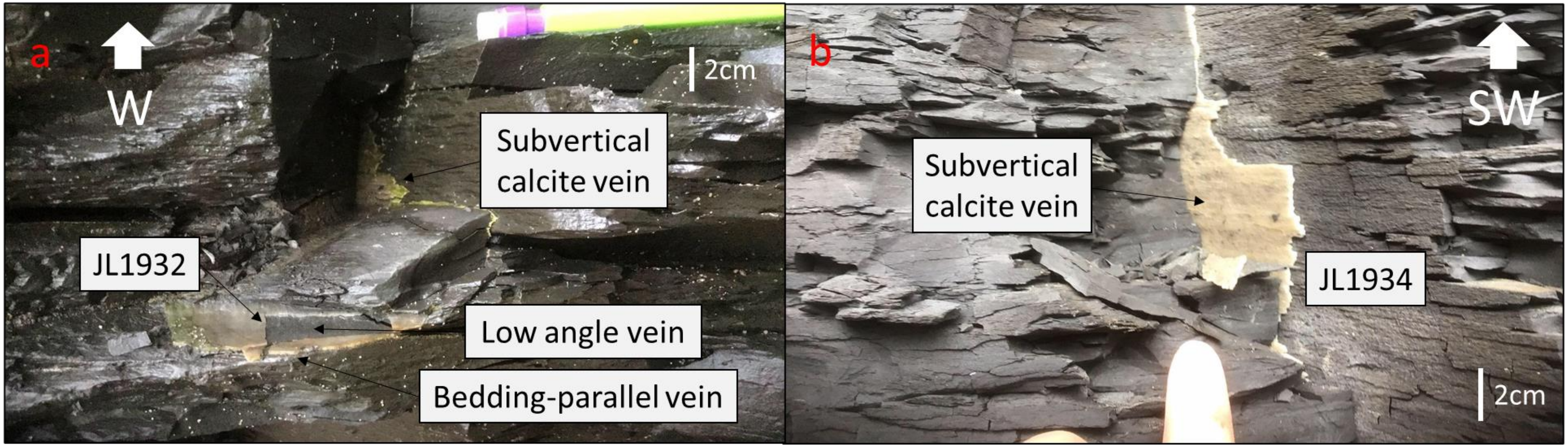


*Fig 3.33. a) Sectional photograph of low angle to bedding parallel 1-2mm thick calcite veins (JL1932) with slickenlines at Sandsend. The low angle and bedding-parallel veins link up to a subvertical and act as accommodation features at 90° to main fracture. b) Sectional images of a subvertical NNW-SSE trending calcite vein (JL1934) in the cliff wall at Sandsend. The vein follows a discrete planar fracture.*

## 3.3 Palaeostress Analysis

Faults and fracture fill kinematics from the Peak Fault at Ravenscar have been used in a stress inversion using the methodology laid out in Section 2.1.3 and are summarised in Fig 3.34. The Peak Fault at Ravenscar was analysed as it represents the largest structure exposed onshore and therefore has the highest probability of reflecting the regional tectonics and stress regime. The slickenlines utilised here are associated with faults that preserve synchronous calcite mineralisation that are interpreted to have formed during reactivation of the syndepositional regional Peak Fault. Early pre-mineralization fault activity is indicated by the presence of fluidisation structures (mud mounds) and growth strata in the Peak Fault hangingwall.

### 3.3.1 Peak Trough Faults

The stress inversion indicates that the reactivation of the Peak Fault structure occurred in due to E-W extension with a vertically oriented maximum stress, i.e. a normal faulting tectonic regime (Anderson, 1951). The extension direction calculated compares well with mineral fibre directions seen in subvertical veins (Section 3.2.4), which display a similar extension direction 5° counter clockwise of E-W axis. This rotation is shown in the stereonet in Figure 3.34.

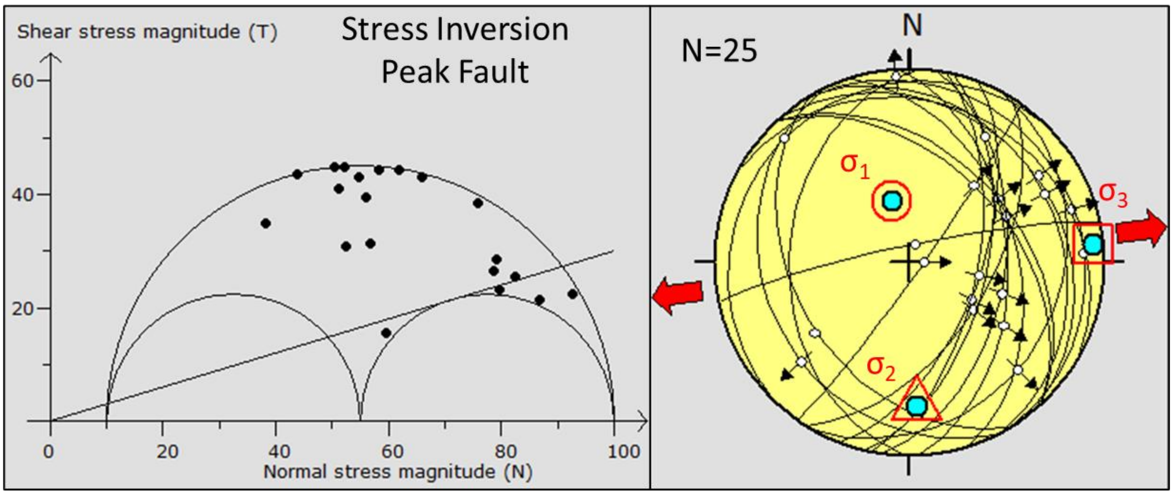


Fig 3.34. Stress inversion for minor fault data from the Peak Fault at Ravenscar using Composite Minimum optimisation function. The data are consistent with E-W extension with a near vertical σ1 and southward oriented σ2. Kinematic data appears to split into two groups oriented 10-15° north of east and 20-30° south of east. More data would be required to distinguish these sets further. The dimensionless Mohr circle describes the difference in principle stress magnitude with low differential stress indicated for Peak Trough faulting.

### 3.3.2 Meso-scale N-S Fault Structures

Stress inversion data from the other N-S fault structures is also presented (Fig 3.35) for comparison with the stress inversion data from Ravenscar (Fig 3.34). Multiple fault zones have been grouped together to increase the data population and produce a more statistically viable result. This stress inversion includes slickenline data from minor faults associated with the Runswick Bay, Staithes, and Port Mulgrave fault zones. The oblique-slip slickenline data for Port Mulgrave has been analysed and presented separately due to the difference in fault kinematics (Fig 3.36).

The stress inversion for the non-Peak Trough fault zones compares well with the results from the Peak Fault at Ravenscar. The fact that the calculated stress regimes compare so well could suggest the Peak Fault and other fault zones with associated calcite mineralisation were active at a similar time. U-Pb geochronology results presented in Chapter 4 will test this hypothesis.

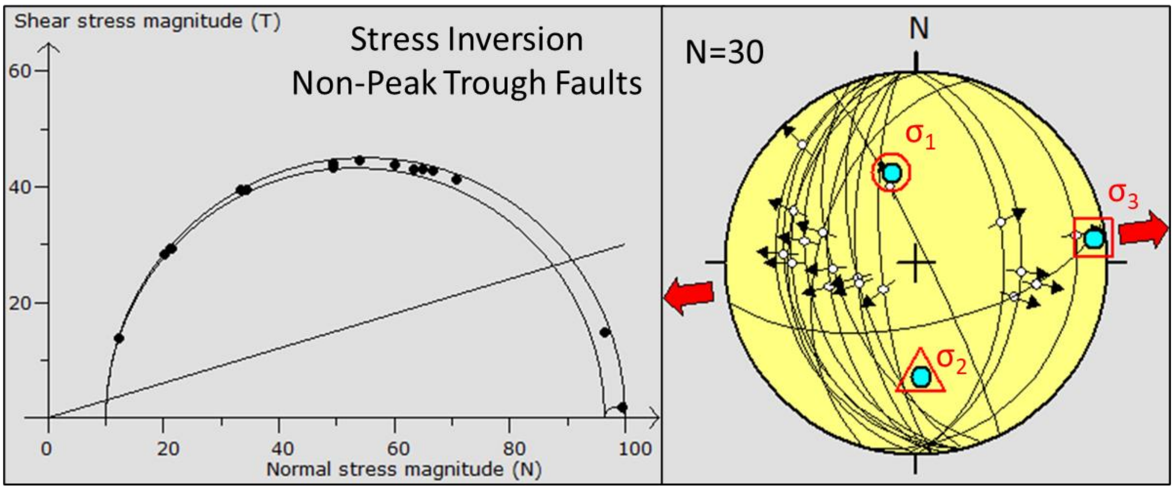


Fig 3.35. Stress inversion for minor fault data from the Runswick Bay, Staithes and Port Mulgrave faults using Composite Minimum optimisation function. The data are consistent with E-W extension with σ2 oriented 10° clockwise of east with a vertical σ1 rotated ~45° to the north of vertical and σ2 tilted 40° from south. The dimensionless Mohr circle describes the difference in principle stress magnitude with high differential stress indicated for the Meso-scale faults.

### 3.3.3 Port Mulgrave Oblique-slip

The stress inversion for the oblique-slip faults (Fig 3.36), however, suggests a different stress regime with a 20-30° anti-clockwise rotation to NE-SW of the minimum principal stress ($\sigma_3$) and a horizontal maximum principal stress ($\sigma_1$) oriented NW-SE with a vertical $\sigma_2$. This orientation of principal stresses is consistent with an Anderson's strike-slip fault regime related to NW-SE compression. The stress inversion presented in Figure 3.36 for the Port Mulgrave oblique-slip faults is also potentially consistent with the interpretation of a distributed zone of dextral deformation due to reactivation of an underlying E-W Mesozoic fault as inferred in Section3.2.3.4 and further discussed in Chapter 6.

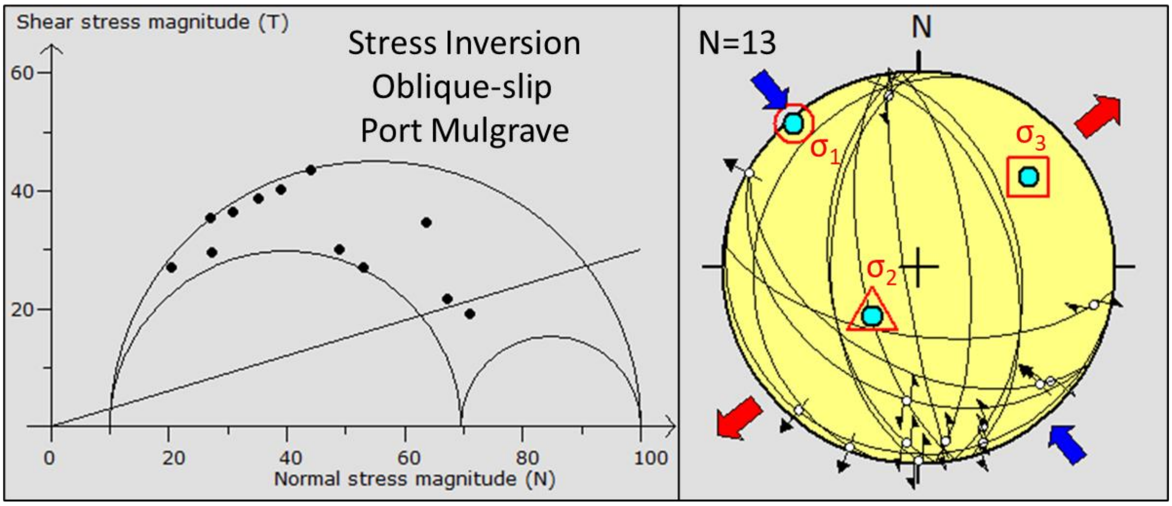


Fig 3.36. Stress inversion for minor fault data from the oblique-slip faults at Port Mulgrave. The pattern of principle stress orientations matches well with a strike-slip regime as proposed by Anderson (1951) with a possible tilting of σ2 to the SW of ~20°. The dimensionless Mohr circle describes the difference in principle stress magnitude with moderate differential stress indicated for the oblique-slip faults in comparison to previous fault types.

### 3.3.4 Regional Stress Regime

Figure 3.37 shows the Palaeostress analyses in on the regional geological map introduced in Chapter 1. This shows that the stress regime, with the exception of the localised oblique-slip at Port Mulgrave is consistent across the area of interest with Meso-scale faults on normal faults at the north end of the area of interest showing a very similar stress inversion pattern to minor structures related to the Peak Fault at the southern end of the area of interest. This suggests that movement occurred in a similar stress regime.

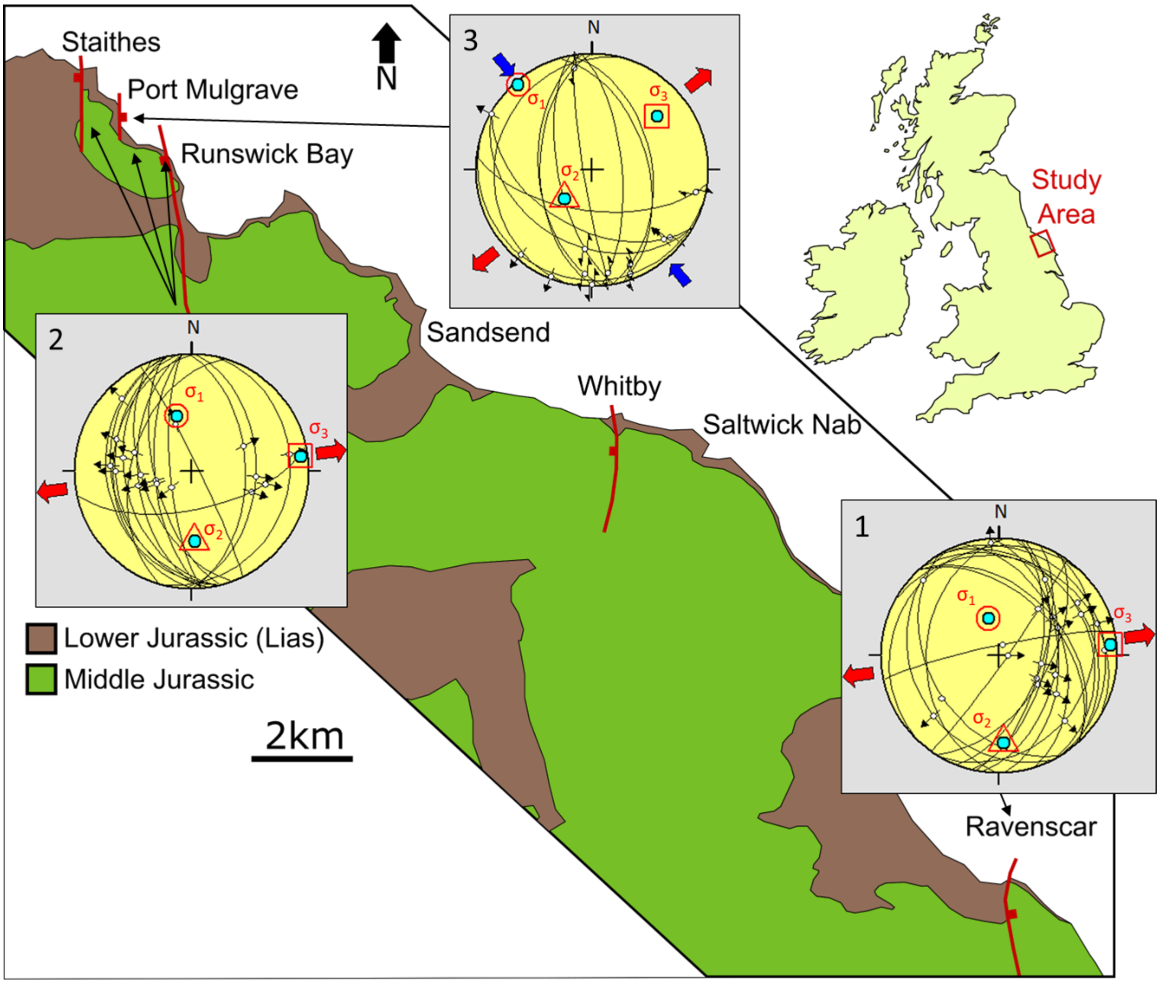


Fig 3.37. Geological and structure map of the coastal section of the Cleveland Basin placing the palaeostress analyses from the Peak Fault (1), Meso-scale fault zones (2) and oblique-slip faults at Port Mulgrave (3) into a regional and structural context.

## 3.4 Summary

A series of structures have been categorised and sampled, which vary in scale from the regional structures (joint sets and Peak Trough faults) to local structures (e.g. faults and localised fracture fills). Each of these structures (Fig 3.38) record different information regarding the local stress field and regional tectonics during brittle deformation and calcite-mineralisation (fluid flow). The following discussion will work on building a relative chronology of structures and discuss the implications for the fluid-flow regime and regional tectonics.

Oblique-slip faulting has been observed at Port Mulgrave and compares well with riedel shears described by Petit (1987).

Overall, the fieldwork observations summarized here suggest that three distinct periods of faulting and fracturing can currently be separated in the Cleveland Basin (Fig 3.38):

- D1: Synsedimentary fault movement (i.e. Peak Fault) during initial rifting with displacement of uncertain natures along both E-W and N-S fault trends,
    - Rawson & Wright (1992) suggests throws of 153m on the Peak Fault, 110m on Cayton Bay Fault and 37m on Red Cliff Fault. It is likely that the majority of this displacement reflects early synsedimentary movement.
- D2: Development of $J_1$ (NW-SE to N-S) and $J_2$ (NE-SW to E-W) jointing sets at maximum burial, displacements of mm to cm with low magnitudes of extension.
- D3a: E-W extension with faulting and fracture development and fluid-flow leading to widespread reactivation of regional structures and calcite mineralisation of structures. 1-2 metre or less offsets on fault structures (supported by analysis by Ashman, 2017) with the magnitude of extension suggested to be <1%.
- D3b: Oblique-slip and local fractures are included in D3, however this assumption will be tested in Chapter 4 using U-Pb calcite geochronology. Magnitudes of strain are difficult to determine but likely very small with local fractures showing very low magnitudes of extension (<0.1%).

Models of fault length versus displacement based on measurements of faults in Iceland by Gudmundsson (2000) suggest that displacements of a couple of metres up to ten metres are associated with faults up to 2km in maximum length. Most of the faults analysed in this study have Cenozoic displacements less than 10m, however, these represent small faults over a larger zone of faulting. It is likely that while each fault has low displacement that the cumulative displacement over a larger fault zone is larger. More study is required to understand the length versus displacement relationships in the Cleveland Basin. Isotopic analysis will be utilised in Chapter 5 to try and identify the capability of these faults for interconnectivity and supporting regional fluid-flow.

### 3.4.3 Implications for Regional Tectonics

The frequent presence of calcite mineralised kinematic structures such as extensional jog and breccia structures and fibrous calcite present, in combination with common slickenlines, in many fills suggests that mineralisation and normal faulting movements during E-W extension are broadly synchronous. It is shown herein that this phase of extension (D3) postdates early Jurassic fault movement (D1) and subsequent jointing (D2) at maximum burial. E-W extension forms a distinct separate phase of regional deformation associated with normal faulting and the reactivation of pre-existing preferentially oriented

N-S striking fault and fractures. These assumptions will be tested further in Chapter 4 through detailed characterisation of sample microstructures.

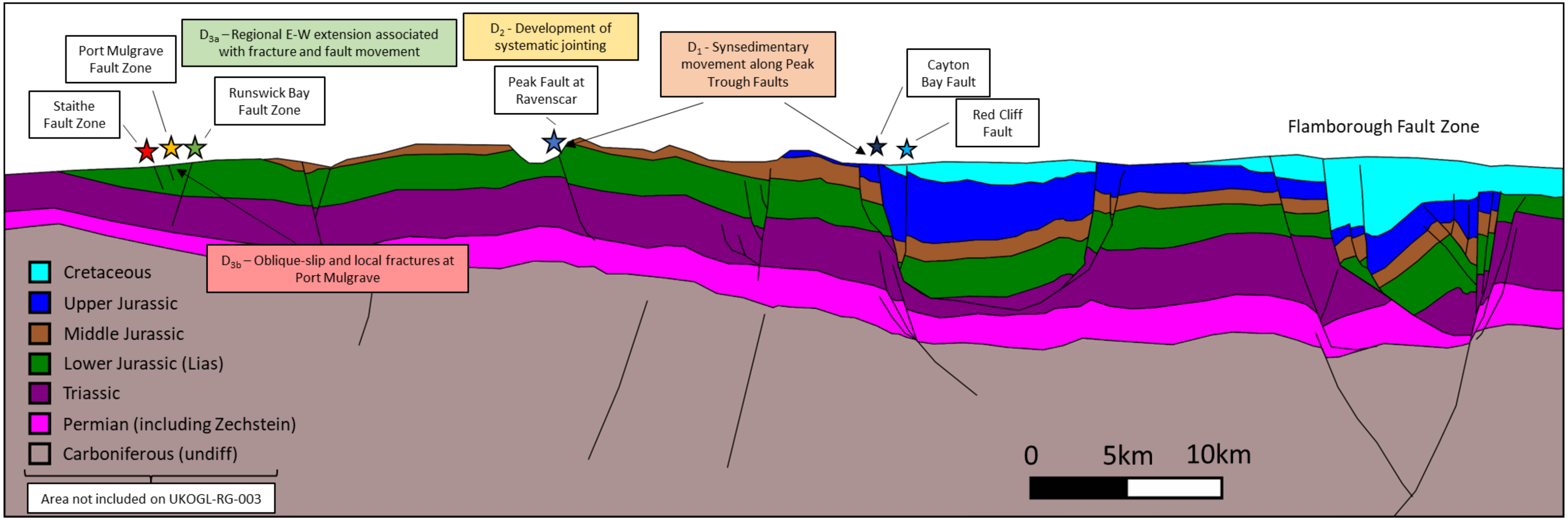


Fig 3.38. Schematic cross section of the Cleveland Basin from Chapter 1 based on Seismic line UKOGL-RG-003 and Emery (2006), outling the timing of deformation and indicating the key locations involved.

# Chapter 4- Microstructural and geochronological evidence for the timing of deformation

## 4.1 Introduction

Microstructural analyses and U-Pb geochronology of specific samples will used to build on the fieldwork-based structural characterisation of the Cleveland Basin outlined in Chapter 3. This chapter will shift focus down to millimetre- and micron-scale analysis of calcite mineralised structures, as well as providing the results from U-Pb calcite geochronology. The analysis of calcite veins and fault fills as indicators of basin-scale (>50 km) down to outcrop-scale evolution (<100 m) poses a number of key issues and considerations:

1) Using microstructural observations to infer the structural evolution of distinct structures and the basin itself.
2) Checking the nature and integrity of samples (e.g. defining discrete calcite generations, evidence of alteration) for further isotopic analyses i.e. U-Pb geochronology and stable carbon and oxygen isotope analysis.
3) Utilising a combination of microstructures and field relations to identify calcite fills that were formed synchronous with fault movement.
4) Correlating distinct phases or modes of mineralisation between structures and localities (e.g. fibrous vs blocky crystal types, relationships between opening-mode versus hybrid mode structures, reactivated structures).

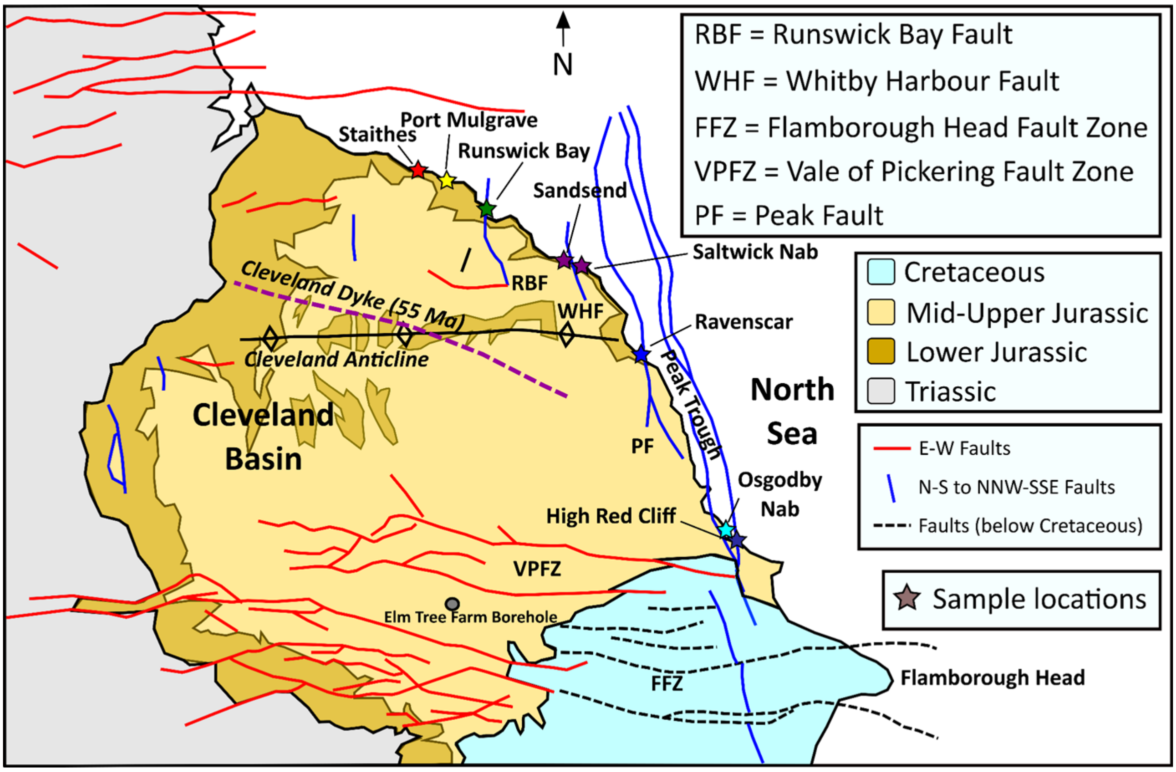


*Fig 4.1. Overview of the Cleveland Basin with the main locations of interest highlighted with stars.*

Microstructural observations of calcite mineralization can provide evidence for processes that may be too small to be observed in the field, and – as this material is then going to be dated - will form the backbone of much of the local and regional-scale interpretation (see Chapter 6). The nature and microtextures of the calcite fills are a unique source of information on fluid-flow processes and/or styles of deformation and stress state.

Microstructures have been imaged in-depth to provide detailed information about what we are dating and sampling for stable and clumped isotopes. Microstructural observations provide the link between outcrop- and basin-scale structures and the U-Pb calcite dates and stable isotope results. In addition, microstructural observations provide evidence of the relative timing of mineralisation and the movement of faults i.e., whether the calcite mineralised during (synkinematic), before (pre-kinematic) or after (post-kinematic) fault movement.

In situ (using laser ablation ICP-MS) U-Pb calcite geochronology has become a popular tool for the analysis of tectonic veins and fault fills in a wide variety of settings due to its relative affordability (compared to other geochemical/isotopic analyses), rapid analysis speed and the ability for high spatial resolution analysis of specific calcite zones (Roberts et al., 2020). The high spatial resolution of the technique resolves issues with the older 'traditional' methods of Isotope Dilution (ID) mass spectrometry, in which severa,l discrete calcite growth phases are typically averaged together for a single datum. To make best use of the in-situ method, however, requires careful petrographic characterisation of each sample, so that the nature and structural context of discrete calcite zones can be determined for U-Pb calcite geochronology. This allows ages to be related to periods of distinct deformation and fluid-flow. Similar considerations are true of stable and clumped isotopic analysis, which combined with the micromilling processes described in Section 2.5, can target distinct generations of calcite mineralisation, therefore enhancing the quality of data and testing of hypotheses.

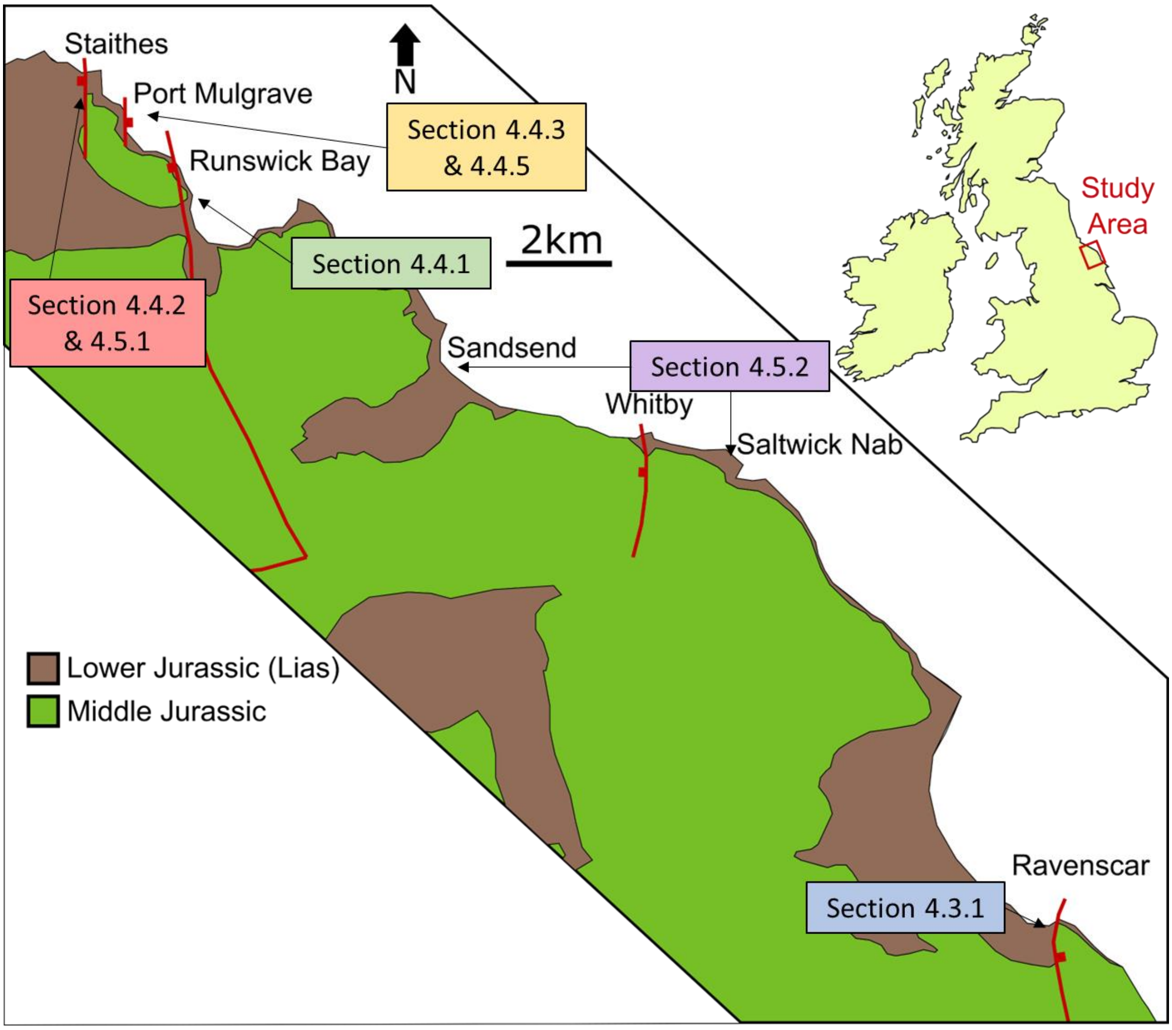


*Fig 4.2. Stylised structure map of the main area of interest with the key sampling locations for samples detailed in this chapter indicated.*

Specific samples were chosen to cover the complete spectrum of structural components and fill types as described in Chapter 3 (Fig 4.1 & 4.2). Additional samples not discussed here are summarised in the table in Appendix 8.2 with images in Appendix 8.1. These are assessed for primary calcite textures and/or evidence of reprecipitation and/or alteration to identify their integrity as kinematic and geochemical indicators. Samples, where possible, are oriented in their field positions with North pointing into the page. The focus then switches to identifying microstructures, growth textures and crystal structures, which provide information on the age of mineralization relative to local and regional deformation events documented in Chapter 3. While syn-kinematic fills can directly date fault movement, pre- and post kinematic fills provide additional constraints on the timing of deformation and period of tectonic quiescence and the continuation of fluid-flow.

Microstructural imaging uses a combination of optical images, mount images, reflected microscopy, plane polarised light (PPL), cross polarised light (XPL), cathodoluminescence

(CL), and SEM techniques such as backscattered electron (BSE) and charge contrast imaging (CCI). PPL and XPL images are only present where companion thin sections were prepared; epoxy resin mounts were initially made to allow easy sampling for isotopic analyses and U-Pb calcite geochronology. However, resin mounts are too thick for light to effectively pass through the sample so are limited to imaging under reflected light. Therefore thin sections were required for PPL and XPL imaging but due to timing and cost restraints were only prepared for key samples. CL and SEM techniques are more specialised and were acquired at the BGS, Keyworth on key samples. The methodology for imaging and sampling is described in Chapter 2.

The microscopy provides a vital link between the regional to outcrop-scale structures documented in Chapter 3 and the geochronological and isotopic analyses described in Chapter 4 & 5. The U-Pb calcite geochronology results are presented in this chapter in relation to the local structural setting, before being placed into a regional context in the Synthesis (Chapter 6).

## 4.2 Microstructural Textures

### 4.2.1 Introduction

Calcite fracture fills are common in many geological settings and provide critical information on their time of precipitation and potentially of the deformational regime at the time. Roberts et al. (2020) look in detail at the strategies for U-Pb calcite geochronology and stress the requirement for microscopic imaging to establish a link between the date and the process of interest (in this case, deformation and/or fluid-flow). Figure 4.3 shows a representative (but not exhaustive) range of different calcite fills. These range from crack-seal-slip fills – thought to be the best indicators of synchronous deformation and mineralization - to 'crack-fill' textures. Thus, slickenfibres and filled pull-apart/jogs are generally the best samples for dating faulting events whilst open vugs are generally the least well constrained.

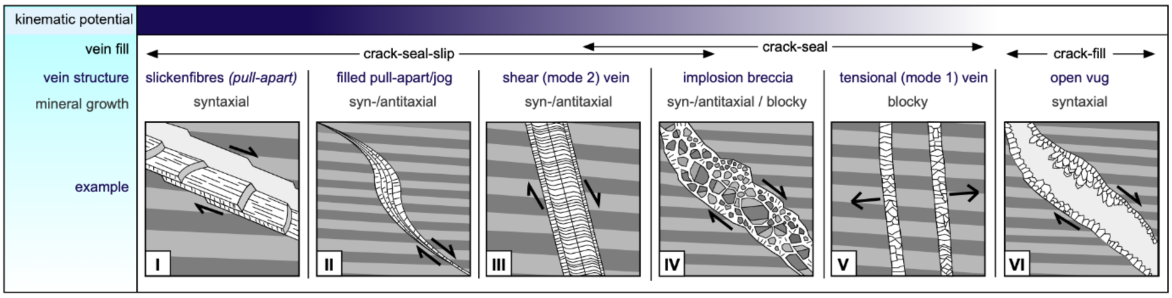


*Fig 4.3. Schematic image from Roberts & Holdsworth (2022) demonstrating a variety of different fault and vein fill types and their strengths as kinematic indicators from I (highest) to V (lowest).*

### 4.2.2 Growth Morphology/Texture

Veins can grow in different ways with different growth morphologies and textures (Fig 4.4), as summarised by Passchier & Trouw (2005) and Bons et al. (2012). Each calcite growth morphology has different implications for the type of fill and the confidence as an indicator of synkinematic precipitation.

*Syntaxial growth* - new material is added at the centre of the vein along a single growth surface with the oldest material at the edges and newest at the centre.

*Antitaxial growth* - new material is added along two growth surfaces positioned at the margins with the oldest calcite at the centre and the youngest at the margins.

*Unitaxial growth* - calcite is added in one direction from a single growth plane.

*Ataxial growth* - no clear localised growth surface is present.

*Composite growth* - multiple growth surfaces exist potentially leading to difficulty in determining the relative ages of the calcite zones.

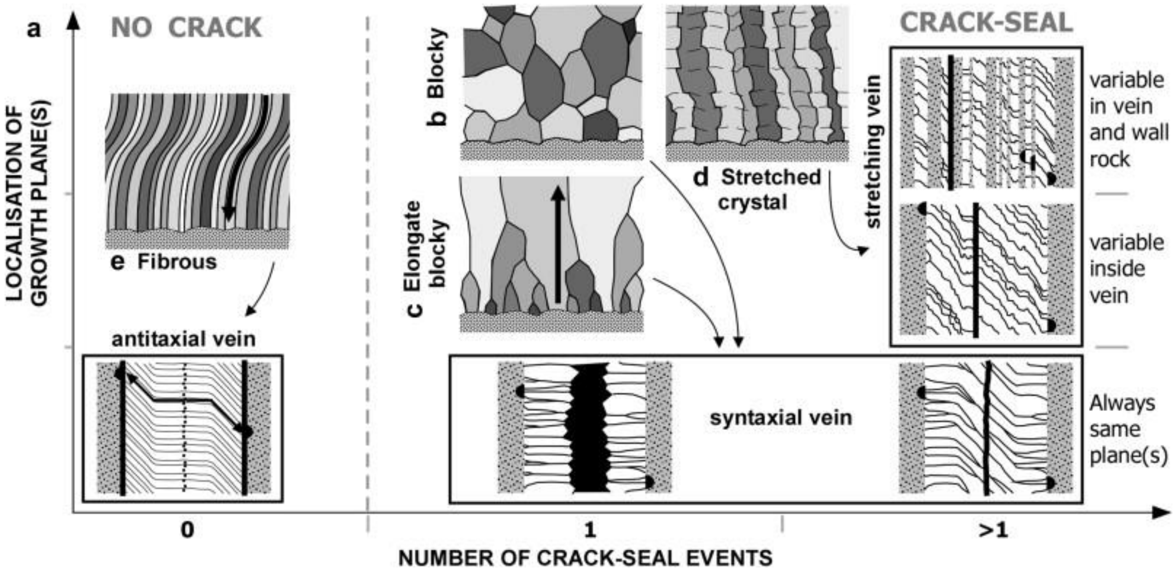


*Fig 4.4. a) Basic schematics of vein growth morphologies (antitaxial, syntaxial, composite) and crystal types from Bons et al. (2012). The schematic image links the main crystal types (b – blocky, c – elongate, d – stretched crystals and e – fibrous).*

Identifying growth textures where possible is crucial, as these fabrics are indicative of primary growth. If these fabrics are absent or cross-cut, it could indicate that later reprecipitation or alteration of the calcite has occurred, which is likely to disturb and/or potentially invalidate geochronology and isotopic results.

### 4.2.3 Crystal type

The crystal morphology of minerals such as calcite provides additional evidence about the rate and direction of opening. A model proposed by Urai et al. (1991) based on numerical models and observations of natural examples indicated that the crystal type is indicative of the amount and rate of opening, with open spaces leading to aggregates of similar crystals (blocky) or slightly elongate crystals. If, however, crystals are forced to open rapidly in a narrow aperture fracture, then highly elongate or fibrous crystals will develop. Such narrow aperture growth commonly develops textures formed during repeated sealing and opening events and the fibres will commonly track the opening direction (Means & Li, 2001).

The use of crystals to track opening direction must be used with care as Cox & Etheridge (1983), Cox (1987) and Williams & Urai (1989) indicate that in an open void, crystals can grow normal (perpendicular) to the vein margins. This means that blocky and elongate crystals cannot be used as high confidence indicators of opening direction without other textures (i.e. inclusion trails and/or inclusion bands) being present. In addition, Williams &

Urai (1989) indicate that curved, strain-free fibrous crystals can form due to deformation and recrystallisation of fibres that were originally orthogonal to the vein wall.

Urai et al. (1991) observed that some fibrous antitaxial veins observed in slate did not track opening directions. Modelling and analysis by Urai et al. (1991) and Oliver & Bons (2001) indicate that fibre growth is controlled by the rate of growth versus the crack width with "true" fibres only forming in narrow cracks. In addition, the assumption that fibres track the opening direction is only indicated to be reliable where the crack is rough with smooth margins potentially leading to non-tracking behaviours.

Crack-seal textures develop leading to the formation of inclusion bands that occur as the vein is opened, filled and resealed repeatedly. Jogs in these bands (Fig 4.5; Bons et al., 2012) track can track opening, as can the alignment of inclusion trails of wall rock or fluid inclusions.

#### 4.2.3.1 Taber growth

The nature and method of growth of elongate and fibrous crystals is still an area of debate with authors such as Taber (1916; 1918) and Means & Li (2001) advocating a mechanism primarily for antitaxial growth by which vein growth occurs due to a crystallisation pressure at the margins (so-called 'Taber growth'). Means & Li (2001) utilised laboratory simulation to demonstrate that antitaxial veins were able to develop without fracturing. Taber growth described by these authors involves advection or diffusion of pore fluid to the vein walls through a porous medium. This is not considered likely in this study, as the hosting lithologies (Section 1.2.4) are typically clay-rich mudstones, which have very low permeabilities. Low permeabilities would inhibit advection or diffusion of fluid to the vein walls to support consistent Taber growth. In addition, characterisation in this study showed that many veins and fills show vertical continuity along fault and fractures structures more suggestive of a plumbing regime with bulk transport of fluids rather than crystallisation from the immediate surrounding host rock. While Taber growth as a mechanism cannot be entirely ruled out here, it is considered to be an unlikely mechanism given patterns of fluid-flow detailed in Chapter 5.

### 4.2.4 Extensional jogs

In contrast to the planar veins that commonly form as fills in opening mode fractures, faults can include more complex multi-phase fills. For example, extensional jog structures might have crystal growth separated by shear planes with sheet like mineral growth as new space becomes available as shown in Figure 4.5. Extensional jog structures often develop a “stair stepping” form due to the separation of sheet like growth by shear plane. The downstepping direction of the extensional jog provides direct evidence of the shear sense (Fig 4.5; Bons et al. (2012). Extensional jog structures therefore can provide high quality indicators, assuming primary calcite is preserved, of synkinematic calcite mineralisation relative to fault movement.

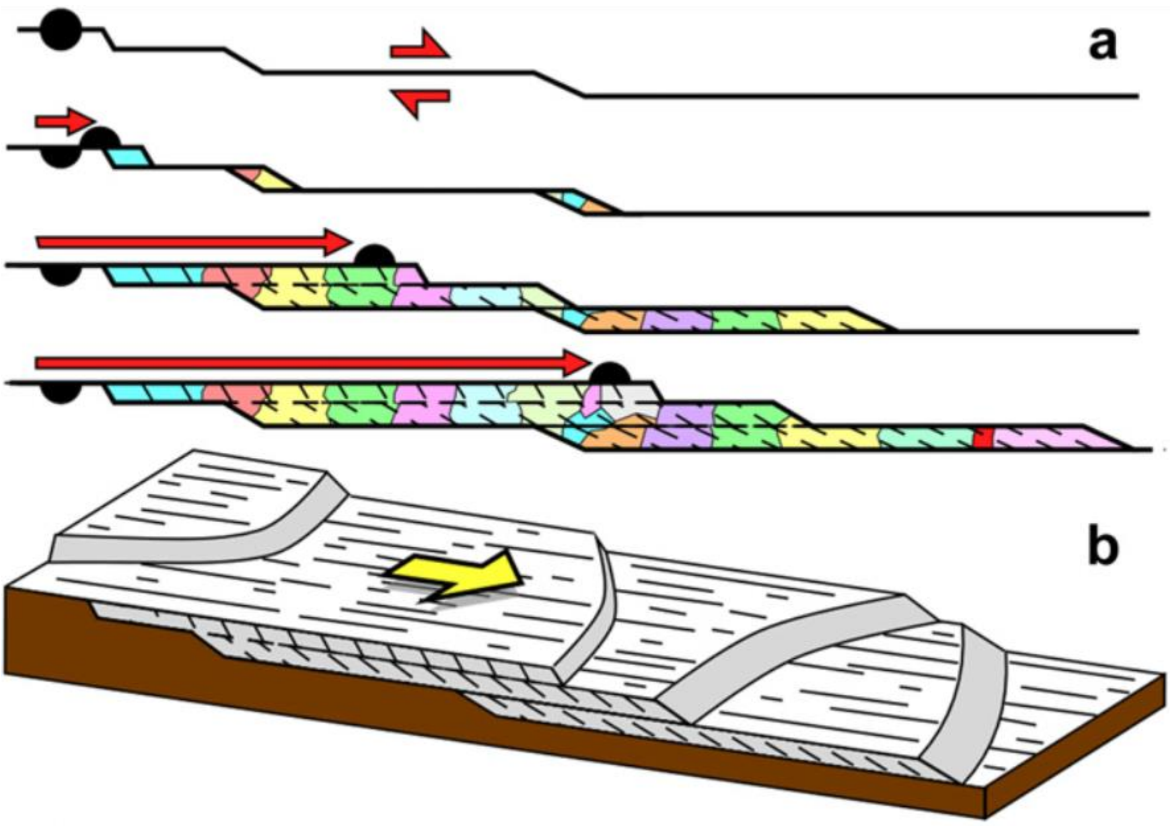


Fig 4.5. Schematic conceptual diagrams of extensional jog formation from Bons et al. (2012). a) A sectional view of the schematic jog with the black hemispheres progressively offset as sheets of calcite are precipitated. b) An oblique view of the schematic jog illustrating the 3D ‘stair-stepping’ architecture with down stepping indication the direction of relative motion.

### 4.2.5 Breccia fills

Breccias are commonly assumed to form due to frictional attrition, distributed crushing and/or implosion during fault movement (e.g. Robertson, 1982; Sibson, 1986). A breccia is described by Sibson (1977) as an incohesive fault rock with visible coarse fragments composing >30% of rock mass and lacking cohesion at the time of faulting. Breccias that maintained cohesion have also been identified and are referred to as crush breccias by Spry (1969) and Higgins (1971). Sibson (1986) went on to define different forms of breccia based on the localised strain (dilation, neutral or compression) within the fault structure; i.e.

implosion (dilational), attrition (neutral) and crush (compressive) breccias. Woodcock et al. (2006) have advocated the use of the terms crackle, mosaic and chaotic for all fault-related breccias based on their textural composition. Mort and Woodcock (2008) propose a classification scheme (Fig. 4.6) based on image analysis using the percentage of sample area occupied by clasts:

1. Crackle breccia is composed >75% clasts with <10° rotation,
2. Mosaic breccia is composed of 60-75% clasts with 10-20° rotation,
3. Chaotic breccia is composed of <60% clasts with >20° rotation,

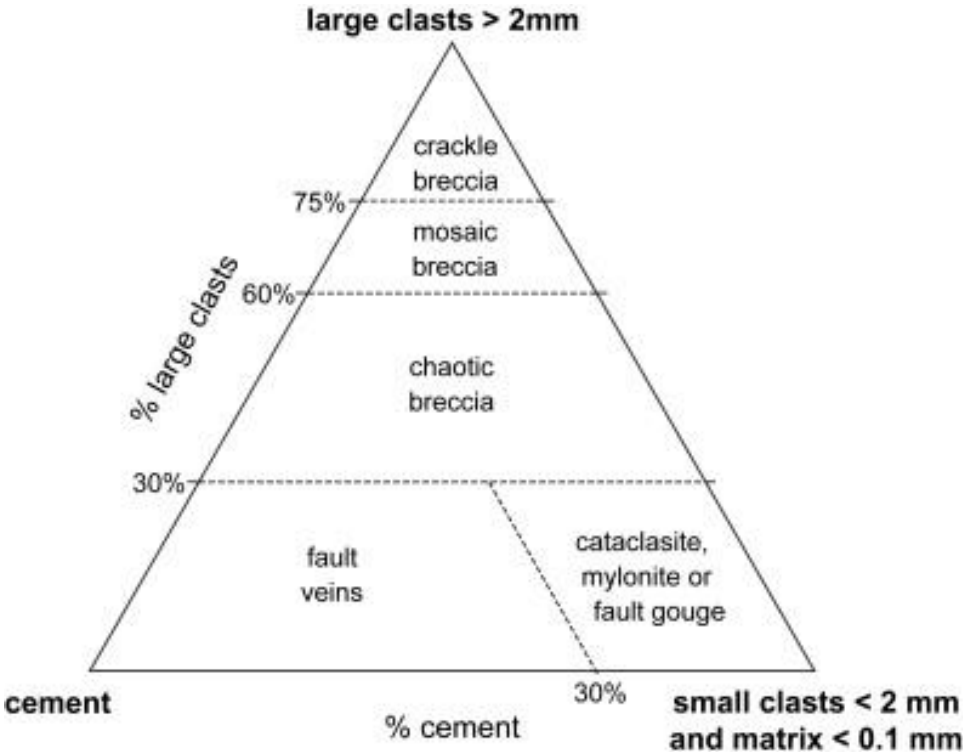


Fig 4.6. Ternary classification diagram from Mort & Woodcock (2008). Samples in this study typically fall in the field of fault veins and or chaotic breccia.

In addition, in the shallow subsurface (<1km) open fissures can form in which mineralisation occurs due to the unrestricted flow of meteoric or deeper sourced fluids in open or partially open fracture systems. Open fissures are typified by microstructures such as cockade textures (Frenzel & Woodcock, 2014), vuggy textures, rind-like mineralization, presence of sediment fills and reworking of previous breccia material (e.g. Cox & Munroe, 2016; Walker et al., 2011; Holdsworth et al., 2019). Varved sediment fills and reworked material in open vugs and fissures have recently been documented in faults cutting the Cretaceous Chalk at Selwicks Bay where they are associated with the final phase of movement along the Flamborough Head Fault Zone, at the southern margin of the Cleveland Basin (Roberts et al. 2020).

### 4.2.6 Cone-in-cone structure

Cone-in-cone structures (Fig 4.7) are caused by displacive growth of calcite in conical bundles of fibres between one or more conical bands of mudstone or shale, i.e. calcite growth within the mudstone forcing it apart (Cobbold et al., 2013). They are mostly found in impermeable sedimentary lithologies such as mudstone and are inferred by Cobbold & Rodriquez (2007) and Cobbold et al. (2013) to be related to disequilibrium compaction or other mechanisms such as petroleum generation, which is a volume generating process and can, along with other processes discussed in Chapter 6, lead to overpressure.

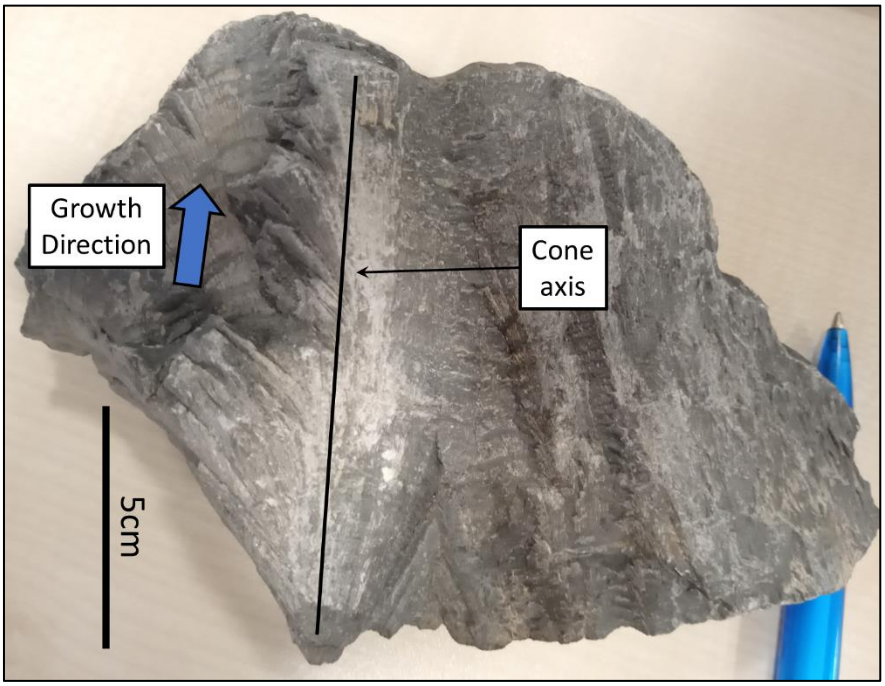


Fig 4.7. A cone in cone structure sampled from the margin of a concretion at Port Mulgrave. A distinct cone-in-cone structure can be seen on the left of the image with successive bands up the cone added as it formed.

## 4.3 Peak Trough Faults

Following the approach used during the field observations (Chapter 3), there are three subdivisions of structures that will be used in this and subsequent sections. These are: the regional Peak Trough faults; “Meso-scale” fault structures; and local fracture fills.

The Peak Trough is a 5-10km wide and >50km long syn-depositional graben (Milsom & Rawson, 1989) that transects the eastern margin of the onshore Cleveland Basin before passing offshore north of Ravenscar. Based on recent BGS mapping inland (Vernon et al., 2020), it is thought to cross-cut – and therefore to post-date – the E-W trending FHFZ which forms the southern margin of the Cleveland Basin (Fig 4.1 & 4.8).

The Peak Fault is the western bounding fault of the Peak Trough and is exposed at Ravenscar (Section 3.2.2.1). The Cayton Bay and Red Cliff faults represent an internal graben, east and west dipping respectively, in the larger Peak Trough and are exposed at the north and south ends of Cayton Bay (Section 3.2.2.2 & 3.2.2.3).

The structural setting, field relationships and sampling locations for Ravenscar (Peak Fault), Osgodby Nab (Cayton Bay Fault) and High Red Cliff (Red Cliff Fault) are detailed in Section 3.2.2. Table 4.1 summarises all microstructural information collected for the Peak Trough faults, with the full results detailed in Appendix 8.2.

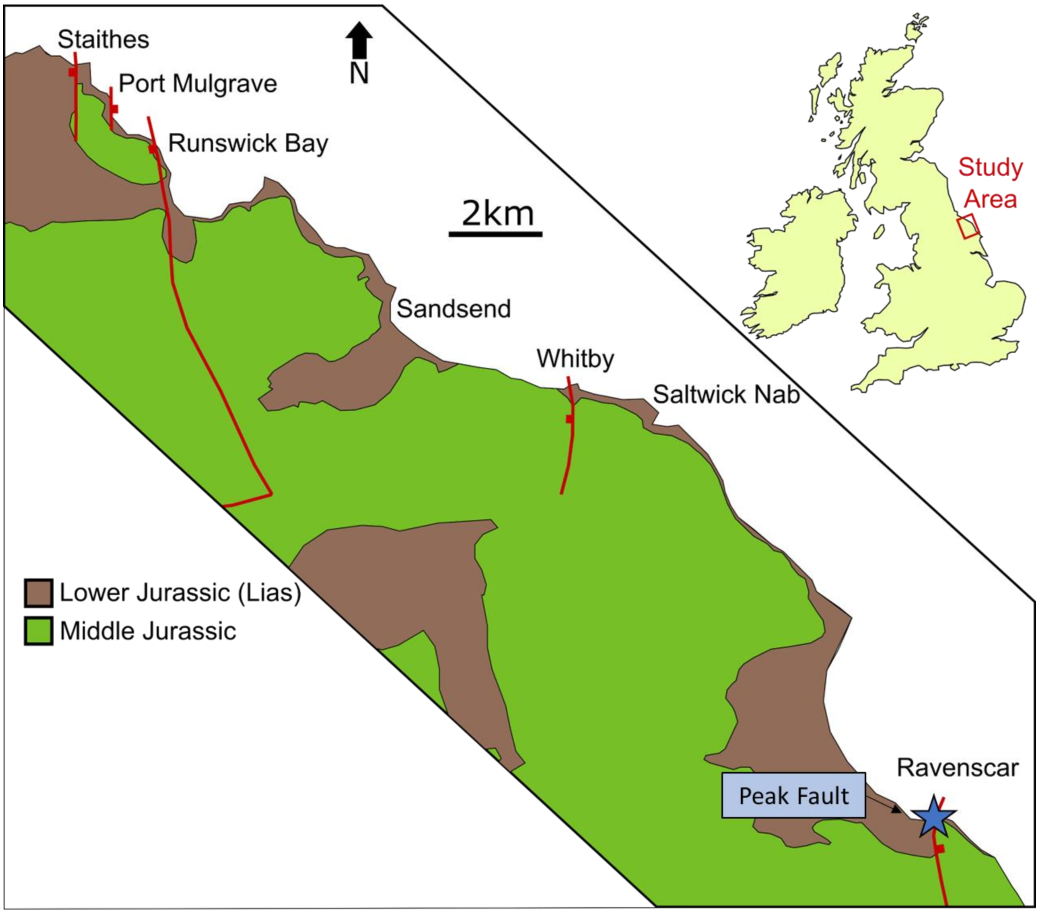


*Fig 4.8. Structural map of the area of interest with the location of the Peak Fault highlighted. Both the Red Cliff Fault and Cayton Bay Fault are off the map to the south.*

### 4.3.1 Peak Fault (Ravenscar)

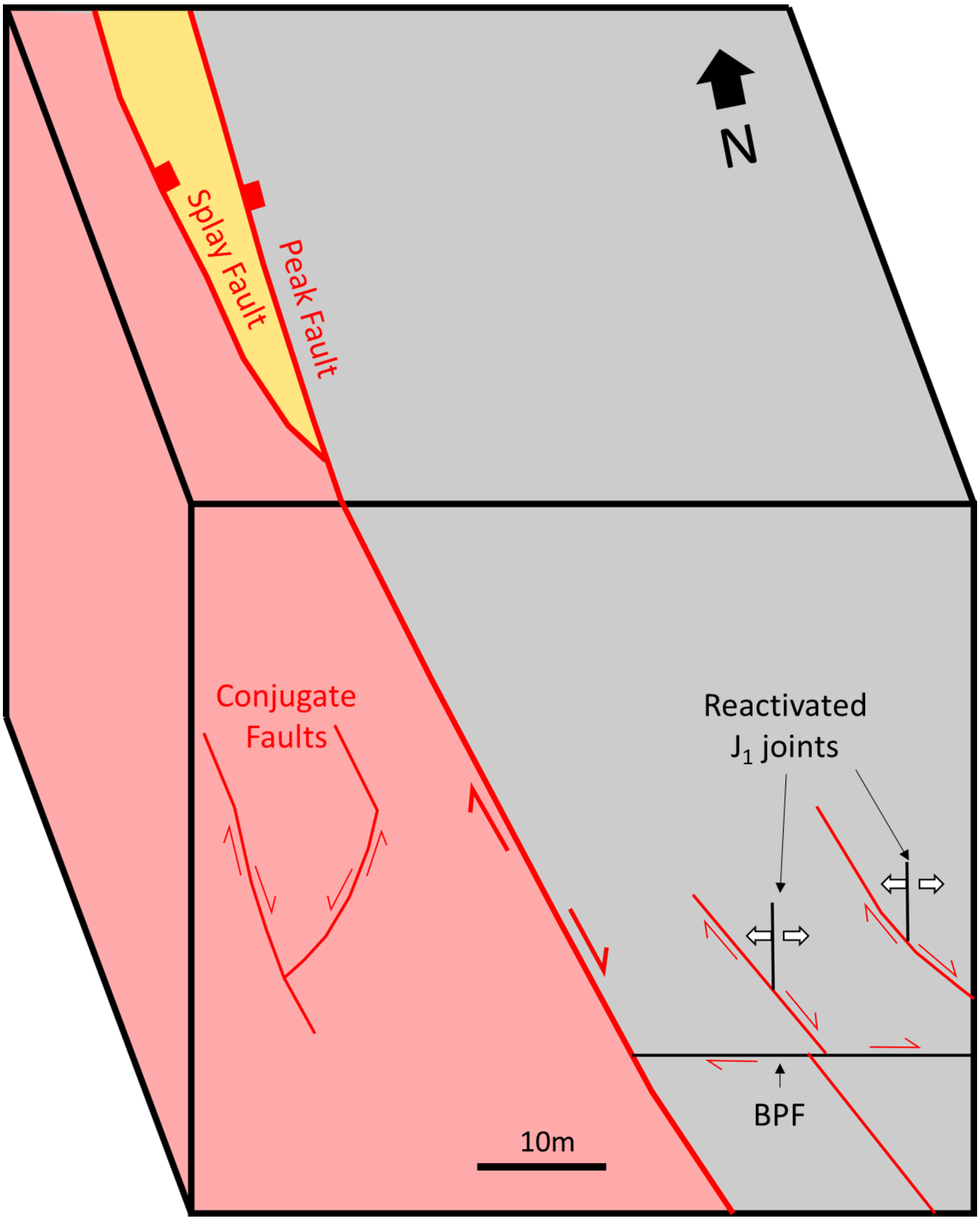


*Fig 4.9. Schematic diagram of the key field relations and kinematics of calcite mineralised structures at the Peak Fault at Ravenscar. The normal offset Peak Fault is shown to splay in the foreshore. Inclined conjugate normal faults and a top to the east bedding-parallel fault (BPF) are present in the damage zone of the Peak Fault. Inclined conjugate east- and west-dipping normal faults reactivate J1 joints in dilation with subvertical calcite veins developed.*

The structural components of the Peak Fault at Ravenscar are discussed in detail in Section 3.2.2.1 with calcite mineralised structures subdivided into three sets:

4.3.1.1 – Main & Splay Fault

4.3.1.2 – Conjugate Normal Faults

4.3.1.3 – Reactivated $J_1$ Joints

In total, 11 samples have been taken from the Peak Fault at Ravenscar of which a subset are shown here focussed on providing representative examples of a wide selection of fill types, microstructures and kinematic evidence.

| Sample | Zone | Main Structure | Minor Structure | UTM N | UTM E | Calcite Fill | Texture | Kinematics | Dating |
|---|---|---|---|---|---|---|---|---|---|
| JL2021 | 1 | Ravenscar - Peak Fault | Main Fault | 662724 | 6031788 | Extensional Jog | Blocky | Syn to Post kinematic | - |
| - | 2 | - | - | - | - | - | Blocky | Syn-kinematic | - |
| - | 3 | - | - | - | - | - | Blocky | Syn to Post kinematic | Y |
| NR1619 | 1 | Ravenscar - Peak Fault | Splay Fault | 662753 | 6031771 | Extensional Jog | Blocky | Syn to Post kinematic | Y |
| NR1620 | 1 | Ravenscar - Peak Fault | jugate Normal Fa | 662818 | 6031988 | 3-5mm thick vein | Fibrous | Post Kinematic | Y |
| - | 2 | - | - | - | - | - | Fibrous | Post Kinematic | Y |
| NR1623 | 1 | Ravenscar - Peak Fault | jugate Normal Fa | 662715 | 6031838 | Breccia (mosaic) | Fibrous | Syn-kinematic | - |
| - | 2 | - | - | - | - | - | Blocky | Syn-kinematic | Y |
| JL2020 | 1 | Ravenscar - Peak Fault | jugate Normal Fa | 662718 | 6031771 | Extensional Jog | Fibrous | Syn to Post kinematic | Y |
| - | 2 | - | - | - | - | - | Blocky | Syn-kinematic | - |
| - | 3 | - | - | - | - | - | Blocky | Syn to Post kinematic | - |
| JL2022 | 1 | Ravenscar - Peak Fault | jugate Shear Frac | 662729 | 6031771 | 0.5mm thick Vein | Fibrous | Syn to Post kinematic | Y |
| JL2024 | 1 | Ravenscar - Peak Fault | jugate Normal Fa | 662749 | 6031781 | 2-4mm thick Fault Fill | Fibrous | Syn to post kinematic | Y |
| - | 2 | - | - | - | - | - | Blocky | Post kinematic | - |
| NR1617 | 1 | Ravenscar - Peak Fault | Vein - Vertical | 662727 | 6031789 | 1cm thick Vein | Blocky | Syn to Post kinematic | Y |
| NR1622 | 1 | Ravenscar - Peak Fault | Vein - Vertical | 662715 | 6031838 | Breccia | Blocky | Syn-kinematic | Y |
| NR1621 | 1 | Ravenscar - Peak Fault | Vein - Vertical | 662715 | 6031838 | 2-3cm thick Vein | Bladed | Syn to Post kinematic | Y |
| JL2023 | 1 | Ravenscar - Peak Fault | Vein - Vertical | 662749 | 6031785 | 6-7mm thick Vein | Fibrous | Syn to post kinematic | Y |
| - | 2 | - | - | - | - | - | Blocky | Post kinematic | Y |

*Table 4.1. Summary table of calcite fills from the Peak Fault at Ravenscar (Fig 4.8) analysed in this chapter. Samples not discussed here are presented in Appendix 8.1 & 8.2.*

#### 4.3.1.1 Main and Splay Faults

The main Peak Fault and splay fault have distinct phases of deformation with initial syn-sedimentary movement and later reactivation (Section 3.2.2).

<u>JL2021</u>

One sample (JL2021) was taken from the main fault plane on the wavecut platform (Fig 3.7). JL2021 is an extensional jog structure with a thin (2-3cm thick) blocky calcite fill in hand specimen. Figure 4.10 shows a schematic sketch of JL2021 with the jog situated 5cm below a N-S striking plane of cone-in-cone structures with cones widening east towards the main fault plane.

Three distinct zones of calcite are recognised:

Zone 1 – Fibrous calcite (1.0-1.5mm thick; Fig 4.11a & b) with inclusion bands visible in cross-polarised (XPL) and plane polarised (PPL) light microscopy that track opening mode dilation directions. Calcite fibres demonstrate primary antitaxial growth and track opening at 90° to the fill margin.

Zone 2 – Microspar calcite (0.2-4.0mm thick; Fig 4.11c) with a crystal size <50µm and frequent bands of inclusions that are indicative of crack-sealing (Fig 4.11). Zone 2 has no obvious growth plane and is likely ataxial. The microspar is cross-cut by later stair-step geometry microfaults (~1mm long) at the top margin of Figure 4.11c, which offset bands of wall rock inclusions. Microfaulting is associated with calcite thickening and variation of included mudstone bands across the microfaults suggesting fault movement occurred synchronous with calcite growth. This variation is used to infer that microfaulting was synchronous with calcite precipitation in Zone 2 and likely reflects that mineralization was synchronous with movement of the Peak Fault.

Zone 3 – Macrospar calcite (Fig 4.11b) is shown in XPL to cross-cut Zone 2. The macrospar is highlighted in blue on the interpretation in Figure 4.11c and has no inclusion bands and infrequent wall rock inclusions (1-2%). There is no obvious localised growth plane (ataxial) and Zone 3 has a crack-fill texture.

The macrospar calcite (Zone 3) from JL2021 (Fig 4.11c) has been successfully dated at 37.8 ± 8.0Ma with an MSWD of 1.4 (Fig 4.13a). The high uncertainty in this age provides a 16Ma window during which this calcite fill could have formed. However, it is interpreted (above) that this is the latest calcite zone and postdates earlier calcite zones with clear syn-kinematic indicators. This date likely still reflects dilation of the jog structure due to fault slip and provides a reasonable constraint on this phase of fault movement and associated fluid-flow.

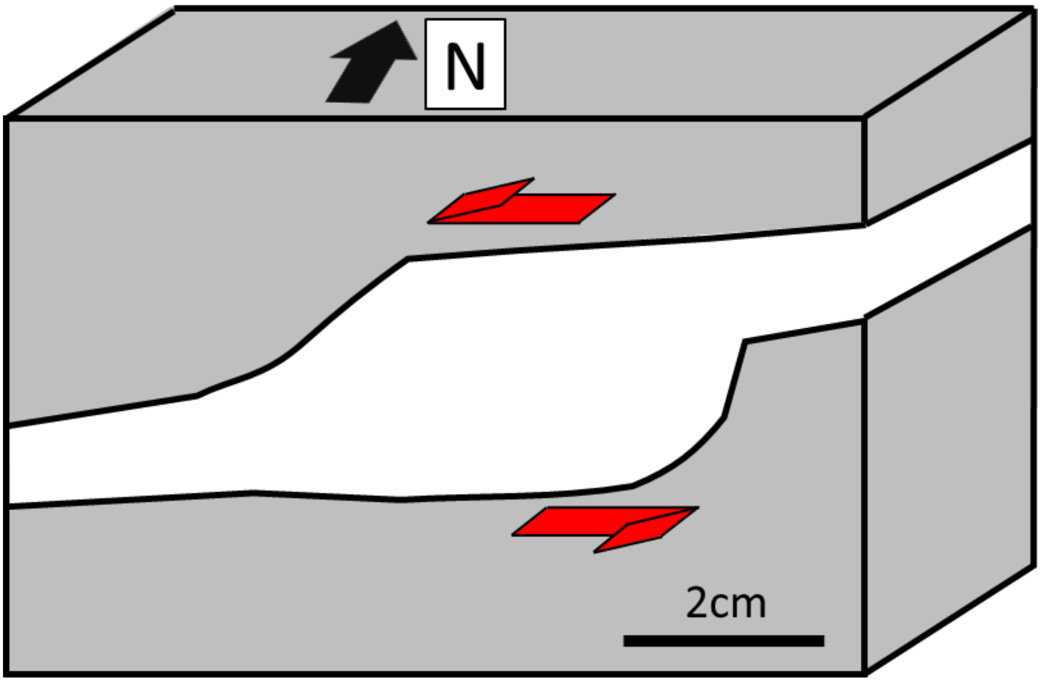


*Fig 4.10. Schematic diagram of JL2021 (white), an extensional jog structure which was formed by eastward normal reactivation of the Peak Fault.*

<u>NR1619</u>

NR1619 is a 3-4cm blocky calcite fill in an extensional jog (Fig 4.12b; inset sketches) from the Splay Fault (Fig 4.12a) where it downthrows the Staithes Sandstone Formation against the Redcar Mudstone Formation.

NR1619 has a clear syntaxial texture with crystal size increasing towards the centre of the fill (Fig 4.12c). The crystals range from ~50µm at the margins up to 1000µm in size near the centre. The calcite is optically clear in the resin mount and is typically free of included clasts except along the upper margin (Fig 4.12c). Inclusion bands are present along the upper margin but die out within 2mm. The centimetre-scale vugs evident in the field are not sampled in the thin section.

Inset trace element maps in Figure 4.12 show the relative concentrations of Iron (Fe), Vanadium (V) and Uranium (U) scaling from yellow (high concentrations) to black (low concentrations). The trace element mapping (Fig 4.12) for NR1619 suggests that higher concentrations of iron, vanadium and uranium occur at the vein margins.

NR1619 reflects dilational movement along the extensional jog with space opened for a blocky texture to form, with initial syn-kinematic crack-seal opening changing to crack-fill as the extensional jog opened further. The blocky syntaxial calcite of NR1619 has been dated at 28.58 ± 1.02Ma (Fig 4.113) with an MSWD of 1.2.

Summary

The two fault fills from the Peak Fault (JL2021) and Splay Fault (NR1619) with JL2021 observed to have crack-seal calcite zones (1&2) in an extensional jog structures with a later crack-fill zone (Zone 3). NR1619, in contrast, has some inclusion bands along the right margin in Figure 4.12f but no other clear indicators of crack-seal. While we cannot prove that calcite zones dated are syn-kinematic, the calcite fills are either syn- to post kinematic and provide a lower limit for fault movement. However, the association of the fills with other syn-kinematic fills (i.e. pre, post- or syn- to post-kinematic) suggests that mineralisation could be synchronous with a late stage of local fault movement. The U-Pb calcite dates of these fills do not overlap within uncertainty indicating that they formed from separate fluid-flow events along different part of the same fault system.

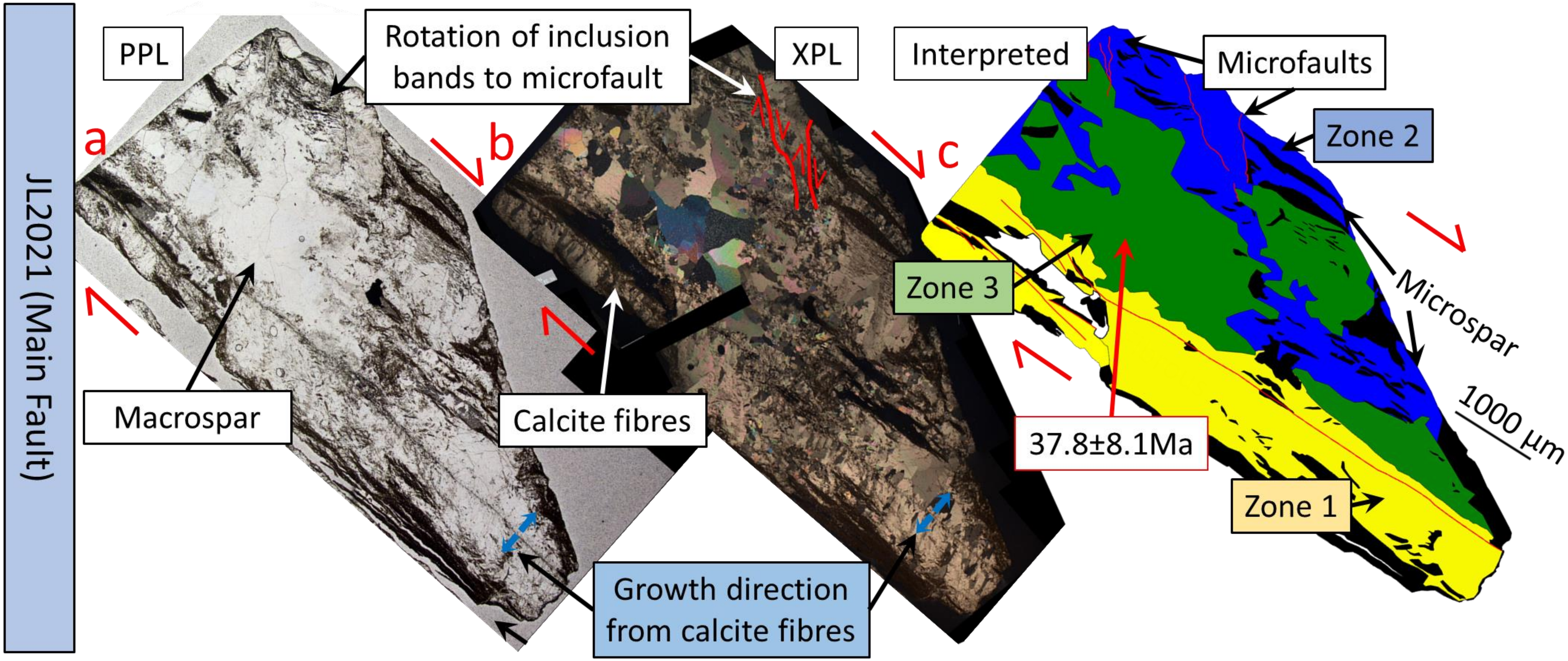


*Fig 4.11. JL2021 – Highly complex calcite fill in an extensional jog structure with apparent normal down plunge shear sense. a) PPL image showing the complexity of the fill with calcite fibres. b) is an XPL image showing the calcite fibre tracking margin perpendicular opening (blue arrows) in Zone 1. The three calcite zones are shown in the intepretation (c) with an inferred order of precipitatation from yellow (Zone 1 – fibrous to bladed) then blue (Zone 2 – fine blocky/spar with frequent clasts) with green (Zone 3 – blocky with infrequent clasts) a later crack-fill texture. Multiple accretion planes (red) are inferred. Minor faults (b) at the top left of the image demonstrate apparent normal movement with stepping down of marginal blocky calcite but no obvious consistent dislocation of clast layers visible. A Terra-Wasserburg plot shows the U-Pb date taken from Zone 3 of 37.79 ± 7.99Ma with an MSWD of 1.4.*

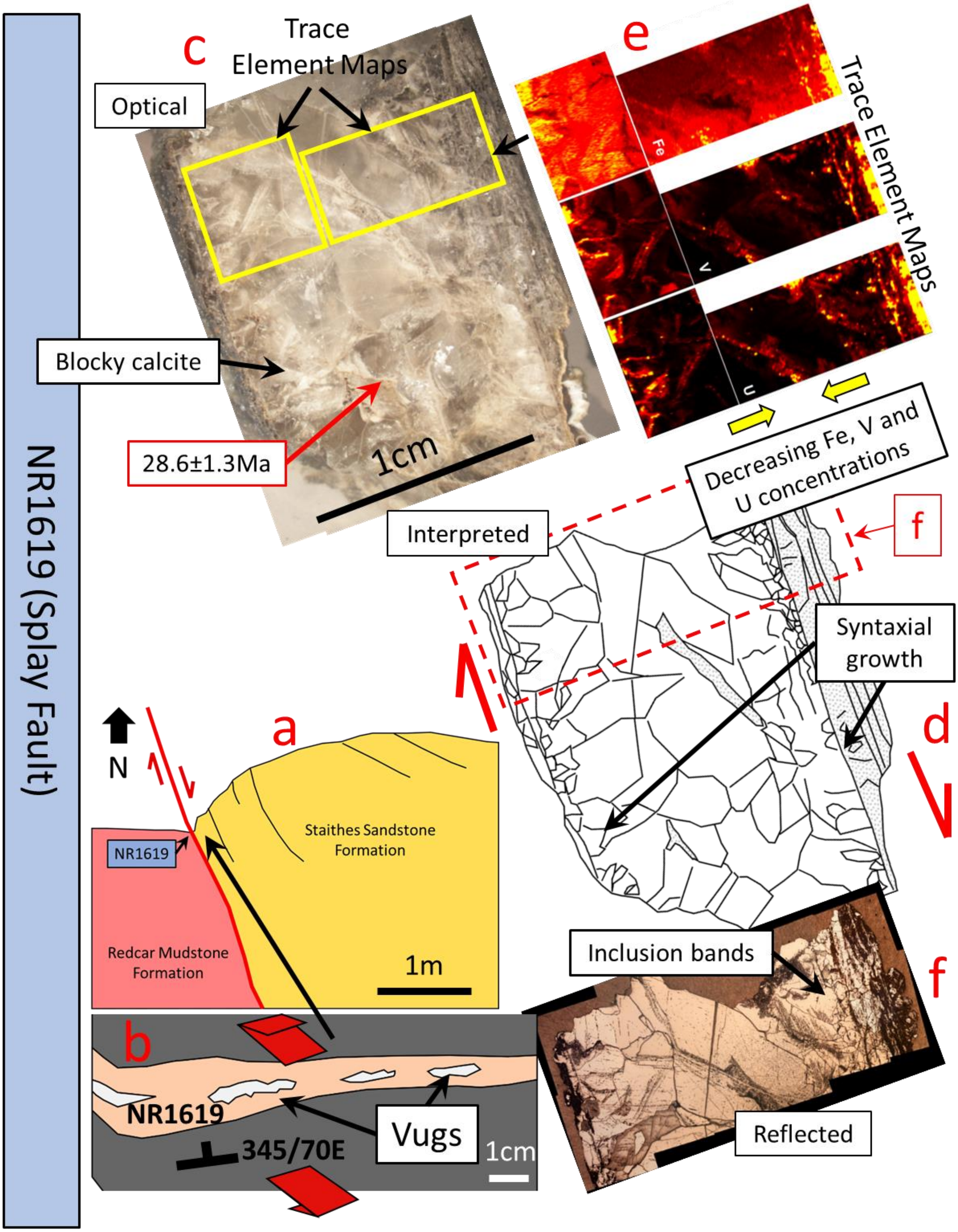


*Fig 4.12. NR1619 was sampled from the splay fault of the Peak fault (a). The sample is from an extensional jog structure (b) caused by normal movement of the fault. The jog structure has vugs in hand specimen, which are not seen in microscopy. c) Optical Microscopy shows a blocky calcite fills with 10-15%cm-scale vugs along the Splay Fault at Ravenscar. d) The interpretation shows increasing calcite size and decreasing crystal number towards the centre of the sample, which are indicative of syntaxial growth. e) Trace element maps are shown for the areas indicated in yellow: Fe=iron, V=vanadium and U=uranium. f) Reflected microscopy shows inclusion bands at the upper right of the fill suggesting somoe period of crack-seal.*

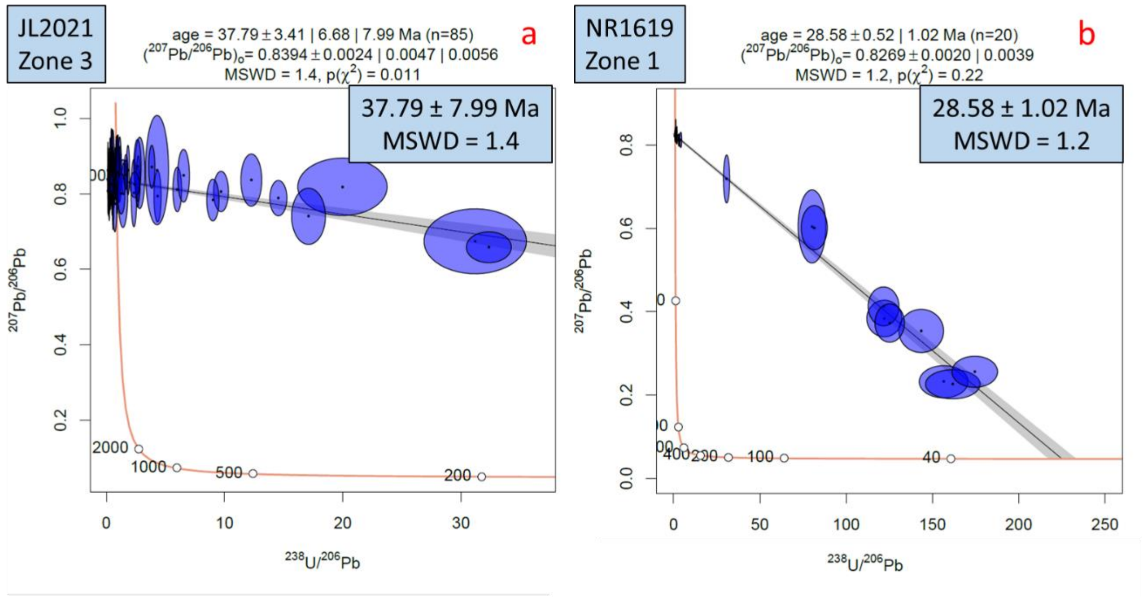


*Fig 4.13. Tera-Wasserburg (T-W) plots from the Main Peak fault (JL2021) and the Splay Fault (NR1619).*

### 4.3.1.2 Conjugate Normal Faults

Conjugate sets of inclined N-S striking faults (5-10m long fault traces) are present in the ~10m damage zone surrounding the main Peak Fault plane (Fig 4.9). These faults formed due to extensional reactivation of the Peak Fault post-burial and lithification (Section 3.2.2.1). Down-dip slickenlines, extensional jogs (Fig 4.14), systematic offsets of marker beds and extensional reactivation of N-S striking joints are used to infer normal movement. Calcite fills along conjugate fault planes are present as a mixture of veins oriented along the fault plane, mineralised extensional jogs and subvertical fibrous veins in reactivated $J_1$ joints (Fig 4.14).

Five samples have been taken from the conjugate normal faults. JL2024 and NR1620 are the best representatives and are described below, whilst the microstructures and U-Pb geochronology of the other samples are outlined in Table 4.1.

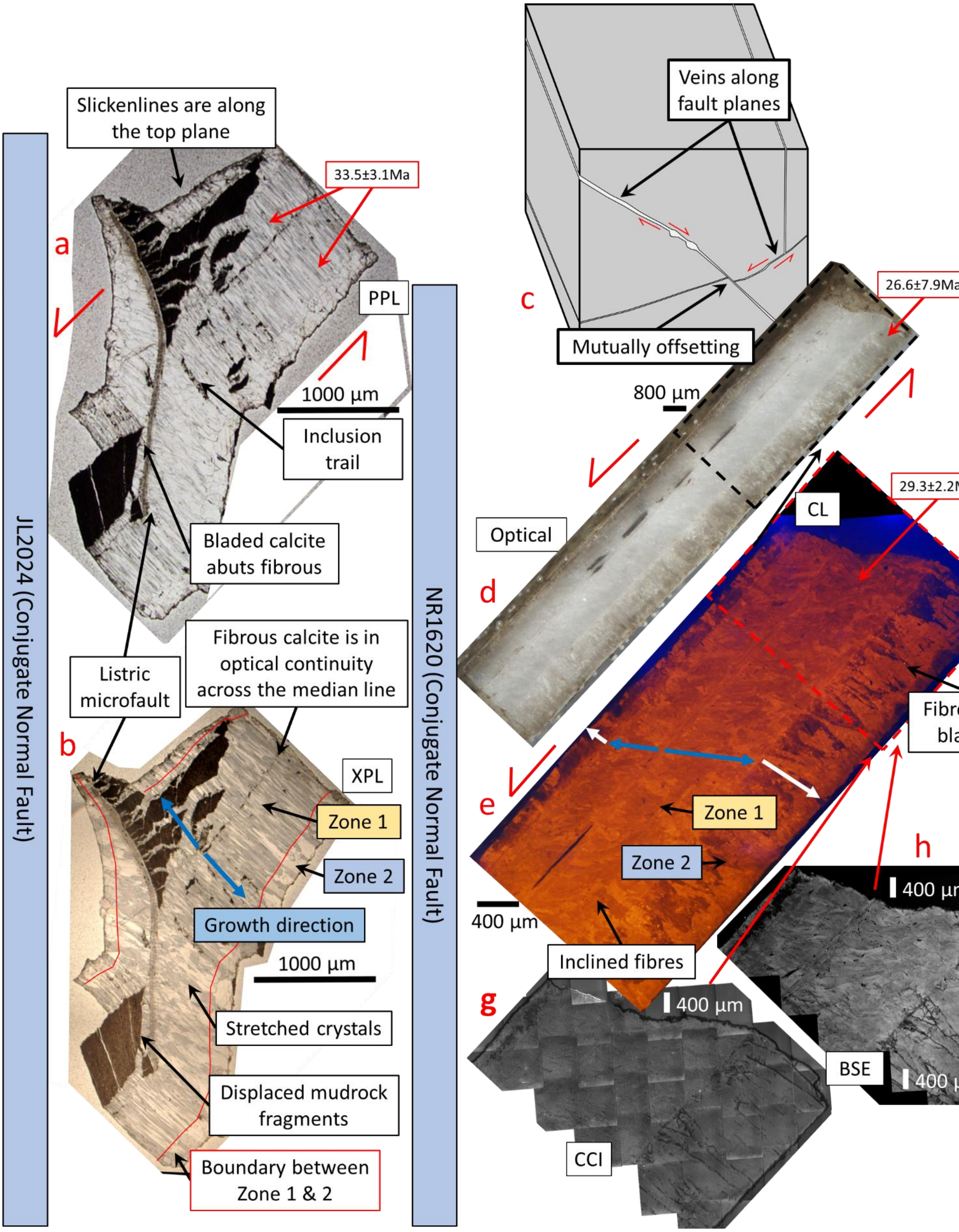


*Fig 4.14. Schematic block model of the conjugate normal faults demonstrating the types of calcite fills and the cross cutting relationships to each other. The white denotes calcite fills in extensional jog structures, reactivated joints and dilation along fault planes.*

JL2024

JL2024 is a 2-4mm thick vein that fills the central plane of an N-S striking eastward dipping normal fault plane. The calcite vein is oriented 193/57E with preserved slickenlines oriented 32-020 along the upper margin of the plane. The vein has complex microstructural relationships in thin section (Fig 4.15a) and is subdivided into two distinct zones of calcite (Fig 4.15b):

Zone 1 is an internal generation of fibrous calcite (0.2-2mm thick) with antitaxial growth. Fibrous growth, smeared trails of mudstone inclusions and inclusion bands track predominantly opening mode dilation with crack-seal textures. Zone 1 is offset at one point by a listric microfault (Fig 4.15a) running approximately parallel to the main fault plane, a layer of mudstone inclusions is downthrown to the bottom left. The calcite fibres near the microfault demonstrate apparent stretching and thickening indicative of movement synchronous with calcite precipitation (Fig 4.15a).

Zone 2 (Fig 4.15b) is a thin (0.15-0.20mm thick) blocky calcite fill with no obvious indicators of crack-seal. This zone is present only on the outer margins of the fill and displays relatively little variation in thickness. The fill is interpreted as a crack-fill texture and likely represents a different phase of opening where the rate of calcite growth was less than the opening rate.

Thickening of calcite into the microfault is used to infer that fault movement bracketed calcite mineralisation normal to the crack margins. This inference is consistent with observed fault movement and slickenlines. While calcite in Zone 1 tracks crack normal growth the record of bracketing and cross-cutting fault slip observed in the calcite zone suggests it was formed during a period of continuing intermittent fault movement with mineralisation in inter-slip periods. Zone 1 fill of JL2024 (fibrous calcite; Fig 4.15b) has been U-Pb calcite dated at 33.5 ± 3.1Ma with an MSWD of 1.6 (Fig 4.16a). This provides an absolute age on the dilation of the normal fault plane with later development of the bladed crystals in Zone 2 and the slickenlines on the uppermost plane of the vein. These slickenlines are not clearly seen in the calcite chip sampled (Fig 4.15a&b).

NR1620

NR1620 is a 3-5mm thick fill along a N-S striking fault plane dipping to the east that has been subdivided into two zones of antitaxial fibrous calcite (Fig 4.15e).

Zone 1 is an earlier internal phase of inclined fibre growth oriented at 60° to the vein margins (400-800µm thick Fig 4.15d). The median line has infrequent mudstone inclusions (1-2%). Cathodoluminescence (CL) clearly shows inclined fibres tracking opening (crack-seal-slip) during normal fault movement, i.e., these fibres are clearly synkinematic with faulting.

Zone 2 is an asymmetric calcite phase formed on the external margins of Zone 1 (50-600µm thick) and is composed of margin-perpendicular fibres/blades tracking a later phase of opening mode dilation (crack-seal). The growth of calcite fibres "normal" to the crack/vein margins is used here to infer to track dilation/opening of the fault.

Zone 1 of NR1620 (Fig 4.15e) has been dated at 29.3 ± 4.4Ma with an MSWD of 1.3 (Fig 4.16f) with Zone 2 (Fig 4.15d) dated with a much higher uncertainty at 26.6 ± 8.0Ma also with an MSWD of 1.3 (Fig 4.16g). These dates indicate that both calcite zones are broadly contemporaneous within uncertainty.

Additional U-Pb calcite dates for three samples (JL2022, JL2020 and NR1623) have also been dated but are not discussed here in order to focus on better quality images and reduce repetition. Tera-Wasserburg plots for these samples are shown in Figure 4.16 with all images shown in Appendix 8.1 and microstructures summarised in Appendix 8.2.

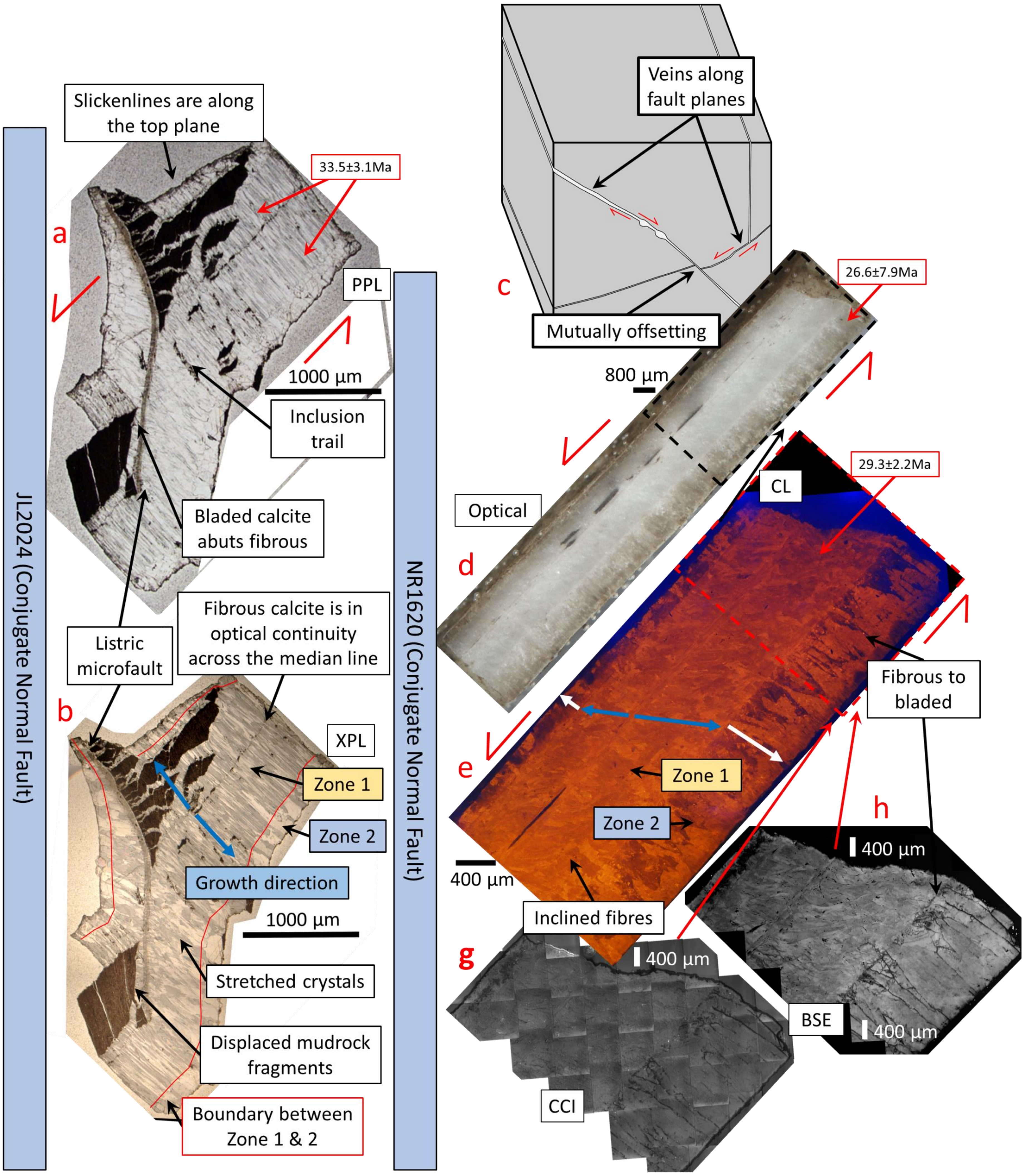


*Fig 4.15. a-h) Microscopy of two key calcite samples (JL2024 & NR1620) from conjugate normal faults located in the hangingwall of the Peak Fault at Ravenscar. A schematic sketch (c) shows the position of the samples oriented along thefault planes. JL2024 (a-b) and NR1620 (d-h) both strike approximately N-S and dip to the east at ~50°. Both samples are dominated by fibrous calcite growth. JL2024 (a): 85% fibrous calcite, 10% clasts &5% blocky calcite. NR1620 (d): 100% fibrous calcite. Both samples have antitaxial calcite fibres oriented perpendicular with a listric microfault in JL2024 and inclined calcite fibres in NR1620 indicating periods of shear/oblique opening.*

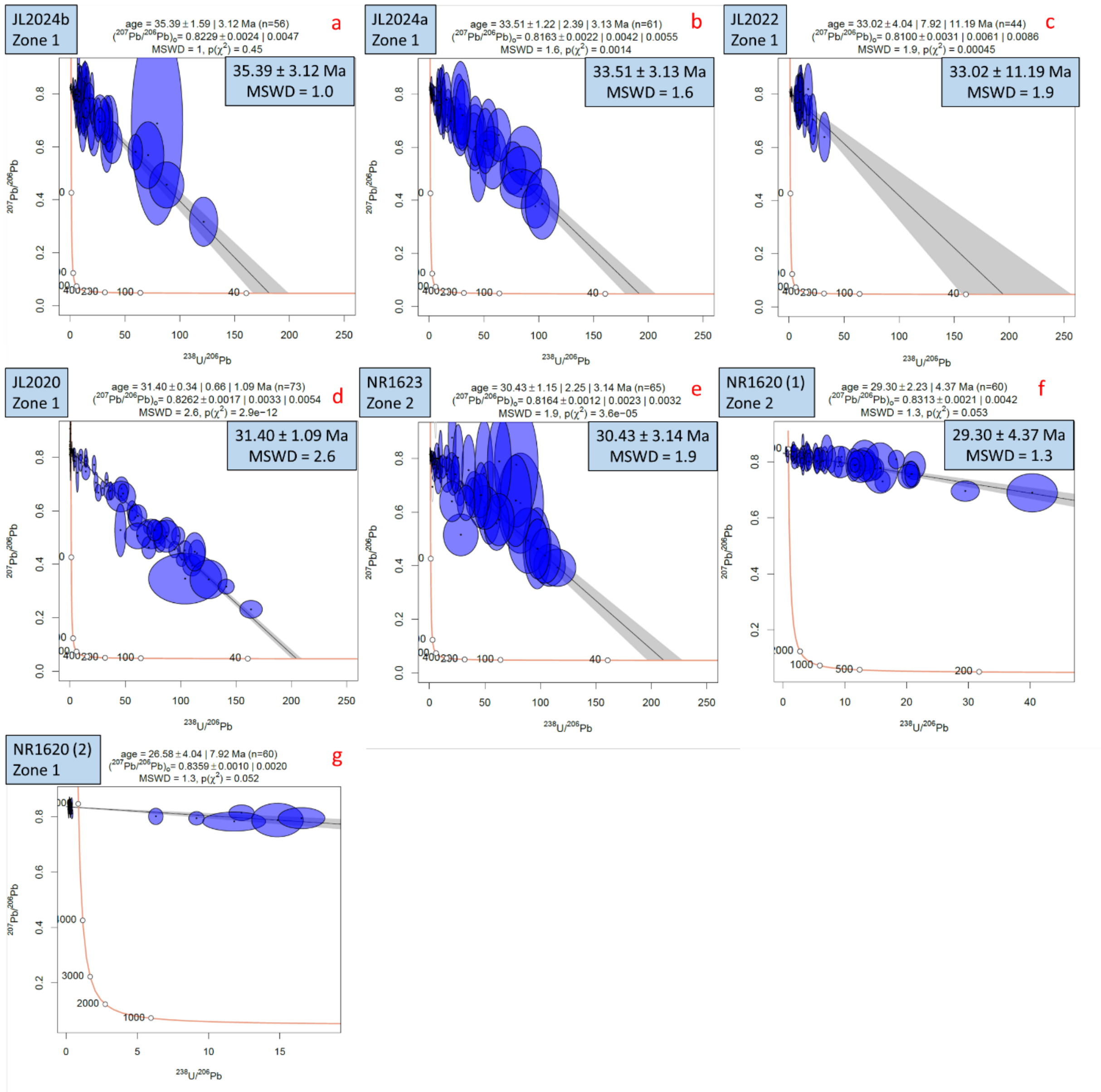


*Fig 4.16. Tera-Wasserburg (T-W) plots for calcite fills in conjugate faults from the Peak Fault. Images of samples not described in the text can be found in Appendix 8.1 & 8.2.*

Summary

While both samples summarised are predominantly composed of fibrous/bladed calcite that tracks vein opening, Figure 4.15 shows a contrast in their appearance with JL2024 highly asymmetric with many mudstone inclusions tracking progressive opening. While NR1620 is asymmetric as well, it is much cleaner with two distinct phases of fibres at an angle to the margins and perpendicular to the margins. Both samples track opening normal to fault plane and represent periods of quiescence, which are bracketed by fault movement. The samples are inferred to represent inter-slip periods i.e. periods of passive tensile opening bracketed by periods of fault movement with slickenline development. The samples therefore are good records quiescent periods during continued deformation and are termed post-kinematic as the calcite fill records periods of mineralisation post-dating fault related dilation. Veins not discussed here are shown and summarised in the Appendix 8.1 & 8.2. These veins show a combination of syn-kinematic and blocky fills with no kinematic indicators.

#### 4.3.1.3 Subvertical Veins

As discussed in Section 3.2.1, N-S $J_1$ Joints are frequently reactivated during displacements along nearby inclined normal faults (Figure 4.14). Three samples (NR1621, NR1622 & JL2023) of calcite fills from these $J_1$ joints are shown in Figure 4.17, whilst microstructural observations are summarised in Table 4.1. The three veins show highly variable microstructures and textures.

NR1622

NR1622 (Fig 4.17a) is a breccia fill along a reactivated $J_1$ joint and, similar to NR1621 (see below), has a single zone of blocky, syntaxial calcite. However, in contrast to NR1621, it preserves common, mostly randomly-oriented mudstone clasts which vary from <50µm to 0.5mm thick and large, 3mm long and 1mm thick clasts roughly aligned to the margins. The plane of growth is difficult to determine with significant brecciation of the host mudstones. Blocky calcite zones have clear syntaxial growth textures with crystal size increasing towards the centre of the vein. Large clasts show apparent boudinage (Fig 4.17b) and plucking apart suggesting gradual deformation during calcite growth. This texture is used to infer an implosion breccia fill, with large clasts becoming increasingly dislocated as the vein formed. The breccia texture ranges between vein fill and chaotic breccia with between 5% and 40% clasts supported in a calcite matrix. The presence of an implosion breccia texture is used to infer that calcite mineralisation was syn-kinematic with faulting as the opening direction of the vein is consistent with dilation due to reactivation caused by nearby normal fault movement.

Two ages have been achieved for the breccia fill of NR1622 (Fig 4.17c) of 30.2 ± 1.6Ma with an MSWD of 1.3 (Fig 4.18c) and 29.8 ± 3.9Ma with an MSWD of 2.8 (Fig 4.18d). These ages are very similar and overlap in uncertainty providing good constraint on the timing of brecciation and fracture dilation due to fault movement.

<u>NR1621</u>

NR1621 (Fig 4.15f) is a 5mm thick subvertical calcite vein with a single zone of blocky to bladed calcite spar with no clear median line. The growth texture in CL (Fig 4.17g) is difficult to determine and is likely ataxial. A thin selvage (100µm thick) is clearly shown under CL to mark the right-hand margin of the vein. The fill shows no obvious overprinting by later deformation or fluid-flow. Bladed calcite is utilised to infer rapid sealing of the fracture based on the imaging work by McNamara et al. (2016).

The blocky to bladed calcite of NR1621 (Fig 4.15g) has been dated at 31.1 ± 1.2Ma with an MSWD of 2.3 (Fig 4.18b). This puts an absolute age on crack-sealing providing a good constraint on fracture dilation.

<u>JL2023</u>

JL2023 (Fig 4.15h&i) shows two zones of calcite and is dominated by fibrous calcite growth (Zone 1; 4mm thick; Fig 4.17i) offsetting pulled-apart mudstone clasts. Calcite growth in Zone 1 (Fig 4.17i) is antitaxial with multiple, well-developed inclusion bands indicative of crack-seal.

Mudstone inclusion trails and fibres are shown in cross-polarised light (XPL; Fig 4.17i) to track the directions of growth which, whilst sinuous, are angled approximately perpendicular to the vein margins. The high roughness of the crack and additional inclusions gives confidence that the fibres track the opening direction. JL2023 has a thin external phase of blocky calcite (Zone 2; 200µm thick; Fig 4.17h) with no evidence of crack-seal textures such as inclusion bands. This sample likely reflects a change from crack-seal to crack-fill between Zone 1 and Zone 2 (Fig 4.17h).

A date has been achieved for Zone 1 of JL2023 (Fig 4.15h) of 38.9 ± 9.7Ma with an MSWD of 3.6 (Fig 4.18a). This age has a relatively large error but overlaps in uncertainty with other ages from subvertical veins.

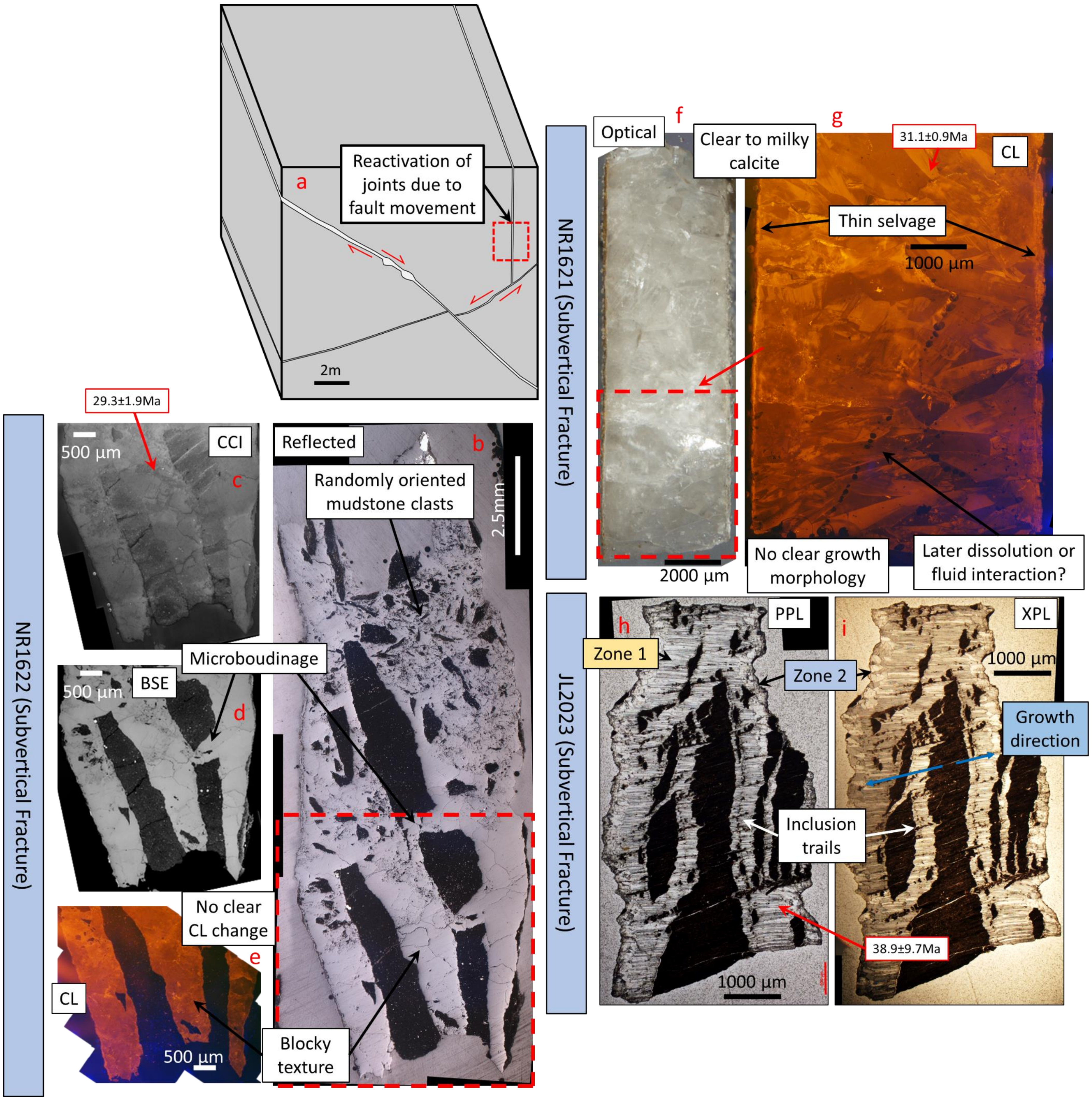


Fig 4.17. Microscopy from three calcite fills (b-i) in subvertical fractures with contrasting fill textures. a) Schematic diagram of calcite mineralised structures associated with conjugate fault sets at Ravenscar. NR1622 (b-e) is a breccia fill that varies between 5-40% clast fill. Dilation appears to be dominant, indicating an implosion breccia with chaotic or vein fill texture. NR1621 (f&g) is a blocky vein with little evident structure. JL2023 (h&i), in contrast, has a fibrous fill with external blocky calcite. Inclusion bands and trails follow the fibrous calcite crystals that track margin normal dilation.

Summary

JL2023 demonstrates clear evidence of calcite precipitation synchronous with crack dilation. No clear dilation direction is clear in NR1622, but systematic offsetting of larger clasts is indicative of implosion breccia development with brecciated mudstone clasts progressively entombed in calcite during repeated crack-seal associated with vein dilation. Bladed calcite in NR1621, observable in CL (Fig 4.17g) is used as evidence of primary calcite growth tracking crack opening based on the findings of the imaging work by McNamara et al. (2016).

The highlighted subvertical veins underwent reactivation due to displacement along the conjugate normal faults leading to dilation and precipitation of calcite. Thus, the dated calcite fills also give the age of associated local fault movements. The exact relationship between the three different fill types i.e. breccia, blocky and antitaxial fibrous not always absolutely clear, but could be related to local variations in stress magnitude, direction and/or pore fluid pressure during reactivation.

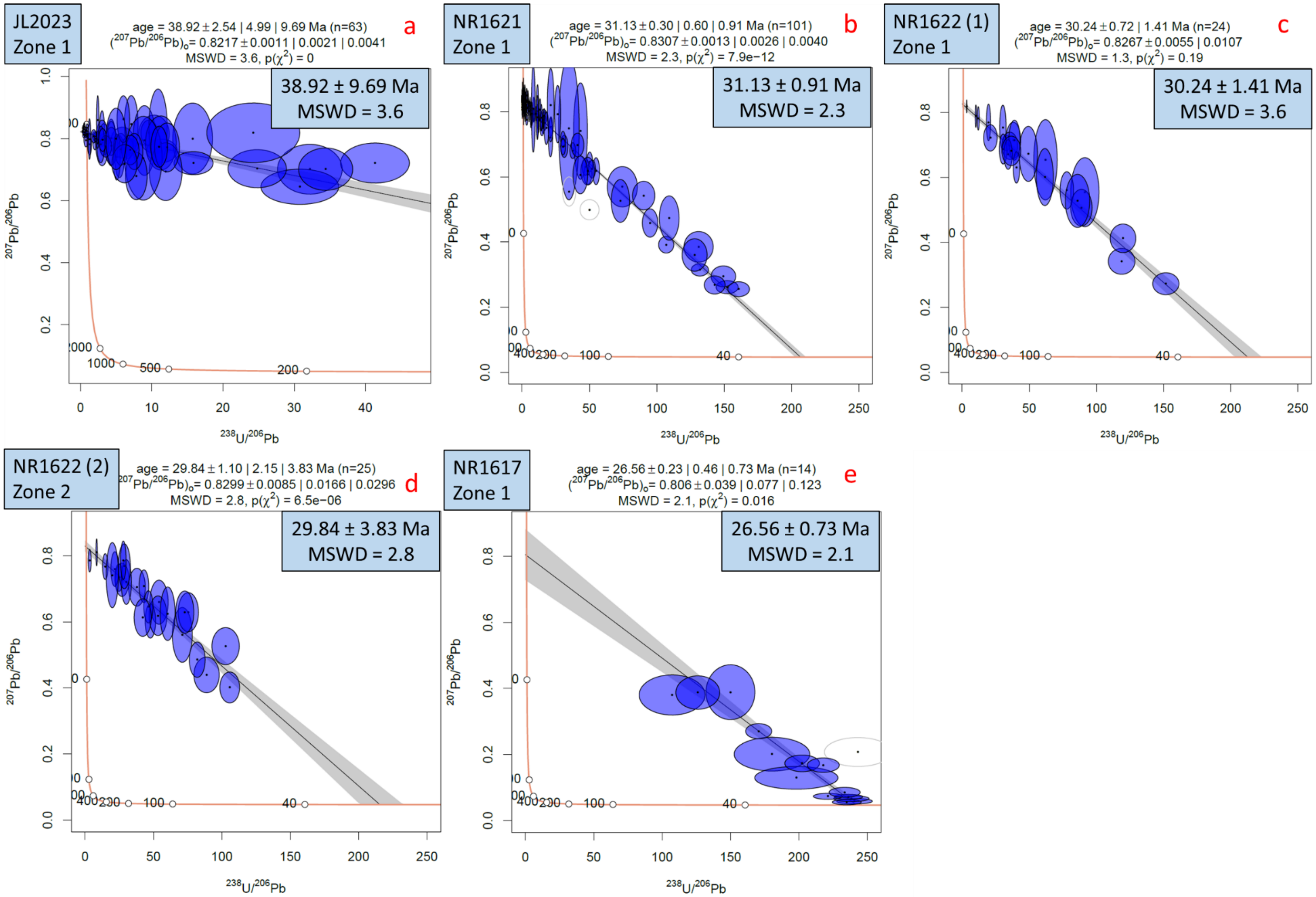


*Fig 4.18. T-W plots of four samples from subvertical veins associated with fault reactivation along the Peak Fault, Ravenscar.*

## 4.3.2 Cayton Bay and Red Cliff Faults

### 4.3.2.1 Cayton Bay Fault (Osgodby Nab)

The Cayton Bay Fault (Fig 4.19) is an NNE-SSW trending normal fault (Section 3.2.2.2) that forms a 1km wide graben structure with the Red Cliff Fault (Section 4.3.2.2).

Four samples have been taken from the Cayton Bay Fault (JL2030) and from reactivated joints (JL2026 & JL2027 are E-W striking and JL2029 N-S striking) in the wider damage zone of the fault. Microscopy for two samples (JL2026 & JL2030) is shown in Figure 4.20. JL2026 is representative of textures seen in the other subvertical calcite vein samples (JL2027 & JL2029).

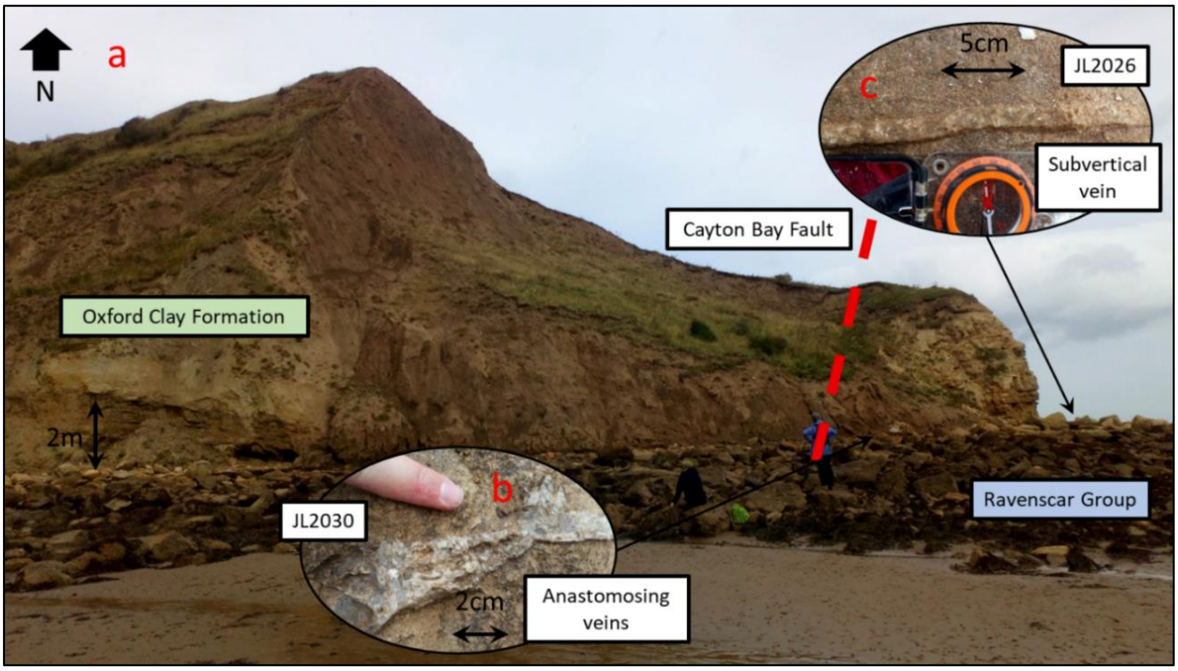


*Fig 4.19. Sectional view of Osgodby Nab (a) with samples JL2030 (b) and JL2026 (c) shown. JL2030 is a set of anastomosing calcite veins trending approximately N-S. JL2026 is an E-W striking, 2-3cm thick subvertical calcite vein. Fault movement is inferred to have reactivated N-S and E-W striking joints in this location similar to the Peak Fault at Ravenscar.*

| Sample | Zone | Main Structure | Minor Structure | UTM N | UTM E | Calcite Fill | Texture | Kinematics | Dating |
|---|---|---|---|---|---|---|---|---|---|
| JL2026 | 1 | Cayton Bay Fault | Vein - Vertical | 671580 | 6014911 | 2-3cm thick Vein | Blocky | Syn to Post kinematic | Y |
| JL2027 | 1 | Cayton Bay Fault | Vein - Vertical | 671564 | 6014970 | 2-3cm thick Vein | Blocky | Syn to Post kinematic | - |
| JL2029 | 1 | Cayton Bay Fault | Vein - Vertical | 671580 | 6014958 | 2-3cm thick Vein | Blocky | Syn to post kinematic | - |
| JL2030 | 1 | Cayton Bay Fault | Cayton Bay Fault | 671537 | 6014841 | Anastomosing Veins | Blocky | Syn to Post kinematic | Y |

*Table 4.2. Summary table of calcite fills from the Cayton Bay Fault at Osgodby Nab, Cayton Bay (Fig 4.1) analysed in this chapter. Samples not discussed here are presented in Appendix 8.1 & 8.2.*

<u>JL2026</u>

JL2026 (Fig 4.20a) is an E-W striking subvertical vein in a reactivated E-W joint cutting an ooidal limestone of the Ravenscar Group. It has a single fill (1cm thick) of blocky syntaxial calcite (Fig 4.20b). The sample shows no evidence of crack-sealing and is likely a crack-fill emplaced during or after crack opening.

The blocky calcite of JL2026 has been dated at 36.2 ± 3.7Ma with a high MWSD of 4.7 (Fig 4.23a). This date has a low error but a high MSWD suggesting that significant scatter exists in the data likely due to spurious data points or a second data population. However, microscopic analysis suggests the calcite is homogeneous, so this second option is considered unlikely.

<u>JL2030</u>

JL2030 (Fig 4.20c) was taken from the anastomosing calcite veins with an approximate N-S trend in the Cayton Bay Fault fault core and has large blocky calcite crystals (>1mm wide crystals; Fig 4.20c) with no clear evidence of growth or crack-seal textures (ataxial). In the field, cm-scale vugs are present, which support a hypothesis of crack-fill during, or after crack opening.

The blocky calcite of JL2030 (Fig 4.20d) has been dated at 32.9 ± 5.1Ma with an MSWD of 1.1 (Fig 4.23b) and this overlaps in uncertainty with JL2030 and provides a constraint on when fault-related voids along Cayton Bay Fault were open with fluid-flow leading to calcite mineralisation.

<u>Summary</u>

Both samples from JL2026 and JL2030 are crack-fill with no indications of crack-sealing or slip. As there is no field or microstructural evidence linking these fills to fault movement the fills are classified as syn- to post kinematic. The samples still record a phase of important fluid-flow and provide a constraint by which fault movement has caused dilation along the fault and related joints creating space for synchronous or subsequent calcite mineralisation. The samples are overlapping in age, which means they could relate to the same phase of fluid-flow and deformation. Isotopic analysis will attempt to identify whether the veins have similar carbon and oxygen isotopic values. The mineralisation of predominantly E-W joints at this location is anomalous and could represent a locally different stress regime, however, further work is required to constrain this further.

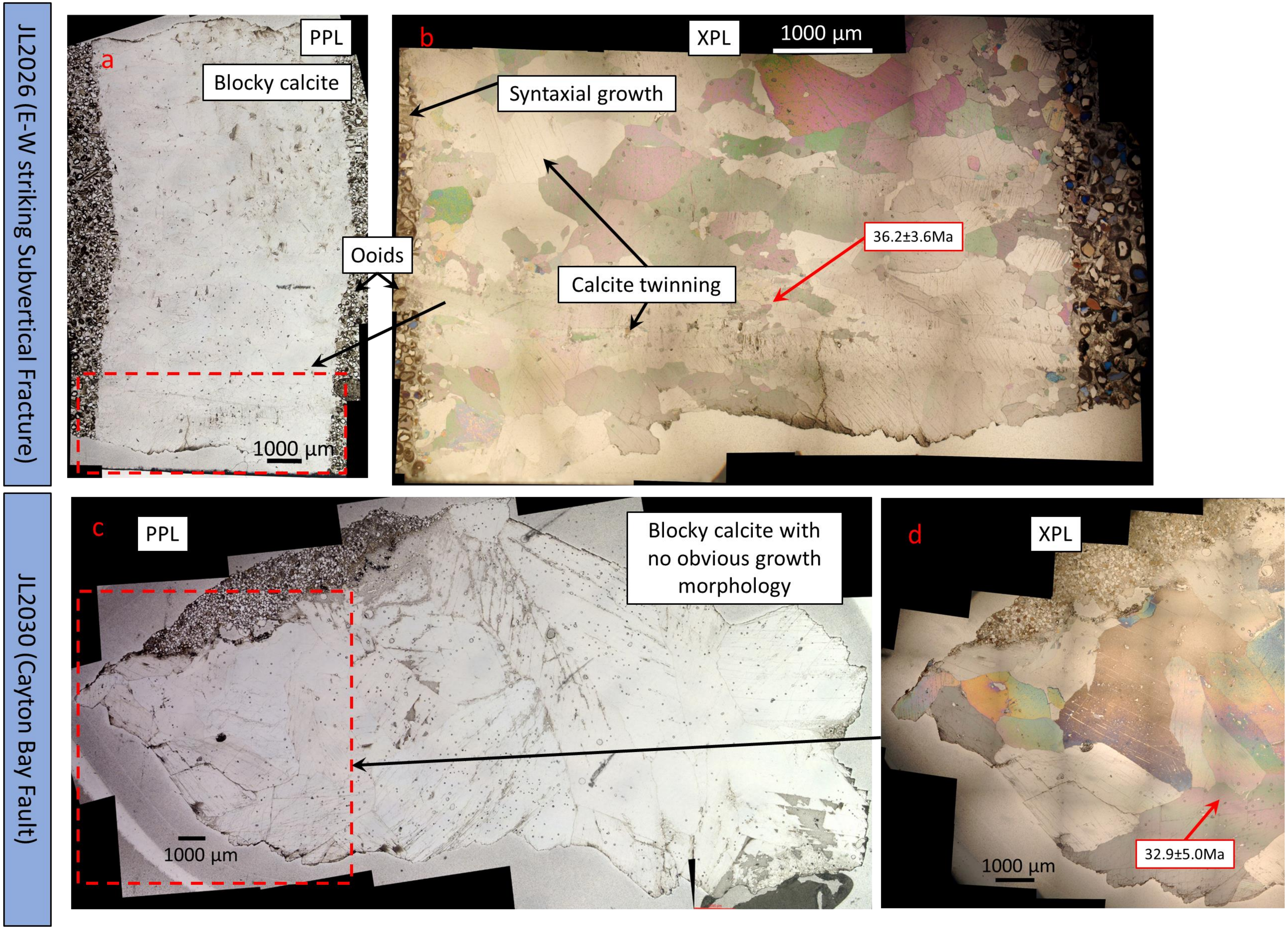


*Fig 4.20. Microscopy from two calcite fills (a-d) from the Cayton Bay Fault at Osgodby Nab. Both JL2026 (a&b) and JL2030 (c&d) are dominated by millimetre-scale blocky calcite with JL2026 showing an evident syntaxial growth morphology (b).*

### 4.3.2.2 Red Cliff Fault (High Red Cliff)

The Red Cliff Fault is a west-dipping fault (Fig 4.21) that forms the eastern boundary of the 1km wide graben structure with the Cayton Bay Fault. One sample (JL2033) was taken from extensional jogs along the main fault plane but has not yet been analysed due to administrative and laboratory issues during the COVID-19 pandemic. Two samples were taken from loose blocks in a recent mudslide shown in Figure 4.21 and are not in-situ so cannot be reliably used as kinematic indicators. One of these samples (JL2031) is discussed here (Fig 4.22).

| Sample | Zone | Main Structure | Minor Structure | UTM N | UTM E | Calcite Fill | Texture | Kinematics | Dating |
|---|---|---|---|---|---|---|---|---|---|
| JL2031 | 1 | Red Cliff Fault | Unknown | 673110 | 6013607 | Cone-in-cone | - | Unknown | Y |
| JL2032 | 1 | Red Cliff Fault | Unknown | 673108 | 6013588 | Blocky calcite | Blocky | Unknown | Y |

*Table 4.3. Summary table of calcite fills from the Red Cliff Fault at High Red Cliff, Cayton Bay (Fig 4.1) analysed in this chapter. Samples not discussed here are presented in Appendix 8.1 & 8.2.*

JL2031 is a 7cm thick sample of bladed calcite (Fig 4.22). That was sampled from the mudflow (Fig 4.21).

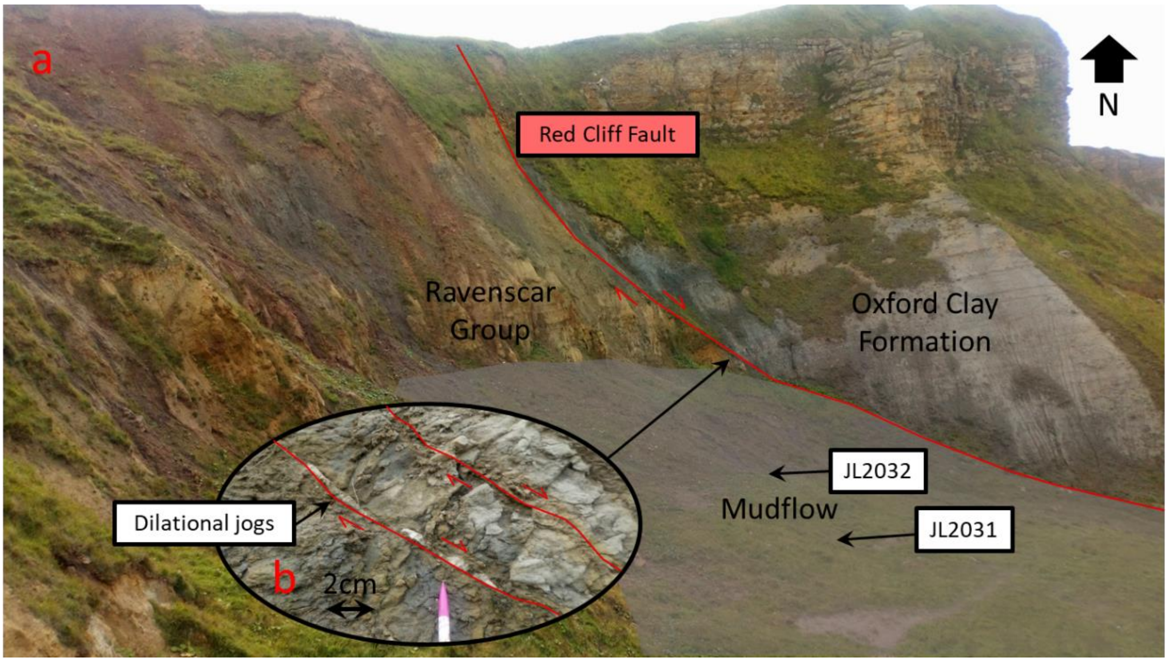


*Fig 4.21. Sectional view of the Red Cliff Fault with the locations of samples JL2032 and JL2031 indicated in the recent mudflow.*

Bladed calcite has been dated at 46.5 ± 2.2 with an MSWD of 1.6 (Fig 4.20c) with an additional fill of blocky calcite (JL2032) included in Appendix 8.1 and dated at 55.0 ± 2.2 with an MSWD of 0.9 (Fig 4.23d). These suggest fluid-flow near the fault during the Palaeocene but cannot be used to make any direct learnings about fault kinematics.

JL2031 (High Red Cliff)

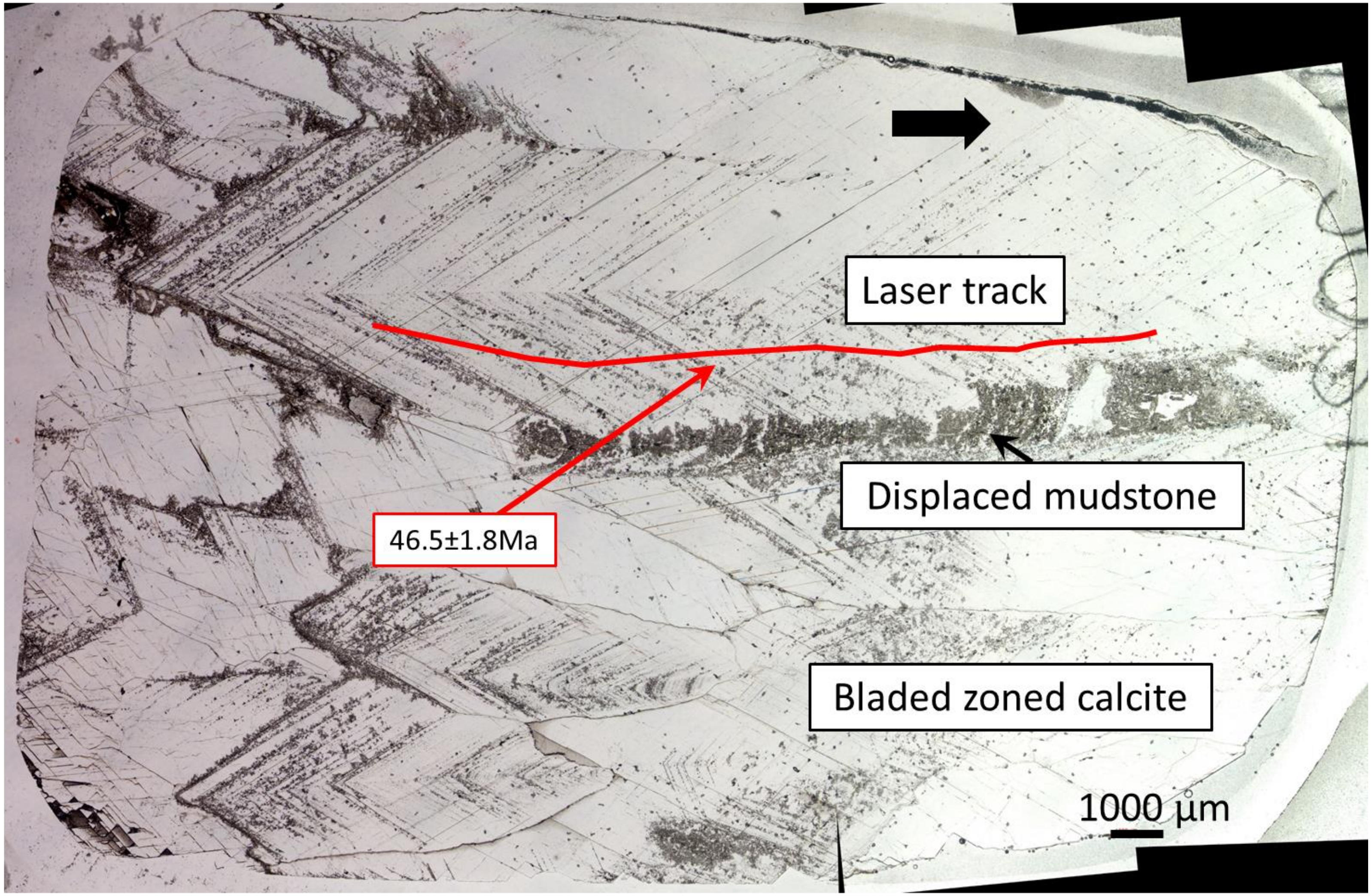


*Fig 4.22. A PPL image of bladed structures from sample JL2031 found not in-situ below the Red Cliff Fault.*

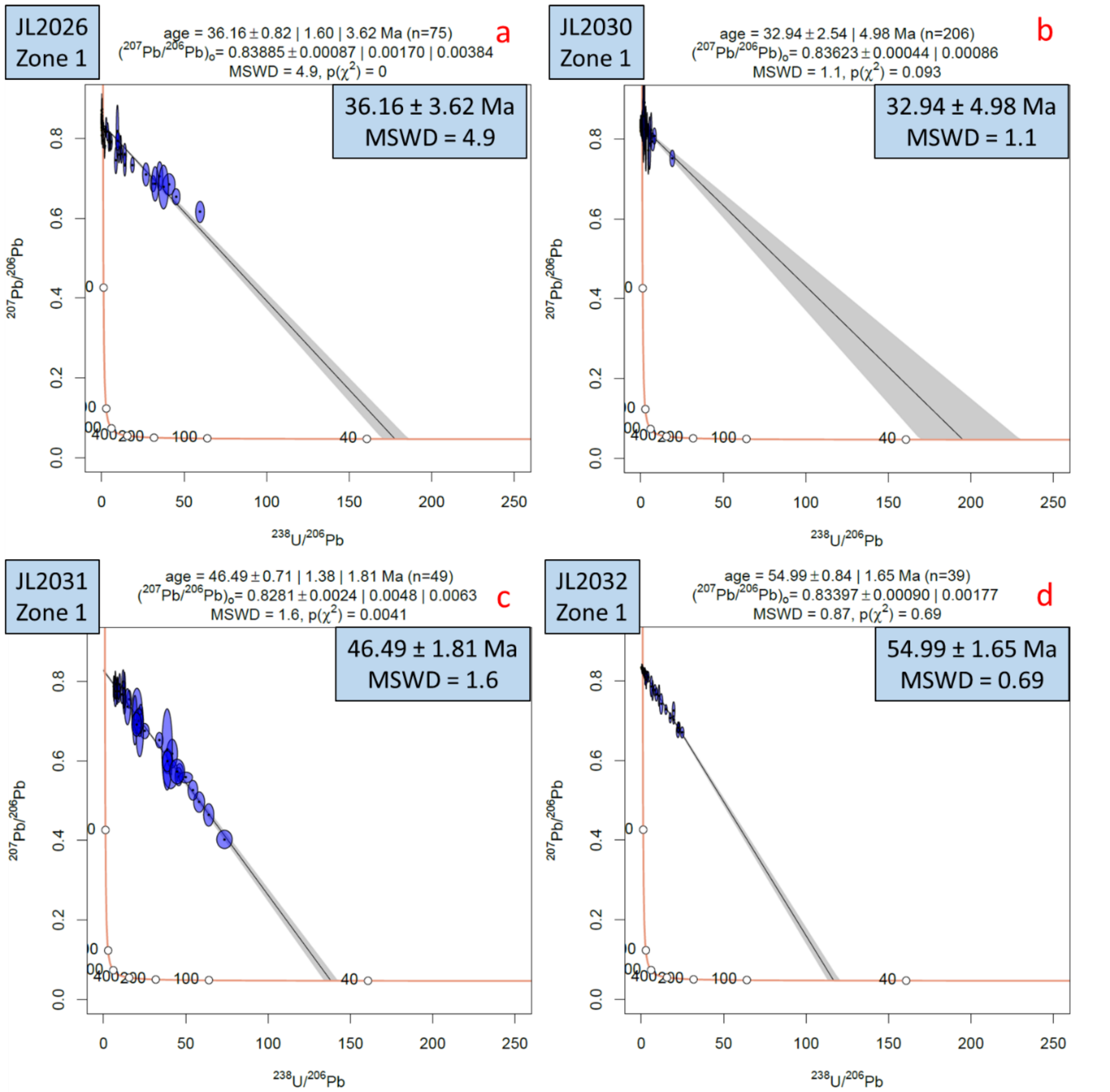


*Fig 4.23. T-W plots for U-Pb calcite ages from the Cayton Bay and Red Cliff faults. JL2032 is not discussed here but can be found in Appendix 8.1 & 8.2.*

### 4.3.3 Summary of Peak Trough Microstructures

A variety of textures (Table 4.1) have been observed from a wide set of structures at Ravenscar (Peak Fault), Osgodby Nab (Cayton Bay Fault) and High Red Cliff (Red Cliff Fault).

Microstructural textures that track vein or fill opening have been utilised in combination with field relations described in Chapter 3 to determine the relationship of calcite mineralisation to fault movement. The full microstructural results are tabulated in Appendix 8.2.

The samples analysed represent a wide range of subvertical veins, extensional jogs and fault plane fills with a mixture of fibrous, bladed and blocky calcite mineralisation. The veins sampled from the Peak Fault at Ravenscar show a wide range of pre-, syn- and post-kinematic mineralisation (Fig 4.24). NR1623 and NR1622 reflect syn-kinematic calcite precipitation while many other samples include calcite fills that precipitated either during or after fault movement (coloured red in Fig 4.24). These fills still help to indicate a period by which extension was occurring with additional post-kinematic calcite (NR1620) helping to provide information on periods at which faulting had finished or was quiescent.

The Cayton Bay Fault shows no signs of syn-kinematic mineralisation but dating of calcite fills still places important constraints on the timing by which regional deformation had occurred and at which fluid-flow occurred. The Red Cliff Fault samples, in contrast, were not sampled in situ so prevent any firm deductions to be made but are suggestive of an early phase of fluid-flow associated with the fault.

Calcite U-Pb geochronology has provided a wide range of ages for the Peak Trough Faults (Fig 4.24) with date ranges from 38.9 to 26.6Ma for the Peak Fault itself, 36.2 to 32.9Ma for the Cayton Bay Fault and 55.0 to 46.5Ma for the samples (not in-situ) near to the Red Cliff Fault. These data suggest a long period of activity for the Peak Trough and associated larger faults. This likely also accounts for the quite diverse range of growth textures and local relative timing relationships to faulting. The exact length of fault movement is difficult to constrain but Table 4.2 utilises the U-Pb results with and without uncertainties to describe minimum and maximum windows described by the data. This window of fault movement likely reflects a period over which local fault movements occurred as part of a wider picture of regional E-W extensional. The implications of these data are discussed further in Section 4.6.

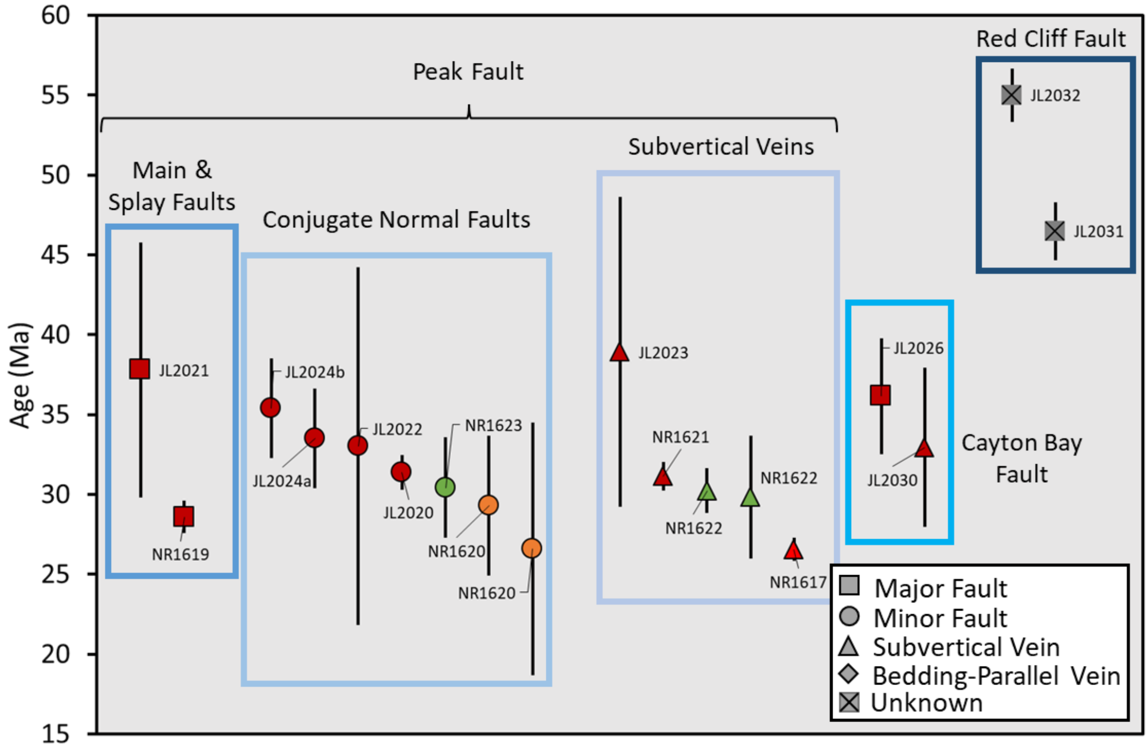


*Fig 4.24. Plot of U-Pb calcite geochronology results from the Peak Trough samples versus Time/Age (Ma) with the symbols organised by the structure type. Green - syn-kinematic, Red - syn- to post-kinematic, Orange – post-kinematic and Grey - unknown.*

| | All | Peak Fault | Cayton Bay Fault | Red Cliff Fault |
|---|---|---|---|---|
| **Dates difference (Ma)** | **28.4** | **12.3** | **3.2** | **8.5** |
| **Max Activity (Ma)** | **38.0** | **30.0** | **11.8** | **12.0** |
| **Min Activity (Ma)** | **26.1** | **5.0** | **-** | **5.0** |
| **Overlap in ages (Ma)** | **-** | **-** | **5.4** | **-** |

*Table 4.4. Compilation of the different age separations for the Peak Trough Faults based on U-Pb calcite geochronology results with the Dates difference – the difference between the maximum and minimum date without uncertainty (2s), Maximum activity – the maximum period the structures could be active i.e. the maximum difference between the maximum age and minimum age including uncertainty, Minimum activity – the minimum period the structures are indicated to be active i.e. the minimum difference between the maximum age and minimum age including uncertainty. In some cases, there will not be separation between a set of ages for a structure in which case the overlap in ages is also stated.*

## 4.4 Meso-Scale Faults

"Meso-scale faults", with along-strike lengths running onshore up to 10 km, cross-cut the Early Jurassic stratigraphy of the northern Cleveland Basin in a number of locations (Milsom & Rawson, 1989 and 1:25,000 BGS geological mapping – BGS, 2022). The faults outlined in Section 3.2.3 range in scale from the Runswick Bay Fault (~10km length; BGS, 2022) down the local scale structures at Staithes which are suggested by the 1:25,000 BGS geological maps (BGS, 2022) to be related to a 1.5km long fault at Jet Wyke (NZ 792 187). No fault is indicated on the BGS 1:25,000 map, but the Port Mulgrave Fault can be traced on aerial photography for at least half a kilometre and is likely of a similar length to the fault exposed at Jet Wyke.

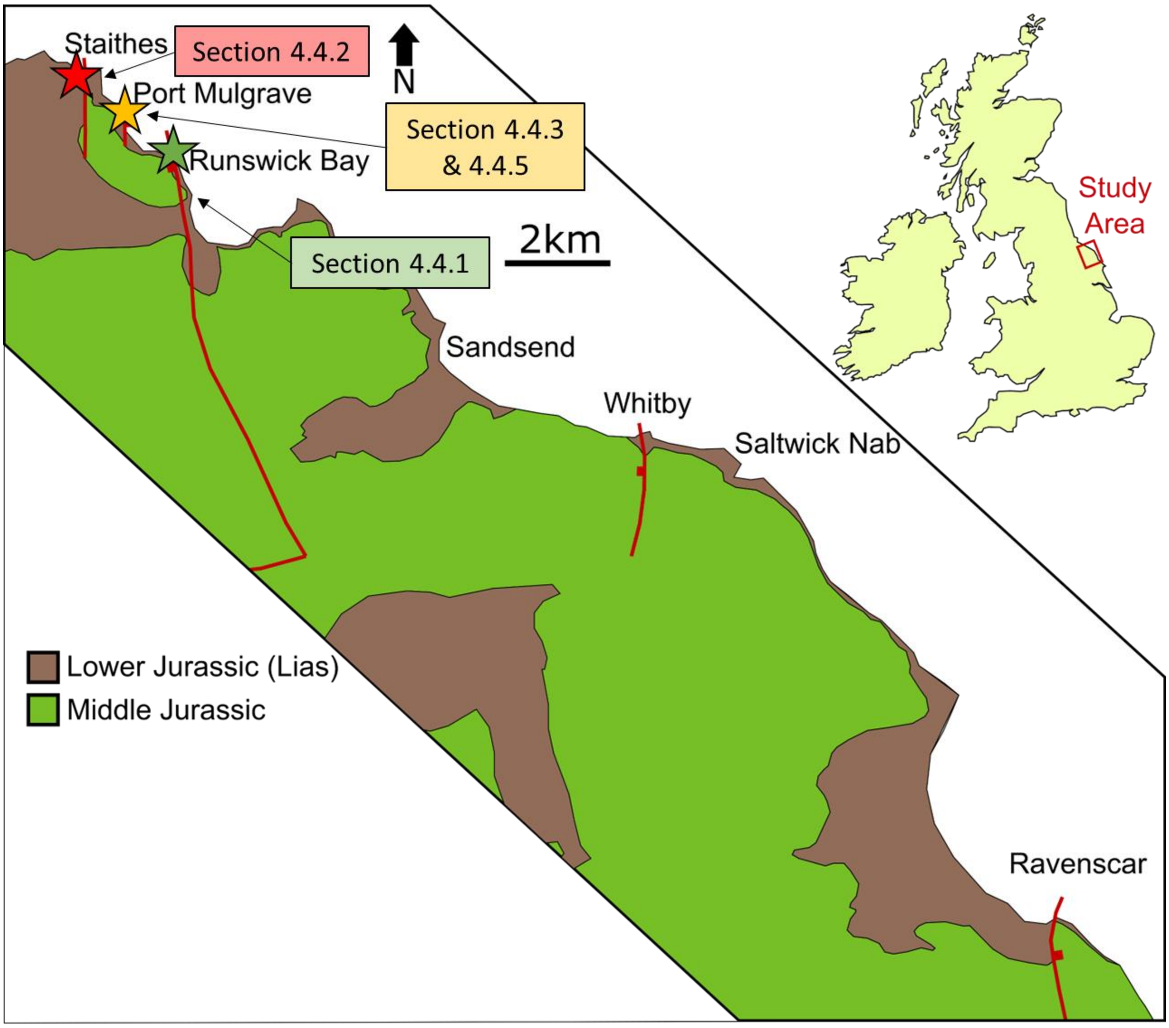


*Fig 4.25. Structural Map detailing the locations of the Meso-scale fault zones including the Runswick Bay Fault Zone, Staithes Fault Zone, Port Mulgrave Fault Zone and the zone of oblique-slip faulting at Port Mulgrave.*

## 4.4.1 Runswick Bay Fault Zone (Runswick Bay)

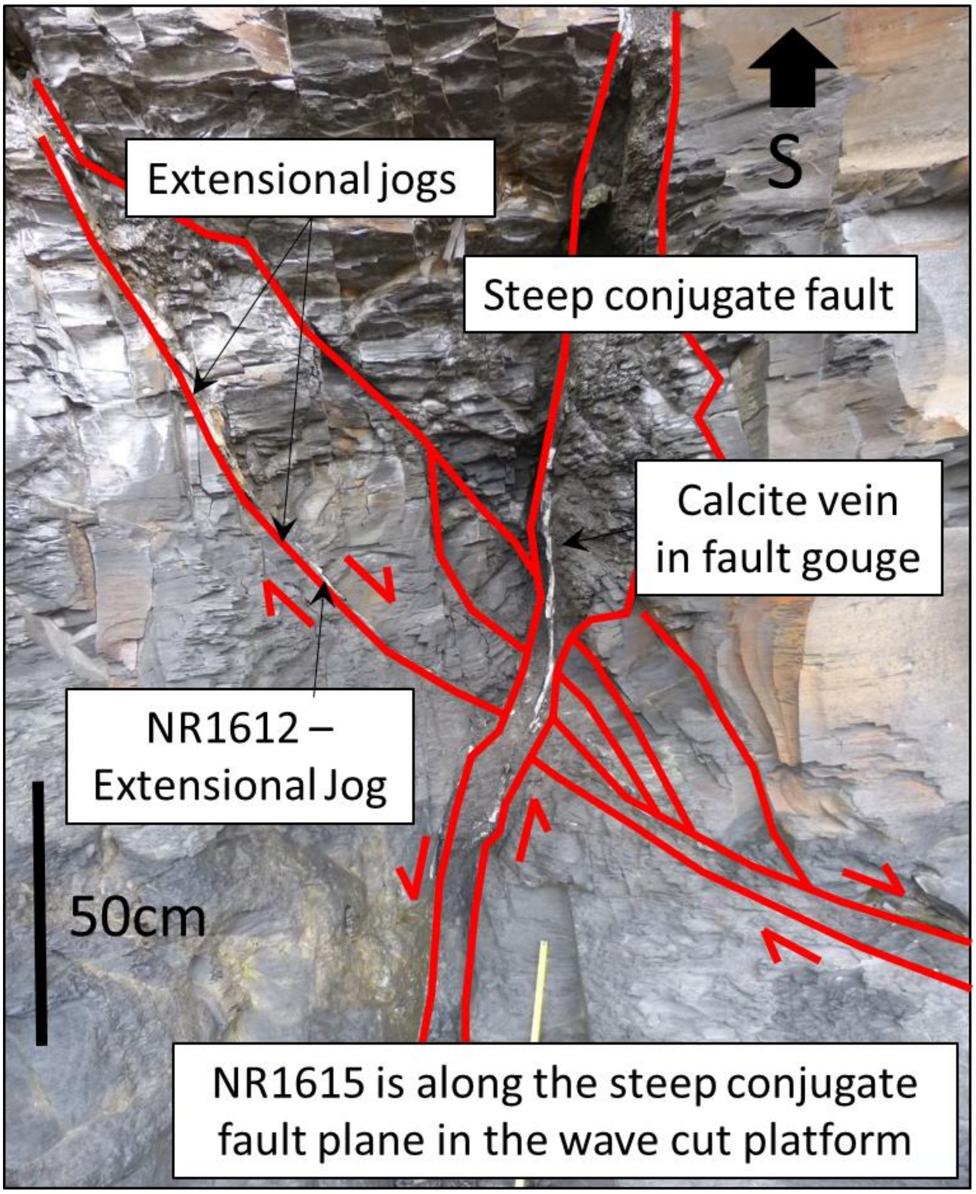


*Fig 4.26. Sectional view of the Runswick Bay Fault with the main listric fault plane dipping west with a steep east dipping conjugate developed. NR1612 is an extensional jog along the main fault with NR1615, a weathered fill, on the steep conjugate fault in the wave cut platform.*

The Runswick Bay Fault (Fig 4.25) is an N-S to NW-SE trending normal fault exposed in the cliff and wavecut platform north of the coastal village of Runswick Bay (Section 3.2.3.1). Four samples were taken from the Runswick Bay fault of which two representative samples (NR1612 & NR1615) are highlighted here for discussion. NR1612 comes from an extensional jog that was sampled from a listric N-S striking fault plane (Fig. 4.26) dipping 50° to the west with down plunge slickenlines. NR1615 comes from a subvertical fault in the wavecut platform. The fill is likely to be a breccia fill or extensional jog but the exact form is difficult to tell due to the effects of recent erosional processes. Additional microstructural information from JL2010 (extensional jog in a ramp-flat fault; Section 3.2.3.1) and JL2012, a thin (0.4mm wide) subvertical blocky vein in a $J_1$ joint reactivated in a similar manner to those shown in Figure 4.14 are summarised in Table 4.3 with full microstructures detailed in Appendix 8.2 with imaging shown in Appendix 8.1.

| Sample | Zone | Main Structure | Minor Structure | UTM N | UTM E | Calcite Fill | Texture | Kinematics | Dating |
|---|---|---|---|---|---|---|---|---|---|
| NR1615 | 1 | Runswick Bay Fault Zone | Main Fault | 645420 | 6046223 | Breccia + Jog | Blocky | Syn-kinematic | Y |
| NR1612 | 1 | Runswick Bay Fault Zone | Fault - Normal | 645370 | 6046175 | Extensional Jog | Blocky | Syn to post kinematic | Y |
| JL2010 | 1 | Runswick Bay Fault Zone | Fault - Normal | 645727 | 6045194 | Extensional Jog | Blocky | Syn-kinematic | - |
| JL2012 | 1 | Runswick Bay Fault Zone | Vein - Vertical | 645758 | 6045157 | 0.5mm thick Vein | Fibrous | Syn to post kinematic | - |

*Table 4.5. Summary table of calcite fills from the Runswick Bay Fault Zone at Runswick Bay (Fig 4.25) analysed in this chapter. Samples not discussed here are presented in Appendix 8.1 & 8.2.*

<u>NR1612</u>

NR1612 has a blocky ataxial calcite fill (Fig 4.27a; left hand side) with infrequent inclusion bands of host mudstone suggestive of intermittent crack-seal. No obvious growth plane is evident, but the calcite fill does not appear to have been overprinted as inclusion bands are preserved.

NR1612 has a highly variable clast distribution, with the lower part of the jog characterised by up 70% mudstone clasts with 2-5° rotation set in a calcite matrix (mosaic implosion breccia), with a sheared mudstone texture at the base of the sample (Fig 4.27a). This shear texture shows clear normal fault movement with synchronous calcite cementation of sheared mudstone fragments. The sheared mudstone clasts in combination with implosion breccia textures and field geometry is used to infer syn-kinematic calcite mineralisation.

Blocky calcite of NR1612 has been dated at 32.8 ± 2.1 with an MSWD of 4.6 (Fig 4.27a) and provided a good constraint on brecciation and kinematic movement.

<u>NR1615</u>

NR1615 is a breccia fill and is inferred to be located along the main trace of the Runswick Bay Fault shown in Figure 4.26.

NR1615 has a blocky implosion breccia texture with 10-15% large >1mm clasts and 5-10% vugs. No localised growth plane is obvious, and the samples is interpreted to have a crack-fill texture with <1% volume pore space preserved (Fig 4.27d).

NR1612 has preserved crack-seal textures and shows no clear indications as to whether mineralisation was synchronous with fault slip or postdates fault movements. This fill is therefore inferred to reflect to syn- to post-kinematic precipitation of calcite, while NR1615, in contrast, has no evident crack-seal textures, however, evidence of an implosion breccia texture means that the sample is characterised as syn-kinematic.

The breccia fill from NR1615 has a very similar age (32.3 ± 1.4 with an MSWD of 2.6; Fig 4.28b) to that from NR1612 suggesting that they likely relate to a similar phase of fault movement, mineralisation and fluid flow.

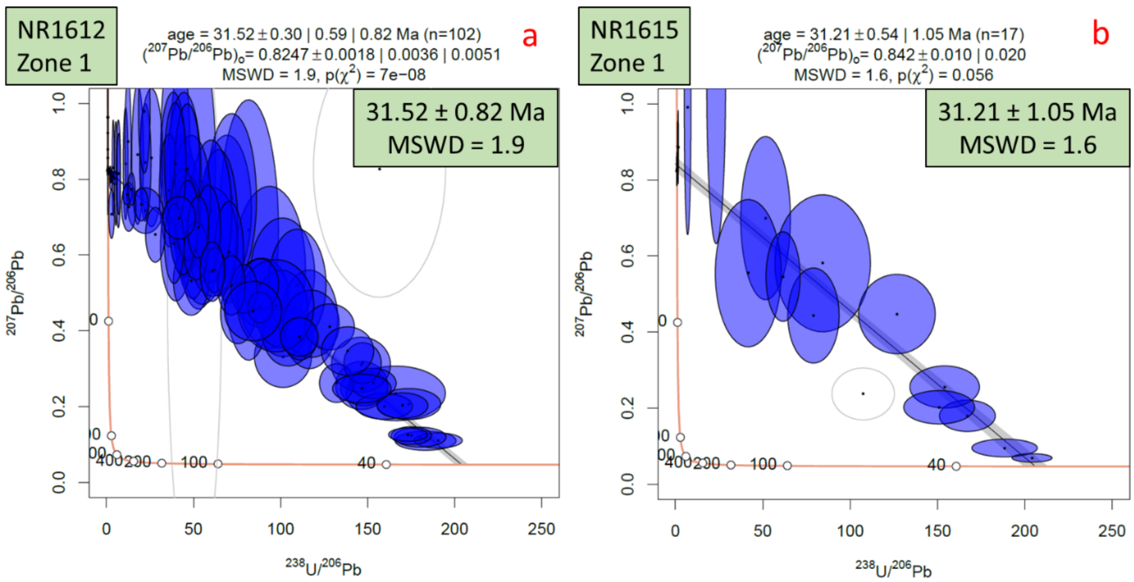


*Fig 4.28.T-W plots for U-Pb calcite ages from Runswick Bay Fault Zone.*

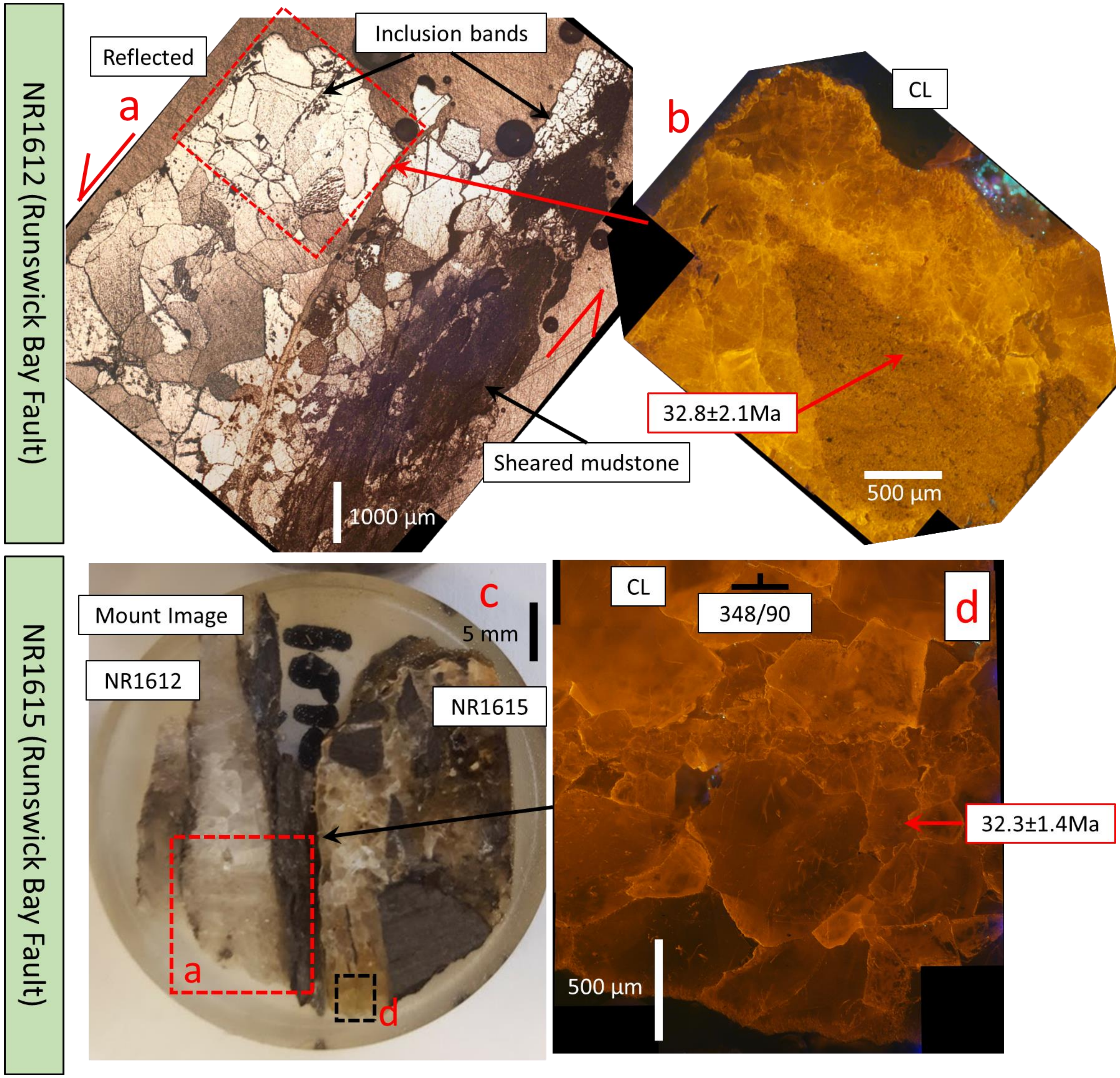


*Fig 4.27. Microscopy images from NR1612 and NR1615 from the Runswick Bay Fault. Both samples have typically blocky textures with NR1615 appearing to be an implosion breccia with irregularly sized clasts oriented in a blocky calcite matrix with no obvious growth texture. NR1612, in addition to breccia textures, has margin parallel inclusion bands suggesting possible sealing. The lower margin is characterised by sheared mudstone clasts and might represent early gouge development with cementation. This zone has common inclusion bands indicative of crack-seal textures, which appear to die out upwards.*

### 4.4.2 Staithes Fault Zone

A series of N-S striking normal faults (Fig 4.28) cross-cut the Staithes Sandstone and Cleveland Ironstone formations between Staithes Harbour and Old Nab (Section 3.2.3.2) and form what is termed here the Staithes Fault Zone. The faults have metre-scale throws and die out upwards (over 10-20 m) in the cliff face. The faults are grouped into two sets forming conjugate structures with east dipping faults (40° to 80°) and steeper westward dipping structures with dips between 75° and 90°; collectively these commonly form ~20m wide graben structures (Fig. 4.29).

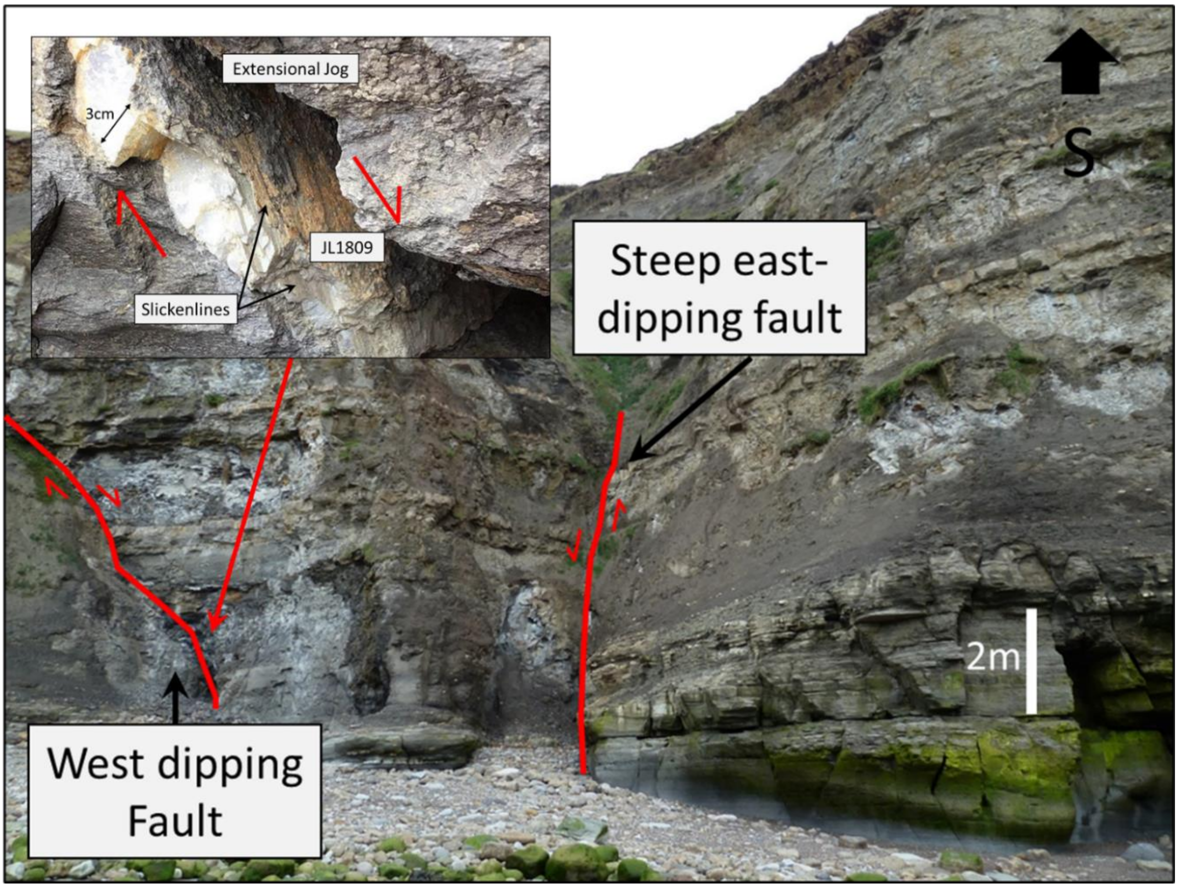


*Fig 4.29. A sectional view of normal conjugate faults in a small graben structure near Staithes. An inset shows sample JL1809, which is an excellent example of an extensional jog structures with down plunge slickenlines.*

| Sample | Zone | Main Structure | Minor Structure | UTM N | UTM E | Calcite Fill | Texture | Kinematics | Dating |
|---|---|---|---|---|---|---|---|---|---|
| NR1501 | 1 | Staithes Fault Zone | Fault - Normal | 643061 | 6047936 | Calcite in Gouge | Blocky | Pre-kinematic | Y |
| NR1602 | 1 | Staithes Fault Zone | Fault - Normal | 643296 | 6048179 | Calcite in Gouge | Blocky | Pre-kinematic | Y |
| NR1603 | 1 | Staithes Fault Zone | Fault - Normal | 643294 | 6048169 | 6-7mm vein along fault | Blocky | Syn-kinematic | Y |
| NR1604 | 1 | Staithes Fault Zone | Fault - Normal | 643294 | 6048169 | Thin vein/jog | Blocky | Syn to post kinematic | Y |
| JL1809 | 1 | Staithes Fault Zone | Fault - Normal | 643209 | 6047954 | Extensional Jog | Blocky | Syn-kinematic | - |
| - | 2 | - | - | - | - | - | Blocky | Syn-kinematic | Y |
| - | 3 | - | - | - | - | - | Blocky | Syn-kinematic | Y |
| NR1503 | 1 | Staithes Fault Zone | Vein - Vertical | 643565 | 6047800 | 0.5cm thick vein | Blocky | Syn to post kinematic | - |
| - | 2 | - | - | - | - | - | Blocky | Syn to post kinematic | - |
| - | 3 | - | - | - | - | - | Blocky | Syn to post kinematic | Y |

*Table 4.6. Summary table of calcite fills from the Staithes Fault Zone at Staithes (Fig 4.25) analysed in this chapter. Samples not discussed here are presented in Appendix 8.1 & 8.2.*

NR1503 (subvertical vein) and JL1809 (extensional jog; Fig 4.29) are sampled from normal faults in the vicinity of Staithes harbour with seven additional samples summarised in Table 4.3. Both samples (Fig 4.30) have blocky macroscopic calcite and appear to be composite multiple calcite veins each of which is separated by distinct planes oriented subparallel to the fill margins.

NR1503

NR1503 is a subvertical vein along a reactivated $J_1$ joint and is composed of three generations (Zones 1-3 from upper right to bottom left on Fig 4.30a) of optically clear calcite with a large vein on the left of Figure 4.30a (~2000µm thick) and thinner veins (~200µm thick) at the upper margin. The zones have apparent syntaxial structures with the boundary between Zone 1 and 2 displaying stylolitic textures indicative of dissolution along the planes. Zone 1 has inclusion bands suggestive of crack-seal. Crack-seal textures are not evident in other zones potentially due to a change from crack-seal to crack-fill over time.

The blocky syntaxial calcite of Zone 1 from NR1503 has been dated at 31.4 ± 3.6Ma with an MSWD of 1.7 (Fig 4.31g). The relative age of calcite zones is difficult to determine with no definitive evidence of relative ages identified in Figure 26a&b. In addition, no clear evidence is observed that records the vein's relationship to fault movement and therefore the fill is considered to be synchronous with, or postdating fault movement.

JL1809

JL1809 is also a composite vein (200-5000µm thick) with three zones (Fig 4.30c) separated by highly irregular boundaries. These boundaries appear to truncate underlying zones of calcite which is suggestive of stylotisation along pre-existing shear planes. Mudstone clasts of variable size (<50µm to 2000µm) are suspended in a blocky calcite matrix (0-40%) and suggest an implosion breccia (syn-kinematic) with fault vein to chaotic breccia textures based on the classification scheme by Mort & Woodcock (2008). JL1809 in the field shows a clear extensional jog structure with down stepping textures on multiple planes with slickenfibres consistent with syn-kinematic calcite precipitation.

Truncating relationships suggest that Zone 1 was formed first with later shear leading to truncation and precipitation of Zone 2 and then Zone 3 subsequently. The blocky calcite of Zone 2 in JL1809 has been U-Pb calcite dated at 25.2 ± 6.2Ma with an MSWD of 0.87 (Fig 4.31h) and at 23.3 ± 6.1Ma with an MSWD of 1.5 (Fig 4.31h). Additionally Zone 3 has been dated at 36.1 ± 6.2Ma with an MSWD of 1.7 (Fig 4.31b) and 31.4 ± 6.1Ma with as MSWD of

1.8 (Fig 4.31c). U-Pb calcite dates achieved are consistent with the relative ages assigned and suggest a significant age gap between Zone 1 & 2 and Zone 3.

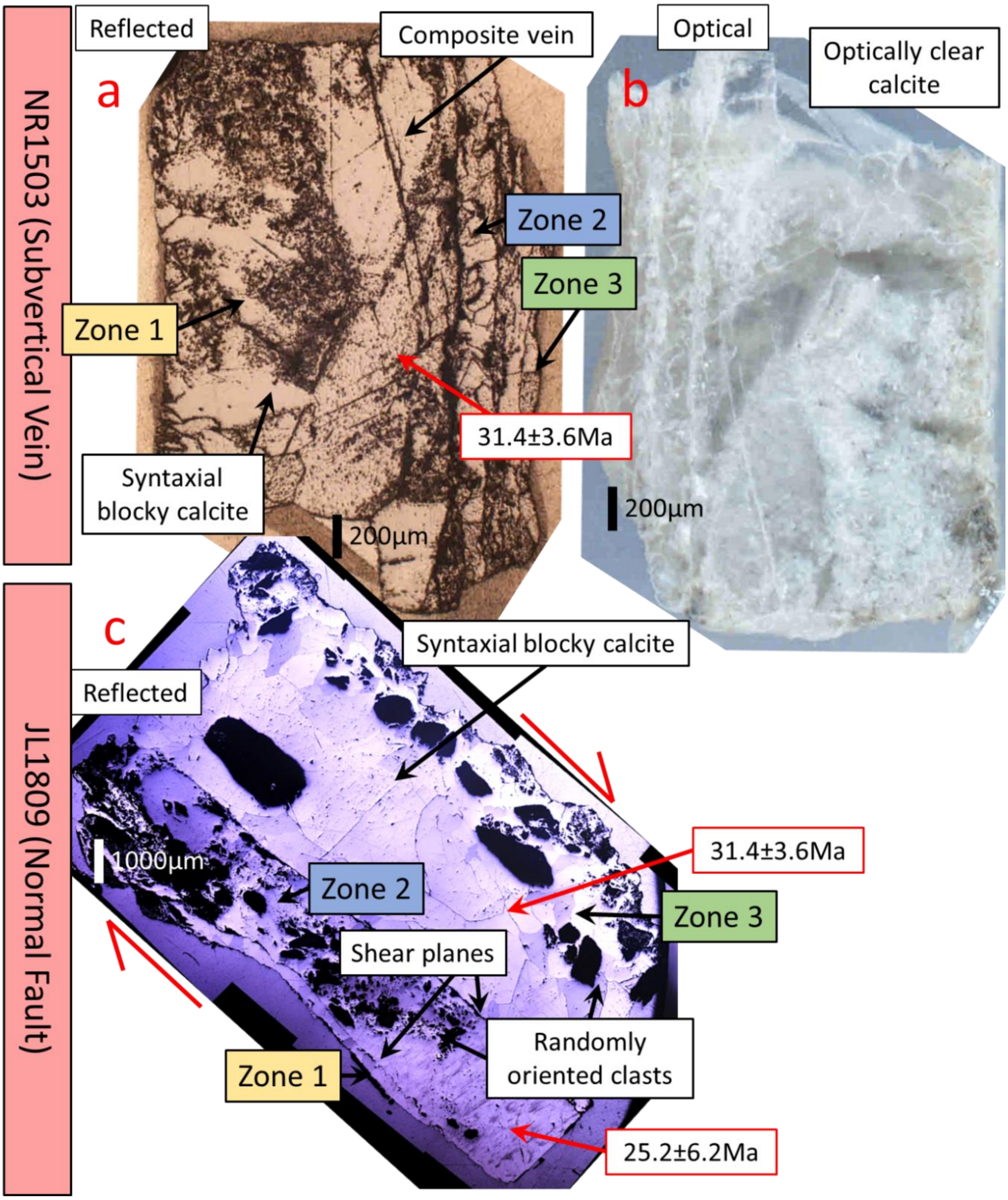


*Fig 4.30. Microscopy images of samples NR1503 and JL1809 from normal faults outcropping at Staithes. Both samples have blocky textures. NR1503 is composed of multiple clean blocky zones whilst JL1809 contains multiple zones with variable mudstone clasts.*

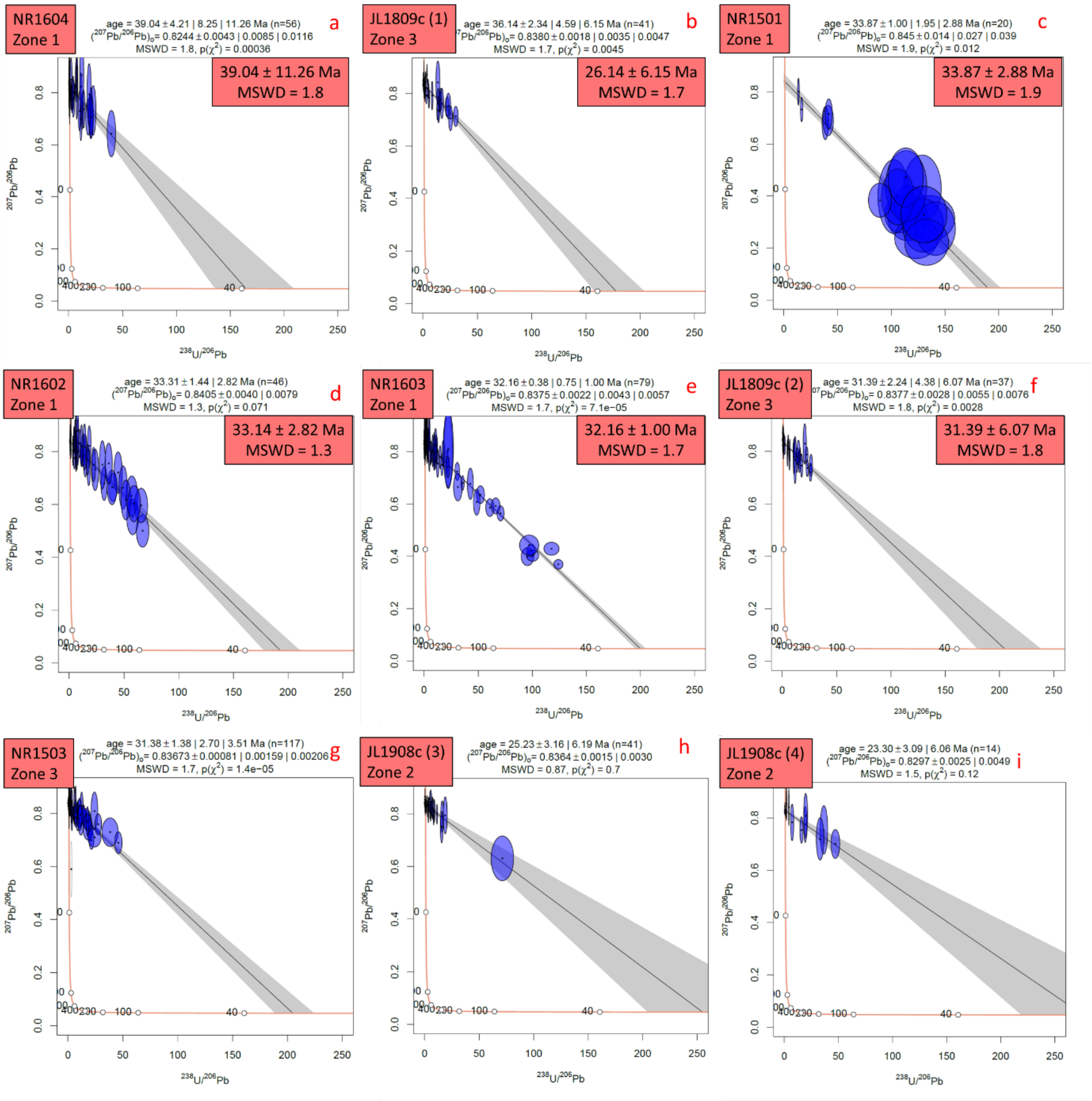


*Fig 4.31. T-W plots from the Staithes Fault Zone.*

### 4.4.3 Port Mulgrave Fault Zone

The Port Mulgrave Fault Zone has not been included previously in mapping by the British Geological Survey (BGS, 2022) but can be traced on aerial photography. The fault is a composite structure composed of multiple west-dipping fault planes, one of which is shown in Fig 4.25. Extensional jogs are developed along the normal fault and duplex structures (JL2001, JL2016, JL2017, NR1504 & NR1505) with local reactivation of bedding (JL2002) and pre-existing $J_1$ joints (NR1609) in associated fault damage zones.

Three samples (NR1609, NR1504 & NR1505) are detailed here from the area of Port Mulgrave Headland (NZ 799 159) and two samples (JL2001 & JL2016) from exposures at Port Mulgrave beach (NZ 798 175).

| Sample | Zone | Main Structure | Minor Structure | UTM N | UTM E | Calcite Fill | Texture | Kinematics | Dating |
|---|---|---|---|---|---|---|---|---|---|
| JL2017 | 1 | Port Mulgrave Fault Zone | Fault - Normal | 644445 | 6046552 | Extensional Jog | Fibrous | Pre-kinematic | - |
| - | 2 | - | - | - | - | - | Blocky | Syn to post kinematic | Y |
| NR1504 | 1 | Port Mulgrave Fault Zone | Fault - Normal | 644433 | 6046965 | Extensional Jog | Blocky | Syn to post kinematic | Y |
| NR1505 | 1 | Port Mulgrave Fault Zone | Fault - Normal | 644433 | 6046965 | Extensional Jog | Blocky | Syn to post kinematic | Y |
| JL2016 | 1 | Port Mulgrave Fault Zone | Fault - Normal | 644448 | 6046559 | Extensional Jog | Fibrous | Pre-kinematic | Y |
| JL2001 | 1 | Port Mulgrave Fault Zone | Imbricate Zone | 644501 | 6046612 | Extensional Jog | Blocky | Syn to post kinematic | Y |
| JL2004 | 1 | Port Mulgrave Fault Zone | Vein - Vertical | 644483 | 6046531 | 0.5mm thick Vein | Fibrous | Syn to post kinematic | - |
| NR1609 | 1 | Port Mulgrave Fault Zone | Vein - Vertical | 644534 | 6047178 | 1-2mm thick vein | Blocky | Syn-kinematic | Y |
| - | 2 | - | - | - | - | - | Fibrous | Syn-kinematic | Y |
| - | 3 | - | - | - | - | - | Blocky | Syn to post kinematic | - |
| JL2002 | 1 | Port Mulgrave Fault Zone | Vein - Bedding-parallel (Imbricate) | 644501 | 6046612 | 0.5-1mm thick vein | Blocky | Syn-kinematic | Y |
| - | 2 | - | - | - | - | - | Blocky | Syn-kinematic | - |

*Table 4.7. Summary table of calcite fills from the Port Mulgrave Fault Zone at Port Mulgrave (Fig 4.1) analysed in this chapter. Samples not discussed here are presented in Appendix 8.1 & 8.2.*

NR1504 and NR1505 (Fig 4.33) are both located in extensional jog structures, but due to early sampling techniques by Nick Roberts which collected unoriented calcite fragments, are only now composed of randomly oriented chips of blocky macroscopic calcite set in the resin mounts. Crack-seal and syndeformational textures are therefore difficult to determine. The samples are composed of blocky spar with minor, sub-millimetre, mudstone inclusions. It is reasonable to conclude, however, that the vein fills are syn-deformational as field observations in Chapter 3 demonstrate that they are associated with clear dilational jog features.

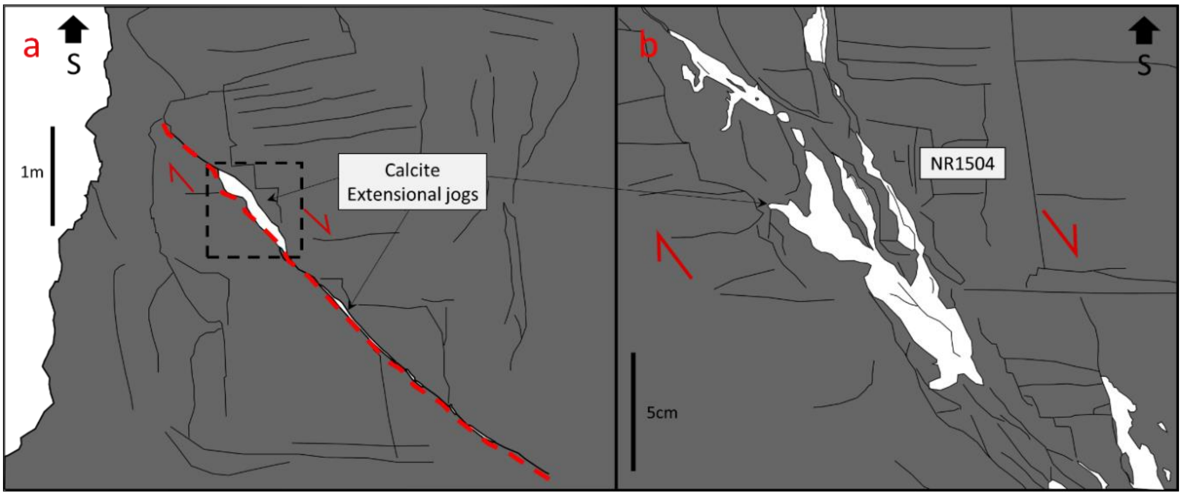


*Fig 4.32. Sectional sketches of the Port Mulgrave Fault (a) at Port Mulgrave Headland. NR1504 (b) is an extensional jog structure along a west dipping fault structure. NR1609 is a subvertical vein taken 10m to west of the sketch and is inferred to be a reactivated joint due to fluid-flow and/or dilation related to the fault movement.*

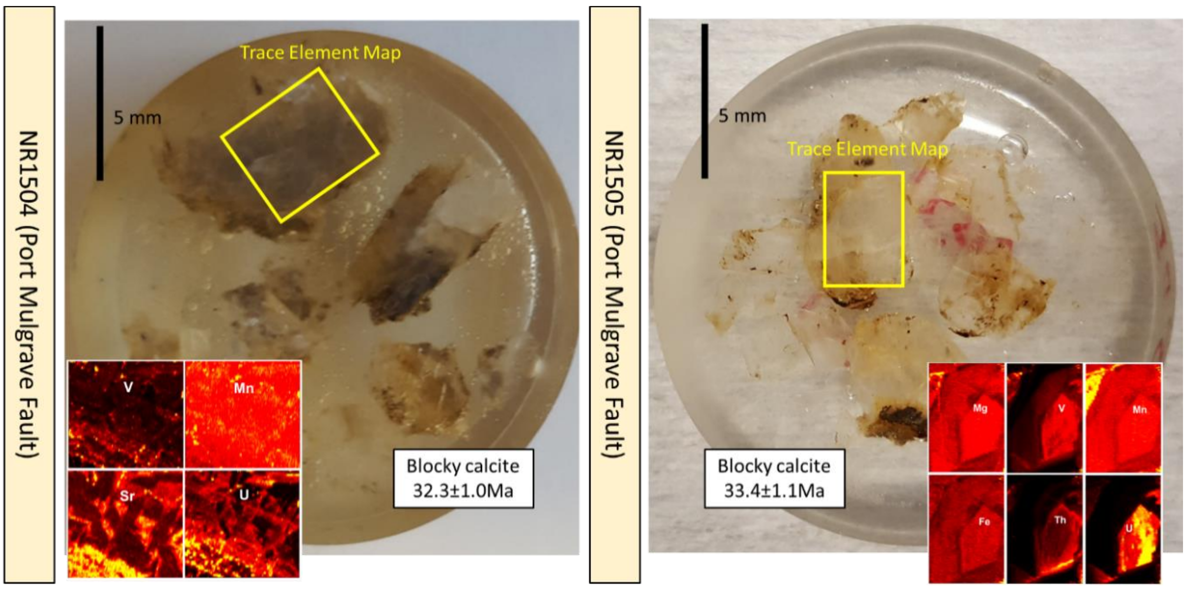


*Fig 4.33. Mount images from NR1504 and NR1505. Both samples are composed of blocky calcite chips in circular epoxy resin mounts. Trace element maps are shown for the areas outlined in yellow. The trace element maps show heat maps for the relative concentrations of Mg, Mn, V, Sr, Fe, Th and U scaling from yellow (high) to black (low).*

Blocky calcite was dated from both NR1504 and NR1505 at 32.3 ± 0.9Ma with an MSWD 2.4 and 33.5 ± 1.0Ma with an MSWD 1.7 (Fig 4.37d). These dates overlap in uncertainty and provide estimates for the age of calcite mineralisation with good levels of precision (ca. 1Myr).

NR1609

NR1609 is a subvertical vein (Fig 4.34) taken from a jet miner's hole 10m into the hangingwall of the Port Mulgrave Fault. The vein is interpreted to be a $J_1$ joint reactivated in association with fault movement. The sample is a composite vein with three distinct zones of calcite and distinctive bitumen-filled vugs (Fig 4.34a&b) and staining.

Zone 1 - An internal zone of blocky calcite (2mm wide; Fig 4.34c-e) has open central vugs that suggest syntaxial growth. The calcite zone contains rounded plucked mudstone clasts 800µm thick and 400µm wide along with irregularly shaped vugs filled with bitumen. The irregularity and roughness of the crack supports the inference that fibres have tracked the opening direction.

Zone 2 - Zone 1 is flanked by a 0.5-2.0mm thick zone of fibrous calcite tracking margin perpendicular growth. The fibres appear to grow thicker away from the vein centre suggestive of antitaxial growth.

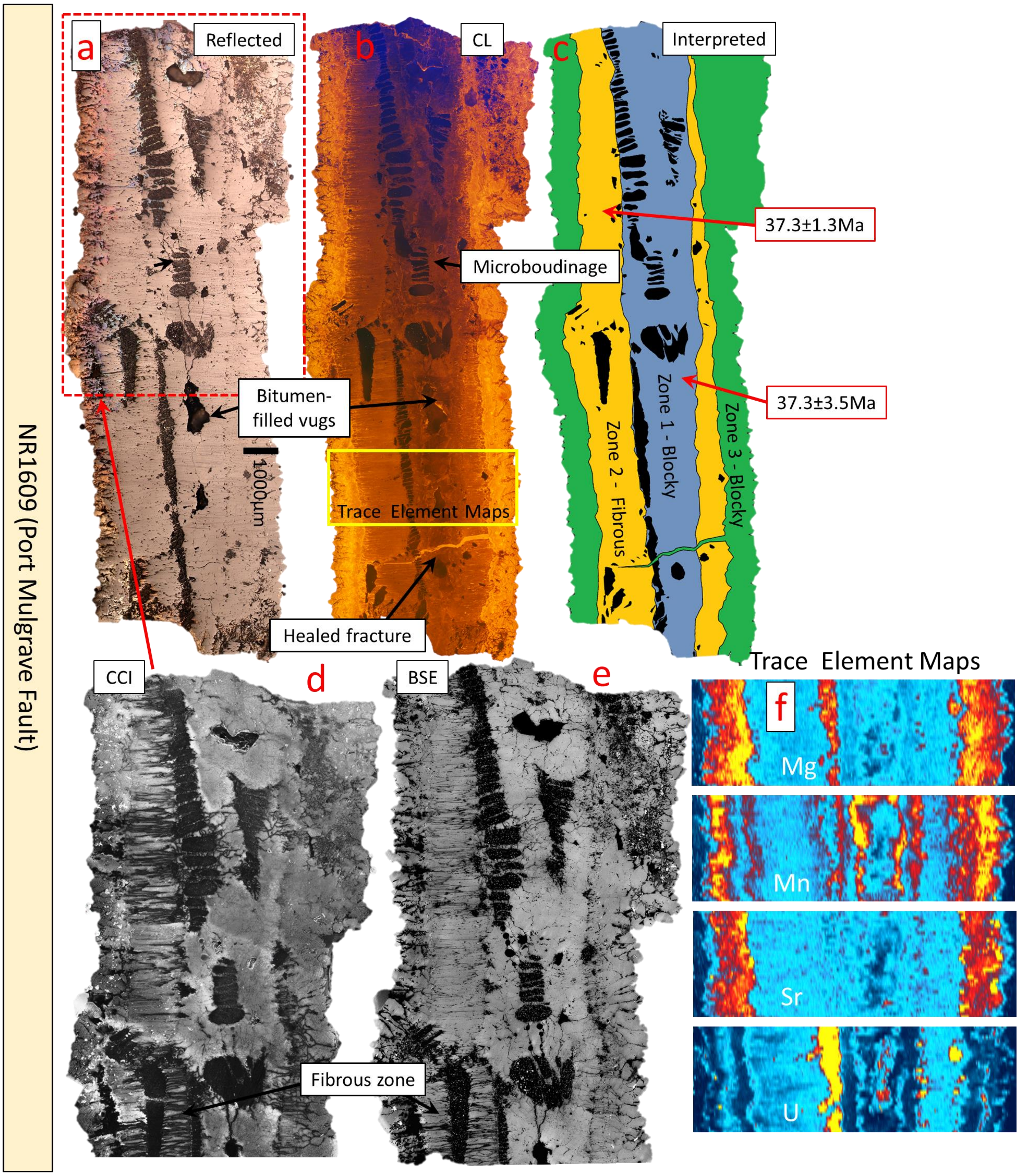


*Fig 4.34. Microscopic and mount images of three samples taken from the Port Mulgrave Fault at Port Mulgrave Headland. NR1609 is a complex vein structure (a-e) with three calcite zones (c): Zone 1 (Blue), Zone 2 (Yellow) and Zone 3 (Green). f) Trace element maps showing heat maps of Mg, Mn, Sr and U concentrations.*

Zone 3 - an outer zone of zoned blocky calcite (0.5-3mm wide) shows a distinct bright CL (Fig 4.34b) and is shown by trace element maps (Fig 4.34f) to be enriched in magnesium, manganese and strontium relative to the other zones. A healed fracture (CL; Fig 4.34b) from Zone 3 extends through the other zones indicating that it formed last. Trace element maps show Uranium to be relatively depleted in most zones except in the included mudstone clasts (Fig 4.34f).

Zone 1 and Zone 2 have been successfully dated from NR1609: 37.3 ± 3.5Ma with an MSWD of 1.5 (Fig 4.37a) and 37.3 ± 1.3Ma with an MSWD of 1.4 (Fig 4.37b) respectively. The same age has been achieved for both zones and suggests that they formed soon after each other geologically. Dating was attempted on Zone 3 but uranium concentrations were not high enough for a date to be produced. It is inferred that the vein initially formed with the blocky calcite of Zone 1 with a high frequency of mudstone inclusions sourced from the countryrock. Zone 2 was then flanked by fibrous calcite of Zone 2 with later precipitation of Zone 3, which is brighter in CL and is shown to cross cut Zone 1 & 2.

JL2016

JL2016 (Fig 4.34) is a highly complex extensional jog structure (2-3cm in thickness) taken from a normal fault similar to the one shown in Fig 4.25 with predominantly blocky calcite centred around a central growth plane. JL2016 has been subdivided into two zones.

Zone 1 is a reworked fibrous antitaxial phase (200-300µm thick; Fig 4.35a) in a mudstone clast that has been incorporated into – and therefore predates - Zone 2.

Zone 2 is a blocky fill with ataxial or unitaxial growth. Plucked and brecciated mudstone clasts are common along with crack-seal textures. The boundaries on the top left and bottom right are relatively planar with potential displacement representing planes of dislocation and shear and likely represent slickenfibres (Fig 4.35a) formed through mineralisation along slip planes during fault slip. The slickenfibres mark the boundaries of the extensional jog. Slickenfibres (Fig 4.35a) at the margins of the fill are consistent with field observations of extensional jog movement and indicate of syn-kinematic calcite precipitation of Zone 2.

Zone 2 of JL2016 (Fig 4.35b) has been dated at 30.4 ± 1.4Ma with an MSWD of 1.1 (Fig 4.37g). This zone is inferred to provide a good constraint of fault movement.

JL2001

JL2001 (Fig 4.36a) is a bedding-parallel blocky calcite vein (030/52W) associated with a metre-scale duplex structure documented in Section 3.2.3.3 at Locality B in the poorly exposed Port Mulgrave Fault trace at Port Mulgrave Beach. In comparison to JL2016, it is relatively simple. It displays a single zone of 5mm thick zone of syntaxial blocky calcite with inclusion bands (Fig 4.36a) present along the lower margin suggesting early crack-seal prior to crack-fill. The central zone has pores preserved along the crystal boundaries (1-2%; Fig 4.36a) supporting a hypothesis of later crack-fill.

JL2001 (Fig 4.36b) has been dated at 27.2 ± 0.9Ma with an MSWD of 1.2 (Fig 4.37h) from the area of the fill with crack-seal likely dating early fracture opening and mineralisation.

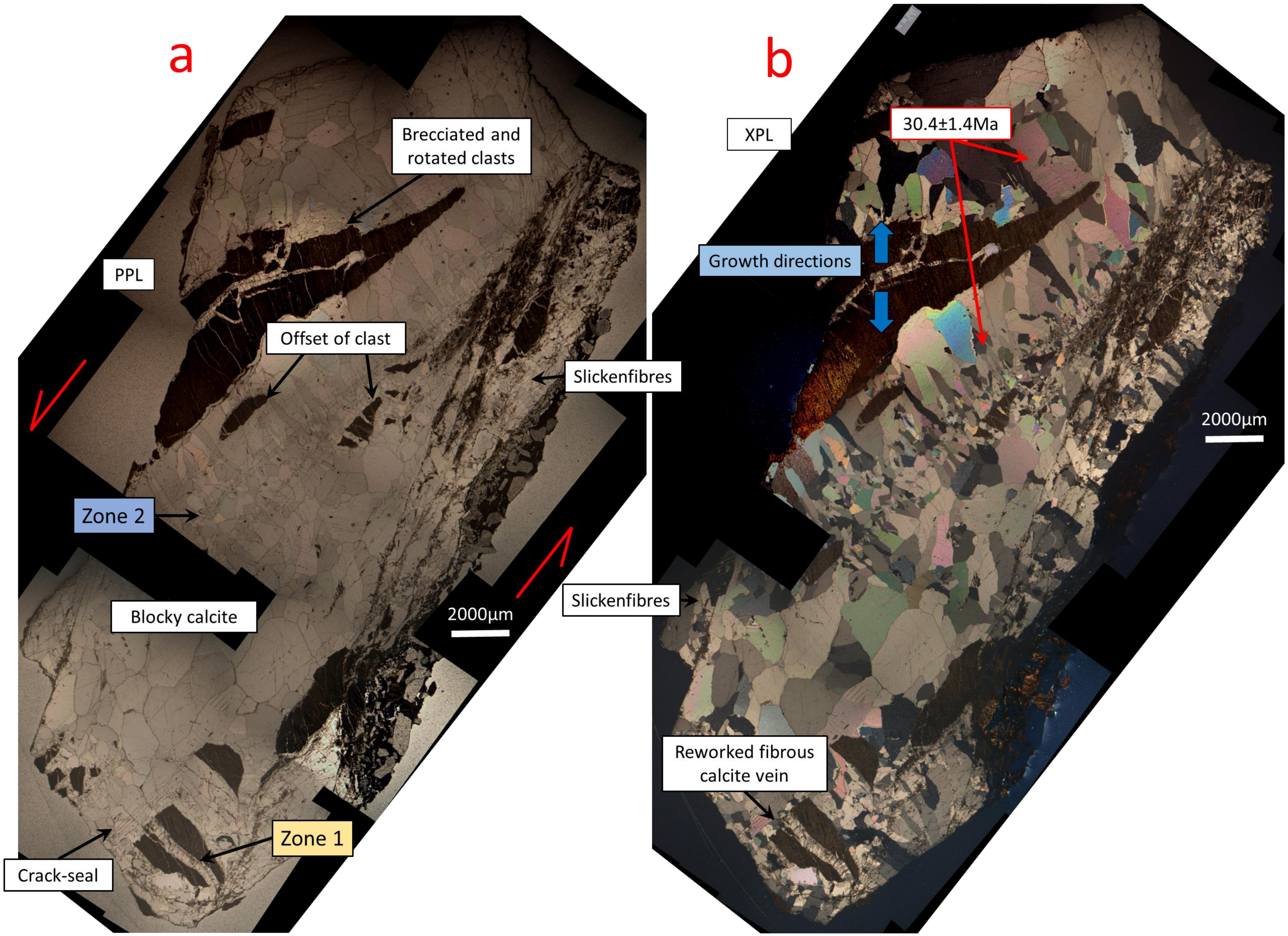


*Fig 4.35. Microscopy images of an extensional jog structure (JL2016) from the extension of the Port Mulgrave Fault onto the beach at Port Mulgrave. JL2016 has complicated structures with multiple generations of calcite, which are split into two main zones of reworked fibrous calcite and blocky syn-kinematic fill. Growth directions are shown with blue arrows and are based on fibrous calcite tracking opening and systematically offset clasts.*

JL2001 (Port Mulgrave Fault)

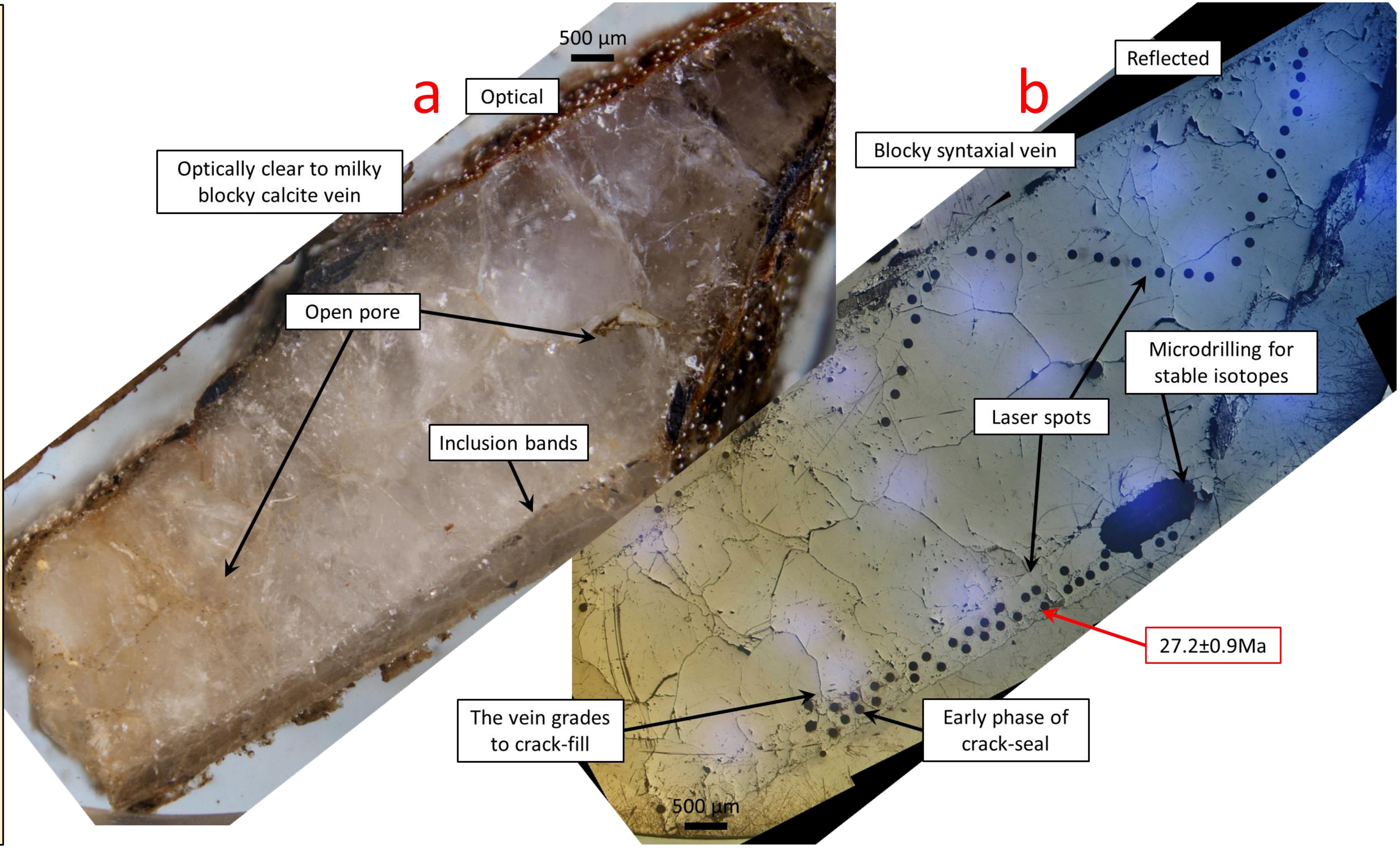


*Fig 4.36. Optical and reflected microscopy of JL2001. JL2001 is relatively simple, compared to JL2016, with syntaxial calcite (5-6mm thick) and a thin (0.5mm thick) of inclusion bands at the margins.*

Summary

NR1609 shows a variety of microstructures with Zone 2 characterised by fibrous calcite that tracks fracture opening. Plucked clasts in Zone 1 provides some confidence in mineralisation being synchronous with fracturing opening. However, Zone 3 records little evidence of syn-kinematic calcite with no clear textures. It is inferred that the NR1609 represents dilation of subvertical veins in response to movement of the Port Mulgrave Fault Zone.

JL2016 has a high degree of variability. Zone 1 is made up of fibrous calcite that likely tracked opening before being reworked in clasts in the large blocky fill that followed. Shear bands and slickenfibres indicate synkinematic calcite precipitation during fault movement. This interpretation is supported by systematic offsetting of mudstone clasts, which are plucked apart indicating oblique opening.

JL2001 shows gradation from initial crack-seal textures to crack-fill but shows little clear evidence of synkinematic mineralisation. NR1504 and NR1505 were sampled as individual unoriented pieces of calcite and show no clear indicators of synkinematic behaviour or crack-seal.

Figure 4.37 shows the variation in calcite ages from the Port Mulgrave Fault Zone with calcite ages varying from 37.3Ma in Zone 1 of NR1609 (Fig 4.37a) and 22.1Ma in Zone 1 of JL2002 (Fig 4.37i). The youngest ages are associated with 27.2Ma (Fig 4.37h) and 22.1Ma are associated with JL2001 and JL2002, which have both been sampled from the imbricate structures discussed in Section 3.2.3.3. This could suggest that these imbricate structures represent a later stage of deformation than earlier extensional fault associated deformation (37.3-30.4Ma; Fig 4.37a-g).

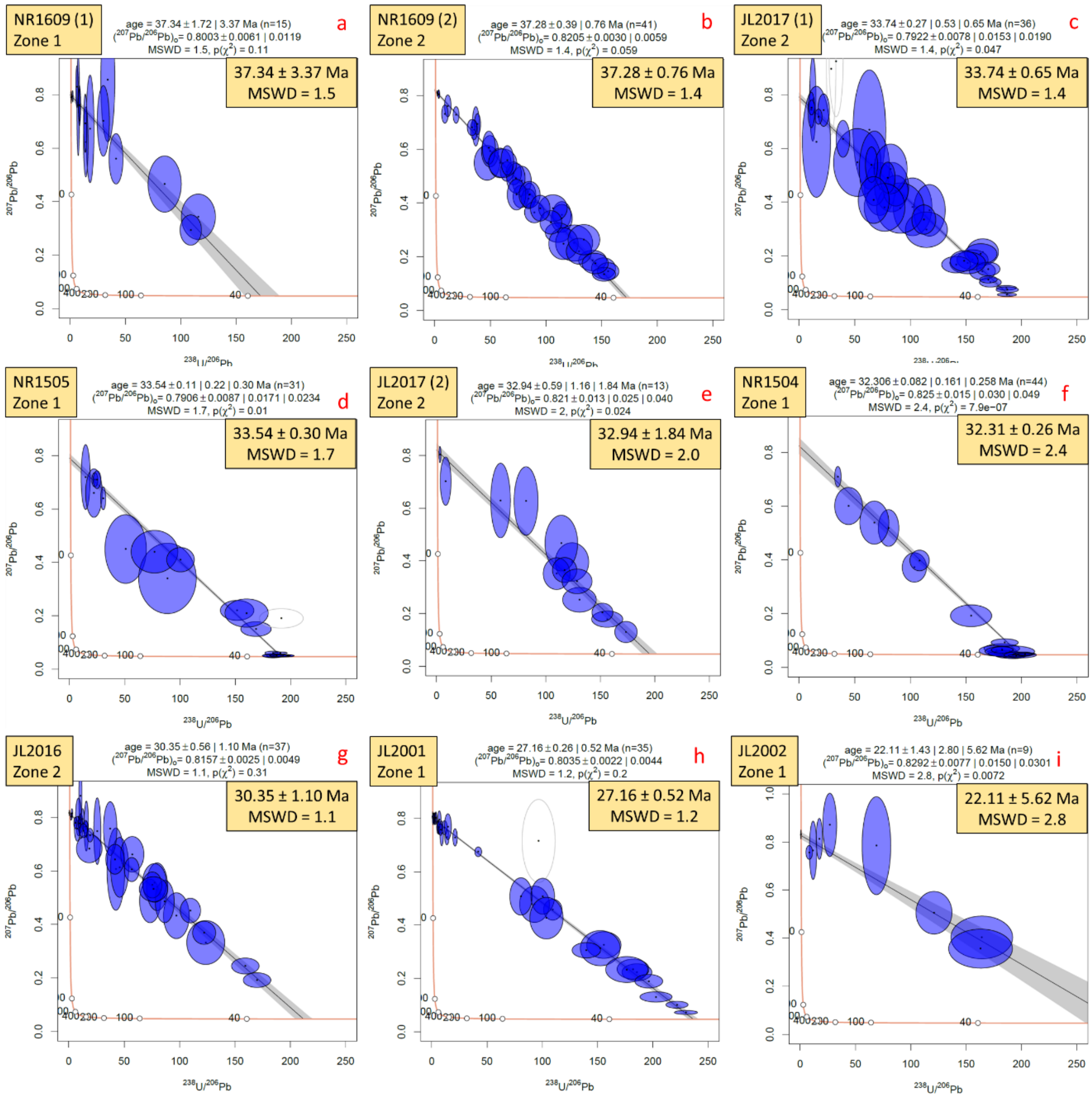


*Fig 4.37. T-W plots from the Port Mulgrave Fault Zone.*

## 4.4.4 Oblique-Slip Faulting (Port Mulgrave Beach)

Section 3.2.3.4 discusses the oblique-slip dextral and sinistral structures at Port Mulgrave Beach. Five samples have been taken from oblique-slip faults with two representative samples (JL1812b & JL2006) presented. JL1812a is from a dextral oblique-slip structure (Fig 3.25) and JL2006 from a rotated block in a sinistral fault zone (Fig 3.26). Microstructures and U-Pb geochronology results for all samples are outlined in Table 4.3.

| Sample | Zone | Main Structure | Minor Structure | UTM N | UTM E | Calcite Fill | Texture | Kinematics | Dating |
|---|---|---|---|---|---|---|---|---|---|
| JL1812a | 1 | Dextral Oblique-slip PM | Fault - Dextral Oblique | 644521 | 6046542 | Extensional Jog | Blocky | Syn to post kinematic | Y |
| JL1812b | 1 | Dextral Oblique-slip PM | Fault - Dextral Oblique | 644521 | 6046542 | Extensional Jog | Blocky | Syn-kinematic | Y |
| JL2007 | 1 | Sinistral Oblique-slip PM | Low angle fault | 644479 | 6046511 | 1-3cm thick sigmoidal vein | Blocky | Syn-kinematic | Y |
| - | 2 | - | - | - | - | - | Blocky | Syn-kinematic | Y |
| JL2006 | 1 | Sinistral Oblique-slip PM | Low angle fault | 644479 | 6046511 | 2-3cm thick sigmoidal vein | Blocky | Syn-kinematic | Y |
| JL2005 | 1 | Sinistral Oblique-slip PM | Vein - Vertical | 644479 | 6046511 | 1-2mm thick vein | Fibrous | Syn-dilation | Y |

*Table 4.8. Summary table of calcite fills from the oblique-slip faulting at Port Mulgrave (Fig 4.1) analysed in this chapter. Samples not discussed here are presented in Appendix 8.1 & 8.2.*

JL1812b

JL1812b (Fig 4.38a) is from an extensional jog structure (3-4cm thick) taken from an E-W striking dextral oblique-slip fault shown in Fig 3.26. The oblique-slip fault also has nested cone-in-cone structures (Fig 3.25d), which are described in Section 3.2.3.4. The cone-in-cone structures are inferred to form in a splay of the fault plane and are interpreted to have formed synchronous with faulting. The samples have been sampled but have not been successfully dated.

JL1812b has a single generation of blocky calcite (Fig 4.38a&b) with well-developed inclusion bands that record a clear opening direction, shown in Backscatter Electron (BSE; Fig 4.38a) imaging, indicative of crack-seal-slip with jogs in these bands showing the vector of opening. The fill has infrequent mudstone clasts (1-2%; Fig 4.38b). The blocky calcite fill has a unitaxial texture with calcite crystals growing approximately in the direction of opening as dilation continued. JL1812b is considered a good example of a syn-kinematic extensional jog fill with inclusion bands tracking oblique opening consistent with the interpretation in Section 3.2.3.4 of an oblique-slip dextral movement.

Three ages have been achieved for JL1812b. The ages are 33.1 ± 3.1Ma with an MSWD of 1.6, 32.7 ± 1.6Ma with an MSWD of 1.9 (Fig 4.39c) and 38.6 ± 8.0Ma with an MSWD of 4.0 (Fig 4.39a); all ages overlap in uncertainty. These constrain well the overall age of oblique syn-kinematic mineralisation in the dextral fault. An age of 33.0 ± 2.9Ma and an MSWD of 1.6 (Fig 4.39b) has also been obtained for a companion fill (JL1812a) in the same fault. This fill is blocky calcite with 1-2% vugs observed in the field and was dated at 23.8 ± 2.6Ma with an MSWD of 1.6 (Fig 4.39d). This fill has not been discussed in detail due to a lack of syn-kinematic evidence but is significantly younger then JL1812b and likely records a phase of post kinematic calcite mineralisation and is included in Appendix 8.1.

JL2006

JL2006 (Fig 4.40a) is a sigmoidal vein (2-3cm thick) associated with a top-to-the-west low angle fault with E-W slickenlines (09-007) in a rotated block from a sinistral fault zone (Fig 3.26) described in Section 3.2.3.4. The fill preserves multiple generations of blocky calcite with infrequent inclusion bands, which preserve bedding-parallel shear planes. The sample records crack-seal with planes of shearing recording evidence of syn-kinematic bedding-parallel shear, which supports field observation of top-to-the-west (right on Fig 4.40a) shear.

The laser spots for JL2006 are shown in Figure 4.40b with an age of 28.8 ± 2.5Ma with an MSWD of 2.1 (Fig 4.42a). This is inferred to reflect syn-kinematic mineralisation due to the presence of shear planes. JL2005 and JL2007 shown in Appendix 8.1 show similar styles of syn-kinematic with blocky calcite with shear planes parallel to the vein margins.

JL1812 (Oblique-Slip Fault - Dextral)

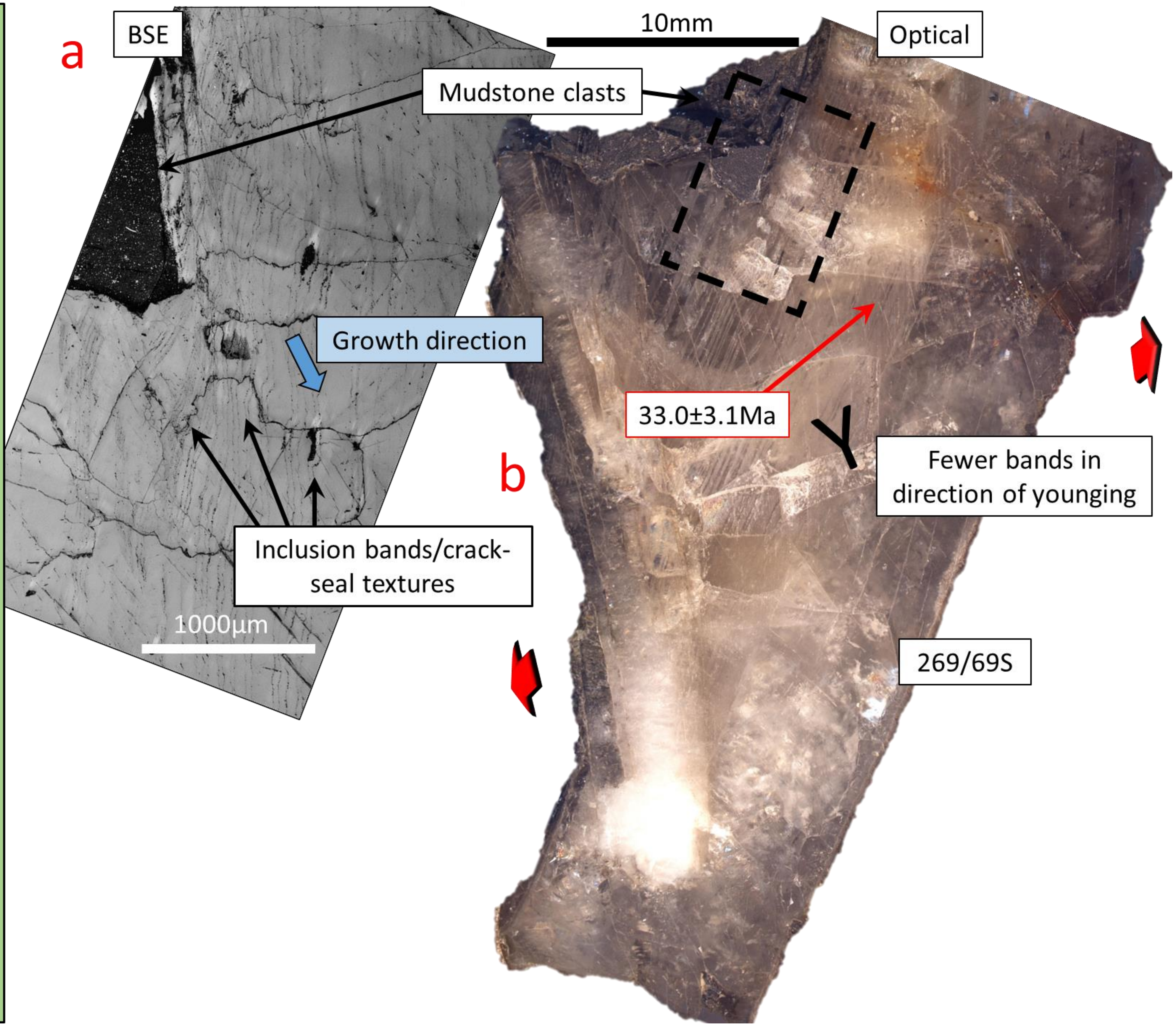


*Fig 4.38. Microscopy images from JL1812b from Port Mulgrave Beach (Fig 3.25). JL1812 is a blocky calcite fill taken from an extensional jog structure along a plane 269/69S along an oblique slip dextral fault. JL1812 has common crack-seal textures (inclusion bands) which are indicative of the direction of growth. a) BSE image of the fill showing clear inclusion bands with jogs indicating the direction of growth. b) Optical image of the fill with mudstone clasts at the top left growing less frequent into the milky blocky calcite. The blue arrow shows the interpreted direction of calcite growth with red arrows indicating the inferred motion of the dextral fault with respect to JL1812b.*

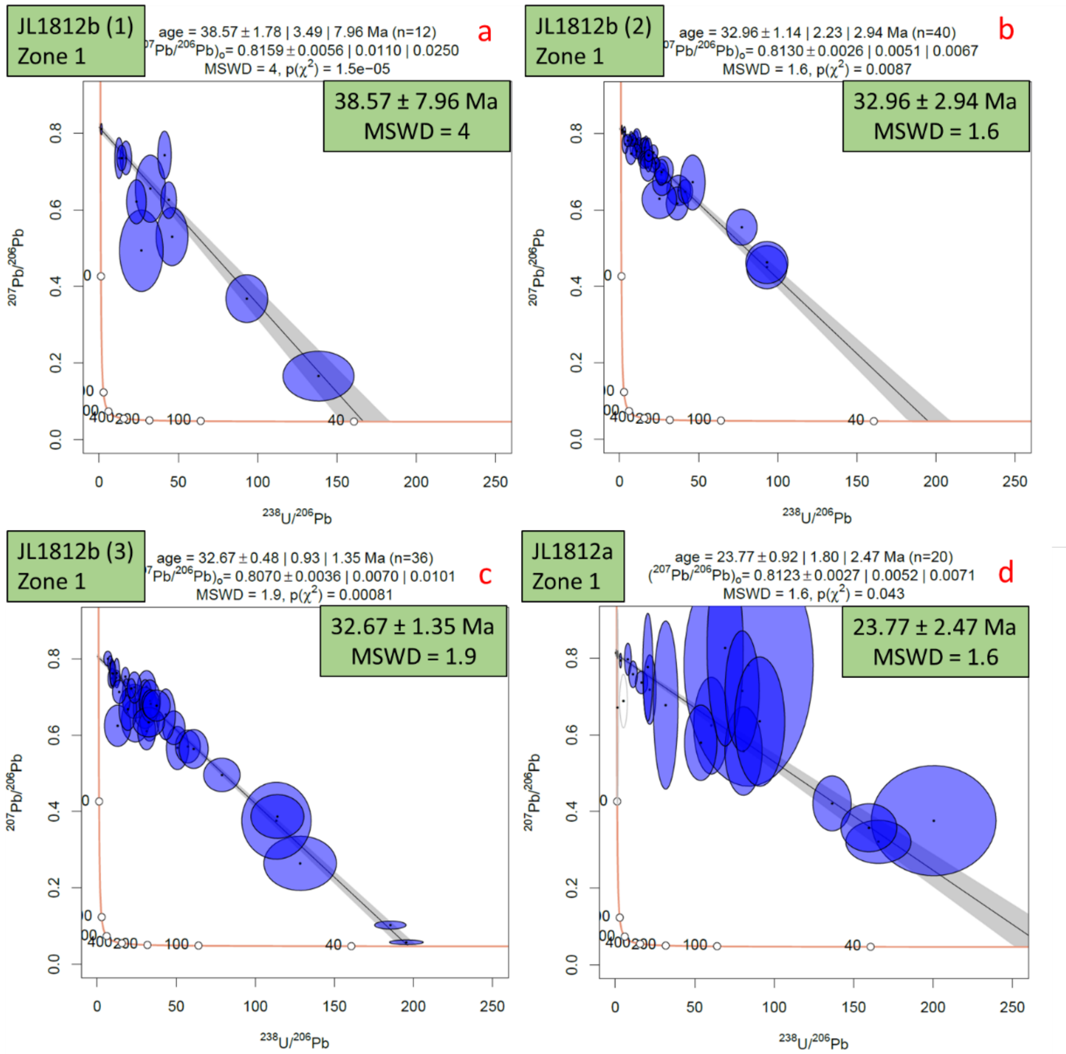


*Fig 4.39. T-W plots from the dextral oblique-slip fault ages from Port Mulgrave.*

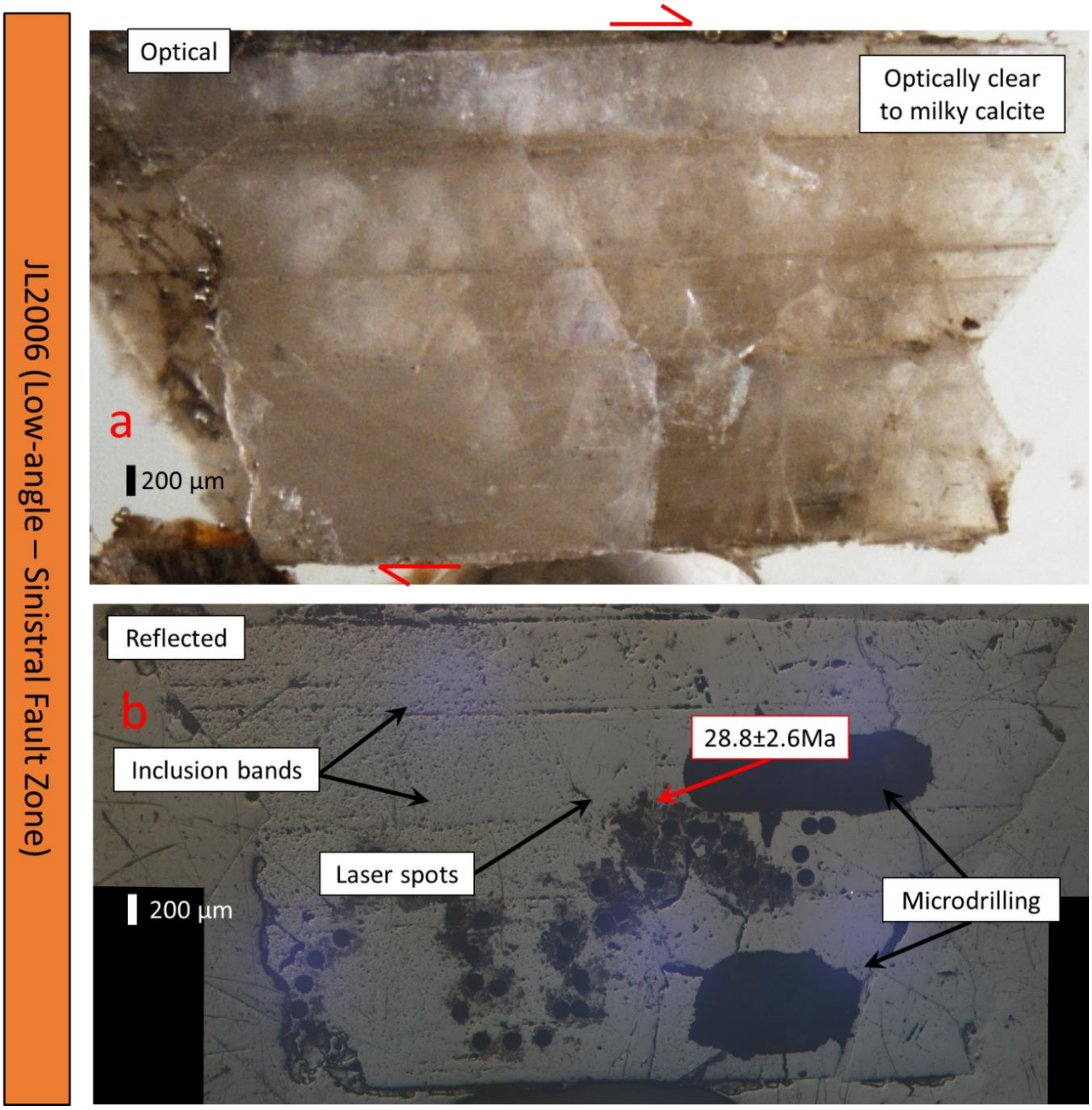


*Fig 4.40. Microscopy image from JL2006 from Port Mulgrave Beach. JL2006 is a blocky fill with inclusion bands from a low angle calcite vein in a sinistral fault zone.*

## 4.4.5 Elm Tree Farm Borehole

Elm Tree Farm Borehole is a water well borehole drilled to a depth of 60’80” (20.3m) near Kirby Misperton. Three samples were taken from core at the British Geological Survey Core store but due to the nature of core samples, no orientation can be attributed to these samples. Microscopy images for SSK110596 are displayed in Figure 4.40a with all samples detailed in Table 4.3.

| Sample | Zone | Main Structure | Minor Structure | UTM N | UTM E | Calcite Fill | Texture | Kinematics | Dating |
|---|---|---|---|---|---|---|---|---|---|
| SSK110588 | 1 | Elm Tree Farm Borehole | Fault | 478910 | 478770 | Inclined fault | Blocky | Syn-kinematic | Y |
| SSK110596 | 1 | Elm Tree Farm Borehole | Fault | 478910 | 478770 | Calcite in gouge | Blocky | Unclear | - |
| SSK110598 | 1 | Elm Tree Farm Borehole | Fault | 478910 | 478770 | Calcite in gouge | Blocky | Unclear | - |

*Table 4.9. Summary table of calcite fills from the Elm Tree Farm Borehole, Kirby Misperton (Fig 4.1) analysed in this chapter. Samples not discussed here are presented in Appendix 8.1 & 8.2.*

<u>SSK110588</u>

SSK110588 (Fig 4.41a) was sampled from a fault plane (2cm thick) dipping 60° across the core (Fig 4.41b). It is composed of a single generation of blocky syntaxial calcite bordered by multiple areas of mudstone inclusions sheared prior to vein formation (Fig 4.41a). In some areas, inclusion bands are evident suggesting intermittent crack-sealing. These inclusion bands decrease in visibility away from the margins, suggesting a change from crack-seal to crack-fill through time. The sample shows clear series of jogs, which are indicative of a dextral shear sense. This dextral shear sense indicates that vein fill formed synchronous with fault slip at some stage.

The dextral syn-kinematic fill of SSK110588 has an age of 28.3 ± 3.3Ma with an MSWD of 2.3 (Fig 4.42f). This compares well with the timing of deformation for other Meso-scale faults described above. This dating could suggest that deformation in the Elm Tree Farm Borehole relates to the same period of E-W extension observed on the coast.

SSK110588 (Dilational jog)

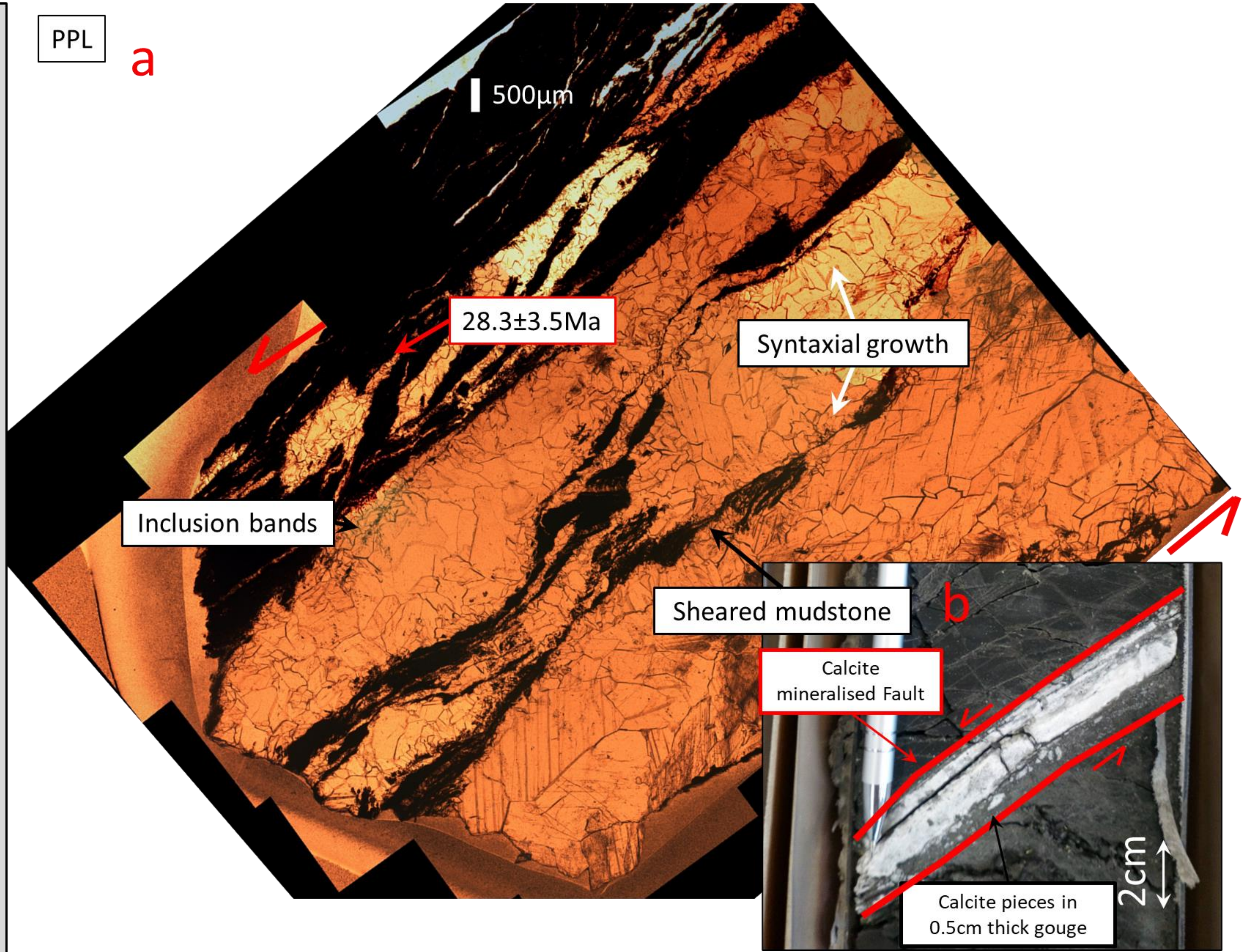


*Fig 4.41. Microscopy images of SSK110588. SSK110588 was sampled from calcite in a fault zones (b). SSK110588 appears to be an extensional jog structure with sheared mudstone layers separating syntaxial blocky calcite.*

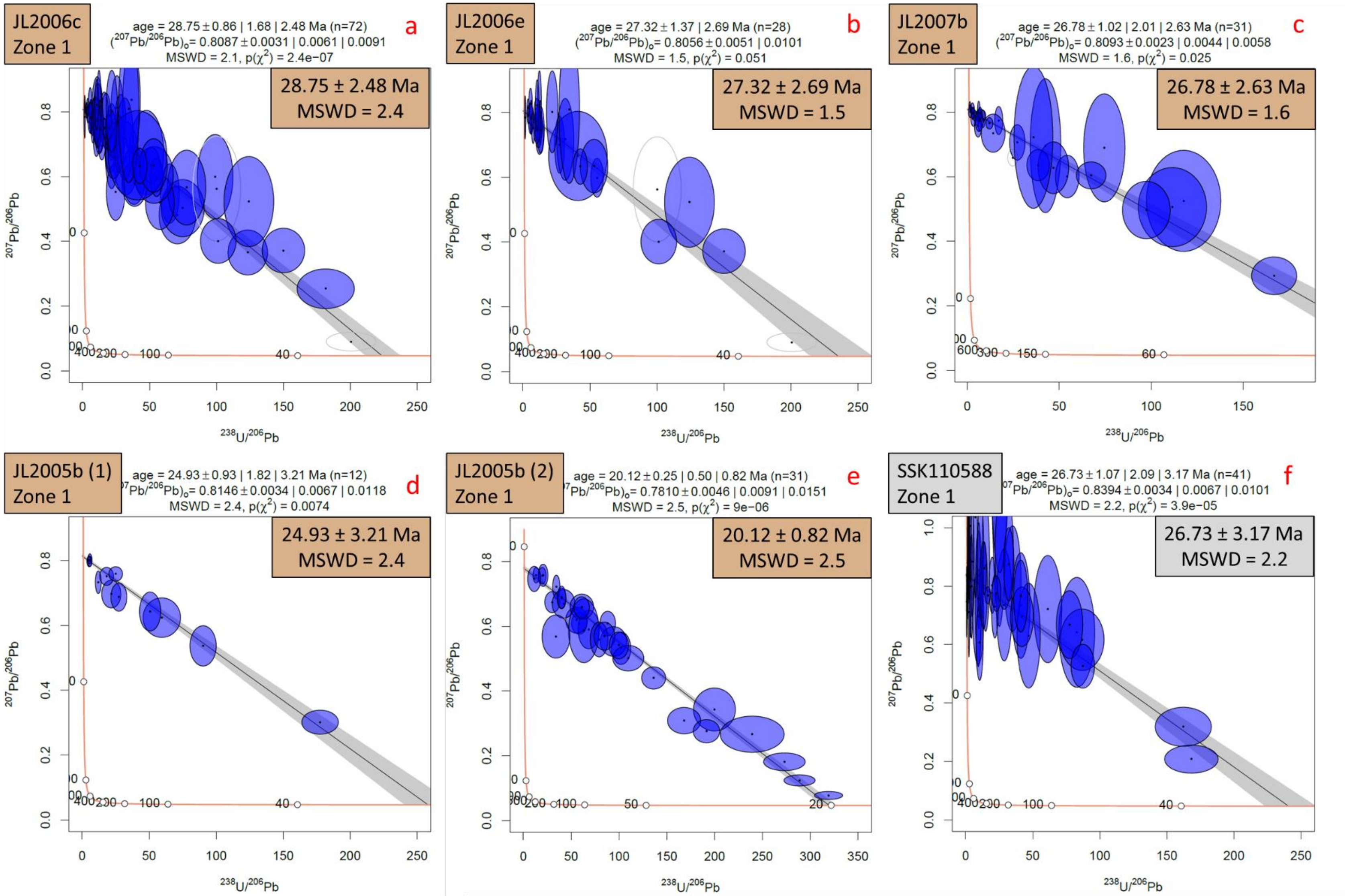


*Fig 4.42. T-W plots from the sinistral oblique-slip faults from Port Mulgrave and SSK110588 from the Elm Tree Farm Borehole.*

### 4.4.6 Summary of Meso-scale Fault Microstructures

Microstructural analysis of calcite fills from the Runswick Bay, Staithes and Port Mulgrave faults and the Elm Tree Farm borehole are summarised in Table 4.3. The calcite fills are from a mixture of fault plane fills and subvertical and bedding-parallel vein structures formed or reactivated in response to fault movement. Similar to the Peak Fault at Ravenscar, the fills themselves show a diverse range of forms including breccia, extensional jogs, calcite in gouges and mm and cm-scale veins along fault planes, joints and bedding-parallel fractures.

Calcite microstructural textures are diverse (Table 4.3) with a large number of calcite fills showing evidence of syn-kinematic mineralisation with some syn- to post-kinematic fills (Fig 4.43). The samples are typically consistent with primary calcite with minimal evidence of alteration or recrystallization although there is evidence that NR1501 and NR1602 have undergone cataclasis and represent reworked calcite embedded in later fault gouges. The direction of opening/growth is difficult to determine due to lack of fibrous crystals tracking growth, but in several cases the opening direction has been determined using dislocated mudstone clasts, inclusion bands and inclusion trails. The opening direction, where determined, shows a mixture of opening-mode dilation and oblique opening, which are consistent with fills forming synchronous with fault slip. This relationship means that there is high confidence that mineralisation reflects ongoing fault movement due to E-W extension described in Chapter 3.

Growth textures and crystal size are highly variable and likely reflect complex controls on fill growth in a variety of structures over a wide timespan. Ataxial, unitaxial, syntaxial, antitaxial or uncertain growth textures have all been recorded. Evidence of crack-seal varies from vein to vein, with samples such as JL1812 from the Port Mulgrave fault demonstrating clear inclusion bands while samples from the Staithes faults seem to completely lack crack-seal textures, with the exception of the subvertical vein NR1503 where inclusion bands are present in Zone 1. Clast inclusions are typically low, with only JL1809c having over 20% with 30-40% clasts. Vugs are uncommon with only NR1615, a breccia/jog fill along the Runswick Bay Fault recording more than 5% vugs (5-10%).

Successfully dated samples are plotted in Fig 4.43 and cover a wide timespan of activity for structures with the dates spanning from ca. 39Ma (NR1604) to 20Ma (JL2005b). This represents a possibility that the total fault activity covered a period of ~19Ma. As in the summary of the Peak Trough faults (Section 4.3.3), Table 4.4 summarises the minimum and maximum period of activity expected for the “Meso-scale faults”. Further discussion of the U-Pb geochronology will be included in Section 4.6.

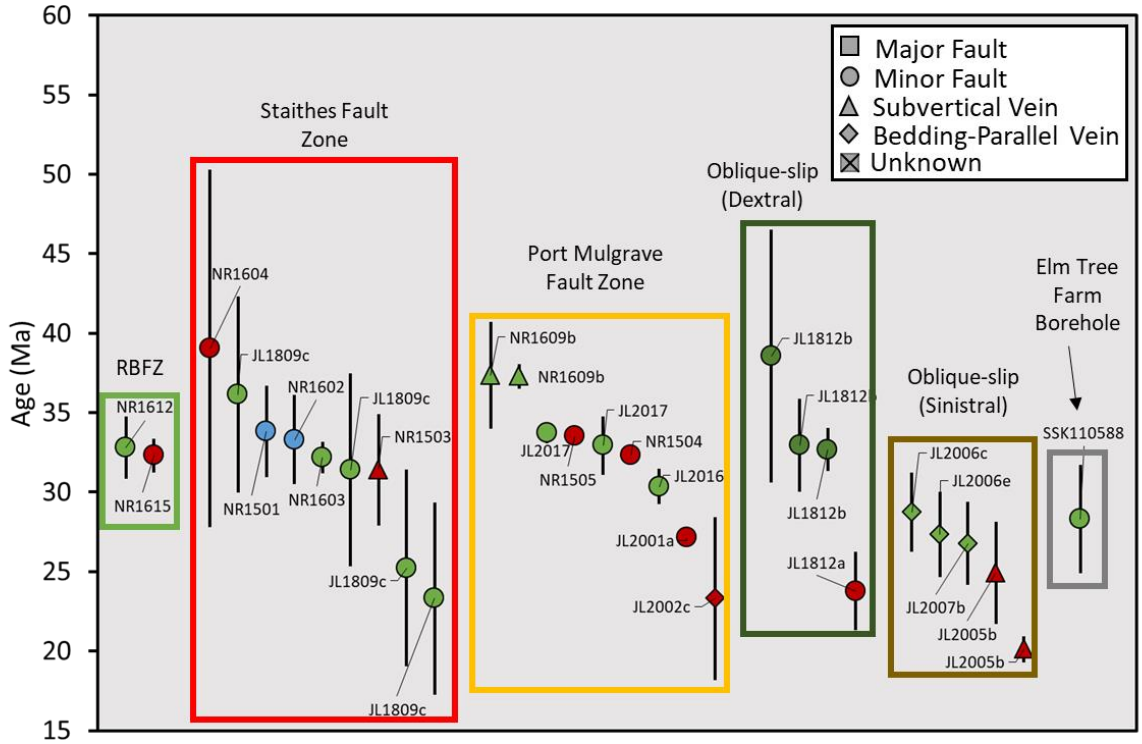


*Fig 4.43. Plot of U-Pb calcite geochronology results from the Meso-scale fault structures versus Time/Age (Ma) with the symbols organised by the structure type. Blue - pre-kinematic, Green - syn-kinematic, Red - syn- to post kinematic.*

| | Runswick Bay Fault | Staithes Faults | Port Mulgrave Fault | Dextral Oblique-slip Faults | Sinistral Oblique-slip Faults | Elm Tree Farm Borehole |
|---|---|---|---|---|---|---|
| Dates difference (Ma) | 0.5 | 15.7 | 15.2 | 14.8 | 8.6 | - |
| Max Activity (Ma) | 3.9 | 33.1 | 24.2 | 25.2 | 11.9 | 6.8 |
| Min Activity (Ma) | - | 1.8 | 8.8 | 5.1 | 5.3 | - |
| Overlap in ages (Ma) | 2.1 | - | - | - | - | - |

*Table 4.10. Compilation of the different age separations for the Small Scale Faults based on U-Pb calcite geochronology results with the Dates difference – the difference between the maximum and minimum date without uncertainty (2s), Maximum activity – the maximum period the structures could be active i.e. the maximum difference between the maximum age and minimum age including uncertainty, Minimum activity – the minimum period the structures are indicated to be active i.e. the minimum difference between the maximum age and minimum age including uncertainty. In some cases there will not be separation between a set of ages for a structure in which case the overlap in ages is also stated.*

## 4.5 Local Fracture Fills

In addition to calcite mineralisation directly related to fault movement, local calcite filled structures are present in the basin, which are not located adjacent to fault structures. Two types of structures are recognised and discussed here: veins in bedding-parallel fracture swarms at Staithes and subvertical calcite veins filling $J_1$ joints at Saltwick Nab and Sandsend (Fig 4.45). These subvertical veins occur due to reactivation of the joints in the absence of any clear evidence of associated faulting and so are considered to represent a potentially different phenomenon to those discussed in Sections 4.3 & 4.4.

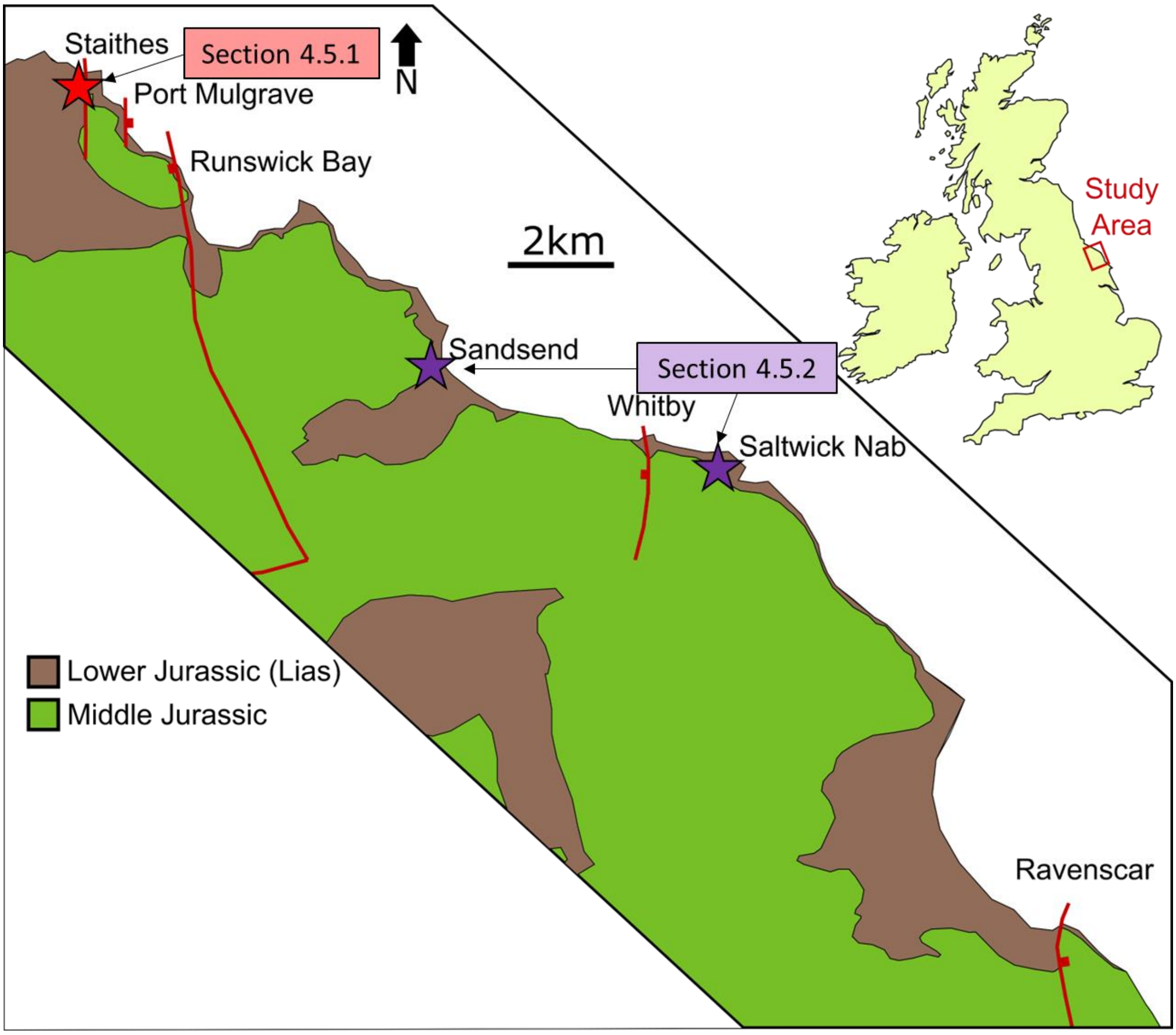


*Fig 4.45. Structural Map detailing the locations of the "Local Fracture Fills" at Staithes, Saltwick Nab and Sandsend.*

### 4.5.1 Bedding-parallel Veins (Staithes)

Bedding-parallel fractures (Section 3.2.4.1) form distinctive >400m long notches in the cliffs near Staithes (NZ 787 188). The fractures are in some cases filled with 2-5mm thick calcite veins (Fig 3.29a) with apparent blocky fills in hand specimen. The veins show some degree of apparent folding (Fig 3.29b), which is not observed in the country rock. The top of the vein is marked with a thin millimetre thick gouge developed along the upper margins. No obvious shear indicators have been observed in the gouge bordering the calcite fill. Two samples have been taken from bedding-parallel calcite veins of which NR1607 is discussed in detail. Further information on both samples are included in Table 4.5.

| Sample | Zone | Main Structure | Minor Structure | UTM N | UTM E | Calcite Fill | Texture | Kinematics | Dating |
|---|---|---|---|---|---|---|---|---|---|
| NR1606 | 1 | Bedding parallel - Staithes | Vein - Bedding-parallel | 643623 | 6047354 | 3-4mm thick vein | Fibrous | Post kinematic | Y |
| - | 2 | - | - | - | - | - | Blocky | Post kinematic | - |
| NR1607 | 1 | Bedding parallel - Staithes | Vein - Bedding-parallel | 643676 | 6047326 | 5mm thick vein | Blocky | Post kinematic | Y |
| - | 2 | - | - | - | - | - | Blocky | Post kinematic | Y |
| - | 3 | - | - | - | - | - | Fibrous & Blocky | Post kinematic | - |
| - | 4 | - | - | - | - | - | Blocky | Post kinematic | - |

*Table 4.11. Summary table of calcite fills from the bedding-parallel veins at Staithes (Fig 4.45) analysed in this chapter. Samples not discussed here are presented in Appendix 8.1 & 8.2.*

NR1607

NR1607 is a complex vein with four generations of calcite highlighted in Figures 4.46 & 4.47a: The zones (Fig 4.47c) show progressively higher degrees of truncation by the next calcite zone from Zone 4 (youngest) which is undeformed to Zone 1 (oldest). Zone 2 has been heavily truncated and has apparent fold structures. Zone 2 has tighter apparent folds with an interlimb angle of ~120° than the folds in Zone 3 (~100°), which is suggestive of fold tightening due to progressive deformation. Truncation and folding are inferred to relate to top-to-the-left (east) shear, due to reactivation of the structure at high differential stress and lower pore fluid pressure.

Figure 4.47 displays optical (a) and reflected (b) microscopy images for NR1607 with two zones of calcite successfully dated. The veins are a complex combination of fibrous and blocky calcite with reflected light microscopy showing clear truncation of the inclusion bands by the next calcite zone in NR1607a. Margin parallel shear is supported by observations of a thin gouge (<1mm thick) on the upper margins of the veins (Section 3.4.2.1). The truncation relationships in Figure 4.47c suggest that opening, tracked by fibrous layers, was interspersed by shear reactivation, which from the change in folding amplitude was repeated multiple times.

Four ages for NR1607 have been achieved one from Zone 1 (29.8 ± 5.9Ma – MSWD of 1.4; Fig 4.48a) and three from Zone 3 (22.5 ± 3.9Ma - MSWD of 1.6, 21.8 ± 2.8Ma – MSWD of 1.1 & 21.1 ± 4.2Ma – MSWD of 2.5; Fig 4.48d) supporting the interpretation summarised in Figure 4.32 that Zone 1 formed first before folding, truncation and precipitation of Zone 2. This cycle was then repeated at least twice more during precipitation of Zones 3 and 4. These ages at ~21Ma are some of the youngest recorded in the basin with only JL2005 later at ~20Ma. These ages do overlap in ages with JL2002, a bedding-parallel vein from the imbricate structures of the Port Mulgrave Fault Zone but form a distinct late phase of combined shear and bedding normal dilation not observed elsewhere.

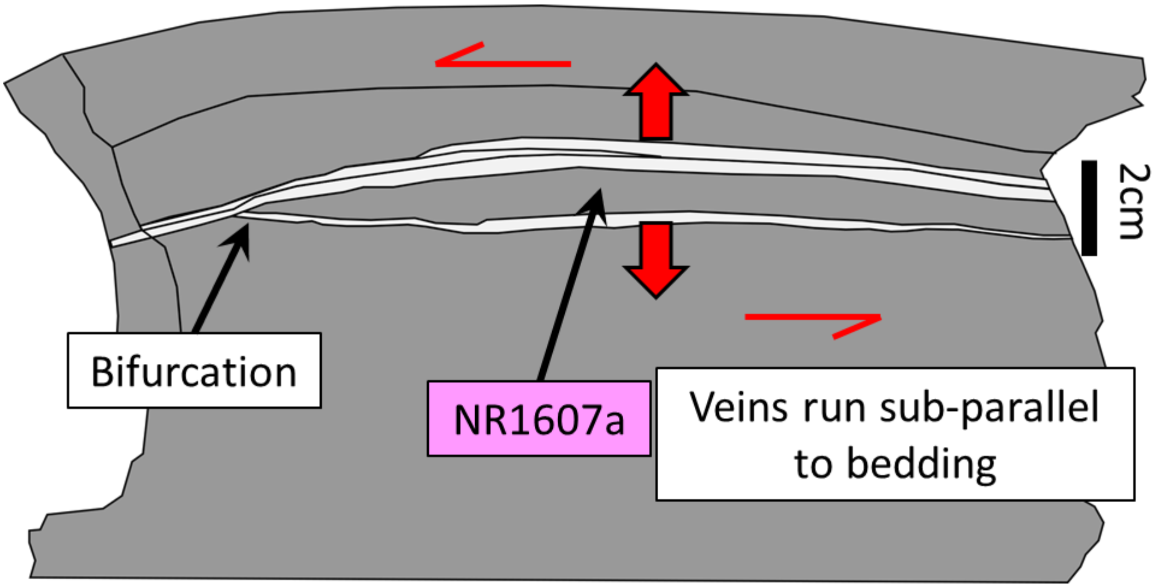


*Fig 4.46. Schematic diagram of the bedding-parallel veins with the relative opening direction shown and shear direction.*

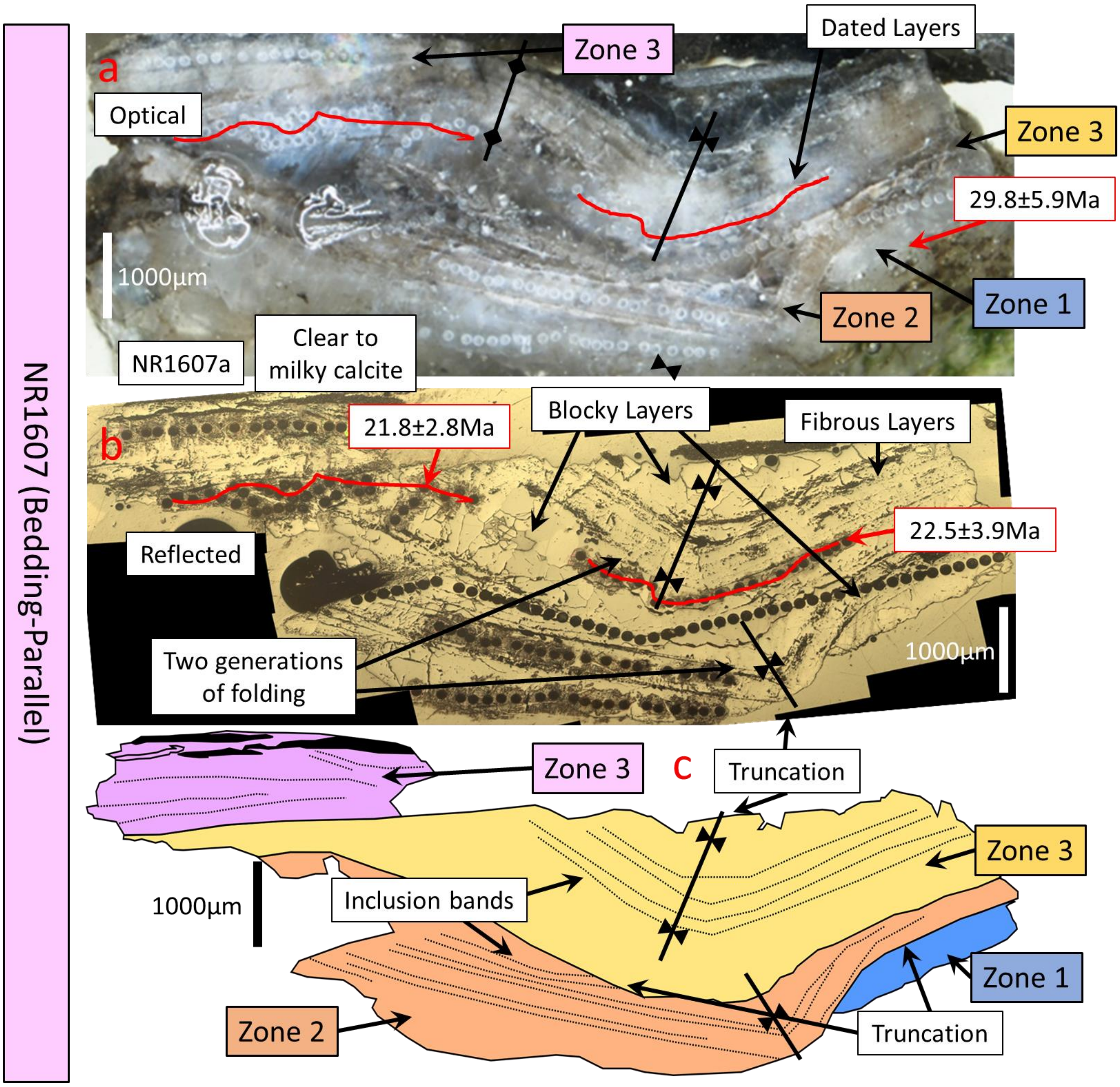


*Fig 4.47. Microscopic images from NR1607a with optical and reflected microscopy shown for both samples. NR1607 has at least two inferred generations of folding and truncation of inclusion bands (b&c).*

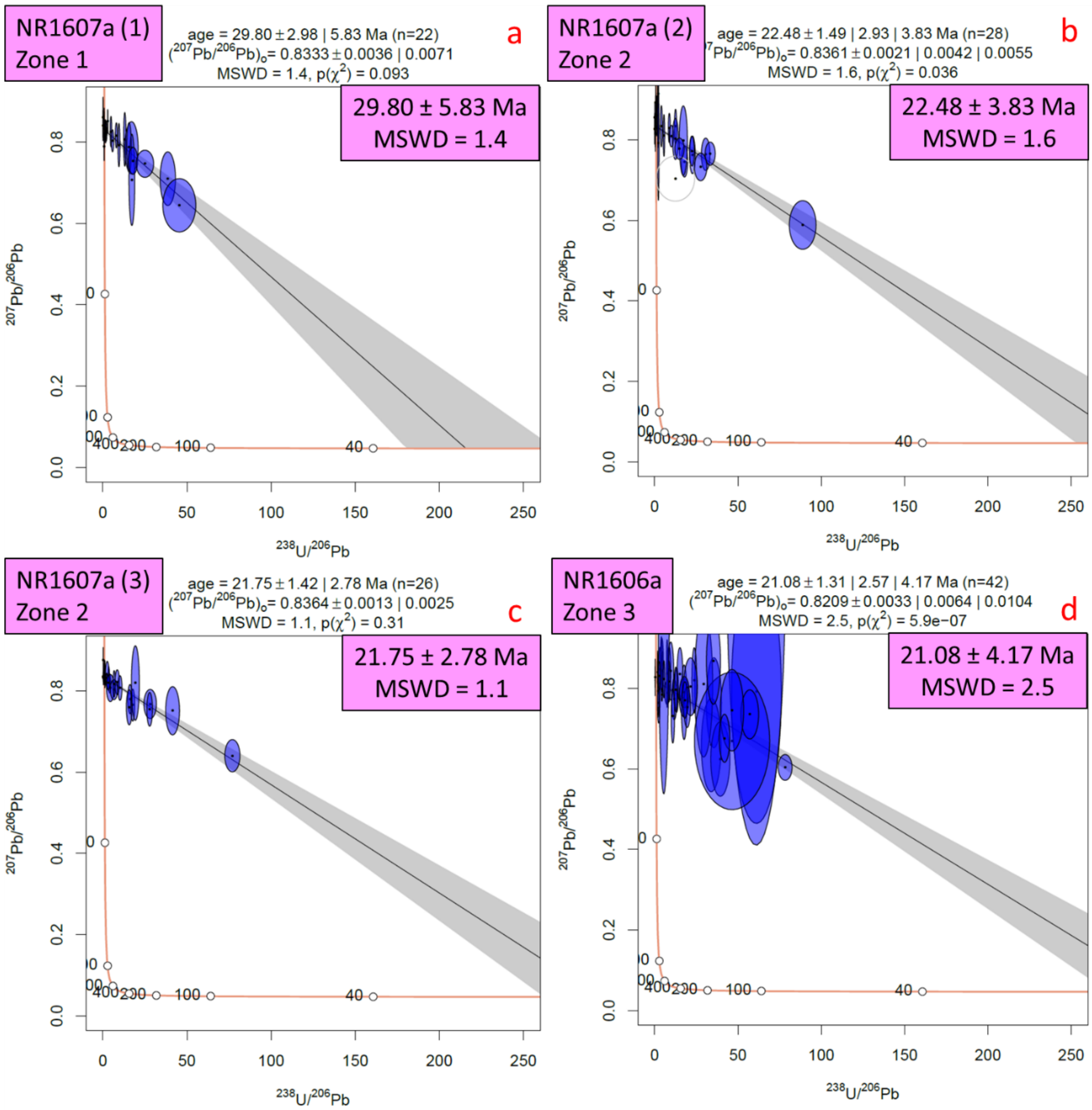


*Fig 4.48. T-W plots from the bedding-parallel calcite veins at Staithes.*

### 4.5.2 Subvertical Joint fills (Saltwick Nab and Sandsend)

Section 3.2.1 demonstrates the likelihood that N-S striking joints ($J_1$) at Saltwick Nab and Sandsend (Fig 4.45) have been reactivated and discontinuously filled with fibrous calcite veins (Fig 4.49). Four samples from subvertical veins have been analysed with images from three vein samples (JL1815, JL1934 and 1939) shown in Figure 4.50.

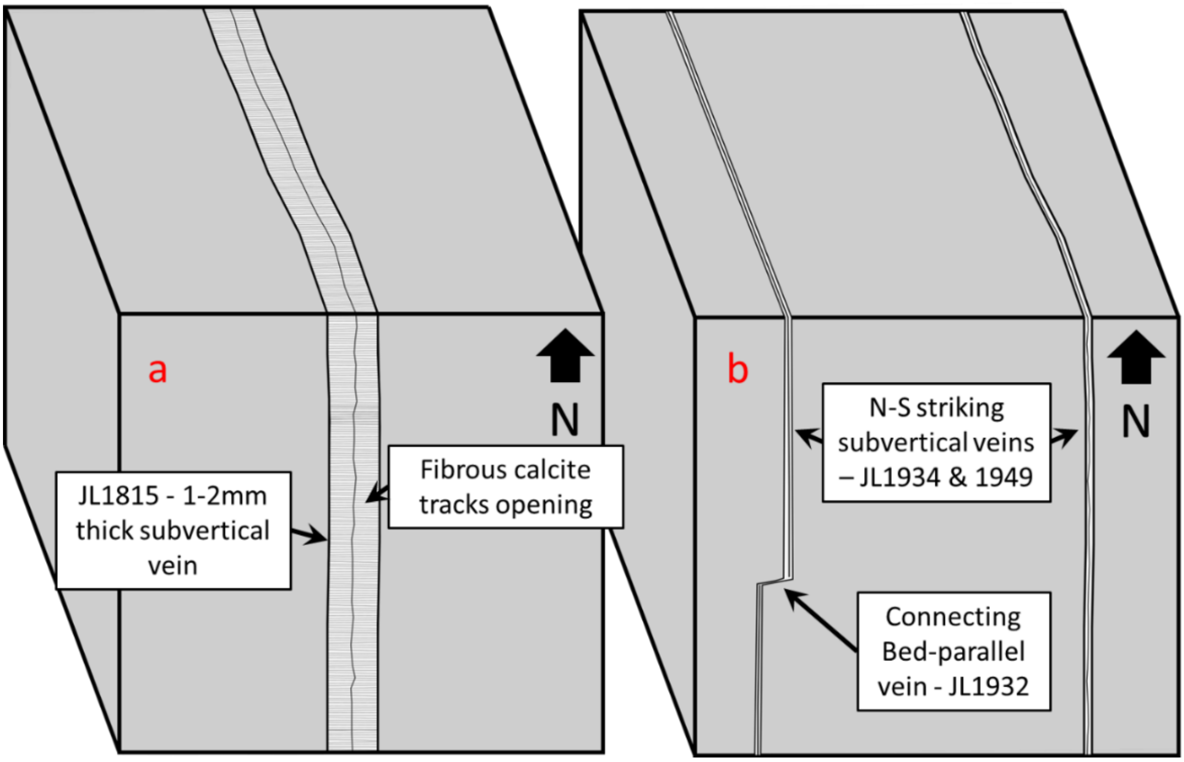


*Fig 4.49. Schematic block diagrams of subvertical veins in reactivated J1 joints at Saltwick Nab and Sandsend. a) A thin subvertical calcite vein with irregular median line and calcite veins tracking E-W opening similar to JL1815 at Saltwick Nab. b) Thin subvertical calcite veins similar to JL1934 and JL1939. A thin bedding-parallel vein (JL1932) connects two subvertical veins.*

The samples are indicative of predominantly Type I opening-mode veins undergoing dilation due to E-W extension, described previously in Chapter 3.

| Sample | Zone | Main Structure | Minor Structure | UTM N | UTM E | Calcite Fill | Texture | Kinematics | Dating |
|---|---|---|---|---|---|---|---|---|---|
| JL1815 | 1 | J1 Joints - Saltwick Nab | Vein - Vertical | 656232 | 6040793 | 1-2mm thick vein | Fibrous | Syn-dilation | Y |
| - | 2 | - | - | - | - | - | Blocky | Post dilation | - |
| JL1934 | 1 | J1 Joints - Sandsend | Vein - Vertical | 650693 | 6042954 | 1-2mm thick vein | Fibrous | Syn-dilation | Y |
| JL1939 | 1 | J1 Joints - Sandsend | Vein - Vertical | 650778 | 6043115 | 2-3mm thick vein | Fibrous | Syn-dilation | Y |
| JL1932 | 1 | J1 Joints - Sandsend | Vein - Bedding-parallel | 650684 | 6042769 | 1-2mm thick vein | Fibrous | Syn-dilation | Y |

*Table 4.12. Summary table of calcite fills from the subvertical veins at Saltwick Nab and Sandsend (Fig 4.45) analysed in this chapter. Samples not discussed here are presented in Appendix 8.1 & 8.2.*

JL1815 (Saltwick Nab)

JL1815 is a thin ~1mm thick calcite vein in a subvertical fracture with two zones of calcite (Fig 4.50a-c).

Zone 1 is composed of antitaxial fibrous calcite (800µm wide) that tracks opening perpendicular to the margins with an anastomosing median line with frequent mudstone inclusions. The anastomosing median line suggests high crack roughness and therefore good confidence in calcite fibres tracking opening.

Zone 2 is a thin layer of blocky calcite (<50µm wide) at the western margin and is interpreted to postdate the fibrous zone. The edge of the vein has patches of pyrite mineralisation, which is shown as white under reflected light (Fig 4.50a).

JL1934 & JL1939 (Sandsend)

JL1934 (Fig 4.50d-e) and JL1939 (Fig 4.50f-g) are similar to JL1815 but show a higher degree of undulation/vein roughness; both show antitaxial fibre growth, with fibres between 0.4-0.5mm long. Both samples show highly irregular/rough margins and median lines, which suggest a high likelihood of fibres tracking the fracture opening direction. JL1934 has a higher frequency of mudstone clasts (1-2%) relative to JL1939, with reflected microscopy showing common pyrite along the margins.

All subvertical veins contain primary fibrous calcite growth, which is inferred to track the opening direction. These veins are considered as high confidence zones for targeting during U-Pb geochronology and isotopic analyses although their thickness makes drilling for stable and clumped isotopes difficult.

Fibrous calcite from Zone 1 of JL1815 has been dated at 43.3 ± 1.8Ma with an MSWD of 1.3 (Fig 4.51b) and 45.4 ± 3.8Ma with an MSWD of 1.0 (Fig 4.51a). Both of these dates overlap in uncertainty and provide a good constraint on the timing of fracture dilation and sealing.

Zone 1 from JL1934 and Zone 2 from JL1932 and JL1939 have been dated at 43.1 ± 3.2Ma with an MSWD of 1.7 (Fig 4.51c), 39.0 ± 3.7Ma with an MSWD of 1.4 (Fig 4.51e) and 41.8 ± 3.0Ma with an MSWD of 1.2 (Fig 4.51d), respectively. These ages describe a period of joint reactivation, as described in Section 3.2.1, prior to fault movement. Therefore, it is clear that millimetre-wide subvertical calcite veins sampled at Saltwick Nab and Sandsend form a separate phase of E-W extension that predates later fault related deformation.

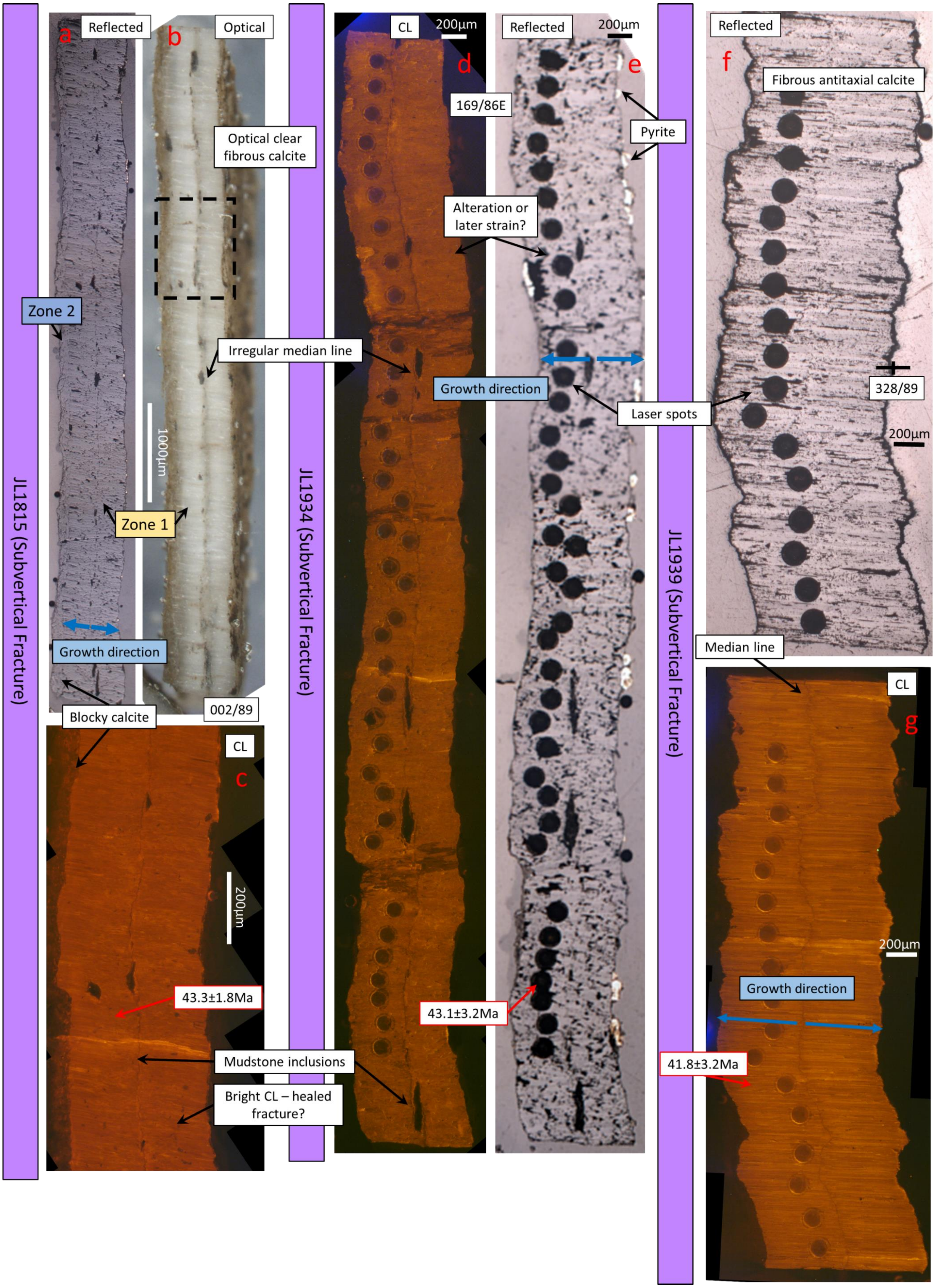


*Fig 4.50. Microscopy images of three predominantly fibrous calcite veins from subvertical joints at Saltwick Nab (Jl1815) and Sandsend (JL1934 & JL1939). 100µm diameter laser spots for U-Pb calcite dating can be seen. All samples have are have primary fibrous with margin perpendicular growth with inferred antitaxial growth.*

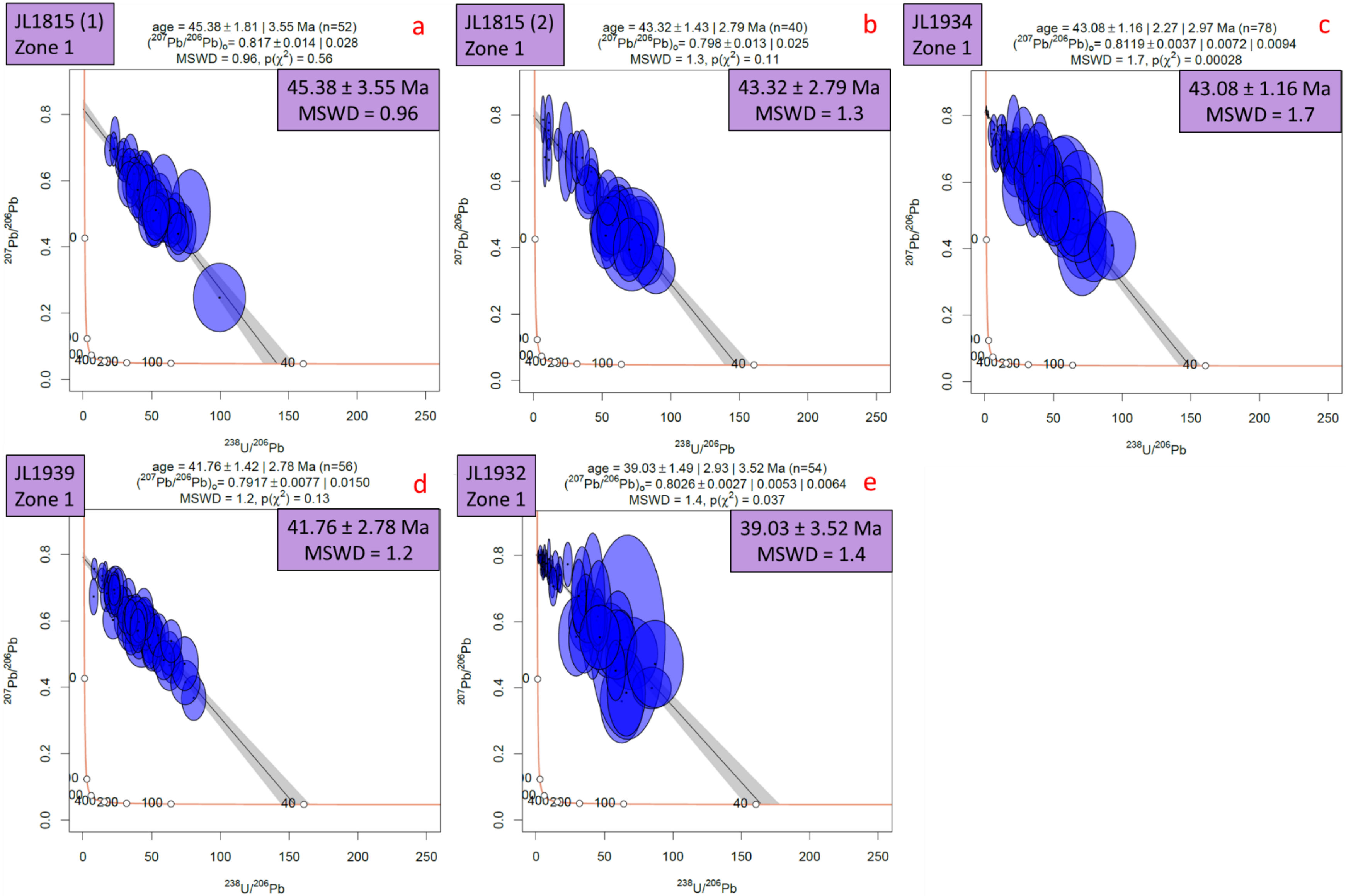


*Fig 4.51. T-W plots from the subvertical calcite veins at Saltwick Nab (JL1815) and Sandsend (JL1934, JL1939 & JL1932).*

### 4.5.5 Summary of Fracture Microstructures

Calcite fills from a variety of calcite fracture fills are presented from local fracture fills including subvertical and bedding-parallel veins.

#### 4.5.5.1 Bedding-parallel Veins

Bedding-parallel calcite samples from bedding-parallel fracture swarms at Staithes (Section 3.2.4.1) are complex veins with multiple generations of blocky and fibrous calcite that show progressive truncation and folding from youngest to oldest suggestive of repeated cycles of vertical dilation and bedding-parallel shear. The preserved calcites show primary textures with frequent inclusion bands indicative of crack-sealing. Fibrous calcite and inclusion bands detail vertical growth of calcite with shear evidently truncating material between growth phases. Alternating bedding-parallel shear and dilation likely reflects differential stress variation with tensile opening mode fracturing at low differential stress and shearing at higher differential stresses.

Bedding-parallel veins vary in age from ca. 30 to 21Ma (Fig 4.52). Two calcite zones have been dated in NR1607 with Zone 1 providing a date of 29.8Ma and Zone 3 giving dates of 22.5 and 21.8Ma. These dates indicate that a significant period of millions of years passed between phases of calcite precipitation in the bed parallel veins. Table 4.6 described the minimum and maximum expected period of activity/mineralisation along the bedding-parallel and subvertical veins.

#### 4.5.5.2 Subvertical Veins

Subvertical calcite veins are present at Saltwick Nab and Sandsend due to reactivation of the $J_1$ joint set (Section 3.2.4.2) with mm to cm-scale fibrous calcite fills formed. The veins demonstrate relatively simple primary calcite with antitaxial growth; calcite fibres track margin perpendicular growth (E-W dilation).

Subvertical veins vary in calcite age date from ca. 45 to 39Ma (Fig 4.52) and overlap in uncertainty. The constrained age range and lack of evidence of composite veins and multiple generations are suggestive of a well-constrained phase of deformation and associated fluid-flow associated with joint reactivation in a state of E-W extension.

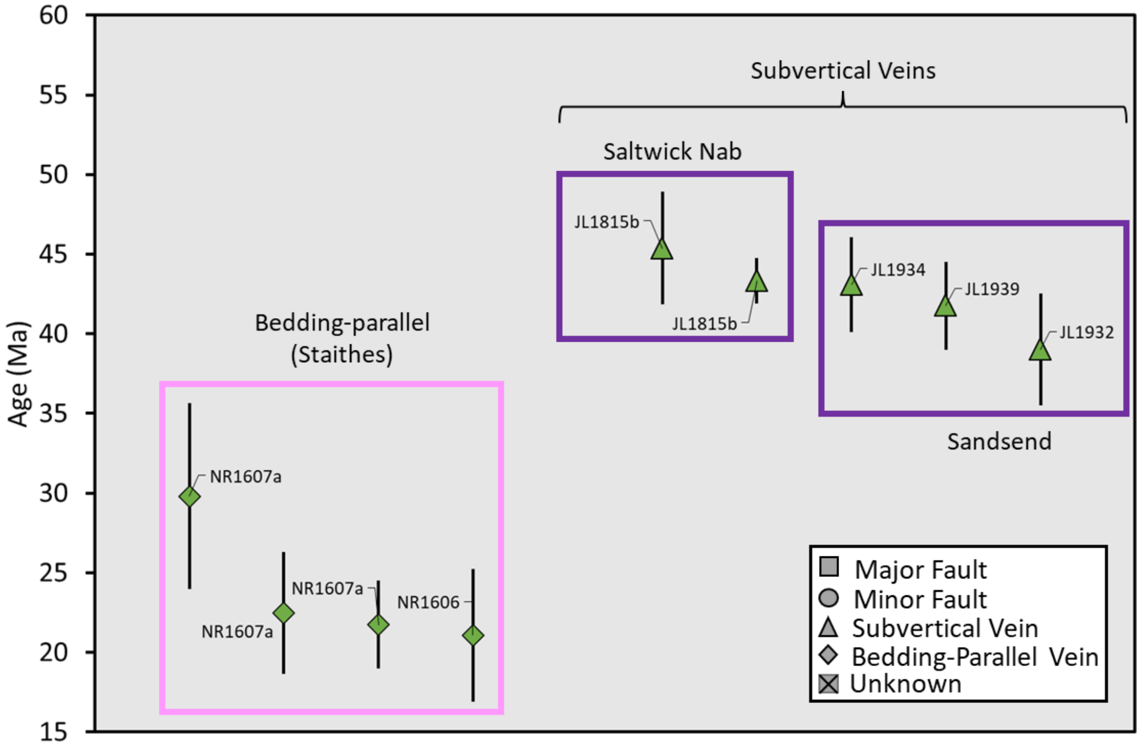


*Fig 4.52. Plot of U-Pb calcite geochronology results from local fracture structures versus Time/Age (Ma) with the symbols organised by the structure type. Green –samples are synchronous with fracture opening and dilation. As subvertical veins are inferred to be unrelated to fault movement the calcite is analysed with respect to dilational filling with fibres tracking crack dilation.*

| | Bed-parallel Veins | Subvertical Veins |
|---|---|---|
| Dates difference (Ma) | 8.7 | 6.4 |
| Max Activity (Ma) | 18.7 | 13.4 |
| Min Activity (Ma) | - | - |
| Overlap in ages (Ma) | 0.6 | 0.6 |

*Table 4.13. Compilation of the different age separations for the Local Fractures based on U-Pb calcite geochronology results with the Dates difference – the difference between the maximum and minimum date without uncertainty (2s), Maximum activity – the maximum period the structures could be active i.e. the maximum difference between the maximum age and minimum age including uncertainty, Minimum activity – the minimum period the structures are indicated to be active i.e. the minimum difference between the maximum age and minimum age including uncertainty. In some cases there will not be separation between a set of ages for a structure in which case the overlap in ages is also stated.*

## 4.6 Discussion

Examples of calcite fills from all key structure types are presented and demonstrate a variety of different fill types including extensional jog structures, opening-mode veins, breccia fills and slickenfibres. Full summaries of the microstructures are compiled in Appendix 8.2. This discussion will focus on the further implications of the U-Pb geochronology and microstructural results.

### 4.6.1 Preservation of Primary Calcite and Evidence for Crack-seal

Examples of calcite fills from all key structure types are presented and demonstrate a variety of different fill types including extensional jog structures, opening-mode veins, breccia fills and slickenfibres. In addition to the importance of considering the suitability of samples as synchronous to mineralisation and local faulting (Section 4.6.2), it is important first to determine the presence of primary calcite mineralisation or evidence of recrystallisation.

Good evidence of primary calcite mineralisation is considered here to include:

- The preservation of primary calcite with clear growth textures (syntaxial, antitaxial, unitaxial and ataxial); Bons, 2000; Bons et al., 2012);
- Little or no evidence of later deformation (cataclasis), alteration or reprecipitation;
- Evidence of growth direction e.g. inclusion trails, crack-seal textures and/or fibres (Ramsay et al., 1983; Köhn & Passchier, 2000).

The calcite veins studied are inferred to be primary, unaltered calcite with few indications of possible alteration and/or reprecipitation. Also of importance is the lack of evidence described for widespread cataclastically-deformed calcite, except SSK110588, or evidence for later dynamic recrystallisation.

Fibrous growth with crack-seal textures are suggested as the best options for U-Pb calcite dating where possible. In general, the roughness of calcite veins (JL1815, JL1934 & JL1939) are supportive of tracking behaviour of calcite fibres (Urai et al., 1991). This is further compounded by evidence in JL2023 and JL2024 of inclusion trails tracking growth in a similar opening mode direction as calcite fibres. NR1620, in contrast, shows smooth margins and fibres oriented normal to the fault plane might not track opening as in cases documented by Means & Li (2001).

Taber growth, where crack dilation occurs due to crystallisation pressure as discussed by Means & Li (2001), is considered unlikely as, in addition to issues highlighted in Section 4.3.2.1 regarding the source of fluid through an impermeable wall rock, many fibrous calcite veins analysed are consistent with a gradual transition from antitaxial fibrous crack-seal to blocky crack-fill (JL1815, JL2023 & JL2024). Crack-fill requires an open void for calcite to precipitate into with calcite growth slower than the opening rate, as shown by Passchier & Trouw (2005). This transition from fibrous to blocky calcite suggests that opening was controlled by tectonic dilation and not by local crystallisation pressure.

### 4.6.2 Syn-kinematic mineralisation

An important objective of the microscopic analyses described herein is establishing the relationship of mineralisation to fault movement. Structural observations and stress inversion analysis in Chapter 3 worked to describe a period of E-W extension with U-Pb calcite geochronology and isotopic analyses focussed on dating and fingerprinting this period of deformation and associated fluid-flow. It is, therefore, critical to determine that the mineralisation sampled is related to the same period of deformation described from field relations.

Determining the kinematic relationship of a sample can be complicated and utilises a combination of the field setting of a sample combined with the microstructural textures as described above. While a typical crack-seal vein might not be considered syn-kinematic, an extensional jog with clear crack-seal is highly likely to reflect the opening of that structure assuming consistent shear direction. In this manner, samples have been analysed with relation to their field geometries with additional features such as shear planes, inclined fibres, crack-seal textures and slickenfibres used to help refine interpretations.

However, this does not mean that other samples are not of use: pre-kinematic samples that have been incorporated into later gouges through cataclasis, and post-kinematic fills enable lower and upper margins to be applied to the timing of fault movement. In addition, post to syn-kinematic help define times during which fault movement or dilation for fractures had already occurred and during which fluid-flow was still occurring after deformation leading to associated calcite mineralisation. Conventional stable and clumped isotopic analyses in Chapter 5 will analyse a wide range of fills to try and identify systematic relationships in fluid temperatures and isotopic compositions.

#### 4.6.2.1 Breccia structures

Breccia structures are important to consider as many samples show brecciation or plucking of clasts. Describing observations of breccia samples will allow their relation to kinematic fault movement to be better understood and determined. The breccias, described herein, are inferred to be dominated by dilation with typically 5-60% clasts. These are therefore classified texturally as fault fills or chaotic breccias (Fig 4.53). The breccia samples classified here are shown to be dominated by dilation and therefore based on the system developed by Sibson (1986) are classified as implosion breccias. This is established by the common relationships of clasts with included clasts commonly aligned with the margins (NR1622, JL2023, & JL1809) or showing a systematic plucking or brecciation apart from each other, as observed in samples NR1609, JL1809, and JL2016.

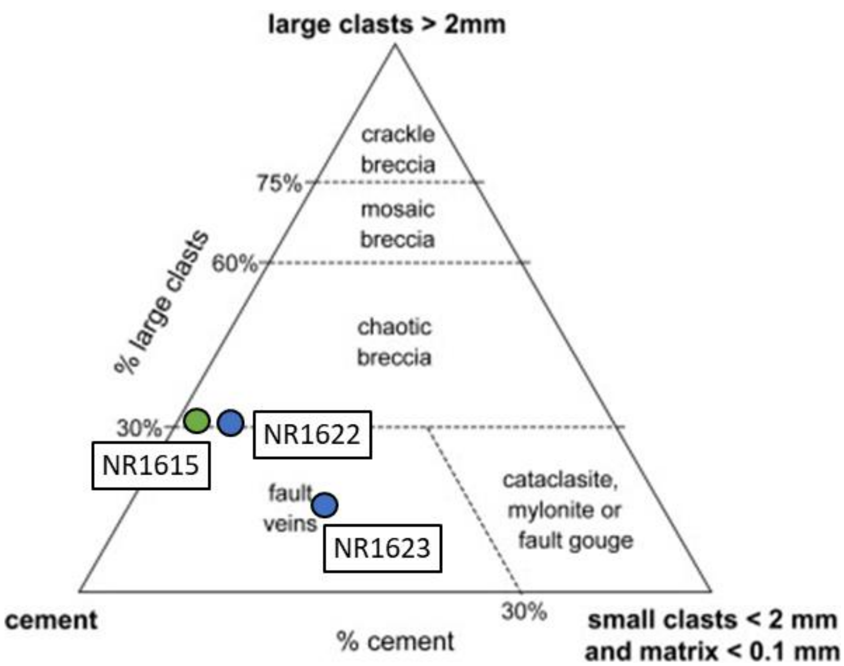


*Fig 4.53. Ternary classification diagram from Mort & Woodcock (2008). Breccia samples NR1622, NR1623 and NR1615 are shown as having fault vein to chaotic breccia textures.*

The implications of these classifications suggest that all the breccia structures analysed are dominated by dilation, which is consistent with the stress inversion presented in Chapter 3. The textures show typically few clasts and plot around the "Fault Vein" field based on the classification scheme by Mort & Woodcock (2008). This is suggestive that mineralisation is dominant and crack opening is dominant over shear and brecciation. The decreasing proportion of clasts towards the centre of syntaxial fault veins (JL1809c & NR1615) is indicative that mudstone clasts are incorporated early in the cycle of vein development with little strain localised along the vein post development.

Breccia samples analysed are typically dilational and are consistent with expected dilation directions from fault movement with many breccias formed in dilational jogs or as fault plane veins along extensional faults. This consistency of brecciation style further backs up the inferred stress regime from observations in Chapter 3 and stress inversion analysis in Section 3.3.

### 4.6.3 Summary

Geochronological and isotopic analyses have attempted to constrain and analyse all crystal textures and zones. This is important, as while syn-kinematic calcite precipitation needs to be constrained, post-kinematic crack-fill textures can provide information on periods of tectonic quiescence or the timing by which tectonic deformation had ceased and calcite was precipitated passively into previously opened space.

Isotopic analyses in the next chapter will focus on building on the microstructural and U-Pb calcite geochronology results and analysis described herein with the aim of analysing and constraining the Cenozoic fluid-flow regime in the Cleveland Basin associated with the prolonged period of E-W extension.

# Chapter 5- Cenozoic fluid-flow in the Cleveland Basin

## 5.1 Introduction

In the previous chapters, I have utilised structural analyses combined with targeted U-Pb calcite geochronology to describe an extended period of Cenozoic deformation and fluid-flow in the Cleveland Basin. I have suggested that faults and fractures have acted as fluid-flow conduits in the subsurface, allowing fluids to move through low permeability, Liassic, clay-rich mudstones. The aim of this chapter is to utilise isotopic analyses to further interrogate the origins of fluids, the source of carbon and the possible connectivity of potential fluid conduits, i.e. the range of observed faults and fractures.

This chapter will focus on the following objectives:

1. For carbonate fracture fills, describe and summarise (a) conventional carbon and oxygen stable isotope data and (b) clumped isotope and fluid inclusion analyses, highlighting populations and trends within the datasets.

2. Determine the temperature and fluid source of the calcite fracture fills.

3. Present a model for the fluid system in the Cleveland Basin, inferring the origin of mineralising fluids and flow paths through fine-grained sedimentary sequences.

4. Compare the isotopic results to analogous results from the Flamborough Head Fault Zone and the Wessex Basin.

The appraisal of fluid sourcing and the nature of calcite mineralising fluids in the Cleveland Basin will provide important understandings about a poorly constrained period of subsurface fluid-flow through fracture permeability in organic-rich mudstones of the Lower Jurassic. No previous studies have appraised the composition or controls on Cenozoic fluid-flow and associated calcite mineralisation in the Cleveland Basin. The low permeability mudstones of the Jurassic, however, provide an excellent opportunity to interrogate the role of extensional deformation in fluid migration through analogue $CO_2$ and hydrocarbon seal or source rocks in the subsurface.

The work in Chapters 3 & 4 described a period of Cenozoic extension from < 40 Ma and no previous work has analysed the contemporaneous fluid-flow regime that resulted in calcite mineralisation in the associated faults and fractures. Faÿ-Gomord et al. (2018), however, has utilised a combination of stable, clumped and strontium isotopes and fluid inclusion analysis to interrogate fluid-flow along the Frontal Fault Zone at Selwicks Bay. The Frontal Fault Zone is part of the larger Flamborough Head Fault Zone and has been U-Pb calcite dated by Roberts et al. (2020) at 63-55 Ma. These analyses will be discussed in Section 5.4.5 and Chapter 6 to compare the results described herein and determine the relationship of early fluid-flow at Selwicks Bay to the fluid-flow regime described in this work.

Previous work has utilised isotopic and other geochemical analyses to trace fluid-flow in similar tectonic regimes and to determine the relationship of calcite veins to fluid-flow. Worden et al. (2016) utilised stable isotopes and fluid inclusion analysis to describe Jurassic, mudstone-hosted tectonic calcite veins from the Wessex Basin. These veins will be discussed further in Section 5.4.5 as a comparison to the results described herein. In addition, other work by Bergman et al. (2013) and MacDonald et al. (2020) have used clumped isotopes to constrain the origin of tectonic calcite veins. Bergman et al. (2013) utilised clumped isotopes on calcite to identify the isotopic composition of fluids and temperature variations associated with the Moab Fault, Utah. Both isotopic composition and temperature varied systematically away from the main fault plane. MacDonald et al. (2020) used clumped isotopes along with trace elements and U-Pb geochronology to interrogate fluid flow related to Devonian Montrose Volcanic Formation at Lunan Bay (Montrose, Scotland). Timings and isotopic composition were used to suggest precipitation from a shallow surface water source with significant fluid-rock interaction.

### 5.1.1 Isotopic Fractionation

Stable Isotopes are non-radioactive atoms whose nucleus contains the same number of protons but a different number of neutrons (Hoefs, 1997). The two main stable isotopes that will be discussed here are oxygen (Section 5.3.2) and carbon (Section 5.3.3) isotopes. Stable isotopes can undergo isotopic fractionation during processes such as evaporation or condensation which can lead to enrichment or depletion relative to a standard of an isotope in a reactant or product. By comparing isotopic results to standards of known isotopic concentration stable isotope results can be used in fracture systems as indicators of fluid or host rock properties. Pee Dee Belemnite (PDB) is a common isotopic standard utilised for stable isotope analysis in carbonates which compares samples to a Belemnitella americana from the Peedee Formation (Craig, 1957) or more mmonly the equivalent Vienna PDB as the original sample is no longer available. Further explanation of the fundamentals of stable isotope geochemistry is beyond the scope of this thesis but can be found in Hoef (2018).

### 5.1.2 Sampling

A sampling strategy for isotopic analyses was decided prior to the initial conventional carbonate stable isotope analysis and evolved as results were generated. The initial strategy was to sample a wide range of different structures reflecting both crack-fill and crack-seal textures with the aim to provide a complete picture of the entire history of fluid-flow. Sampling for clumped isotopes and fluid inclusion analysis was done based on structural criteria to better constrain the temperature and fluid composition and was focused on crack-seal samples from all the key localities. Pre-screening of samples from thin section and resin mounts allowed targeting of sampling towards samples that had a higher chance of analytical success and data quality. This pre-screening involved the identification of primary calcite growth textures and syn-kinematic indicators, as described in detail in Chapter 4. Calcite fills were subdivided into distinct zones/generations. Samples were chosen for isotopic analysis where confidence existed about the style and absolute timing of deformation.

## 5.2 Isotopic Results

### 5.2.1 Conventional Carbonate C-O Stable Isotopes

In total 39 samples were microdrilled for carbon and oxygen stable isotope analysis. These samples were chosen to cover a wide range of fill types and structural divisions. No millimetre-scale veins were initially analysed due to their small size and because they were considered at high risk of epoxy resin contamination.

All samples were analysed at the NIGL facilities at the British Geological Survey as described in Section 2.5. The stable isotope results for 39 C-O conventional carbonate stable isotope samples are shown in full in Table 5.1 and averages, minimum and maximum statistics are summarised in Table 5.2. The samples show variation from -15.9‰ to -6.0‰ $\delta^{18}O_{PDB}$ and from -12.3‰ to +16.0‰ $\delta^{13}C_{PDB}$, with averages of -12.7‰ $\delta^{18}O_{PDB}$ and -4.5‰ $\delta^{13}C_{PDB}$. The isotopic results are described by structural division in Table 5.2. These are subdivided into two main populations.

| | N | Avg δ13C (‰) PDB | Min δ13C (‰) PDB | Max δ13C (‰) PDB | Avg δ18O (‰) PDB | Min δ18O (‰) PDB | Max δ18O (‰) PDB | Mean δ18O (‰) VSMOW | Min δ18O (‰) VSMOW | Max δ18O (‰) VSMOW |
|---|---|---|---|---|---|---|---|---|---|---|
| All | 39 | -4.46 | -12.33 | 15.95 | -12.70 | -15.86 | -5.98 | 17.82 | 14.56 | 24.74 |
| Peak Fault | 3 | -1.57 | -10.60 | 12.23 | -11.81 | -13.54 | -9.19 | 18.73 | 16.95 | 21.43 |
| Cayton Bay Fault | 4 | -2.00 | -3.29 | -0.91 | -12.68 | -13.78 | -11.92 | 17.84 | 16.70 | 18.63 |
| Red Cliff Fault | 2 | 0.51 | 0.37 | 0.66 | -15.47 | -15.71 | -15.23 | 14.96 | 14.71 | 15.21 |
| Runswick Bay Fault | 7 | -4.69 | -6.02 | -3.90 | -13.72 | -15.86 | -9.50 | 16.77 | 14.56 | 21.12 |
| Staithes Faults | 7 | -4.09 | -12.33 | 15.95 | -12.84 | -14.32 | -10.02 | 17.67 | 16.15 | 20.58 |
| Port Mulgrave Fault | 11 | -6.85 | -11.57 | -0.09 | -12.23 | -15.20 | -5.98 | 18.30 | 15.24 | 24.74 |
| Dextral Oblique-slip Faults | 0 | - | - | - | - | - | - | - | - | - |
| Sinistral Oblique-slip Faults | 3 | -4.99 | -5.73 | -3.89 | -11.68 | -12.34 | -11.28 | 18.87 | 18.19 | 19.28 |
| Elm Tree Farm Borehole | 2 | -5.32 | -6.92 | -3.72 | -11.31 | -11.33 | -11.29 | 19.25 | 19.23 | 19.27 |
| Subvertical Veins | 0 | - | - | - | - | - | - | - | - | - |

*Table 5.2. Statistical information for the stable isotope results subdivided by the structural divisions outlined first in Chapter 3. Carbon and oxygen isotope data from clumped isotope analysis (circles in Fig 5.1 & 5.2) are not included in this statistical analysis.*

| Structure | | | Sample | | | | | | U-Pb Calcite Geochronology | Bulk Carbonate Stable Isotopes | | | | | | |
|---|---|---|---|---|---|---|---|---|---|---|---|---|---|---|---|---|
| Major | Locality | Subsidiary | Fill Type | Name | Zone | Thickness | Crystal Texture | Synkinematic | Calcite Date (Ma) | $\delta^{18}O$ (‰) PDB | $\delta^{13}C$ (‰) PDB | Replicates $\delta^{18}O$ (‰) PDB | Replicates $\delta^{13}C$ (‰) PDB | Mean $\delta^{13}C$ (‰) PDB | Mean $\delta^{18}O$ (‰) PDB | Mean $\delta^{18}O$ (‰) VSMOW |
| Peak Fault | Ravenscar | Splay Fault Plane | Extensional Jog | NR1619 | 1 | 2-3cm | Blocky | Syn or post-kinematic | 28.6 | -13.47 | -10.77 | -13.61 | -10.60 | -10.68 | -13.54 | 16.95 |
| | | | - | NR1619 | 1 | - | - | Syn or post-kinematic | 28.6 | -12.64 | -6.61 | -12.78 | -6.10 | -6.35 | -12.71 | 17.81 |
| | | | Extensional Jog | JL2020 | 3 | 3-4mm | Blocky | Syn or post-kinematic | - | -9.19 | 12.23 | | | 12.23 | -9.19 | 21.43 |
| Cayton Bay Fault | Osgodby Nab | Subvertical Veins | 2-3cm thick Vein | JL2026 | 1 | 1cm | Blocky | Syn or post N-S Opening | 36.2 | -11.92 | -1.32 | | | -1.32 | -11.92 | 18.63 |
| | | | 2-3cm thick Vein | JL2027 | 1 | 3-4mm | Blocky | Syn or post N-S Opening | - | -12.41 | -0.91 | | | -0.91 | -12.41 | 18.11 |
| | | | 2-3cm thick Vein | JL2029 | 1 | 1mm | Blocky | Syn or post E-W Opening | - | -13.71 | -3.24 | -13.85 | -3.33 | -3.29 | -13.78 | 16.70 |
| | | Main Fault | Anastomosing Veins | JL2030 | 1 | >3cm | Blocky | Syn or post-kinematic | 32.9 | -12.59 | -2.49 | | | -2.49 | -12.59 | 17.93 |
| Red Cliff Fault | High Red Cliff | Not in-situ | Cone-in-cone | JL2031 | 1 | >5cm | Cone-in-cone | Unknown | 46.5 | -15.23 | 0.66 | | | 0.66 | -15.23 | 15.21 |
| | | | Blocky calcite | JL2032 | 1 | >5cm | Blocky | Unknown | 55.0 | -15.71 | 0.37 | | | 0.37 | -15.71 | 14.71 |
| Runswick Bay Fault | Runswick Bay | Main Fault | Breccia and jog | NR1615 | 1 | 2cm | Blocky | Syn to post-kinematic | 32.3 | -13.71 | -6.02 | -13.64 | -6.01 | -6.02 | -13.67 | 16.82 |
| | | Normal Faults | Extensional Jog | NR1612 | 1 | 1.5cm | Blocky | Synkinematic | 32.8 | -14.38 | -12.12 | -14.33 | -4.24 | -4.03 | -14.35 | 16.11 |
| | | | - | NR1612 | 1 | - | - | Synkinematic | 32.8 | -14.35 | -3.90 | | | -3.90 | -14.35 | 16.12 |
| | | | - | NR1612 | 1 | - | - | Synkinematic | 32.8 | -14.25 | -4.16 | | | -4.16 | -14.25 | 16.22 |
| | | | - | NR1612 | 1 | - | - | Synkinematic | 32.8 | -14.06 | -4.03 | | | -4.03 | -14.06 | 16.41 |
| | | | Extensional Jog | JL2010 | 1 | >2cm | Blocky | Synkinematic | - | -9.50 | -5.56 | | | -5.56 | -9.50 | 21.12 |
| | | Subvertical Veins | 0.5mm thick Vein | JL2012 | 1 | 400µm | Fibrous | Syn E-W Opening | - | -15.86 | -5.12 | | | -5.12 | -15.86 | 14.56 |
| Staithes Faults | Staithes | Normal Faults | Calcite in gouge | NR1501 | 1 | >2cm | Blocky | Pre to Synkinematic | 33.8 | -13.60 | -11.69 | | | -11.69 | -13.60 | 16.89 |
| | | | - | NR1501 | 1 | - | - | Pre to Synkinematic | - | -13.35 | -11.57 | -13.59 | -12.12 | -11.84 | -13.47 | 17.02 |
| | | | Thin Vein/Jog | NR1604 | 1 | >2cm | Blocky | Synkinematic | 39.0 | -14.07 | -11.06 | | | -11.06 | -14.07 | 16.41 |
| | | | Extensional Jog | NR1809a | 2 | 1.2mm | Blocky | Synkinematic | 25.2 | -14.32 | -12.33 | | | -12.33 | -14.32 | 16.15 |
| | | | - | NR1809a | 3 | 4mm | Blocky | Synkinematic | 36.1 | -13.31 | -11.79 | -13.69 | -11.70 | -11.75 | -13.50 | 16.99 |
| | | Subvertical Veins | 0.5cm thick Vein | NR1503 | 3 | 1.5mm | Blocky | Syn or post E-W Opening | 31.4 | -10.02 | 15.95 | | | 15.95 | -10.02 | 20.58 |
| | | | - | NR1503 | 3 | - | - | Syn or post E-W Opening | - | -10.90 | 14.08 | | | 14.08 | -10.90 | 19.67 |
| Port Mulgrave Fault | Port Mulgrave | Normal Faults | Extensional Jog | NR1504 | 1 | >2mm | Blocky | Syn to post-kinematic | 32.3 | -14.51 | -9.80 | -14.43 | -10.27 | -10.04 | -14.47 | 15.99 |
| | | | - | NR1504 | 1 | - | - | Syn to post-kinematic | 32.3 | -14.27 | -10.76 | | | -10.76 | -14.27 | 16.20 |
| | | | Extensional Jog | NR1505 | 1 | >3mm | Blocky | Syn to post-kinematic | 33.5 | -14.14 | -8.53 | | | -8.53 | -14.14 | 16.33 |
| | | | Extensional Jog | JL2001a | 1 | 1-2cm | Blocky | Syn to post-kinematic | 27.2 | -10.99 | -3.78 | -10.81 | -3.83 | -3.80 | -10.90 | 19.67 |
| | | | - | JL2001a | 1 | - | - | Syn to post-kinematic | 27.2 | -10.75 | -4.58 | -10.67 | -4.49 | -4.54 | -10.71 | 19.87 |
| | | Subvertical Veins | 1-2mm thick vein | NR1609b | 1 | 3mm | Blocky | Syn or post E-W Opening | 37.3 | -14.69 | -10.79 | -13.97, -13.65 | -10.17, -10.09 | -10.35 | -14.10 | 16.37 |
| | | | - | NR1609b | 2 | 1-2mm | Fibrous | Syn Opening | 37.3 | -14.89 | -10.79 | -12.66 | -11.10 | -11.57 | -13.78 | 16.71 |
| | | | - | NR1609b | 3 | 1-3mm | Blocky | Syn or post E-W Opening | - | -6.28 | -10.79 | -6.06, -5.61 | -0.35, 0.41 | -0.09 | -5.98 | 24.74 |
| | | | 0.5mm thick Vein | JL2004 | 1 | 500µm | Fibrous | Syn E-W Opening | - | -15.20 | -6.83 | | | -6.83 | -15.20 | 15.24 |
| | | Bed-parallel Veins | 0.5-1mm thick Vein | JL2002c | 1 | 500-1000µm | Blocky | Syn to post-kinematic | 23.3 | -10.47 | -4.93 | | | -4.93 | -10.47 | 20.11 |
| | | | - | JL2002a | 1 | - | - | Syn to post-kinematic | 23.3 | -10.51 | -3.86 | | | -3.86 | -10.51 | 20.08 |
| Sinistral Oblique-slip Faults | Port Mulgrave | Bed-parallel Veins | 2-3cm thick Vein | JL2007b | 1 | 1-2cm | Blocky | Synkinematic | 26.8 | -11.42 | -5.36 | | | -5.36 | -11.42 | 19.14 |
| | | | - | JL2007b | 1 | - | - | Synkinematic | 26.8 | -11.10 | -3.89 | | | -3.89 | -11.28 | 19.28 |
| | | | - | JL2007a | 1 | - | - | Synkinematic | 26.8 | -12.34 | -5.73 | | | -5.73 | -12.34 | 18.19 |
| Elm Tree Farm Borehole | | Faults | Calcite in gouge | SSK110596 | 1 | 3-4mm | Blocky | Pre to Synkinematic | - | -11.33 | -3.72 | | | -3.72 | -11.33 | 19.23 |
| | | | Calcite in gouge | SSK110598b | 1 | 3-4mm | Blocky | Pre to Synkinematic | - | -11.29 | -6.92 | | | -6.92 | -11.29 | 19.27 |

*Table 5.1. Summary of the conventional carbonate C-O stable isotope results including structure, sample and geochronology information for additional context. Where a single zone has been analysed twice the same U-Pb calcite geochronology age has been applied under the assumption that age is representative of the zone as a whole.*

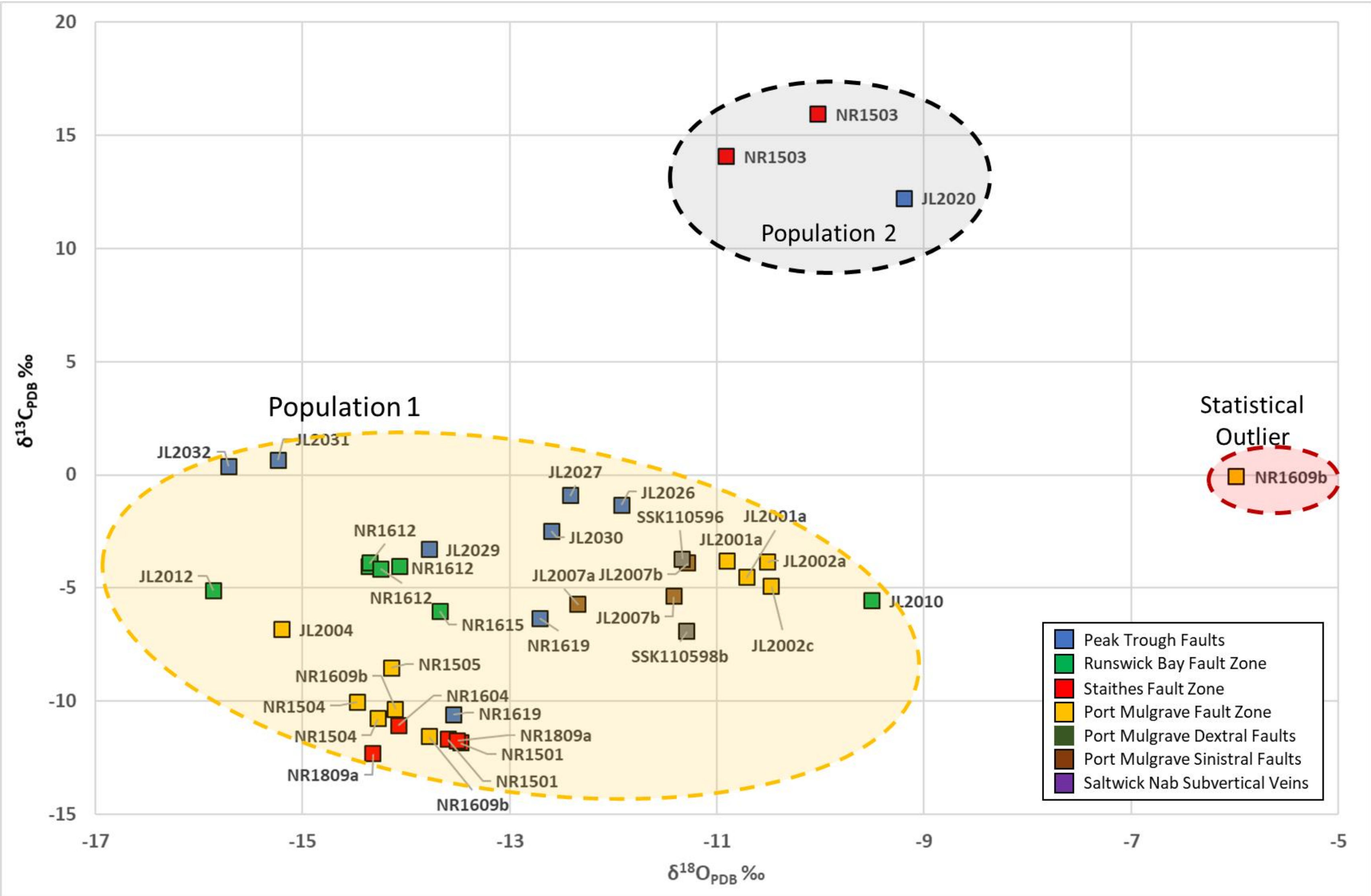


*Fig 5.1. $\delta^{13}C_{PDB}$ vs $\delta^{18}O_{PDB}$ for calcite fracture fills. Squares denote carbon and oxygen isotope data from conventional carbonate analysis. The minimum and maximum extents of the data are described in Table 5.2. Data populations and outlier data are identified and highlighted. NR15609b forms a statistical outlier, 3‰ more positive than any other vein fill sampled.*

### 5.2.1.1 Carbon and Oxygen Populations

The main population of data ranges from -11 and -16‰ $\delta^{18}O_{PDB}$ (Fig 5.3a) and 0.5 and -13‰ $\delta^{13}C_{PDB}$ (Gif 5.3b; Population 1 in Fig 5.1) and includes data from all major structural divisions (Fig 5.2). The data population has significant variation, which could reflect differences in both temperature and fluid source.

The secondary stable isotope population sits at positive $\delta^{13}C_{PDB}$ values: +6 and +16‰ $\delta^{13}C_{PDB}$ and -9 and -11‰ $\delta^{18}O_{PDB}$ (Population 2 in Fig 5.1). The positive $\delta^{13}C$ signature is indicative of fractionation due to microbial reduction of $CO_2$ to $CH_4$. During microbial methanogenesis $^{12}C$-rich $CO_2$ is produced with $^{13}C$ preferentially concentrated in the $CO_2$ residue. This $CO_2$ residue is then incorporated into authigenic minerals of this highly $^{13}C$ positive residue, suggested as an indicator of methanogenesis (Drake et al., 2021).

In addition, a measured sample from NR1609 sits outside the main data population at 0‰ $\delta^{18}O_{PDB}$ and -6‰ $\delta^{13}C_{PDB}$ (Fig 5.1). This statistical outlier will not be discussed here in order to focus on the main data population.

### 5.2.1.2 Subdivisions in the main population

The subdivisions of the C-O conventional carbonate data are illustrated in Figure 5.2 and 5.3. While it is clear that trends in the results exist with data from similar geographical and structural locations such as the Runswick Bay and Staithes fault zones forming distinct populations, data from similar localities and structures still show significant variation, with Port Mulgrave divided into two separate subpopulations.

The Peak Trough faults show significant differences between data populations. The Peak Fault and Cayton Bay subpopulation is centred on -13‰ $\delta^{18}O_{PDB}$ and -3‰ $\delta^{13}C_{PDB}$, however JL2020 sits in the methanogenesis population and NR1619 situated at more negative $\delta^{13}C$ values near the Staithes Fault Zone subpopulation.

The two Red Cliff Fault samples sit away from the main data population at values of -15.5‰ $\delta^{18}O$ and +0.5‰ $\delta^{13}C_{PDB}$.

Data from Runswick Bay form a relatively tight population centred on -14.5‰ $\delta^{18}O_{PDB}$ and -4.5‰ $\delta^{13}O_{PDB}$, with only one outlier (JL2010); the results from Staithes, in contrast, split between the methanogenic population (two samples from NR1503) and a subpopulation centred on -13.5‰ $\delta^{18}O_{PDB}$ and -12‰ $\delta^{18}O_{PDB}$. The Port Mulgrave data is more variable with the majority of data split between two subpopulations (1 & 2) with oblique slip samples (brown and dark green) showing variable $\delta^{18}O$, between -13.5 and -10.5‰ $\delta^{18}O_{PDB}$, at a consistent $\delta^{18}C_{PDB}$ value of ~-5‰. The Elm Tree Farm Borehole samples plot in a small subpopulation at -11.5‰ $\delta^{18}O$ and -5‰ $\delta^{13}C$**.**

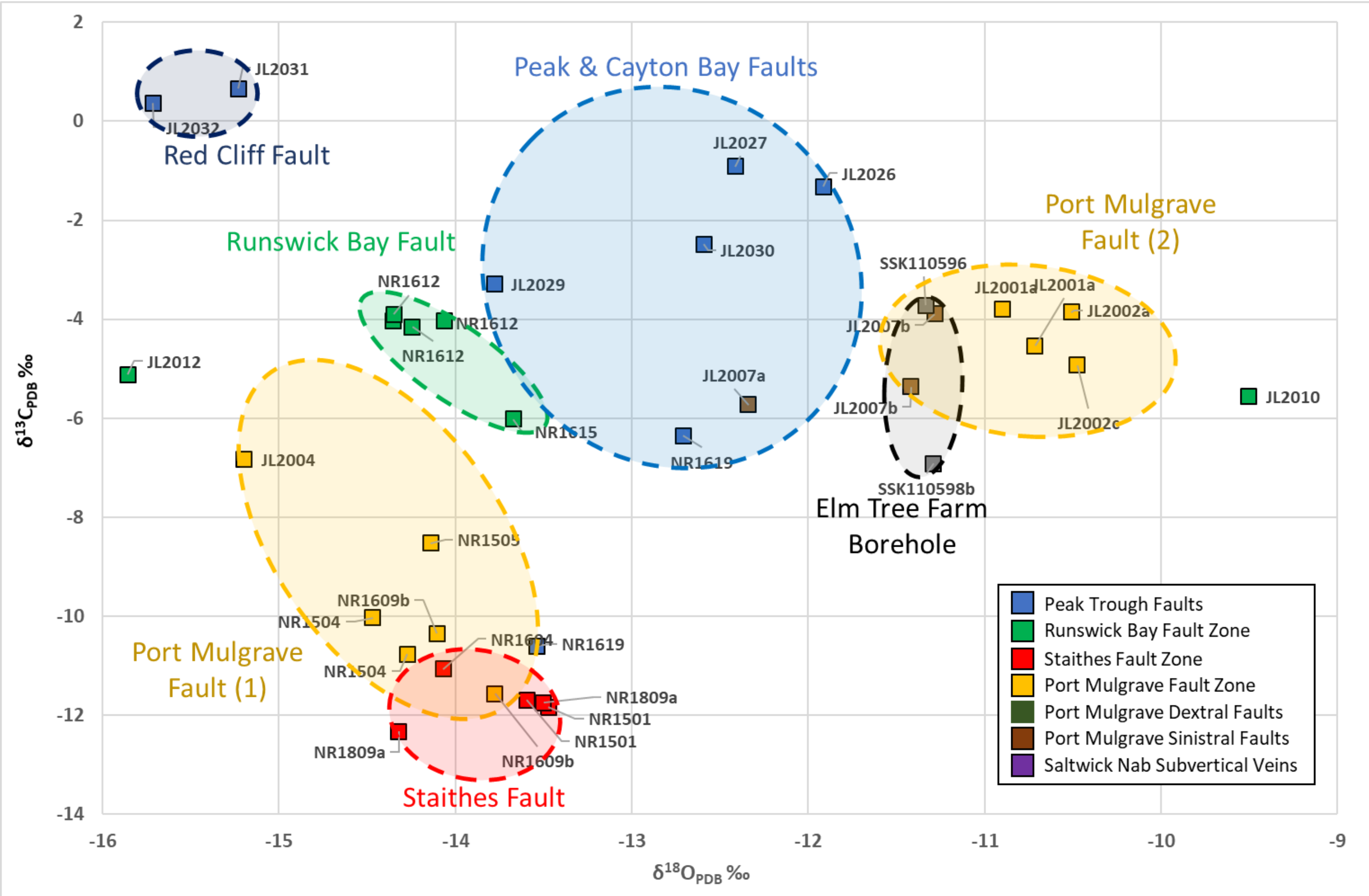


*Fig 5.2. $\delta^{13}C_{PDB}$ vs $\delta^{18}O_{PDB}$ for stable isotope samples coloured by the structural subdivision similarly to Figure 5.1. Ellipses are included to group and subdivide samples with similar isotopic compositions.*

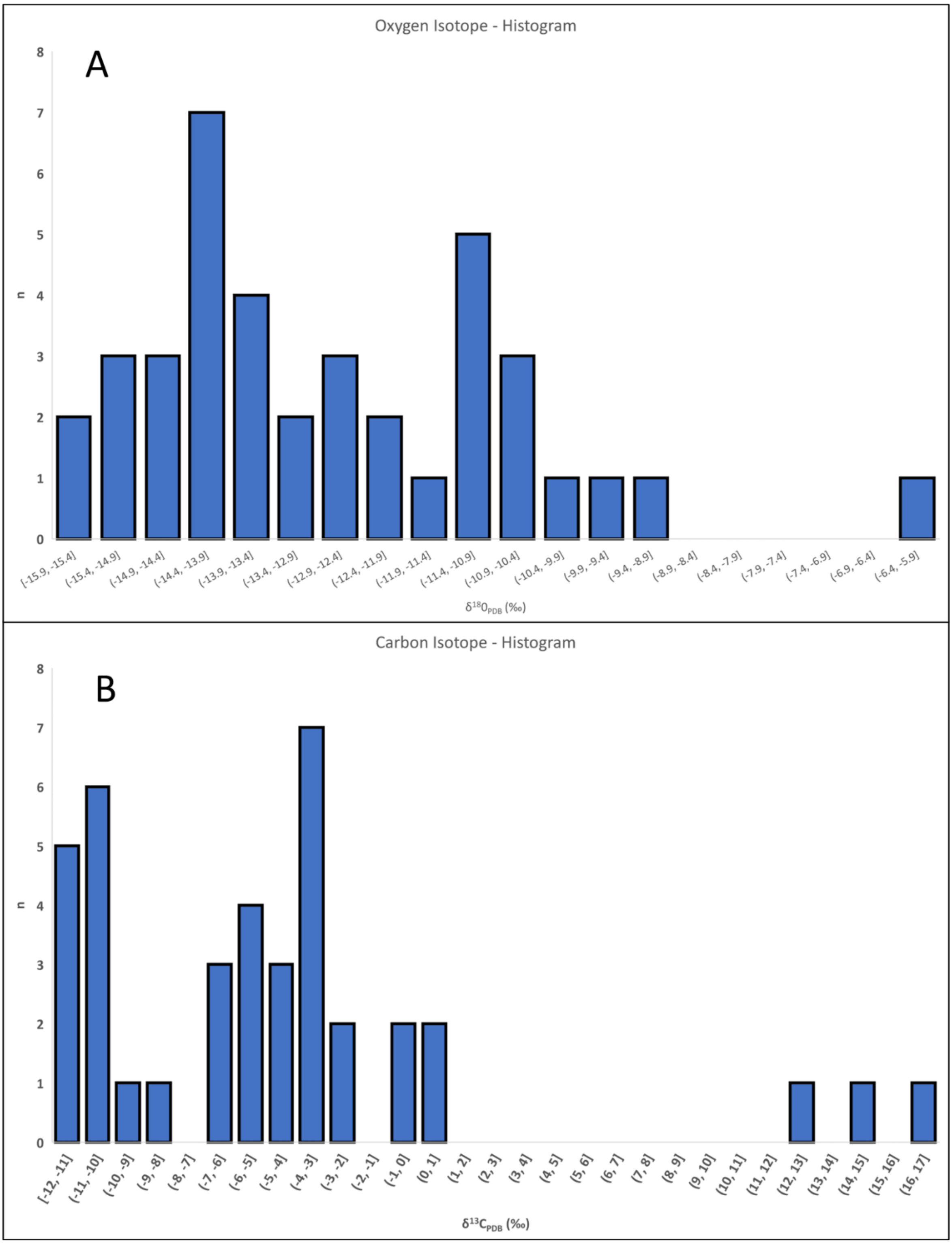


*Fig 5.3. Histograms of $\delta^{18}O_{PDB}$ (A) and $\delta^{13}C_{PDB}$ (B) results. These show that there is a wide distribution of results for both $\delta^{18}O$ and $\delta^{13}C$ isotopes. Both isotopic regimes have significant outliers with bimodal groupings of the main dataset.*

## 5.2.2 Clumped Isotope Thermometry

Clumped isotope thermometry is a geochemical technique that can be utilised to determine the formation temperature of carbonate minerals (Huntington et al., 2009; 2011; Anderson et al., 2021). Clumped isotope thermometry analyses the extent to which

$^{13}C$ and $^{18}O$ atoms form bonds with each other in the lattice of carbonate minerals as a function of temperature (Huntington et al., 2009).

In contrast to conventional carbonate thermometry, clumped isotope thermometry does not require knowledge of an initial fluid composition (Huntington et al., 2011; Anderson et al., 2021). Clumped isotopes are utilised as an independent thermometer for constraining crystallisation temperatures of calcite and for comparison with temperatures that can be calculated from conventional $\delta^{18}O$ data but which require an independent estimate of temperature in order to determine the oxygen isotopic composition of the fluid from which the calcite precipitated (Kim & O'Neil, 1997).

Ten key samples (Table 5.3) were sent to Imperial College London for clumped isotopic analysis, identified from structural and microscopic analysis covering a wide range of geological structures. The methodology for sample analysis is outlined in Section 2.6.

The full results for clumped isotope thermometry are outlined in Table 5.3, with results plotted in Figure 5.4. The carbon and oxygen isotopic results show a similar range as the conventional carbonate stable isotopes (Figures 5.1 & 5.2). The temperature results range from 19-82°C with significant uncertainty. Figures 5.4b&c demonstrate the difference between error envelopes based on one standard deviation (Fig 5.5b) and 95% probability envelopes (Fig 5.4c). Figure 5.4 clearly shows that the temperatures from clumped isotopic analysis are associated with large degrees of uncertainty with uncertainties ranging from 7°C to 28°C (uncertainty range based on standard deviation) and 32°C to 136°C (95% probability envelope). However, even with the large uncertainties shown in Figure 5.5c associated with a 95% probability envelope, a separation of ~15°C exists between two samples with lower uncertainties (NR1612 and JL1812; Table 5.3). This separation indicates that even with high uncertainties differences in mineralisation temperature are discernible and it is considered highly unlikely that the results observed could have been generated from a fluid of homogeneous temperature. This is further supported by the large variations in $\delta^{18}O$ in Fig 5.5a&c, with the wide range of $\delta^{18}O$ suggesting either or both different fluids and precipitation temperatures (Urey, 1947; McCrea, 1950; Kim & O'Neil, 1997; Leng and Marshall, 2004).

The uncertainty expressed as the standard deviation of the temperature range will be utilised in the Discussion (Section 5.4) to enable easier interpretation of trends in the dataset and comparability with analogous studies such as Faÿ-Gomord et al. (2018).

### 5.2.3 Fluid Inclusion Analysis

A selection of 10 samples were sent to NUI Galway's GeoFluid Research Group for fluid inclusion microthermometric analysis. The aim of fluid inclusion analysis was to generate data on the temperature and salinity of the trapped fluids (Limans, 1987). Samples were analysed under transmitted light microscopy prior to selection in order to identify suitable candidates for fluid inclusion analysis. Despite pre-screening to select samples with the highest probability of success, all samples analysed were unsuccessful; only 4-5 fluid inclusions were found in each sample, typically 2-3 microns in size and below workable size limits. No results were generated.

| Sample name | Location | Structure | Fill Type | Mineralogy | Age (Ma) | Nb replicates | d13C VPDB | d13C VPDB (SD) | d13C VPDB (SE) | d13C VPDB (@95CI) | d18O VPDB (Final) | d18O VPDB (SD) | d18O VPDB (SE) | Temp °C | Tmin [+1SE] | Tmax [-1SE] | Tmin [+95%CI] | Tmax [-95%CI] | Fluid equation | Calculate d18O fluid [VSMOW] | d18Omin [±1SE] | d18Omax [±1SE] | d18Omin [±95%CI] | d18Omax [±95%CI] |
|---|---|---|---|---|---|---|---|---|---|---|---|---|---|---|---|---|---|---|---|---|---|---|---|---|
| JL2024 | Ravenscar | Peak Fault (Conjugate) | Fault Fill | Calcite | 33.5 | 3 | -8.3 | 0.2 | 0.1 | 0.5 | -15.3 | 0.2 | 0.1 | 38 | 25 | 53 | -9 | 127 | Kim and O.Neil 1997 | -10.4 | -13.0 | -7.6 | -20.3 | 2.1 |
| NR1623 | Ravenscar | Peak Fault (Conjugate) | Breccia (mosaic) | Calcite | 30.4 | 3 | 7.3 | 0.3 | 0.2 | 0.8 | -10.7 | 0.1 | 0.1 | 19 | 15 | 22 | 4 | 36 | Kim and O.Neil 1997 | -9.4 | -10.4 | -8.7 | -12.5 | -6.4 |
| JL2026 | Osgodby Nab | Cayton Bay Fault | E-W striking Subvert Vein | Calcite | 36.2 | 3 | -1.3 | 0.0 | 0.0 | 0.1 | -13.2 | 0.2 | 0.1 | 82 | 69 | 97 | 33 | 164 | Kim and O.Neil 1997 | -1.1 | -3.1 | 1.1 | -8.7 | 8.0 |
| NR1612 | Runswick Bay | Runswick Bay Fault Zone | Extensional Jog | Calcite | 32.8 | 4 | -4.0 | 0.0 | 0.0 | 0.1 | -14.5 | 0.2 | 0.1 | 71 | 64 | 78 | 52 | 94 | Kim and O.Neil 1997 | -4.0 | -5.2 | -2.9 | -6.8 | -1.1 |
| NR1604 | Staithes | Staithes Fault Zone | Thin Vein/Jog | Calcite | 39.0 | 3 | -11.5 | 0.0 | 0.0 | 0.1 | -13.9 | 0.6 | 0.3 | 47 | 40 | 55 | 19 | 86 | Kim and O.Neil 1997 | -7.4 | -9.0 | -5.6 | -11.2 | -2.8 |
| JL1812A | Port Mulgrave | Oblique-slip | Extensional Jog | Calcite | 23.8 | 3 | -5.4 | 0.0 | 0.0 | 0.1 | -13.5 | 0.1 | 0.1 | 31 | 24 | 38 | 5 | 65 | Kim and O.Neil 1997 | -9.9 | -11.4 | -8.5 | -15.2 | -4.2 |
| JL1812B | Port Mulgrave | Oblique-slip | Extensional Jog | Calcite | 33.0 | 3 | -5.3 | 0.1 | 0.0 | 0.1 | -10.3 | 0.1 | 0.1 | 25 | 21 | 29 | 10 | 43 | Kim and O.Neil 1997 | -7.8 | -8.7 | -6.9 | -10.6 | -4.7 |
| JL2017 | Port Mulgrave | PMFZ | Extensional Jog | Calcite | 33.7 | 3 | -5.3 | 0.1 | 0.0 | 0.2 | -14.5 | 0.0 | 0.0 | 50 | 38 | 63 | 6 | 125 | Kim and O.Neil 1997 | -7.5 | -9.7 | -5.3 | -16.2 | 2.9 |
| JL1815 | Saltwick Nab | Subvert Veins | Subvert Veins | Calcite | 43.3 | 4 | -5.4 | 0.1 | 0.1 | 0.2 | -10.8 | 0.1 | 0.1 | 51 | 43 | 59 | 29 | 79 | Kim and O.Neil 1997 | -3.5 | -5.0 | -2.1 | -7.4 | 0.7 |

*Table 5.3. Clumped isotope results from Imperial College London, with initial fluid composition calculations determined from precipitation temperature, based on Kim & O'Neil (1997).*

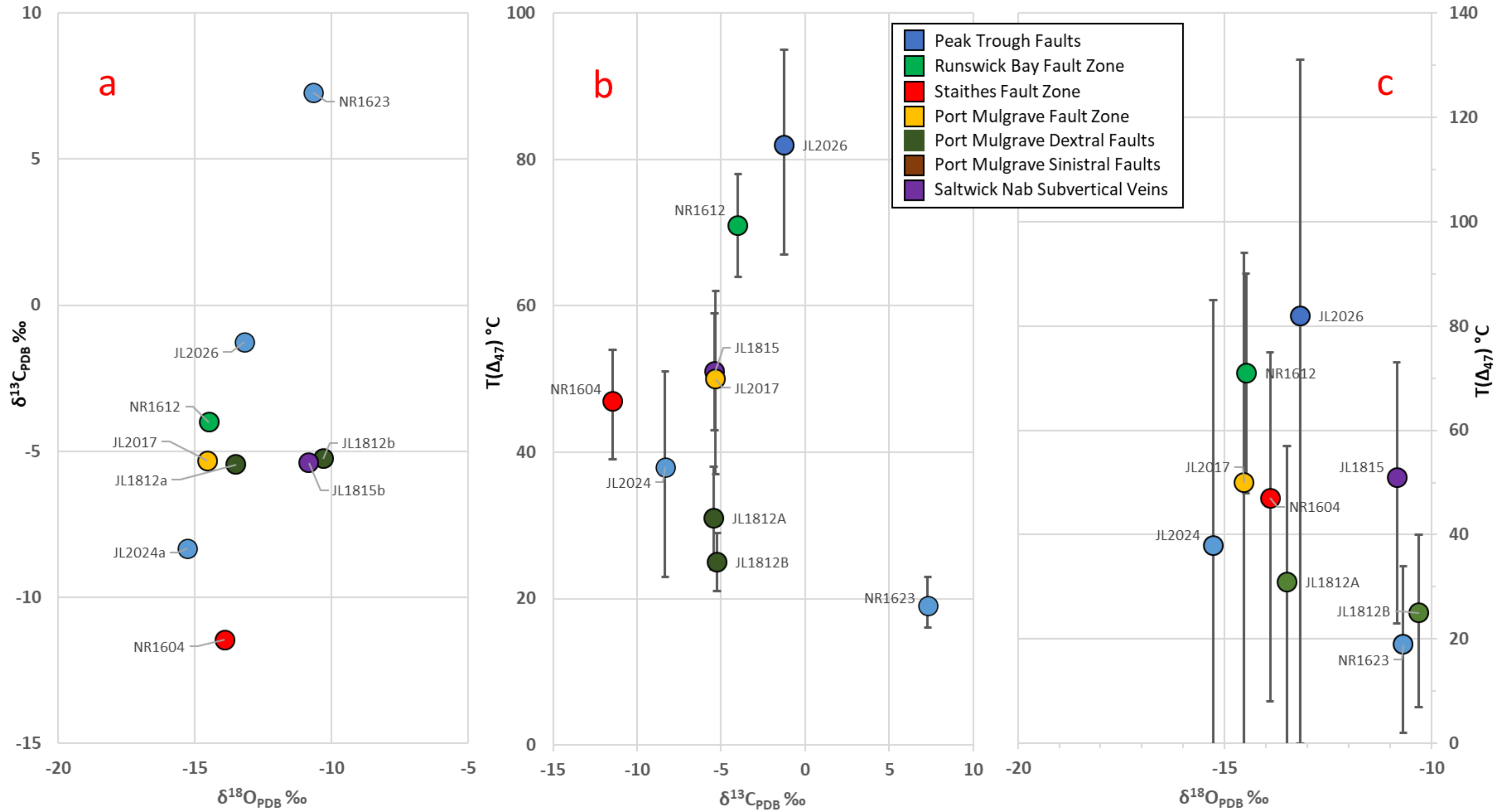


*Fig 5.4. Isotope plots of the clumped isotope data. Results are colour-coded by sampled structure, as in Figs 5.1-5.3. a) Plot of the $\delta^{13}C_{PBD}$ vs $\delta^{18}O_{PBD}$ from clumped isotope data with similar variations visible shown in Fig 5.1-5.3. b) Temperature vs $\delta^{13}C_{PBD}$ in Celsius ($T(\Delta 47)$°C) from Clumped Isotopes with error bars based on the standard deviation of the clumped isotope data. c) $T(\Delta 47)$°C vs $\delta^{18}O_{SMOW}$ with error bars based on the 95% probability envelope for clumped isotope analysis.*

## 5.3 Discussion

### 5.3.1 Age relationships

The results from conventional carbonate stable isotope and clumped isotope analyses show significant variations in both the isotopic composition of the calcite fills and the precipitation temperatures calculated from Δ47 (Section 5.2.2). These data suggest a range of fluid sources that will be discussed in more detail later in this section. Here, we note that significant isotopic differences occur between structures from different localities and, in the case of Port Mulgrave, between two subpopulations of data with the same structural affinity. This variability suggests a lack of fluid connectivity between structures, with highly localised fluid sources and precipitation temperatures.

Figure 5.4-5.7 show plots of oxygen and carbon isotope data against time, coloured by sampled structure and with labels based on synkinematic indicators. Figure 5.6 & 5.7 show both oxygen and carbon isotopes coloured by age and labelled by synkinematic indicators. While there is no clear age relationship a rough trend is seen, with samples with more positive $\delta^{18}O$ in the Port Mulgrave (2) subpopulation having younger ages (23.3-33.0Ma) than more negative data from the Staithes Fault Zone, Runswick Bay Fault Zone and Port Mulgrave (1) subpopulations (25.2-39.0Ma). This trend excludes JL1815 (43.3Ma) which sits within the Port Mulgrave (2) subpopulation and the Peak Trough subpopulations. The Peak Fault and Cayton Bay data sits intermediate to the populations above and has a range of ages between 26.8 and 36.2Ma, with the Red Cliff Fault showing significantly older ages (46.5 and 55.0Ma) and distinctly different oxygen and carbon isotopic signatures (Fig 5.7). These trends suggest that multiple pulses of calcite mineralisation have occurred at different locations. The timings of potential fluid pulse are shown on Figure 5.4 and 5.5 as 39-37Ma, 35-35Ma and 37-23Ma.

It is of particular note that samples JL1812a and JL1812b (dextral fault at Port Mulgrave) show a difference in age of 10 Ma, despite the samples being taken from the same fault structures. JL1812a is a blocky post-kinematic fill, while JL1812a is from an extensional jog with clear syn-kinematic indicators (Section 4.4.4). Both samples have similar temperatures from clumped isotopes, similar $\delta^{13}C$ and a 3‰ difference in $\delta^{18}O$. In contrast, JL2017 and JL1812b are the same age and have the same $\delta^{13}C$ but have different structural affinities (Peak Fault and oblique-slip fault respectively), very different $\delta^{18}O$ and a 25°C temperature difference. These variations highlight the complexity of the data set and suggest that it could be structural affinity, rather than time or other parameters such as fill type that may be the dominant control on fluid source and precipitation temperature.

The results shown in Figure 5.4-5.7 suggest that no clear relationship exists between conventional isotopic data (carbon and oxygen) and kinematically linked calcite samples with an apparently random spread of syn-kinematic, pre-kinematic, post kinematically and syn- to post kinematic samples distributed between the different subpopulations. This suggests that fluid properties are not directly linked to kinematics and that fluid properties likely represent varying connectivity and sourcing of individual structures. Identifying potential oxygen and carbon sources will provide important controls on fluid-flow and mineralisation with the ability to define end-member fluid compositions.

### 5.3.2 Oxygen Isotopes

Oxygen isotope analysis measures the relative proportion of the $^{18}O$ and $^{16}O$ oxygen isotopes (White, 2014); the oxygen isotopic composition of calcite reflects a combination of the fluid $\delta^{18}O_{SMOW}$ composition and the temperature of calcite precipitation (Urey, 1947; McCrea, 1950; Kim & O'Neil, 1997; Leng and Marshall, 2004). As shown in Figures 5.1-5.6, the oxygen isotope composition from stable and clumped isotope analyses shows significant variation (-6 to -16 $\delta^{18}O_{PDB}$). This section will attempt to constrain the sourcing and fractionation control on this 10‰ variability.

One of the main variables in calculating the fluid temperature from the oxygen isotope composition is the assumption of an initial fluid composition. Clumped isotope thermometry circumvents this issue by using preferential bonding of isotope pairs to calculate a precipitation temperature. Therefore, temperatures provided by clumped isotope analysis can be combined with traditional oxygen isotope thermometry (Kim & O'Neil, 1997) to calculate the fluid composition from which the calcite was precipitated (Table 5.3; Fig 5.7). The fluid composition ($\delta^{18}O_{Water}$) can be compared to a series of recent and geological fluid endmembers to attempt to fingerprint the initial fluid source.

Potential end-member fluid sources include Jurassic connate (pore) water (-1‰ $\delta^{18}O_{SMOW}$ - Marshall 1992; Price and Sellwood 1997; Sælen et al., 1996) and Cenozoic meteoric fluid (-6 to -9‰ $\delta^{18}O_{SMOW}$ - Jouzel et al., 1997; BGS Online Viewer). Deeper fluids sourced from the Triassic Sherwood similar to those suggested by Faÿ-Gomord et al. (2018) to have led to mineralisation at Flamborough Head, or fluids from an evolved evaporitic source are also a possible fluid source, with a value of +3‰ $\delta^{18}O_{SMOW}$ used (Egeberg and Aagaard, 1989; Warren et al., 1994).

Temperature calculations (Kim & O'Neil, 1997) based on assumed fluid $\delta^{18}O$ compositions for the $\delta^{18}O$ values produced from conventional carbonate stable isotopic analysis produced average temperatures of 79°C ± 13°C, 44°C ± 11°C and 107°C ± 14°C assuming Jurassic seawater, meteoric water and evaporite water compositions respectively. These results provide important implications for understanding the fluid sources and potential fluid-flow regimes associated with Cenozoic extension.

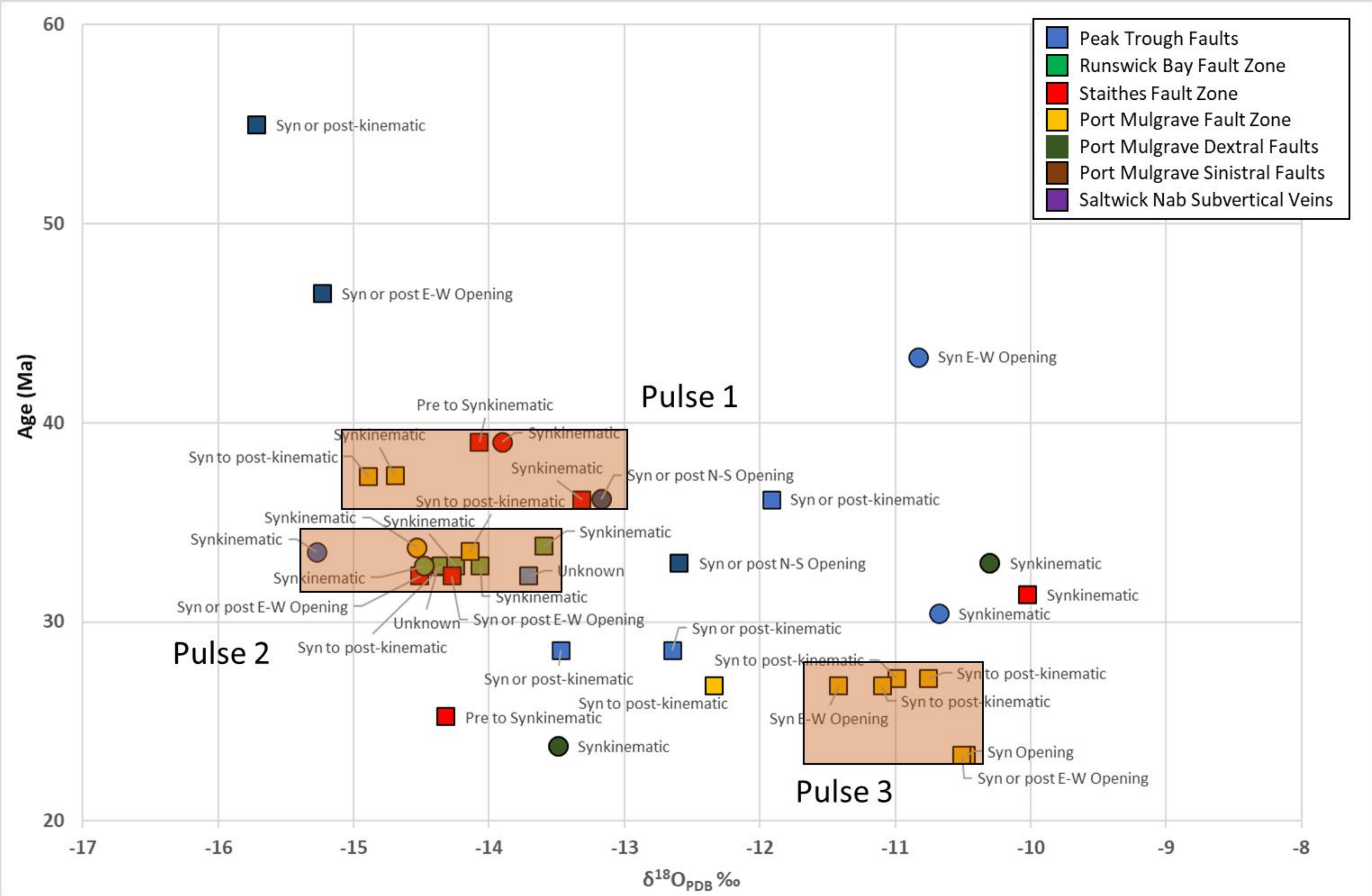


*Fig 5.5. Age (Ma) vs $\delta^{18}O_{PDB}$ coloured by the structure sampled with labels indicating whether the samples are synkinematic, post-kinematic or pre-kinematic. Potential pulses of calcite mineralisation are shown in orange.*

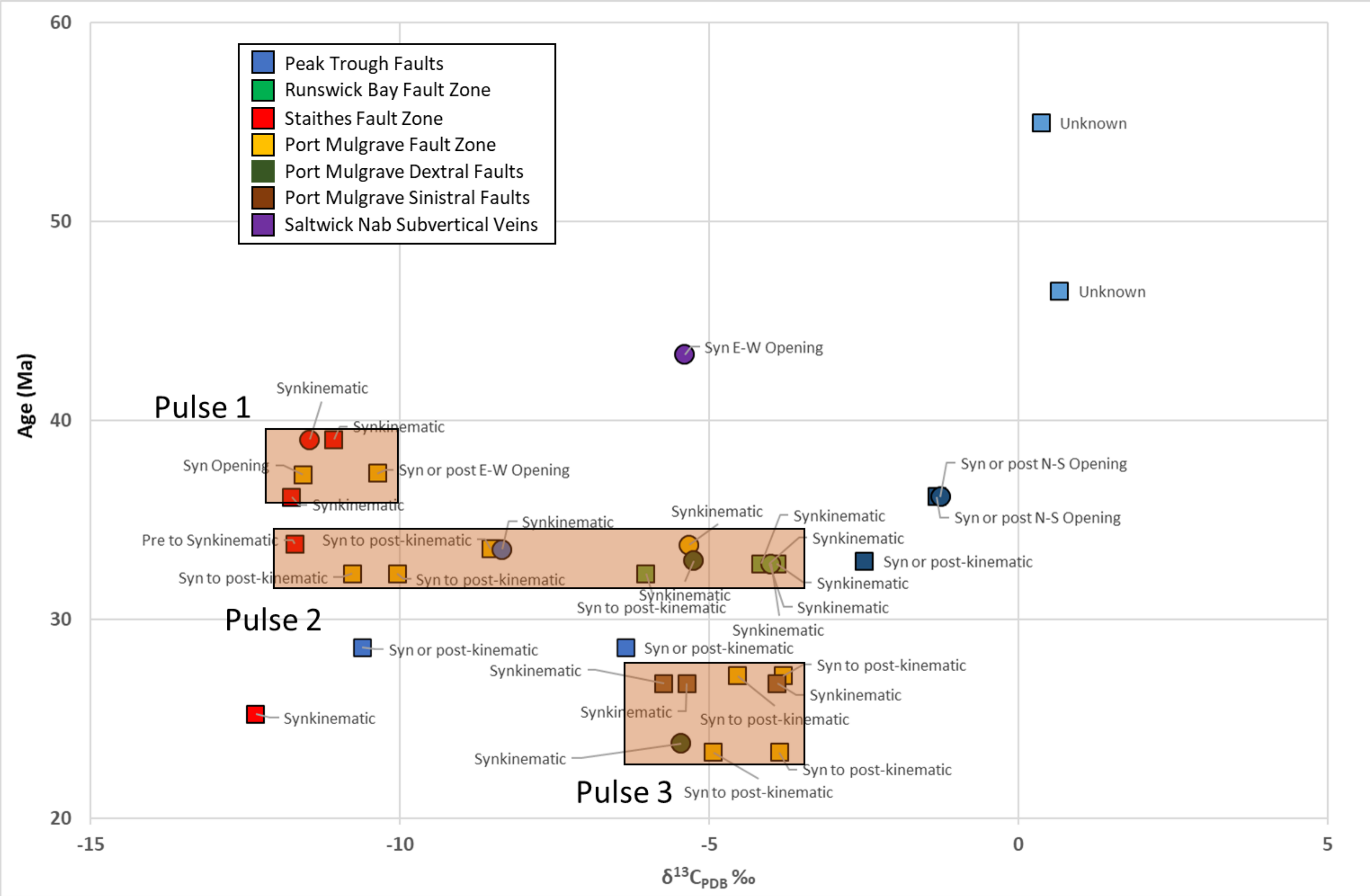


*Fig 5.6. Age (Ma) vs $\delta^{13}C_{PDB}$ coloured by the structure sampled with labels indicating whether the samples are synkinematic, post-kinematic or pre-kinematic. Potential pulses of calcite mineralisation are shown in orange.*

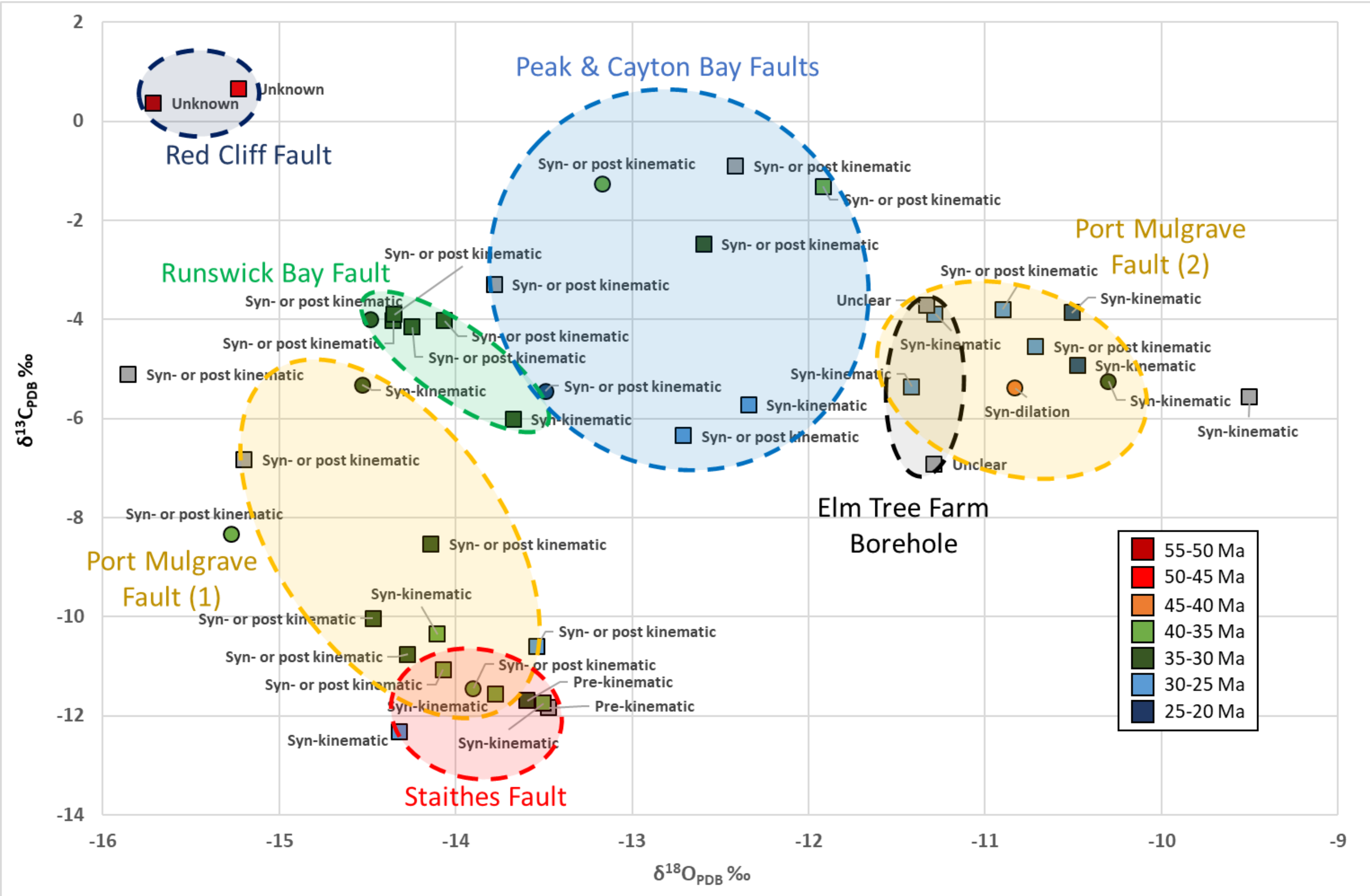


*Fig 5.7. $\delta^{13}C_{PDB}$ vs isotope samples coloured by the calcite fill age determined from U-Pb calcite geochronology. Labels indicate the relationship between samples and deformation with a mixture of syn-kinematic and non-kinematically linked samples. Vein samples are related to opening rather than fault kinematics.*

If calcite precipitated from Jurassic connate water, then it must either be at 1.5-2.5km based on geothermal gradients from Green (1989), which is similar to burial history estimates from Green (1989), Bray et al. (1992) and Holliday (1999) but lower than the 4km burial indicated by Kemp et al. (2005). It is possible, however, that calcite was being precipitated during uplift. Evidence in Chapter 3 contradicts this assumption with a basinal extensional regime indicated with no evidence of widespread compression or uplift during deformation and associated mineralisation. If, however, the fluids are sourced from Permian Evaporite waters then the Jurassic rocks could be much closer to maximum burial when calcite was precipitated. Meteoric waters, in contrast, would suggest shallow burial of <1km. It is clear then that depending on the assumptions made the fluid composition could make a substantial difference in the interpretation of the depth range over which calcite precipitated in the fractures.

The clumped isotope results can be analysed to attempt to constrain this uncertainty. $\delta^{18}O$ and $\delta^{13}C$ results (Fig 5.3 & 5.4a) compare well to conventional stable isotope results from similar samples (within 1‰) and calculated temperatures show a range between ~20 and 80°C. Based on these temperatures, fluid compositions ($\delta^{18}O_{Water}$) are shown in Figure 5.8 and vary from -1.1 to -10.4‰. This variation from an apparent Jurassic connate water to highly $\delta^{18}O$ negative meteoric water indicates that calcite apparently precipitated from radically different fluids. Figure 5.8b suggests a relationship exists between temperature and initial fluid composition, with calcite precipitated from isotopically lighter fluid (~-10‰ $\delta^{18}O_{Water}$) associated with lower temperatures of 20-40°C, and calcite precipitated from isotopically heavier fluids (-1.1 $\delta^{18}O_{Water}$ for JL2026) associated with hotter temperatures of ~80°C. The relationship between more negative $\delta^{18}O_{Water}$ and lower temperature suggests that the wide range of $\delta^{18}O_{calcite}$ relates to variations in both temperature and $\delta^{18}O_{Water}$. Hence, any model for Cenozoic fluid-flow will need to incorporate both temperature and $\delta^{18}O_{Water}$ as key variables, combined with understanding of the sources of carbon, expressed as variations of $\delta^{13}C$.

It is notable that estimates of $\delta^{18}O_{Water}$ from clumped isotopes provide highly negative values, lower than those expected for meteoric water $\delta^{18}O$ (-6 to -9‰ $\delta^{18}O_{SMOW}$ - Jouzel et al., 1997). If these clumped isotope results are correct, however, it would mean that calcite samples analysed were precipitated from both meteoric waters and Jurassic connate waters. A model for fluid-flow will be proposed in Section 5.4.3 but prior to this the carbon isotopes will be discussed to attempt to constrain the variability seen in Figure 5.2 & 5.3.

### 5.3.3 Carbon Isotopes

$\delta^{13}C$ is a measurement of the relative proportions of the $^{13}C$ and $^{12}C$ isotopes of a sample (White, 2014). While oxygen is abundant in water, carbon is present as dissolved carbonate species (mainly $HCO_3^-$ and $CO_3^{2-}$, depending on pH), and the $\delta^{13}C$ signal of any calcite sample is inferred to represent the source of this carbon. Potential carbon sources include dissolution of marine carbonate from shells in sediment (0 to +6‰ $\delta^{13}C_{PDB}$), carbon from organic matter from sediments (~-27.5‰ $\delta^{13}C_{org}$), especially organic-rich units, dissolved soil $CO_2$ (~-25‰ $\delta^{13}C_{CO2}$) or atmospheric $CO_2$ in infiltrating meteoric waters (-6.1‰ $\delta^{13}C_{CO2}$).

A 27‰ range of $\delta^{13}C$ occurs in these samples (Figure 5.1), with most of the data within a range of 13‰. As explained in Section 5.2.1.1, the small number of $\delta^{13}C_{PBD}$ values above + 10‰ can be attributed to microbial methanogenesis, related to $CO_2$ reduction (Botz et al., 1996). Methanogenesis is a process which occurs at optimal temperatures of ~30°C (Megonigal et al., 2003) due to the conversion of carbon dioxide ($CO_2$) to methane ($CH_4$) with fractionation of the heavy $^{13}C$ into the residual $CO_2$ (Drake et al., 2021). It is of note that these samples are among the most positive in $\delta^{18}O$, which would be consistent with lower temperatures, for a given fluid composition.

Non-methanogenic samples have $\delta^{13}C_{PBD}$ values of between 0.5 and -13‰ $\delta^{13}C_{PDB}$, which is inferred to reflect carbon sourced from a variable mixture of marine carbonate and oxidised organic matter. Organic carbon has a light $\delta^{13}C$ signal with typical values for the organic matter of the Jet Rock (Whitby Mudstone Formation) between -26.1 and -37‰ $\delta^{13}C_{org}$, with a mean value of ~27.5‰ $\delta^{13}C_{org}$ (Coleman & Raiswell, 1981; Sælen et al., 2000). Another possible source of carbon would be soil $CO_2$ with typical $\delta^{13}C$ values indicated by White (2014) to be ~-25‰ $\delta^{13}C_{CO2}$. In contrast to these highly negative carbon end-members, marine fossils are common in the Jurassic sediments of the Cleveland Basin and have $\delta^{13}C_{PBD}$ values of 0 to +6‰ $\delta^{13}C_{PDB}$ (Sælen et al., 2000). In addition, Cenozoic atmospheric $CO_2$ forms another likely carbon source with values with average values of -6.1‰ $\delta^{13}C_{CO2}$ (Tipple et al., 2010)

The variation in $\delta^{13}C$ in the main data population can be explained with variable sourcing between a positive marine fossil source of +1 to -2‰ $\delta^{13}C_{PBD}$ and a highly negative organic carbon or soil $CO_2$ source of up to ~25% for Staithes Fault Zone samples with $\delta^{13}C_{PDB}$ values of -12 to -13‰. An organic source is consistent with the organic-rich and early oil mature Jet Rock, although the weak trend between more negative $\delta^{13}C_{PBD}$ and $\delta^{18}O_{Water}$ could suggest either an increasing trend of fluid rock interaction or soil $CO_2$ associated with isotopically light meteoric water.

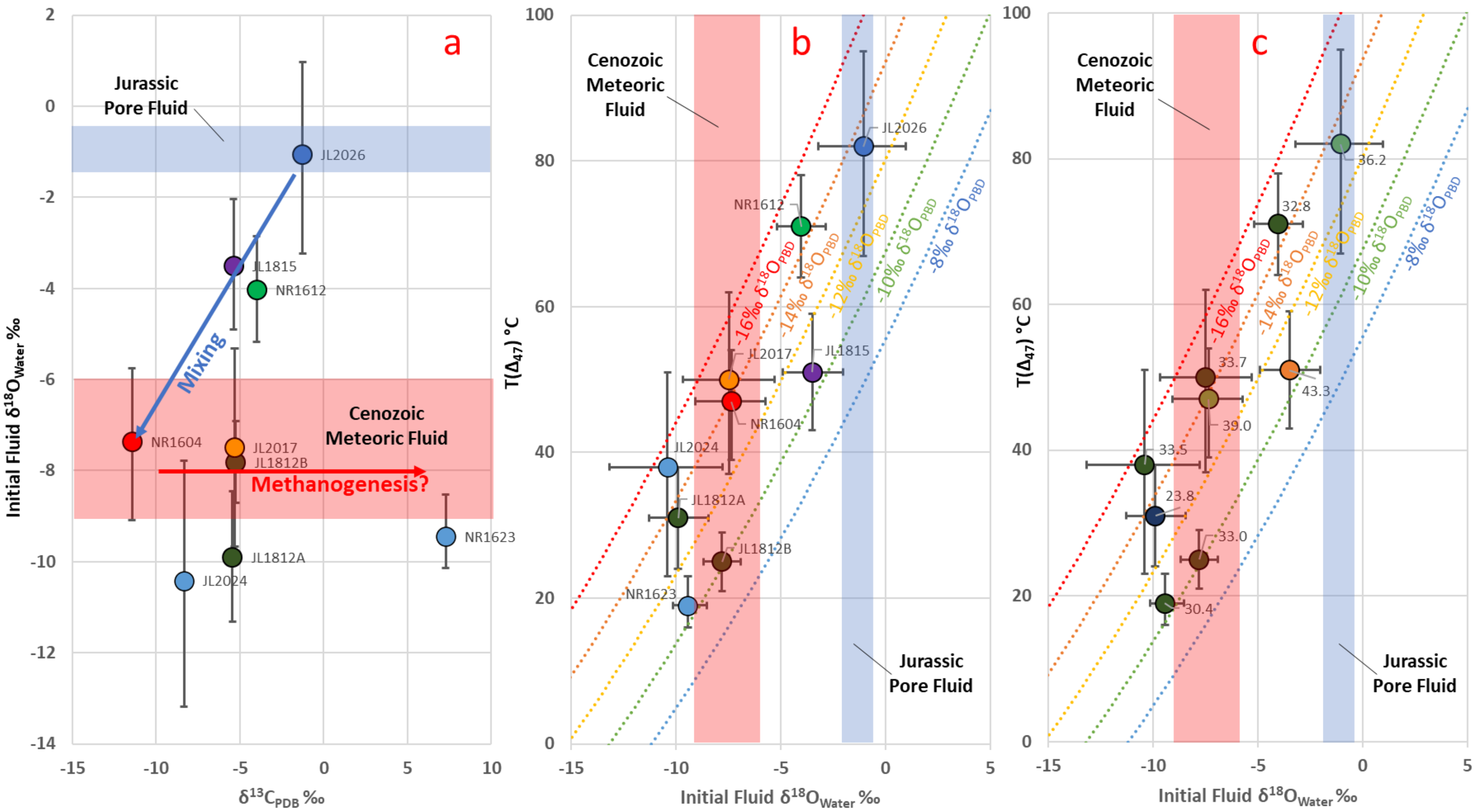


*Fig 5.8. Isotopic plots of the clumped isotope data and interpretations based on the clumped isotope data. a) the initial fluid composition of the calcite calculated using the relationship shown by Kim & O'Neil (1997) vs $\delta^{13}C_{PBD}$, b) T(Δ47)°C vs Initial fluid and c) T(Δ47)°C vs Initial fluid coloured by age from U-Pb calcite dating.*

No clear trend is seen between $\delta^{13}C$ and age from U-Pb calcite geochronology (Figure 5.8). Figure 5.8b & 5.8a show that clear trends exist between temperature and $\delta^{13}C$; $\delta^{13}C$ becomes more negative with decreasing temperature, which could, as for the trend with $\delta^{18}O_{Water}$, suggest increasing organic matter input or increasing soil $CO_2$ input with cooler temperatures.

In summary, it is clear that both the oxygen and carbon isotope systems are complex: calcite has precipitated from waters which are isotopically diverse with respect to both oxygen and carbon (Table 5.1; Figures 5.1-5.8). Determining the relative abundances of each component is beyond the scope of this study, with the focus being on proposing potential models for Cenozoic fluid-flow in the Cleveland Basin. It is, however, suggested that in its simplest manner the $\delta^{13}C$ variation, excluding methanogenesis data, can be explained by simple mixing of organic carbon with marine carbonate.

### 5.3.4 Model for Cenozoic Fluid-flow

The systematic difference shown in temperature between the ~-1‰ $\delta^{18}O_{Water}$ and ~-10‰ $\delta^{18}O_{Water}$ shown in Figure 5.8b&c is used to assume that calcite formed from two fluids at different temperatures (80°C to 20°C). As all calcite fills are sampled from Jurassic host-rocks, there is no stratigraphic difference to explain this temperature differential. It is therefore assumed that one fluid must be in disequilibrium with the host-rock leading to the proposition of a two fluid system. A two fluid system of meteoric water and Jurassic connate (or similar basinal fluid) was involved in the formation of calcite veins. Here, two end-member options are discussed to explain the variation in stable and clumped isotope results and the likely sources of the different fluids. One of the main uncertainties remaining is whether the veins formed at deep burial (>2km) or shallow post-exhumation, so that possibilities include:

1) Infiltration of a cold meteoric fluid (15°C) into warm (~80°C), buried Jurassic host rock with mixing between meteoric water (~-10‰ $\delta^{18}O_{Water}$) and Jurassic connate waters (~-1‰ $\delta^{18}O_{Water}$).
2) Deeper warm (~80°C) fluid (~-1‰ $\delta^{18}O_{Water}$) flowing upwards and mixing with cold (20-40°C) meteoric waters (~-10‰ $\delta^{18}O_{Water}$) in the shallow subsurface, during or after exhumation of the Cleveland Basin.

### 5.3.4.1 Deep Calcite Mineralisation

Green et al. (1989) use AFTA data to suggest a paleogeothermal gradient of ~30°C/km for the Cleveland Basin. This gradient can be calculate an approximate depth of 2km for samples at 80°C, based on clumped isotope data. This calculation of ~2km allows the inference of deep calcite mineralisation with interaction of a downwelling cold meteoric fluid (20-40°C; ~-10‰ $\delta^{18}O_{Water}$) with Jurassic connate waters (~-1‰ $\delta^{18}O_{Water}$) in the still deeply buried host rocks (~80°C). Calcite precipitation is observed predominantly in association with fractures and faults. The fractures and faults, therefore, are the likely conduits for fluid circulation in the Cleveland Basin. This model matches well with burial history plots by Emery (2016) (Fig 6.5), which infers that exhumation post-dated calcite mineralisation. Figure 5.9 shows a model by which this could occur with cool meteoric water drawn-down through fracture permeability and mixing with connate water in-situ. However, a significant issue remaining with this system is the driving mechanism by which meteoric fluid can be circulated to depths of ~2 km. This is despite similar studies from Worden et al. (2016) and Faÿ-Gomord et al. (2018) discussed in Section 5.4.5 suggesting that similar patterns of fluid-flow are seen at Flamborough Head and in the Wessex Basin.

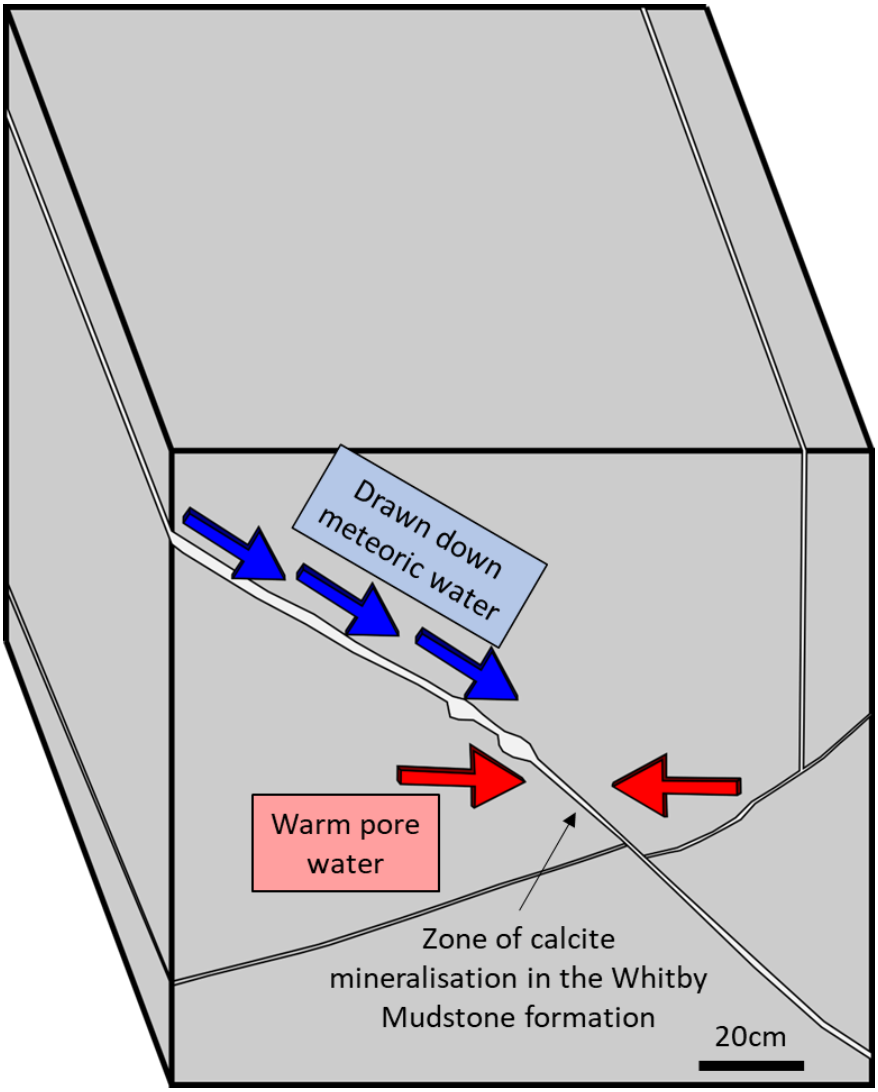

*Fig 5.9. Schematic diagram of a proposed fluid-flow regime with deep precipitation of calcite fills (white) through a variable mix of cold meteoric water (blue arrows) drawn down through fracture permeability and warm pore waters (red arrows) sourced from the mudstone country rock.*

#### 5.3.4.2 Shallow Calcite Mineralisation

In contrast to the model of deep mineralisation described above, calcite mineralisation could have occurred in a shallow setting (<1km) with the mixing of cold meteoric water (as above) circulating along fractures with deeper sourced basinal waters (~-1‰ $\delta^{18}O_{Water}$) up to 80°C, flowing upwards (Fig 5.10). Evaluations of Zechstein seawater from Lee (1990) and Lee (1993) suggest values similar to this. This model is supported by AFTA models by Green (1986) and Bray et al. (1992), which suggest that exhumation of the Cleveland Basin predates the extensional deformation and fluid-flow discussed here. An additional piece of evidence introduced here is the interpretation of methanogenesis, which could be indicative of shallow (<1km) burial at the time of calcite mineralisation with microbial action most effective at temperatures of ~30°C (Megonigal et al., 2003) but continues up to 70°C. This would support a shallower burial depth with meteoric waters, potentially reinfecting the exhumed Liassic mudstones, however this is only based on a couple of data points.

One important unknown is the exact fluid source of the upwelling basinal waters; ~-1‰ $\delta^{18}O_{Water}$ is suggested here based on end-member calculations from temperatures from clumped isotopes; however, fluids could in principle be sourced from deeper formation waters, which are likely to be isotopically heavier as a result of (a) water-rock interaction (e.g. clay mineral recrystallisation) and (b) seawater evaporation, which is plausible since the basin contains Zechstein evaporite deposits. Further work would be required to suggest likely fluid sources, for example Sr isotope analyses of the calcite fracture fills.

In addition, unpublished work by the author, not discussed here, at the Cleveland Dyke has described evidence of a shallow (<1-2km) open fissure fill at a similar stratigraphic level (Lias) to the samples described here. While U-Pb dating was unsuccessful, distinctive thermal spotting of mudstones suggests that mineralisation occurred soon after dyke emplacement (55.8 ± 0.3Ma; Fitch et al., 1978). This evidence would better support an interpretation of shallow burial of the Jurassic stratigraphy, post dyke emplacement.

Further discussion of the depth of burial and implications for calcite precipitation and mineralisation is conducted in Chapter 6.

#### 5.3.4.3 Calcite Recrystallisation and Internal Isotope-exchange

Additional options that require discussion are the possibility that calcite recrystallization (Veillard et al., 2019) and/or internal isotope-exchange (Passey & Henkes, 2012; Stopler & Eiler, 2015) has occurred; in both cases this would compromise the interpretation of fluid sources and precipitation temperatures. Closed system recrystallisation of calcite is important to rule out because clumped isotopes reflect the preferential bonding of carbon and oxygen isotopes related to temperature, so that reordering of bonds in a closed system would alter the initial precipitation temperature (Veillard et al., 2019). Veillard et al. (2019) described a link between temperature from clumped isotopes $T\Delta_{47dol}$ and the initial $\delta^{18}O_{dol}$ water composition, with higher $T\Delta_{47dol}$ correlating with more positive initial $\delta^{18}O_{dol}$ fluid compositions. Similar trends can be seen in Figure 5.8b; however, while recrystallization cannot be fully ruled out, one of the main outcomes of the microscopic analyses in Chapter 4 was the absence of any widespread evidence of recrystallisation. In addition, calcite fills and specific calcite zones for stable and clumped isotope analyses were chosen to minimise any chance of recrystallised textures being sampled. U-Pb calcite geochronology also produced successful age dates, suggesting a direct relationship between U-Pb across a single calcite phase, which would likely be reset or disturbed in the presence of significant recrystallisation. Therefore, the assumption is made here that widespread recrystallisation of samples is unlikely, so that the temperature variations and stable isotopic variations accurately reflect both fluid and precipitation temperature.

In addition to the possibility of recrystallisation, another hypothesis that requires discussion is the potential of internal isotope-exchange reactions and bond reordering as described by Passey & Henkes (2012) and Stopler & Eiler (2015). In contrast to recrystallisation, isotope-exchange is indicated to be sensitive to additional heating whereas the calcite veins sampled are at maximum burial or exhumed, based on AFTA models (Green 1986; Green & Duddy, 2006) and burial history modelling (Emery, 2016). This means that internal isotope-exchange due to increased temperature post-precipitation can be effectively eliminated as a consideration.

### 5.3.5 Comparison to Analogous Veins

While the calcite fault and fracture fills analysed in this chapter have not been dated or isotopically analysed prior to this study, analogous results exist from studies on the

Flamborough Head Fault Zone (Faÿ-Gomord et al., 2018; Roberts et al., 2020) and the Wessex Basin (Worden et al., 2016).

#### 5.3.5.1 Flamborough Head

The data described form a distinct, separate population to those described by Faÿ-Gomord et al. (2018), which examined stable and clumped isotope analyses on calcite veins and chalk matrix from the extensional Frontal Fault Zone (Flamborough Head Fault Zone; Fig 3.1) at Selwicks Bay at the southern edge of the Cleveland Basin. The stable isotope results generated from calcite veins by Faÿ-Gomord et al. (2018) plot in a well-constrained population sitting at -7 to -9‰ $\delta^{18}O_{PDB}$ and 0 to 3‰ $\delta^{13}C_{PDB}$. The only data, which compares well with the data from the Selwicks Bay are non-situ samples (JL2031 & JL2032) from High Red Cliff at Cayton Bay, which have similar $\delta^{13}C$ values (0 to 1‰ $\delta^{13}C_{PDB}$; Fig 5.1) and are distinct from the rest of the main population. It is likely therefore that the voluminous fluid-flow suggested at Selwicks Bay (Roberts et al., 2020) is distinctly separate from the fluid-flow regime in the north of the Cleveland Basin. This is supported by U-Pb calcite geochronology outlined in Roberts et al. (2020), which indicates that fluid-flow and N-S extension along the Flamborough Head Fault Zone (63-55Ma) predated the calcite mineralisation and deformation described here.

In addition to the stable and clumped isotope work done by Faÿ-Gomord et al. (2018) on the Flamborough Head Fault Zone at Selwicks Bay, the authors also produced results from fluid inclusion and strontium isotope analyses. The fluid inclusion work identified homogenisation temperatures ranging from 37-53°C with salinities varying from 0.3 to 10.7 eq. wt% NaCl with most samples below 1 eq. wt% NaCl, reflecting a mainly meteoric signature. The similarities in temperature between samples analysed herein and temperatures from Faÿ-Gomord et al. (2018) could suggest a similar depth of penetration albeit in mudstones rather than chalk. The spread of salinities described by Faÿ-Gomord et al. (2018) was used to infer possible mixing of fluids or dissolution of evaporites. Strontium isotope analysis of calcite veins at Selwicks Bay produced $^{87}Sr/^{86}Sr$ ratios of 0.7103 to 0.7085, which are significantly higher than the $^{87}Sr/^{86}Sr$ ratios of 0.7074 to 0.7075 measured from the chalk matrix. These high strontium isotope ratios were used to infer a deeper connection with the sourcing of mineralising fluids from a clastic reservoir, with the Triassic Sherwood Sandstone suggested, based on the local stratigraphy. The large difference between the isotopic composition of mineralisation at Selwicks Bay as described above is significantly different for the veins analysed herein (Section 5.2.2) and suggests that fluid-flow and mineralisation at Selwicks Bay is likely distinct from the calcite veining described in this chapter. The suggestion of deep fluid sourcing from the Triassic, with potential flow of meteoric fluid could suggest that meteoric fluids have penetrated within the Cleveland Basin down to the Triassic within the past 60 Ma, so that a hypothesis of meteoric and connate water mixing is not unreasonable. In addition, this deep fluid has then been brought up to the surface (Roberts et al., 2020) in large volumes, which would support a model of shallow calcite mineralisation.

#### 5.3.5.2 Wessex Basin

In addition to the Flamborough Head Fault Zone, comparable calcite veins have been analysed from the Lower and Middle Jurassic of the Wessex Basin in Devon. Calcite veins in predominantly N-S striking normal faults, strike-slip faults and fractures have been analysed isotopically by Worden et al. (2016) and were later dated by Parrish et al. (2018) utilising U-Pb calcite geochronology. In contrast to the wide range of fill styles and calcite growth types in the Cleveland Basin, calcite veins from the Wessex Basin are indicated to be predominantly syntaxial crack-fill veins (Worden et al., 2016). Parrish et al. (2018) presented a range of dates for the Jurassic strata between 55 and 25Ma with a tectonic culmination at 34-31 Ma, contemporaneous with fracturing related to folding of the overlying Late Cretaceous Chalk. These ages compare well with the U-Pb calcite dates for the Cleveland Basin presented in Chapter 4 and could indicate a similarities in Cenozoic tectonic history between both basins due to UK wide tectonic controls. However, similarity in calcite mineralisation between to basin is not enough to characterise a period of UK-wide extension. Correlating such an event would take considerable additional data from multiple additional sources and basin. This is considered future work and beyond the scope of this research.

Worden et al. (2016) analysed 53 samples from the Permian through to the Upper Cretaceous along the south coast of the Wessex Basin and produced carbon and oxygen stable isotopic and fluid inclusion results. $\delta^{18}O$ values vary between -9 to -3‰ $\delta^{18}O_{PDB}$ with a strong mode of -7‰, compared to a spread of -6 to -15.9‰ $\delta^{18}O_{PDB}$ with an average of -12.7‰ for the calcite fills presented in this chapter. Similarly, $\delta^{13}C$ values are consistently more positive than the samples discussed here, with a range of -5 to 5‰ $\delta^{13}C_{PDB}$ with a mode of -2‰ compared to a range of -12.3 to 16.0‰ $\delta^{13}C_{PDB}$, with an average of -6.0‰ $\delta^{13}C_{PDB}$, with methanogenic data removed to avoid skewing of the results to these highly positive samples. Similar, however, to the data from the Cleveland Basin is the absence of any consistent geographic trend of $\delta^{18}O$ or $\delta^{13}C$.

Fluid inclusion work carried out by Worden et al. (2016) showed variable salinity results (0-25 wt% NaCl) which were coupled with anomalous homogenisation temperatures of 177-283°C, as burial histories by Stoneley (1982) suggest maximum burial temperatures of ~90°C. These fluid inclusion results, when combined with the presence of sulphide minerals in the calcite veins and the lack of geographic trends in stable isotope or salinity data were used to suggest a mixed connate and meteoric fluid source. Meteoric water is inferred to have interacted with Middle-Upper Triassic halite before being drawn upwards into the Jurassic sediments to form low temperature (30-50°) calcite fault and fracture fills. This evidence suggests that in other comparable basins, mixed connate water and meteoric fluids have been sourced with carbon and oxygen stable isotope data having a similar absence of clear geographic trends, and high geochemical variability.

The analyses described above by Worden et al. (2016) and Faÿ-Gomord et al. (2018) support the potential that meteoric fluid-flow could have percolated into underlying Triassic reservoirs prior to upwelling and mixing with Jurassic connate waters. The presence of occasional pyrite and halite selvages along samples would appear to support this, although as stated in Section 3.2.3.3 this pyrite and halite could equally by sourced from the organic-rich host rock. A significant issue with sourcing of meteoric fluid from deeper reservoirs is the correlation shown in Figure 5.8b where a clear correlation is shown between more negative $\delta^{18}O$ initial fluid composition and low temperatures (20-40°C). This trend suggests that the meteoric component of mixing was cold and hence likely not to be in thermal equilibrium with the hotter host rock. If the fluid had been sourced from deeper reservoirs, then it would be expected that the meteoric fluid would be hotter and the connate water colder, which is not seen.

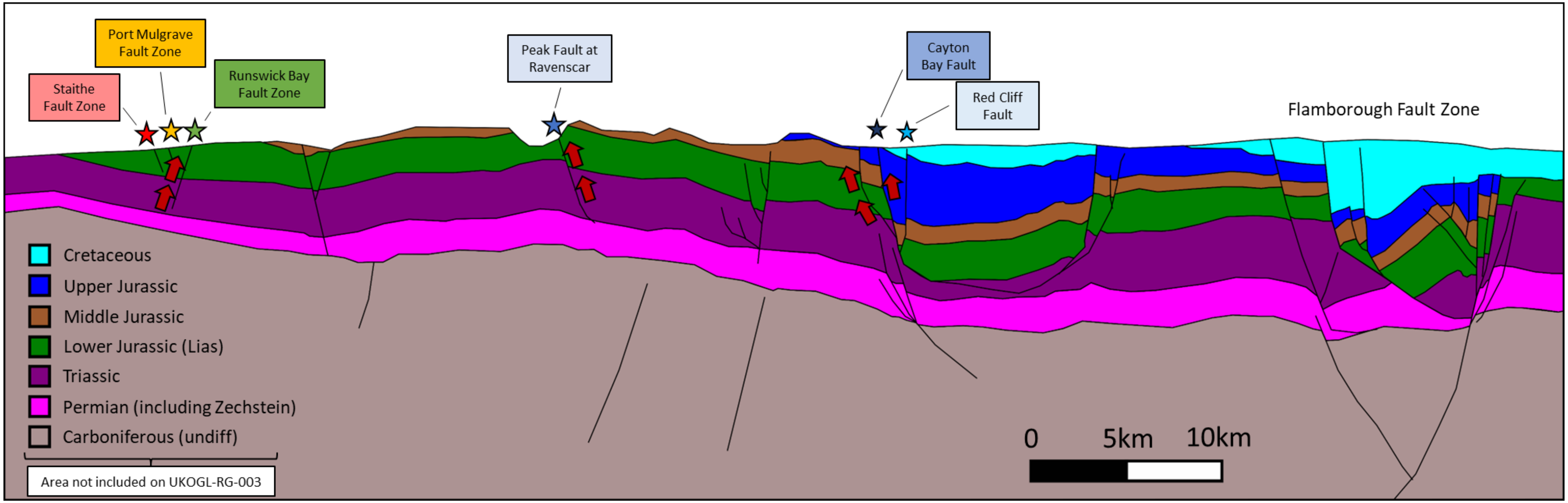


*Fig 5.9. Schematic cross section of the Cleveland Basin showing the possible fluid-flow pathways from the Zechstein or similar lithology upwards to the shallow sub-surface.*

## 5.4 Summary

Significant variation and complexity has been described in not only carbon and oxygen stable isotope results but, in addition, temperatures from clumped isotope analysis. Temperatures from clumped isotope results indicate a variation in temperatures from a minimum of ~20°C to a maximum of ~80°C. This variation in temperature is shown to be broadly contemporaneous with no clear trend of temperature with age.

The oldest samples (55-50Ma) from the Red Cliff Fault were not in situ when sampled but form a distinct population ~15.5‰ $\delta^{18}O_{PBD}$ and ~0.5‰ $\delta^{13}C_{PBD}$. This is contrast to most to the main data population, which shows variation between 15- and -10‰ $\delta^{18}O_{PBD}$ and +1 to -12‰ $\delta^{13}C_{PBD}$. These data describe the main period of E-W extension described in Chapters 3 & 4 and vary in age from 45 to 20Ma.

The wide range of $\delta^{18}O$ is used to infer variation of fluid temperatures and isotopic composition, which is supported by constraints from clumped isotopic results. The variation in isotopic results is used to infer the influence of a) a Jurassic connate water or maybe deeper sourced fluid and b) meteoric surface water.

It has been shown that there is no clear relationship between structural deformation and fluids or the timing of calcite mineralisation. Localised as well as regional variation has been constrained; however, no definitive regional trends can be identified.

Carbon sources include marine carbonate and an organic source. This organic carbon source could either represent soil/atmospheric $CO_2$ or oxidised organic carbon from the organic-rich shales.

A model of Cenozoic fluid-flow is proposed with a two fluid system with mixing of a highly negative $\delta^{18}O$ meteoric water (-10‰ $\delta^{18}O_{Water}$) with a more isotopically positive connate or basinal fluid (-1‰ $\delta^{18}O_{Water}$). One fluid is interpreted to be in disequilibrium with the Jurassic host-rocks, which will be discussed further is Chapter 6.

# Chapter 6 – Synthesis

## 6.1 Introduction

The Cleveland Basin is situated on the western margin of the Southern North Sea (Figure 6.1) on the eastern coastline of Northern England. The tectonic history of the basin reflects a combination of events related to the development of the Southern North Sea (Kent, 1980a; Fig 6.1a) and uplift and differential tilting related to the development of the proto-Iceland plume in NW Britain (White & Lovell, 1997; Łuszczak et al., 2018 and references therein).

The aim of this chapter is to synthesise and discuss the results and evidence laid out in previous chapters and to explore the wider context of their regional importance and implications. A regional model will be proposed to integrate evidence of a prolonged regime of E-W extension and associated fluid-flow in the Cleveland Basin. The main outcomes of this research, however, are the outcomes and implications of the period of Cenozoic extension documented herein and discussed in previous chapters. This study combined a detailed structural analysis of the coastal region of the Cleveland Basin, integrating it with absolute age constraints, microstructural analyses and isotopic results. These results are unique and will be used to build a picture of the Cenozoic history of fluid-flow and deformation in the Cleveland Basin

The key results are highlighted and used to suggest potential areas for future work and analysis to build on. These include aspects that could not be completed here due to the effects of the COVID-19 pandemic will then be discussed.

## 6.2 Cenozoic history of the Cleveland Basin

The Cenozoic tectonic history of the Cleveland Basin is poorly constrained. The results described in previous chapters provide important new insights and additional constraints on the Cenozoic tectonic history of the basin.

### 6.2.1 Synopsis of Mesozoic Tectonic History

The Cleveland Basin formed in the Mesozoic with prolonged periods of subsidence through the Jurassic and Cretaceous (Rawson & Wright, 1992). The N-S trending Peak Trough is shown from interpreted seismic lines by Milsom & Rawson (1989) to have formed as a major synsedimentary graben. Early fault movements associated with the development of the Peak Trough are supported by observations in Chapter 4, which identify mud mounds and potentially the cone-in-cone structures as indicators of fluid migration, possibly related to early fluid movement along the Peak Fault. Later, generally small-offset extensional fault zones are widespread (described in detail in Chapter 3) and appear to have formed during modest amounts of regional Cenozoic extension (Section 6.3.2).

In addition to N-S striking fault structures, E-W brittle faults (Kirby & Swallow, 1987) are present at the southern margin of the basin, i.e., the Flamborough Head Fault Zone and Vale of Pickering Fault Zone. These E-W faults are thought to have originated as Jurassic growth faults, which were intermittently active during the Late Jurassic to Early Cretaceous (Rawson & Wright, 1992). The Flamborough Head Fault Zone separates the Cleveland Basin from the Market Weighton Block to the south and extends for 50-60km inland (Farrant et al., 2016). McKeen (2019) indicates from seismic interpretation that the Flamborough Head Fault Zone is an E-W striking graben of listric faults disconnected from the underlying pre-Mesozoic fault zone by the Permian Zechstein Evaporites. The Flamborough Head Fault Zone is discussed more in Section 6.2.5; however, the focus of this research and discussion is on the N-S striking structures associated with Cenozoic extension.

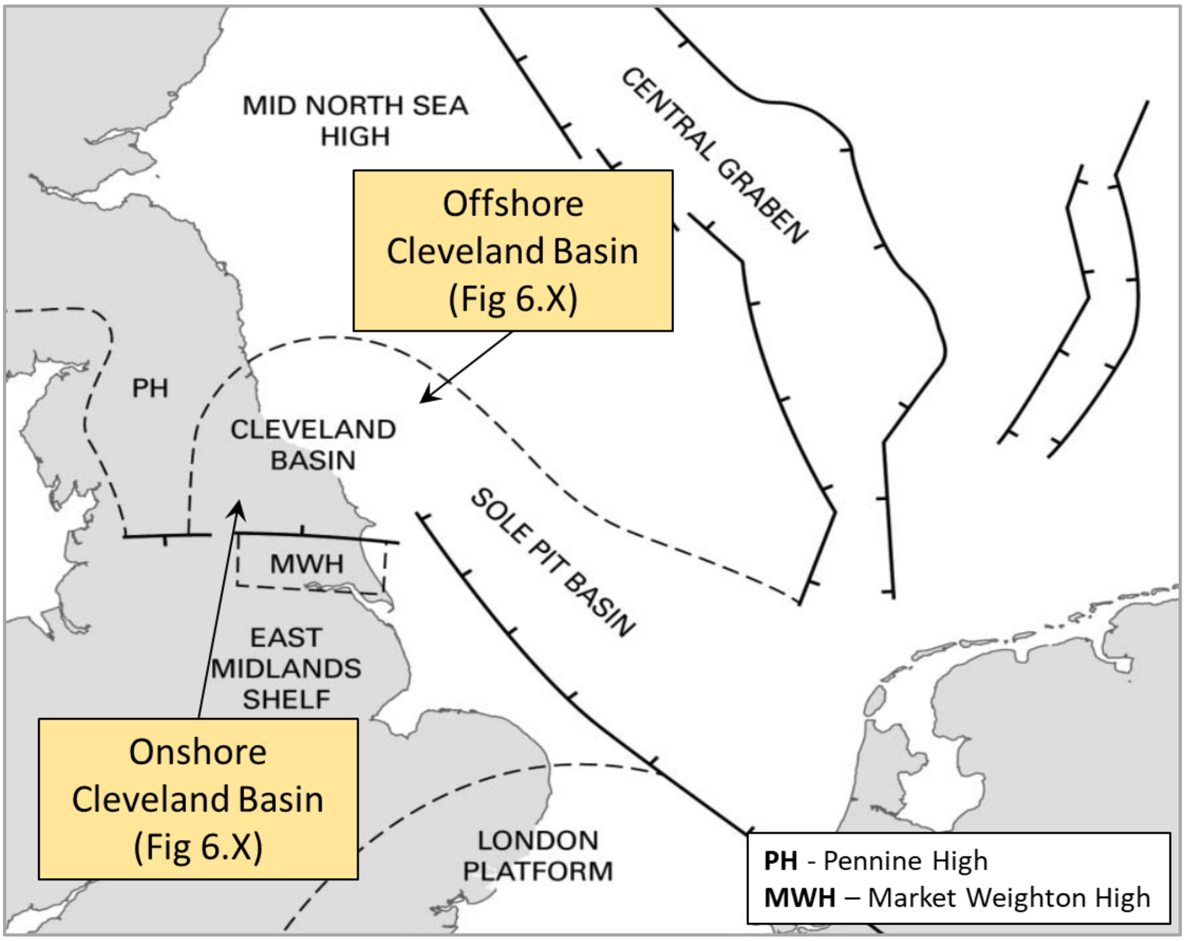


*Fig 6.1. Schematic map showing the Cleveland basin in the context of the larger Southern North Sea and surrounding highs (Powell, 2010).*

### 6.2.2 Maximum Burial

The timing of maximum burial of the Cleveland Basin and subsequent exhumation are still poorly constrained. Estimates of the timing and magnitude of maximum burial in the literature vary, with maximum burial depths ranging between of ~2.5km to 4km for the Lias (Green, 1989; Bray et al., 1992; Holliday, 1999; Kemp et al., 2005) during the end Cretaceous to mid-Cenozoic. Apatite Fission Track models proposed by Green (1989) and Bray et al. (1992) are consistent with maximum burial of the Cleveland Basin and East Midlands Basin during the latest Cretaceous to earliest Paleogene, with uplift commencing very soon after this time.

### 6.2.3 Jointing

At least two sets (Fig 3.2 & 3.4) of orthogonal N-S to NW-SE (J1) and E-W to NW-SW subvertical, predominantly opening mode joints are described in detail in Section 3.2.1. These joint sets have been previously described locally by Rives et al. (1992), Rawnsley et al. (1992), Imber et al. (2014), Emery (2016) and Daniels et al. (Pers. Comms.). Field observations described in Chapter 3, when combined with analyses of the joints at Jet Wyke and Saltwick Nab by Imber et al. (2014) and Emery (2016), support the hypothesis that the dominant joint sets were formed close to maximum burial. The presence of two regional joints sets represent changes in stress orientation (Imber et al., 2014; Emery, 2016) between E-W and N-S extension leading to purely tensile, opening mode fracturing.

### 6.2.4 Uplift and Inversion of the Cleveland Basin

Inversion and uplift of the Cleveland Basin is still poorly constrained but is thought to have occurred during the Late Cretaceous to Early Paleogene (Kent 1980a; Bray et al., 1992; Powell, 2010) <u>or</u> Eocene to Miocene (Hemingway & Riddler, 1982; Williams, 1986; Emery, 2016).

AFTA work in the offshore Sole Pit Basin by Glennie & Boegner (1981) and Green (1986) is used by Haarhoff et al. (2018) to suggest that Late Cretaceous to Paleogene uplift began in the offshore Southern North Sea before migrating northwards to the onshore Cleveland Basin. Rawson & Wright (1992) suggest that both E-W and N-S folding occurred contemporaneous with inversion, with Talbot et al. (1982) suggesting that the E-W Cleveland Anticline formed due to movement and readjustment of the Zechstein Evaporites.

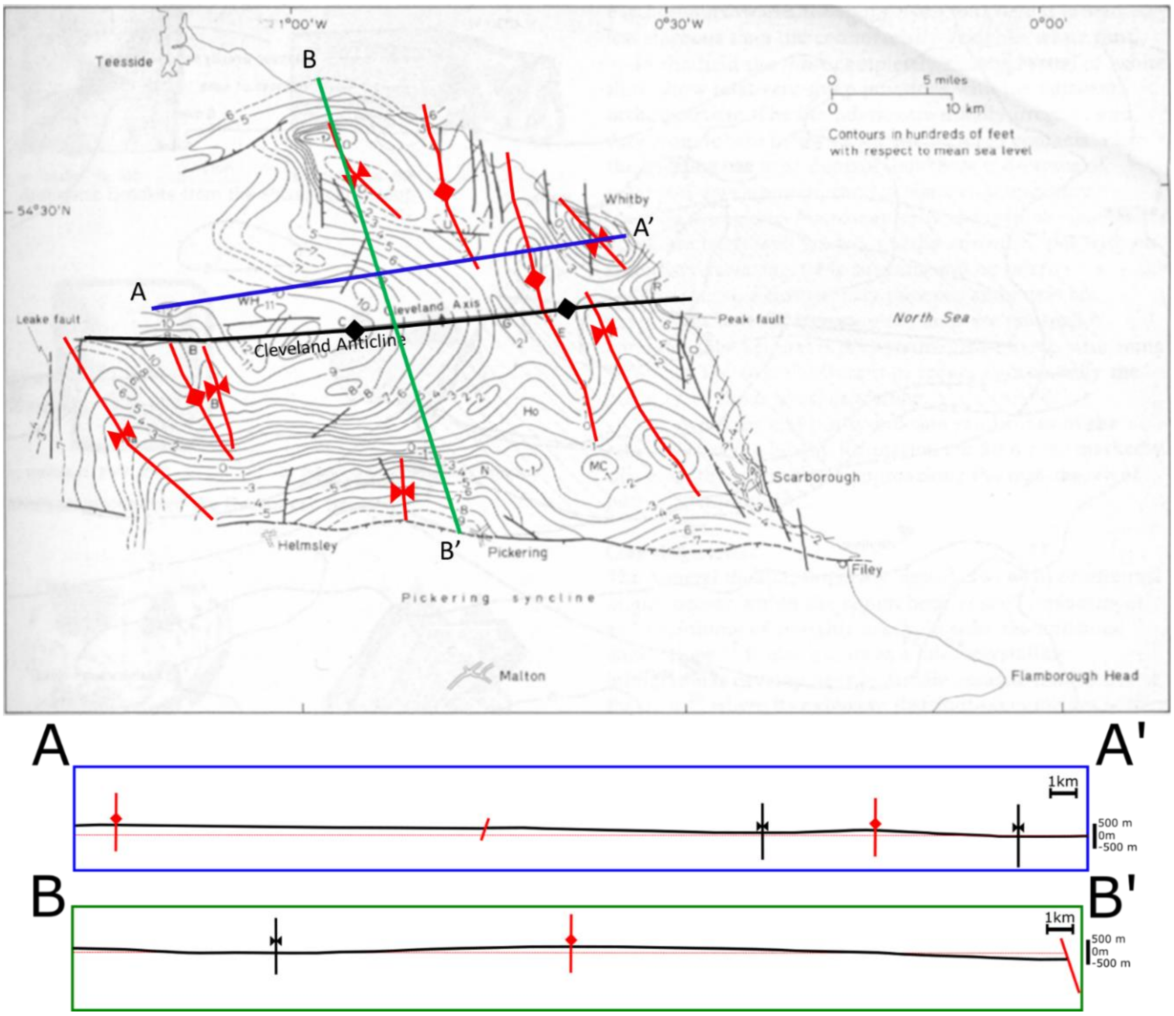


*Fig 6.2. Structure map of the Cleveland Basin projected on to the top Dogger Formation (Modified after Hemingway & Riddler, 1982). Two clear trends of folding exist with NNW-SSE trending folds annotated on in red and the E-W trending Cleveland Anticline in black. The black line shows the Top Dogger Formation with the red line denoting a 0m reference frame. Two cross-sections are shown A to A' (E-W) and B to B' (N-S). These show that folding is very gentle with interlimb angles of 1-2°.*

Cross-sections presented in Figure 6.2 drawn from structure contour maps of the Top Dogger Formation published by Hemingway & Riddler (1982) show that both E-W and N-S oriented folds are extremely gentle structures with interlimb angles >170° and fold limbs dipping at between 0.5-2°. Estimates of shortening based on these cross-sections indicate that the onshore folding is associated with 0.8% shortening E-W and 1.0% shortening in an N-S direction. In addition, the A-A' and B-B' sections (Fig 6.2) combined show a systematic tilt of the basin ~0.7° towards the southeast, which likely relates to Late Cretaceous to Early Paleogene tilting related to Atlantic opening and establishment of the Iceland hotspot. Apatite Fission Track Analysis from the Bowland Basin (Lodhia et al., 2022) supports this interpretation, suggesting that uplift in onshore Britain was initiated in the Late Cretaceous to Early Paleogene.

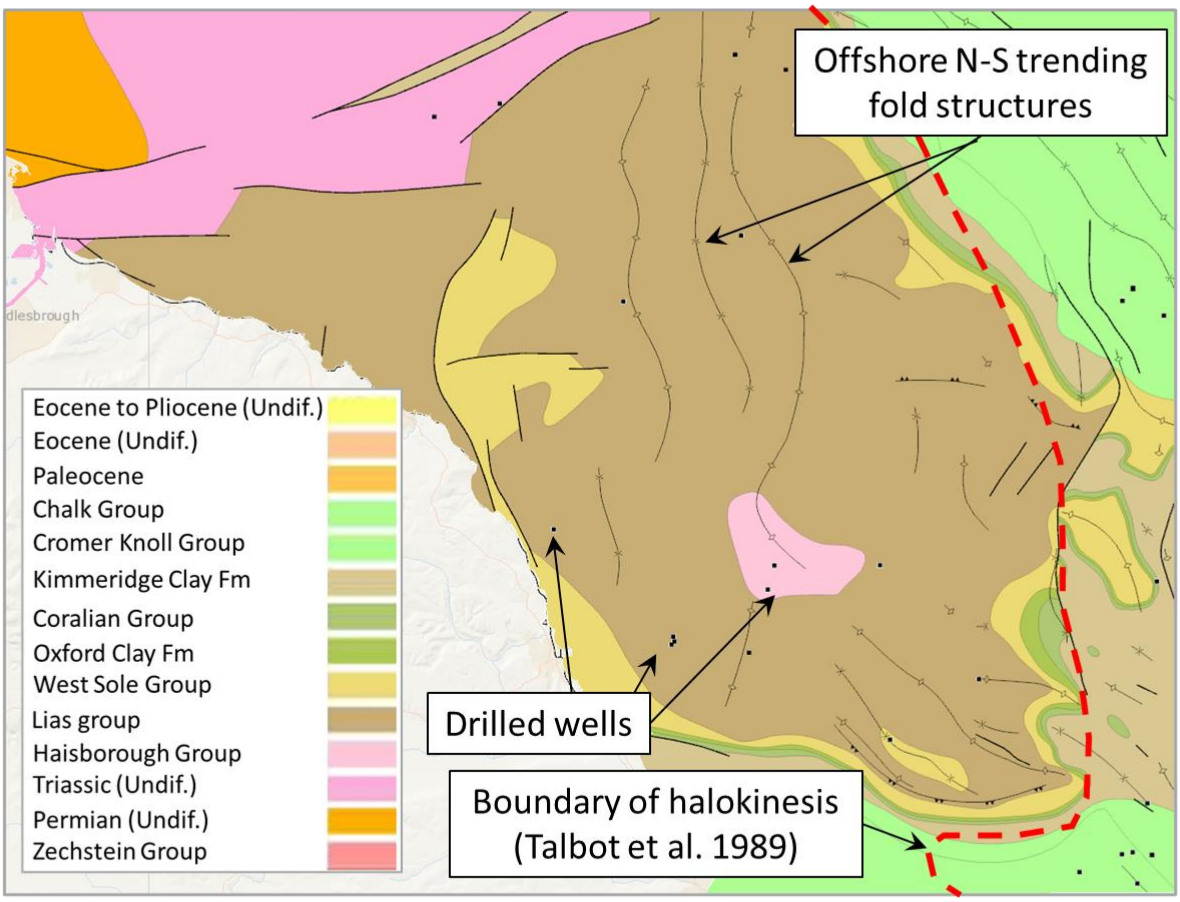


*Figure 6.3. Offshore geology map from the BGS Online Viewer (BGS, 2022) with offshore wells indicated as black squares and offshore fold structures annotated. The boundary of halokinesis based on Talbot et al. (1982) is shown at the eastern boundary of the Cleveland Basin.*

Similar styles of fold structures are present in the offshore Cleveland Basin with Rastall (1905) and Dingle (1971) suggesting that the Cleveland Anticline continues into the offshore Basin. Figure 6.3 shows geological mapping of the offshore Cleveland Basin by the British Geological Society, which indicates the presence of N-S trending anticlines and synclines in the offshore basin fill. Seismic lines presented by Grant et al. (2019) and indicated by Wood (Pers Comm.) do not show any interpreted faults underlying these folds, which are similarly open to the onshore.

### 6.2.5 Flamborough Head Fault Zone

The Flamborough Head Fault Zone is an E-W belt of brittle faults that marks the southern boundary of the Cleveland Basin. Exposures at Selwicks Bay have been described and analysed by many authors such as Peacock and Sanderson (1994), Starmer (1995), Sagi et al. (2016), Faÿ-Gomord et al. (2018) and Roberts et al. (2020). Roberts et al. (2020) involves significant contributions from the author and compliments the research described here. The full paper is included in Appendix 8.4.

Roberts et al. (2020) present U-Pb calcite dating of the Frontal Fault Zone of the Flamborough Head Fault Zone at Selwicks Bay. Normal faulting is the last phase of movement recognised along the Frontal Fault Zone (FFZ), and yields ages in the range ~64 Ma to ~55 Ma. It is clear that these movements were associated with significant fluid flow and associated calcite mineralization. Varved sediment fills are entombed in the calcite mineralisation of the FFZ and indicate that the fracture system was open to the seafloor at this time and was thus likely to be buried to no more than 1-2km based on estimates of the depths to which open fractures can form in the subsurface (Wright, 2009; Walker et al., 2011; Holdsworth et al., 2019; 2020; Hardman et al., 2020). Roberts et al. (2020) suggest that, in contrast to the complex deformation models proposed by Starmer (1995), all the structures observed can be explained by overlapping strike-slip and extensional deformation along the Flamborough Head Fault Zone, and that this deformation is likely linked to uplift and exhumation of NW Britain related to the opening of the North Atlantic. Critically, the study finds no evidence of Pyrenean or Alpine inversion as had been proposed by Starmer (1995).

I did a substantial amount of work for the Roberts et al. (2020) paper, aiding in field work and sampling, microscopic analysis of samples and U-Pb calcite dating of samples. Roberts et al. (2020) presents important evidence that extensional movement of the Flamborough Head Fault Zone at Selwick's Bay was active from 64-55Ma years ago. This contrasts highly with previous results from Starmer (1995) who had linked deformation at Flamborough Head with Pyrenean of Alpine inversion. In addition, the identification of open fissure fills indicates that the fracture system was open to the surface near this time with hard ground deposits washed in. This points to a mineralisation in a shallow geological setting less 1-2km in depth, but I speculate that the fissure depth was likely shallow <1km as the deeper a fracture becomes the more difficult it is to keep it open requiring proppant or substantial fluid pressures.

In addition, it is important to note that calcite mineralisation at Selwick's Bay described by Roberts et al. (2020) is both temporally and isotopically (described in Chapter 5) distinct from the widespread Cenozoic deformation analysed in this study. Further research is required to attempt to date compressional structures and at Selwick's Bay and identify a clear relation (if one exists) between calcite mineralisation along Flamborough Fault Zone and the Jurassic hosted fault and fracture fills focused on herein.

### 6.2.6 The Cleveland Dyke

The Cleveland Dyke forms the southernmost extension of the British Tertiary Volcanic Province (MacDonald et al., 1988) and was emplaced at 55.8 ± 0.3 Ma (Fitch et al., 1978); it is broadly contemporaneous with movements along the FFZ at Selwicks Bay located some 30SE of the furthest extent of the dyke. The dyke originates from the Mull igneous centre and shows an olivine-free, plagioclase- and pyroxene-phyric basaltic andesite composition (MacDonald et al., 1988). The Cleveland Dyke has been studied where it is well exposed at Cliff Rigg quarries near Great Ayton, Yorkshire (Jack Lee, unpublished work). Here, a previously unrecognised, 5-10m wide calcite-zeolite cemented breccia fills a sub-vertical fracture (Fig 6.4a) running through the centre of an en-échelon dyke segment. The fracture fill is composed of angular clasts of wall rock – including thermally spotted shale clasts (Fig 6.4b) - and altered dyke material set in a calcite and zeolite matrix and was observed at the level of the Staithes Sandstone Formation. While U-Pb calcite dating of this material from within the dyke was unsuccessful, the preservation of thermal spotting, the alteration haloes of the dyke's clasts are consistent with the relatively hot temperatures (90°C) obtained from clumped isotopic analysis and indicate that the dyke was likely still hot when the fissure formed and was mineralised. Thus, the calcite mineralization recognized here is likely of a very similar age to that seen associated with the FFZ at Selwicks Bay. There is no evidence in the Cliff Rigg fissure for marine sediment fills however, and the local preservation of rounded grains of quartz in the fissure fill matrix (Holdsworth pers. Comm.) may suggest that the fissure was connected to a sub-aerial surface environment; this too is consistent with the onset of uplift and regional tilting at this time.

Work by Wright (2009), Walker et al. (2011), Holdsworth et al. (2019, 2020) and Hardman et al. (2020) indicates that open fissures typically form in the shallow sub-surface at depths of <1-2 km. This is used to infer that at, or shortly after 55 Ma the Lower Jurassic of the Cleveland Basin was likely within <1-2of the surface and had likely already undergone substantial uplift from maximum burial. This supposition is supported by analysis by Versey (1937) which observed that the trend of the Cleveland Dyke is observed to deflect and follow existing fold axes suggesting that dyke emplacement post-dated some regional folding. These observations are used here to support previous interpretations by Rawson & Wright (1992) that at least some of the folding was associated with basin uplift and pre-dated dyke emplacement during the Late Cretaceous to Early Paleogene.

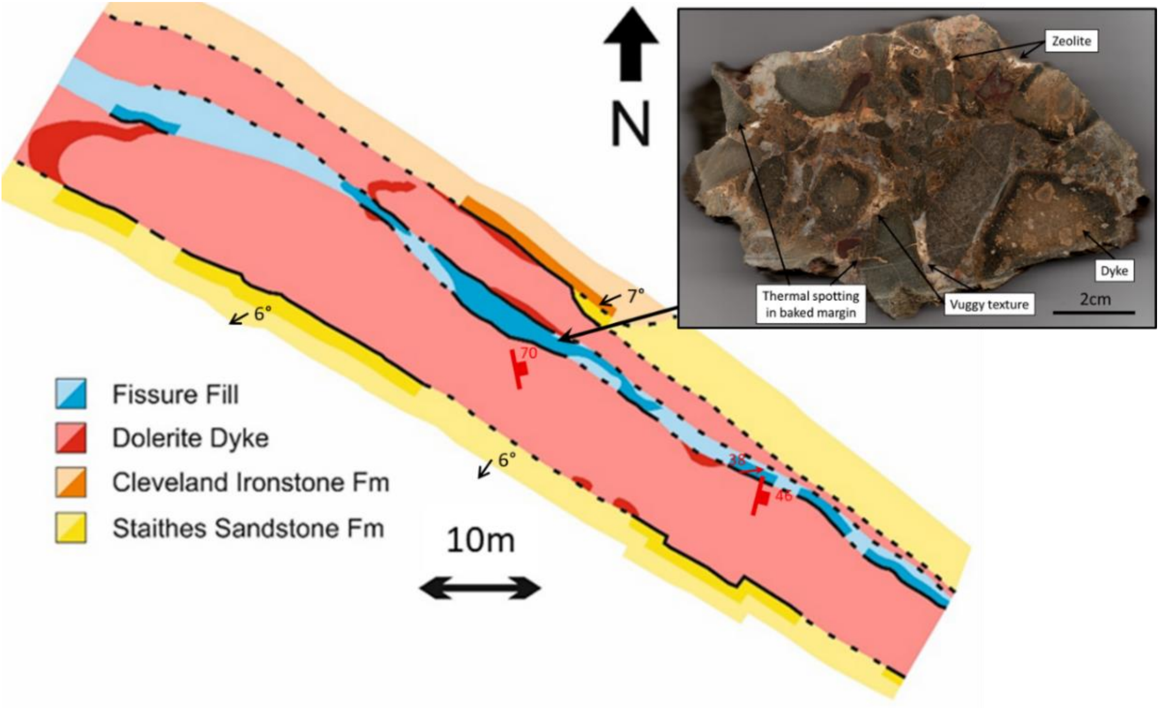


*Fig 6.4. a) Sketch map of the fissure fill running along the centre of the Cleveland Dyke at Cliff Rigg (622261.21, 6040246.64; Zone 30U, BNG). b) Photograph of a cut slab from the fissure fill demonstrating diagnostic thermal spotting of mudstone clasts included.*

### 6.2.7 Red Cliff Fault (55.0-46.5Ma)

As described in Section 3.2.2.3, two calcite samples taken from the Red Cliff Fault at the southern eastern margin of Cayton Bay (JL2031 & JL2032) were successfully dated at 55.0 ± 2.2Ma and 46.5 ± 2.2Ma. Neither sample was taken in-situ but are presumed to be locally derived. One in-situ sample was analysed but uranium concentrations were too low to provide a successful age. The same samples were microdrilled for stable isotopes (Section 5.4.2) and have comparable oxygen and carbon isotope signatures with the Flamborough Head samples. Few firm conclusions can be drawn from these samples but their proximity to the Red Cliff Fault suggests that they are likely related to a period of mineralisation related to fluid movement along the Red Cliff Fault. This phase of fluid-flow postdates earlier mineralisation and E-W extension along the Flamborough Head Fault Zone (Roberts et al., 2020), but predates the period of E-W extension (<45Ma) which forms the main focus of this study. Further in-situ samples are required for a comprehensive analysis of the deformation and fluid-flow at the Red Cliff fault.

## 6.3 Cenozoic Extension

U-Pb dating of calcite has been used in combination with field, microstructural and isotopic results to define a previously unconstrained period of Cenozoic deformation extending from 45 to 20 Ma. This phase of E-W extension postdates prior deformation and mineralisation preserved at Flamborough Head (FFZ; Roberts et al., 2020) which was associated with normal faulting during N-S extension ca. 64 to 55Ma. The results of stress inversion analysis (Section 3.3) show that the calcite mineralization from ca. 45 to 20Ma is associated with a long-lived period of E-W extension (Fig 6.5), with reactivation of the regional basin-scale Peak Trough faults and N-S striking joints and the establishment of N-S trending fault zone networks. Cenozoic faulting is indicative of widespread extension and there is no evidence of basin-wide compression. These structures are therefore interpreted to postdate uplift and gentle folding of the basin along N-S and E-W axes, at least locally.

Figure 6.5 & 6.6 illustrates the relative timing of Cenozoic extension compared to burial history diagrams (Emery, 2016) for the Cleveland Basin and regional tectonic events. Frequency plots for the U-Pb dates are shown demonstrating a distinct peak of calcite mineralisation between 37 and 32Ma (Fig 6.5 & 6.6) with activity continuing until ~20Ma. This peak of mineralisation and associated fluid-flow is pre-dated by the development of subvertical veins from ~45Ma, which represents the first stage of Cenozoic extension.

### 6.3.1 Joint reactivation and subvertical veining (ca. 45-39Ma)

The initial stage of E-W extension is observed at Saltwick Nab and Sandsend, where a sequence of millimetre-wide subvertical veins reactivating and infilling pre-existing N-S to NW-SE ($J_1$) striking joints were precipitated from 45-39Ma.

Subvertical calcite veins are predominantly composed of fibrous calcite growth (Section 4.5.2) that tracks E-W dilation of the pre-existing joints. The millimetre-wide veins occur over an area of ~50m at Saltwick Nab and show low magnitudes of extension (<1%) with similar magnitudes of extension observed at Sandsend. These magnitudes are supported by structural transects (Ashman, 2017), which suggest that magnitudes of extension associated with calcite veining were low.

As stated in Chapter 3, these veins are only easy to recognize in areas lacking faulting. In contrast to later veins, which show dilation due to fault movement, veins at Saltwick Nab and Sandsend show no clear structures capable of causing reactivation and are interpreted to be separate from fault related joint dilation. These calcite veins were hypothesised by

Imber et al. (2014) and Emery (2016) to be representative of hydrofracturing at deep burial. However, prior evidence from the Cleveland Dyke and joint reactivation suggest that these veins *postdate* maximum burial. It is hypothesised here that these calcite veins record the earliest phases of Cenozoic extension and fluid-flow, which was later overprinted by subsequent faulting and associated fluid-flow at other localities.

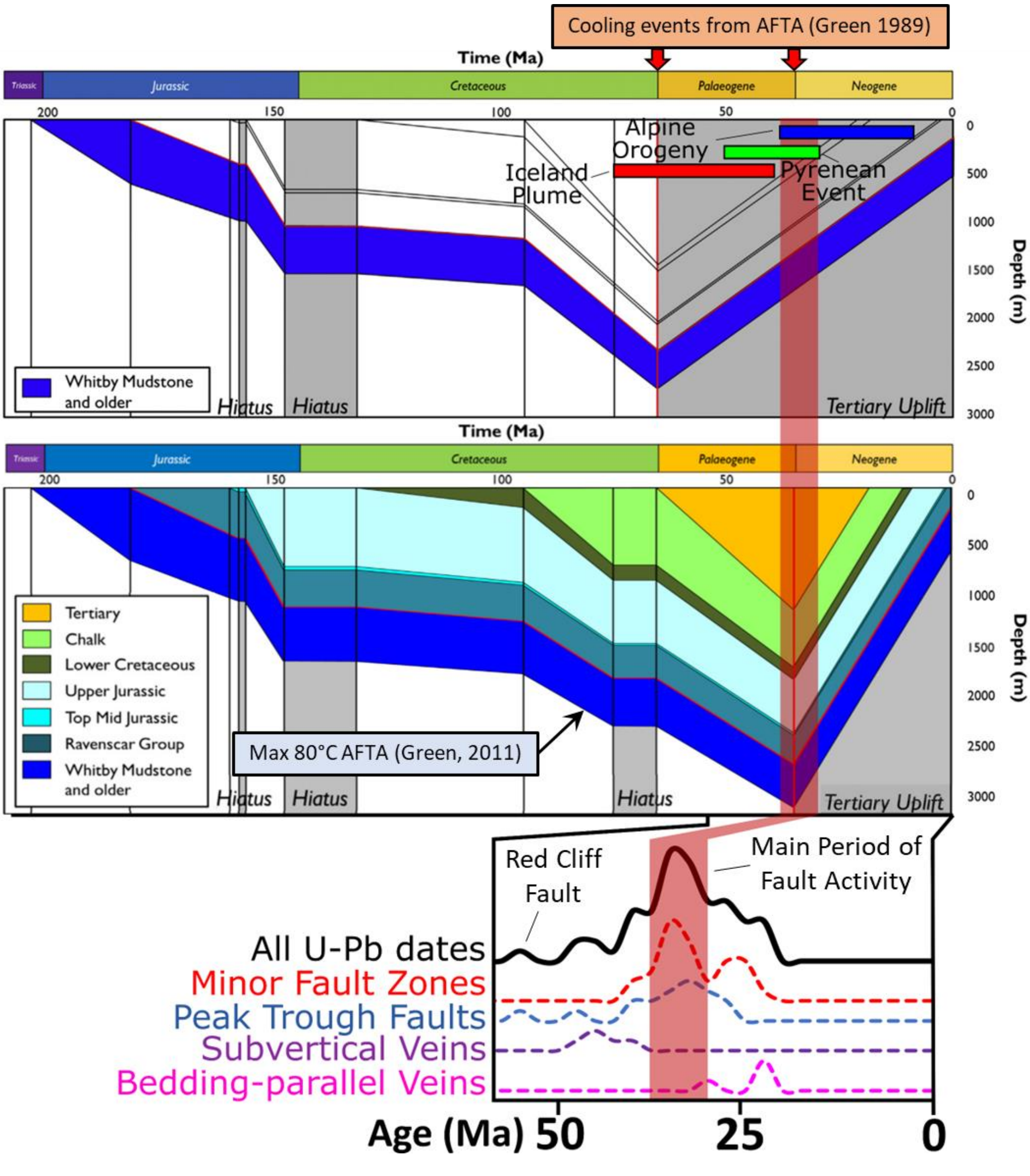


*Fig 6.5. Summary diagram with burial history plots modified after Emery (2016), a summary of the Cenozoic NE Europe tectonic events and frequency plots of the U-Pb calcite geochronology results presented in Chapter 4. 37-32Ma represents the peak of tectonic activity based on U-Pb geochronology. Evidence for shallow (<2km) burial is more compatible with the upper model assuming Late Cretaceous to Early Palaeogene uplift of the Cleveland Basin. Two dominant cooling/uplift events are shown from AFTA models by Green (1989) from the Cloughton-1 Borehole. A maximum temperature from AFTA is also shown from Cloughton-1 from Green (2011). This is suggestive of ~2km of uplift.*

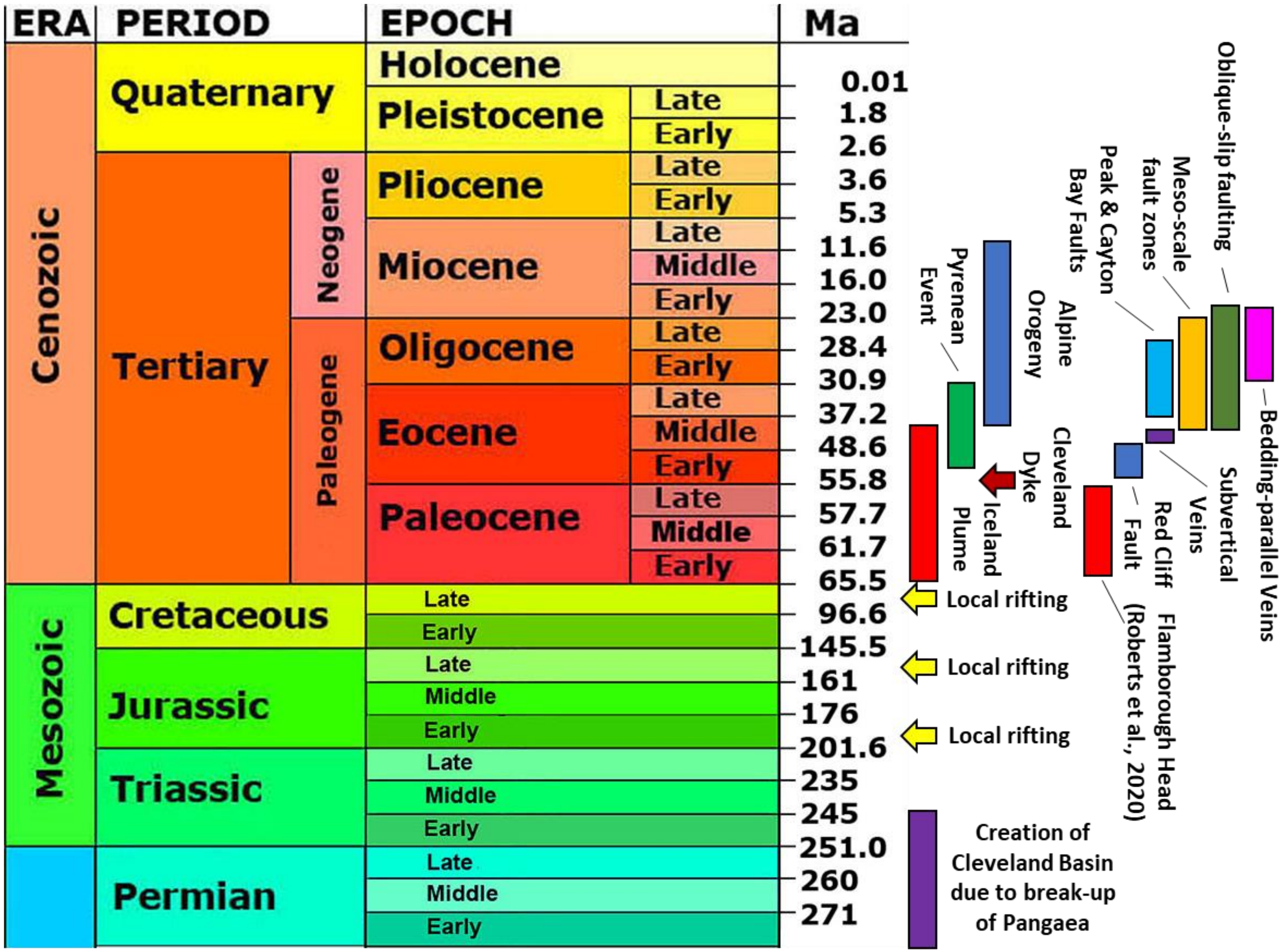


Fig 6.6. Illustration of the tectonic timescale of the Cleveland Basin incorporating the additional timings from U-Pb calcite geochronology presented here. It is clear that the majority of the extensional deformation identified overlaps with the Pyrenean and Alpine orogenies. Extensional deformation post-dates earlier calcite mineralisation dated by Roberts et al. (2020) at Flamborough Head.

### 6.3.2 Fault dominated extension (ca. 39-20Ma)

E-W extensional fault movement and associated calcite mineralisation (Fig 6.6-6.8) is expressed through the development of the Meso-scale normal fault zones (39-23Ma; Section 3.2.3), and reactivation of pre-existing fault structures such as the Peak Fault (38-27Ma; Section 3.2.2).

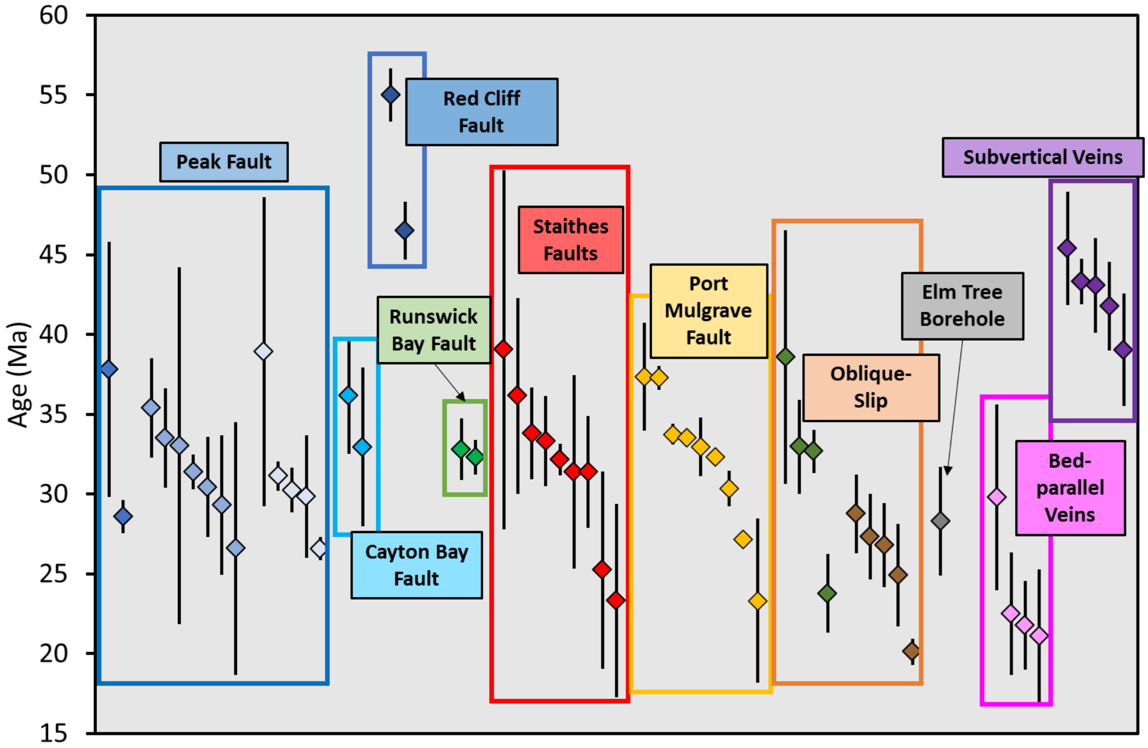


*Fig 6.8. Compilation of all the U-Pb calcite geochronological dates from the Cleveland Basin, coloured by structural grouping.*

#### 6.3.2.1 Peak & Cayton Bay Faults (ca. 38-27Ma)

The Peak Trough faults (Fig 6.9) represent the largest structures associated with calcite mineralisation. As discussed previously (Section 3.2.2) the Peak Trough faults show initial syn-sedimentary movement – likely during N-S Mesozoic extension – before undergoing reactivation under E-W extension during the Cenozoic. The Peak Trough reactivation is associated with mineralisation along the main and splay faults, and along conjugate sets of normal faults and reactivated $J_1$ joints in its associated damage zone.

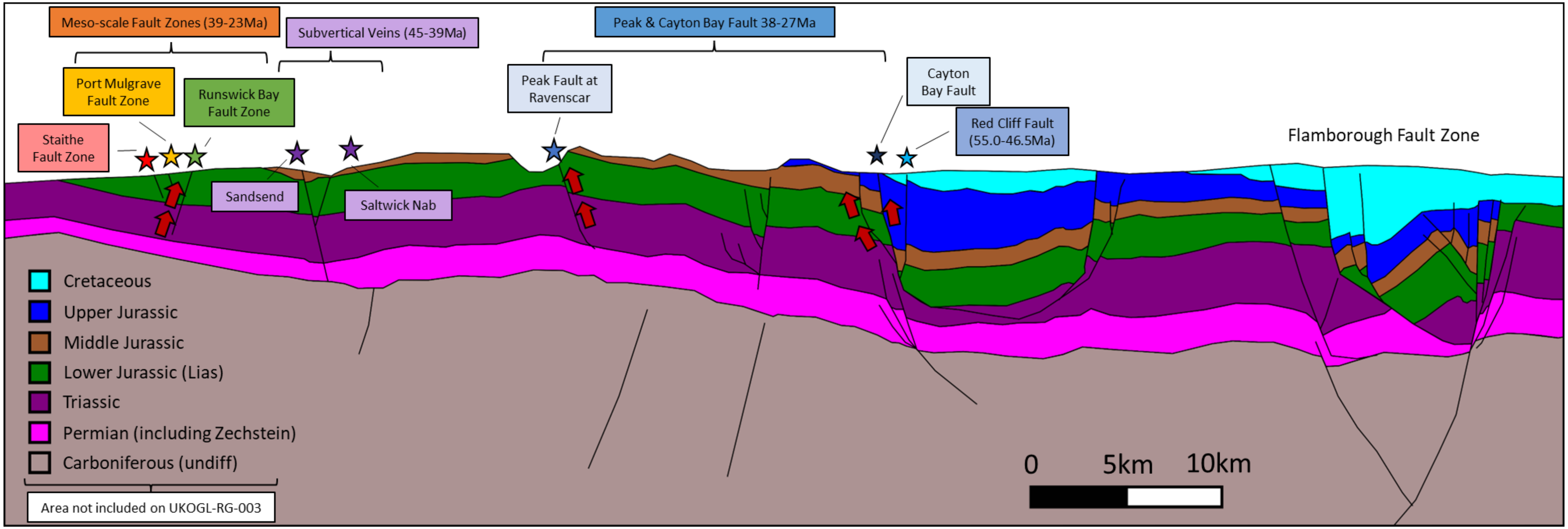


*Fig 6.9. Schematic cross section of the Cleveland Basin from NW-SE as illustrated in Chapter 1. The cross-section shows the structural and geological setting of the U-Pb calcite results discussed herein.*

The conjugate sets of normal faults show discrete planar fault planes and, along with lithified clasts in fault gouges, indicate formation post-lithification. This interpretation is supported by U-Pb calcite geochronology (Chapter 4), which shows that calcite precipitation was synchronous with deformation from ca. 38-27Ma. During extensional reactivation of the main and splay faults, centimetre-thick calcite fills formed syn and post-kinematically in pull-apart jogs. In addition, calcite mineralisation in conjugate normal faults is present along a range of structures such as extensional jogs, fault plane fills and in reactivated $J_1$ joints. While it is not possible to assess the magnitude of Cenozoic movement along the Peak Fault versus that which occurred pre-Cenozoic, offsets on individual minor fault structures are low (<50cm normal displacements) and indicate a low magnitude of extension, similar to that at other localities across the Cleveland Basin.

Calcite fills from the Peak Fault (Fig 6.9) have been analysed in detail for kinematic indicators (Chapter 4; Fig 4.24), with samples varying from those with clear syn-kinematic indicators to others with no kinematic indicators that formed synchronous or after local fault movements. The lack of clear syn-kinematic growth in some samples could indicate localised post-kinematic mineralisation, or syn-kinematic crack-fill growth occurring due to a change in the rate of mineralisation versus the rate of fracture dilation. The age of mineralised structures overlaps with synchronous movement and mineralisation of the main faults, minor normal faults and joint fills, supporting an interpretation that joint dilation at this locality was associated with movement of the fault structures.

The Cayton Bay Fault (Fig 6.9), in contrast, shows no clear evidence of syn-kinematic mineralisation, with mineralisation along the fault zone present in the form of anastomosing, vuggy veins with E-W and N-S joints mineralised near the fault. The magnitude of extension cannot be determined from the exposures available, but mineralisation is similar in style to that documented and dated by Roberts et al. (2020) from the Frontal Fault Zone at Selwicks Bay, where vugs are suggestive of open system fluid-flow (crack-fill) over a metre-scale zone, with centimetre-scale blocky calcite crystals formed. Two U-Pb calcite ages suggest that this mineralisation occurred from ca. 36 to 32Ma with both ages overlapping in uncertainty. Mineralisation and associated deformation at both this location and at the Red Cliff Fault will require further examination and analysis.

### 6.3.2.2 Meso-scale fault zones (ca. 39-23Ma)

In contrast to the deformation described above for the basin-scale Peak Trough faults, a series of smaller, kilometre-scale fault zones (Fig 6.9) were analysed and described, and are here been termed meso-scale fault zones. The fault zones have been described at Runswick bay, Staithes and Port Mulgrave, and are predominantly associated with low magnitudes (<1%) of E-W extension, except at Port Mulgrave where additional evidence for oblique-slip was documented in addition to extensional deformation. While small-scale normal fault structures have been described previously by Imber et al. (2014), no absolute timing constraints have been placed on this deformation.

Based on the discrete nature of the fault planes and the preservation of lithified clasts within gouges and fault breccias, the meso-scale normal fault zones clearly formed post-burial and lithification. They show a long period of activity (ca. 40-20Ma) with uncertainties describing a minimum period of ~18Myrs and a maximum period of ~25Myrs activity. Deformation and associated calcite mineralisation is concentrated along fault zones which are typically characterised by a series of normal faults spaced over zones of 200-500wide. Deformation is focussed around normal fault structures with associated reactivation of joint structures similar to that seen associated with the Peak Fault. Low magnitudes of extension are associated with fault structures (Chapter 3) having metre-scale displacements; this is supported by the structural transects of Ashman (2017), which utilises 20-30long traverses to document variable extension magnitudes ranging from <0.1 to 12% at Port Mulgrave and Staithes. This variability reflects partitioning of strain towards larger fault structures with magnitudes of deformation lower away from faults. In general, the magnitude of extension across the fault zones is likely <1%.

Field observations in this work support previous observations reported by Imber et al. (2014) and Emery (2016), with the mineralisation of extensional jog structures, slickenfibres, and implosion breccia development used to identify a variety of syn-kinematic calcite fills. Microstructural imaging in Chapter 4 has confirmed a number of fills that formed synchronous with fault movement (Fig 4.43. However, other samples with predominantly crack-fill textures do not unambiguously track the timing of vein filling relative to fault movements. These samples are used in conjunction with a minority of samples with cataclastically deformed calcite fragments and post kinematic samples to identify and bracket periods of deformation.

### 6.3.2.3 Oblique-slip faulting (ca. 39-20Ma)

As described in Section 3.2.3.4, localised oblique-slip faulting is present at the Port Mulgrave locality, with dextral and sinistral oblique-slip faults oriented at 60° to one another. A sinistral and a dextral fault are described in detail with associated calcite mineralisation.

The dextral fault has a bifurcated fault plane with a calcite mineralised extensional jog (JL1812b) with clear syn-kinematic mineralisation recorded with slickenlines and cone-in-cone structures (Fig 3.25d) and a crack-fill jog with vugs in hand specimen.

The sinistral fault, in contrast, includes a 10m wide rotated block with tilted bedding and listric and stair-step geometry bounding faults. Calcite mineralisation shows syn-kinematic sigmoidal veins with slickenfibres and a top to the west offset. Shear bands shown in optical images of a bedding-parallel sigmoidal vein are consistent with field observations of shear direction and support an interpretation of syn-kinematic mineralisation.

U-Pb calcite dating from samples from both dextral and sinistral oblique-slip faults indicate that mineralisation on these structures was active from ca. 39 to 20Ma (Fig 6.6-6.8). While samples such as JL2007 and JL1812a have crack-fill textures that likely post-date opening, local oblique-slip faulting was is shown to be synchronous with basin-scale extension (Fig 6.8).

Oblique-slip faulting is shown to be consistent with Riedel shears whilst local joint sets are oriented according to the expectation for T fractures (Petit, 1987). Oblique-slip faulting is shown to be highly localised and must therefore reflect stress conditions restricted to Port Mulgrave. Riedel shears are consistent with a distributed zone of deformation associated with dextral movement along an E-W trending fault zone. It is interpreted here that this dextral E-W fault zone represents a relay zone supporting differential extension of the Port Mulgrave and Staithes fault zones, and the relatively undeformed area located south of Port Mulgrave beach.

### 6.3.2.4 Bedding-parallel veins (29.8-21.1)

Bedding-parallel calcite veins associated with bedding-parallel fracture swarms that extend for >200m and described previously by Imber et al. (2014) and Emery (2016), are shown by the U-Pb calcite dating to correspond to the younger end of the age range for Cenozoic deformation, from ca. 29 to 21Ma. These veins have been previously associated with local dilation effects related to fault movement in the Staithes Fault Zone (Imber et al., 2014).

Bedding-parallel fracturing and calcite mineralisation were shown in Section 4.5.1 to be related to repeated cycles of mineralisation (opening mode fracturing) and shearing (top to the west) with truncation and open folding (approx. N-S trends). Fibrous calcite tracks opening of the fractures at 90° to the bedding. The existence of blocky calcite in addition to fibrous calcite indicates that these fractures were kept open for sustained periods of time, providing evidence for overpressure overcoming a vertical minimum principle stress.

The bedding-parallel veins, typified by NR1607, show evidence for cycles of vein opening and shearing. In Section 4.5.1, four zones of calcite were characterised with zones ordered in terms of increasing deformation and truncation. Zone 1 is heavily truncated while Zone 2 shows relatively tight folding; this contrasts with Zone 3 that is more openly folded and Zone 4 that shows little evidence of folding and/or truncation. This is inferred to represent a cycle of opening (normal) to bedding, which is followed by bedding-parallel shear. This deformation could represent a cyclic variation in the local or regional stress state or pore pressure, with high pore pressure required to overcome the vertical stress. Dilation is followed by shear reactivation along the fractures, which act as zones of weakness. No evidence of cataclasis of calcite zones has been observed but may have occurred elsewhere.

The cycles of opening mode and shear fracturing are attributed here to variations in differential stress (Engelder, 1999), with low differential stress characterising periods of tensile opening and periods of higher differential stress leading to shear fracturing. Therefore, while the calcite in bedding-parallel veins does not directly record syn-kinematic movement, U-Pb dates are suggested to represent intra-slip periods. These ages reflect quiescent periods of low differential slip during a longer repeated cycling of dilation and shearing.

The results from U-Pb calcite geochronology describe a period of bedding-parallel mineralisation from 28.9 to 21.1Ma, which has been shown to be bracketed by repeated fault movements. This suggests that either the structures were only active during the later phase of regional deformation <30Ma, or possibly that earlier fracturing lacked mineralisation, or exists but was not successfully dated, or has been reworked by later deformation and mineralisation.

Imber et al. (2014) explained bedding-parallel veining through dilation effects at the base of normal faults during slip. It is indicated here that while bedding-parallel veins do record periods of shear concurrent with fault movement, bedding-parallel fracture dilation is characterised by periods of low differential stress with fluid pressure propping the fracture open during the precipitation of blocky calcite zones. The fact that the bedding-parallel veins form one of the youngest phases of mineralisation could be consistent with ongoing exhumation and tilting with vertical stress almost as small as or less than the horizontal stresses at the time of formation.

### 6.3.3 Role of Overpressure

Field and microstructural observations provide evidence for the role of pore fluid pressures with pore fluid pressures inferred to reach the minimum principle stress under shallow burial (<2km) leading to hydrofracturing associated with calcite mineralisation in the Cleveland Basin. Multiple observations of cone-in-cone structures, which have been directly linked to overpressure by Cobbold & Rodriquez (2007) and Cobbold et al. (2013), have been made at the Peak Fault and in a dextral fault at Port Mulgrave. While the first example is inconclusive and could be related to early synsedimentary movement, the cone-in-cone structures at Port Mulgrave are directly related to an extensional jog structure (Fig 3.25d) that has been dated at 38.6 ± 8.0, 33.0 ± 2.9 and 32.7 ± 1.4Ma.

In addition to the cone-in-cone structures, bedding-parallel veins are present at Staithes, which were shown in Chapter 4 to have domains of blocky and fibrous growth normal to fracture margins. This means that the fracture was held open by fluid pressure during calcite precipitation or repeatedly opened and incrementally filled. The presence of blocky calcite rules out any inference of crystallisation pressure as was discussed in Section 4.2.3.1. This indicates that at the time of E-W extension, overpressure allowed the bedding-parallel fracturing to propagate, and the fractures to be held open during calcite mineralisation.

The presence of calcite fibre growth normal to the fault plane in a number of calcite veins (NR1620 & JL2024) also indicate that fluid overpressure influenced opening mode fracturing. This suggests a cyclic relationship between shear and pore pressure influenced opening mode dilation that will require further analysis in the future.

The development of repeated cycles of calcite mineralisation bounded by shear in bedding-parallel veins suggests that overpressure was cyclic occurring in pulses of fluid overpressure. These pulses could either represent pressure build-up and release in the sediments themselves or cyclic communication to deeper overpressured stratigraphy via faults as fluid conduits. Overpressure could have caused faults to release and become conduits for overpressured fluids to bypass otherwise impermeable stratigraphy. More study is required to examine in detail the relationship between overpressure and deformation in the Cleveland Basin now that this study has put absolute age constraints on the timing and manner of deformation.

### 6.3.4 Fault-related mineralisation

A number of syn-kinematic and post-kinematic calcite fills were identified in Chapter 4. Chapter 4 focused on identifying primary calcite cements and the relationship of calcite mineralisation to faulting. There is no clear evidence for recrystallisation or post-emplacement alteration of calcite cements. A number of pre-, syn- and post-kinematic fills have been described, with U-Pb calcite dated syn-kinematic fills providing direct constraints on the timing of fault movements. In contrast, while post-kinematic fills do not provide direct evidence of fault movement, they do provide critical evidence for the local timing of cessation of faulting. Pre-kinematic samples, in contrast, represent cataclasis and reworking of pre-existing calcite veins.

Figures 4.24, 4.43 & 4.52 illustrates the range of pre-, syn- and post-kinematic calcite zones dated as part of this study. Syn-kinematic calcite mineralisation becomes less frequent through time, with only JL1809c recording fault movement synchronous with fault movement post 25Ma. This suggests that while mineralisation still occurred via crack-fill (Roberts & Holdsworth, In Press), fault movement and extension was dying off, with only isolated and infrequent shear fracturing. Prior to 25Ma, multiple faults from both the Peak Fault and meso-scale faults indicate synchronous fault movement with some post-kinematic fills suggesting periods of prolonged or episodic fluid-flow beyond the timing of individual fault movements.

Calcite fills vary from simple opening-mode veins with syntaxial (JL2001) or antitaxial (JL1815) fills to highly complex multiphase/compound veins such as JL2016 or JL2021. Blocky and fibrous fills are common, with typical relationships suggesting that blocky fills formed after fibrous fills, such as in NR1609, JL2023 or JL2024. This cycle is repeated in many samples, in addition to samples such as JL2016 where potentially reworked earlier fibrous veins are present. As fibrous fills typically form during rapid filling of thin veins and blocky textures during slower fill of veins, the relative timing of these textures could provide information about the rate of precipitation vs dilation. The relationships observed suggest rapid precipitation or low levels of dilation during initial vein formation with the inverse being true later in the vein formation potentially as strain increases or precipitation rate drops off.

### 6.3.5 Magnitude of Cenozoic Extension

Observations presented in Chapter 3 suggest that the magnitude of Cenozoic extension is low, with offsets on minor faults at Staithes, Runswick Bay and Port Mulgrave on the scale of a few metres. Similarly, extensional reactivation of N-S $J_1$ joints at Saltwick Nab are extremely low with millimetre-wide calcite veins emplaced. These observations are supported by extension estimates based on transect lines by Ashman (2017). Ashman (2017) measured extension from fractures and faults along the coast of the Cleveland Basin at Port Mulgrave, Whitby and Staithes. Estimates vary from 0.001 to ~12% extension. Some estimates of extension are provided for calcite veins alone and these vary in magnitude from 0.1% to just over 1% extension. The variability is likely related to localisation of deformation around faults or fractures. Nevertheless, the very low displacement values along faults mean that these structures are very likely to lie well below the maximum resolution for seismic reflection data, i.e. in an offshore setting, they will in most cases not be imaged.

The magnitudes of extension can be utilised to calculate strain rates utilising following the method of Fossen (2016; his Figure 6.2). If we assume 5% bulk extension over a period of ~25 Myr (based on range of U-Pb calcite dates), this produces a strain rate of $6.342\times10^{-17}$/sec whilst a bulk magnitude of 1% leads to a strain rate a strain rate of $1.268\times10^{-17}$/sec. These values are shown to be comparable with rift related strain rates from other basins by one dimensional modelling from Newman & White (1999). It is worth noting, however that these values are at the lower end of rift related strain rates, with rates lower than $10^{-17}$/sec suggested to mark the termination of rifting.

### 6.3.6 Inferences from fluid-flow

Extensional deformation is closely associated with basin-wide fluid-flow leading to calcite precipitation. Observations in Chapter 3 and isotopic results from Chapter 5 suggest a complicated fluid-flow pathway with individual fault structures showing significant isotopic deviation from other similar contemporaneous extensional structures. In addition, temperature variations from clumped isotope analysis combined with oxygen isotopes have been used to infer the presence of two highly distinct end-member fluids: a ~-1‰ $\delta^{18}O$ fluid similar to a Jurassic connate water (~80°C) and an anomalously light ~-10‰ $\delta^{18}O$ meteoric fluid (~20°C).

In Section 5.4.3 it was identified that a two fluid system best explained the observation of significantly different temperature fluids, identified from clumped isotopes, at the same stratigraphic level. Utilising the evidence for Late Cretaceous to Early Paleogene uplift and exhumation, we can infer that meteoric fluid was circulating in the shallow subsurface (<1-2 km). An assumption of shallow burial supports the interpretation that a "warm" ~80°C fluid was in disequilibrium with uplifted and cool Jurassic host-rocks. It is suggested here that the introduction of a more $\delta^{18}O$ positive, warm fluid from deeper in the basin mixed with meteoric waters and minor amounts of connate waters at shallow burial. Low permeabilities of the Whitby Mudstone Formation ($10^{-18}$-$10^{-21}$ $m^2$ permeability; Houben et al., 2017) suggests that any fluid-flow would have to be facilitated by fracture permeability. This is further supported by observations in Chapter 3, which indicate that calcite mineralisation is localised and focussed near fault and fracture and that it becomes markedly less intense away from these structures.

Flow of deeper sourced basinal fluids indicates that deformation and fluid-flow is not limited to the Jurassic strata exposed on coastal outcrops but that structural fluid-flow conduits (faults and fractures) must extend to ~2in depth based on paleogeothermal gradients of 30-35°C/km for the basin (Green, 1989; Emery, 2016). This inference is supported by similar regimes of deeply sourced fluid-flow at Flamborough Head (Faÿ-Gomord et al., 2018) and Wessex Basin (Worden et al. 2015); both examples are discussed in more detail in Chapter 5.

### 6.3.7 Gravitational Sliding

Exhumation of the Cleveland Basin prior and potentially during to regional extension suggests that Cenozoic deformation could have been driven by related tilting. Thin-skinned deformation of the basin on the underlying Zechstein has been widely documented in Chapter 1 for basin-scale fault structures offshore. Were this detachment to extend onshore, it could support an interpretation of a gravity-driven system. The example interpreted seismic section (Fig 6.10 – which comes from a study of the Orange Basin, offshore Namibia by De Vera et al., 2009) shows a clear definition between the higher extensional domain and the down slope contractional domain, which are linked by a transitional domain. Deformation in these systems is balanced between extension and compression. Gravity-driven basin systems have been described extensively in the literature, for example by Hesthammer & Fossen (1999), Cartwright & Jackson (2008), De Vera et al. (2009) and De Souza et al. (2020).

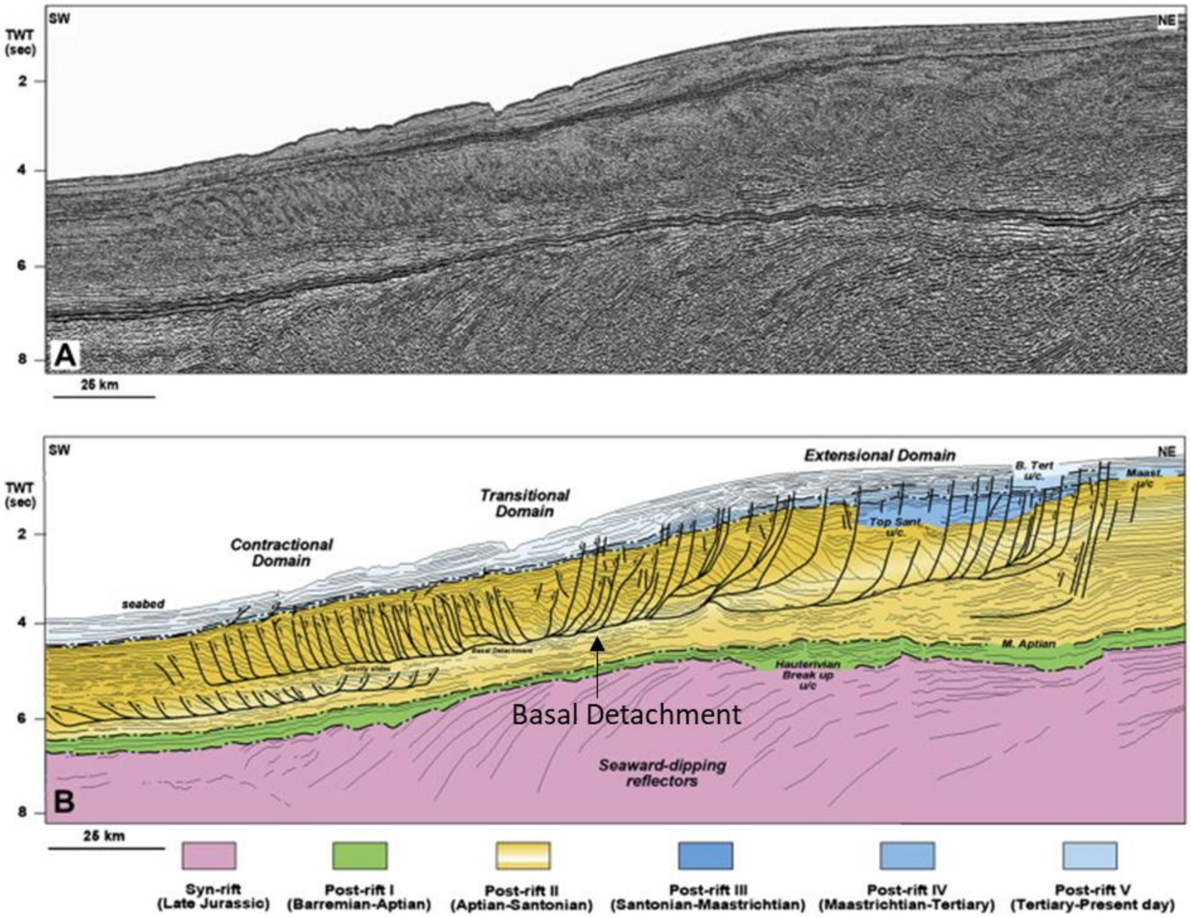


Figure 6.10. Regional Seismic line from of the main depositional Late Cretaceous gravity-driven slide system, Orange Basin, Namibia (De Vera et al., 2009) with the uninterpreted section (a) and interpretation (b).

The calculated rates of $1\times10^{-17}$ to $6\times10^{-17}$/sec (Section 6.3.7) are comparable to halokinetic related deformation but similar to rift related strain rates, lie at the lower end of expected strain rates. This would suggest that any halokinetic driven extension would be associated with low differential stresses (Fig 6.10), to produce the magnitudes of extension and strain rates observed in the onshore Cleveland Basin. This indicates that if detachment on the underlying Zechstein Evaporites drove extension, little salt movement would be required.

### 6.3.8 Role of the Zechstein

The regional model shown in Figure 6.10 from De Vera et al. (2009) shows thin-skinned deformation of the Orange Basin gravitational system. Similar thin-skinned deformation of the Cleveland Basin has been documented by Milsom & Rawson (1989) and McKeen (2019), who utilised seismic interpretations of the Peak Trough and Flamborough Head Fault Zone to show detachment of these structures on the underlying Zechstein Evaporites. Observations from the Boulby Mine exposures by Woods (1979) and Talbot et al. (1982) also describe evidence of flow in the Zechstein Evaporites coupled with thin-skinned deformation in relation to supposed inversion of the pre-Mesozoic basin faults. Despite Talbot et al. (1982) indicating that the onshore Cleveland Basin is situated beyond the halokinetic boundary of the Zechstein Evaporites (Fig 6.3), indicators of evaporite flow suggest that limited strain during Cenozoic extension could have been accommodated by detachment and flow of the Zechstein Evaporites. This halokinetic boundary likely shows the boundary of large-scale salt movement and does not rule out more limited salt flow which would be required to explain the low strain rates and magnitudes of extension calculated for Cenozoic extension in the Cleveland Basin.

Further north on the coast of County Durham, Smith (1995) and Daniels et al. (2020) provide detailed description of the Permian stratigraphy. Smith (1995) has observed substantial brecciation of the Permian carbonate, which the author links to dissolution of the underlying Permian Zechstein Evaporites. Dissolution of these evaporites has led to subsequent collapse and brecciation of the overlying stratigraphy leading to highly localised collapse pipes in the Concretionary Limestone Formation.

### 6.3.9 Regional Model

A regional model is proposed here (Fig 6.11) in which the protracted period of E-W extension documented by this study was driven by partial gravitational collapse/readjustment of the Mesozoic Cleveland Basin in response to uplift and tilting during the latest Cretaceous to Early Paleogene. Minor readjustments and movements of the Permian Zechstein evaporites are suggested to have acted as a detachment zone and facilitated the mild extensional deformation of the mudstones of the Lias. This model is proposed as a hypothesis that best explains the research outlined herein, however, further research is needed to test and rule out alternative hypotheses.

The lack of significantly thick halokinetic evaporites is considered the most likely limit on the magnitude of extension and is suggested as the primary reason why such low strain is documented onshore. The Cleveland Basin sat on the edge of the Southern North Sea Permian salt basin with salt thicknesses thinning westward towards the current margin of the onshore Cleveland Basin (Talbot et al., 1982). These thin evaporite thicknesses are assumed to form a major control on the low magnitudes of extension and strain rates documented in Section 6.3.5.

Examples of other gravitational systems are used to infer the presence of an offshore contractional/compressional zone to balance the onshore extension. It is likely though that the magnitude of any offshore compression is very low and would balance the low magnitude of extension observed onshore (<1%). N-S trending offshore folds are seen on BGS mapping and correlate with where marginal compression would be anticipated with gravity related extension (Fig 6.3).

One potential complication is the fact that onshore folding (as shown in Figure 6.2) exhibits two distinct sets - N-S and E-W trending folds. It is suggested here that the N-S trending folds pre-date extension and relate to an earlier eastward migrating belt of compression as the westward margin of the basin was progressively exhumed and tilted during Late Cretaceous to Early Paleogene. This belt of compression is inferred to have migrated from the onshore basin to the offshore Cleveland Basin due to continuing tilting. The exact age and development of the E-W trending folds including the Cleveland Anticline is unclear, but as stated previously in Section 6.2.4, these very open folds likely formed due to readjustments or N-S compression during Late Cretaceous to Palaeocene exhumation related to Atlantic opening. Folding is likely related to the reactivation of pre-Mesozoic fault structures, which observed in Boulby Mine by Woods (1979). It is suggested here that N-S trending folds likely formed synchronous with compression along the Flamborough Head Fault Zone or due to earlier N-S compression. The magnitude of E-W extension (Section 6.3.5) and E-W shortening (Section 6.2.4) is roughly comparable which is what would be expected in a setting of gravitationally driven deformation.

The regional model is proposed as a hypothesis to best describe the results generated in this study. However, it is important to consider that much of this regional model is based on speculation and more study is required to test this hypothesis.

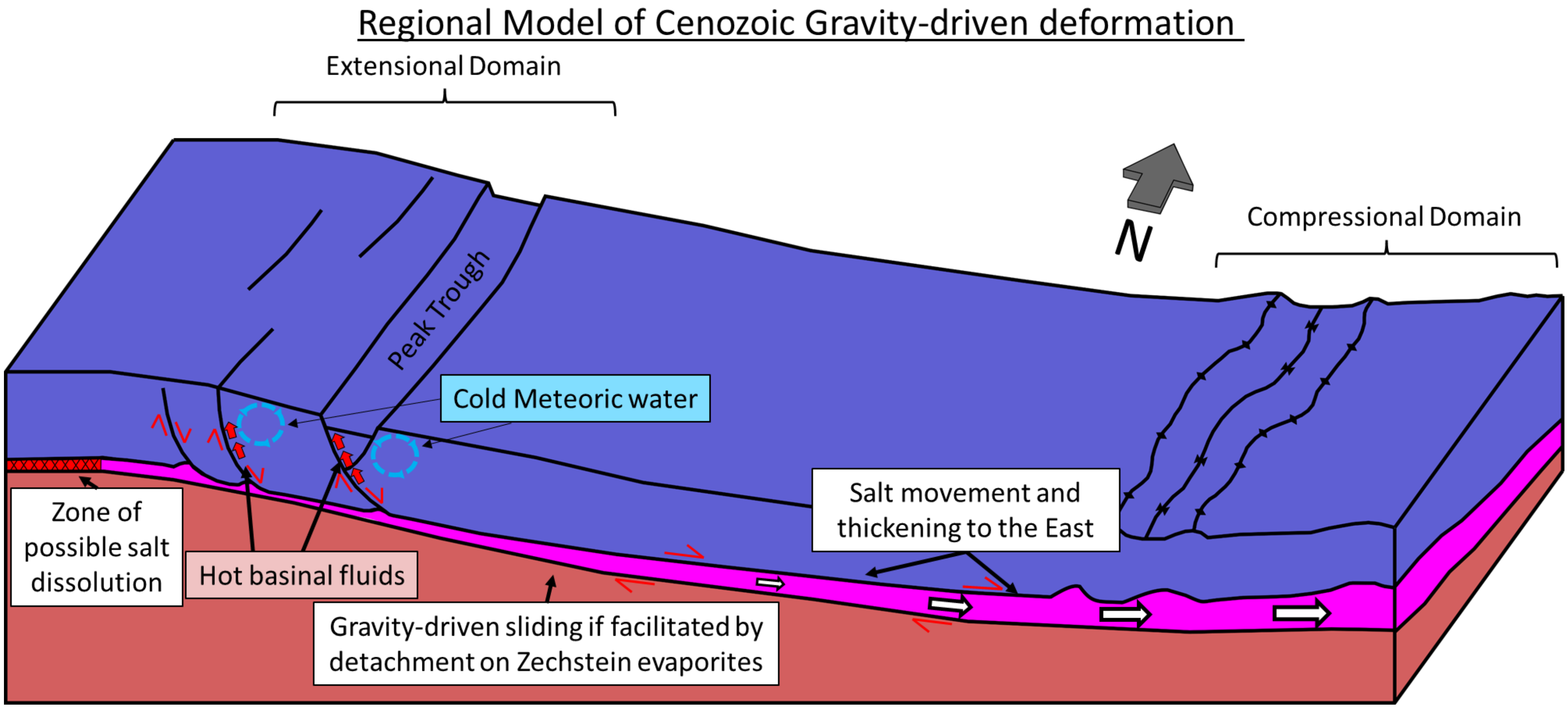


*Fig 6.11. Proposed schematic regional model for the Cleveland Basin with Cenozoic deformation and associated fluid-flow driven by partial gravitation collapse of the Mesozoic basin towards the Southern North Sea with detachment on underlying Zechstein Evaporites. Evaporites are shown to move westward with possible dissolution of the evaporites similar to the Durham coast (Smith, 1995) at the western extent of the salt.*

## 6.4 Implications of this Research

The main outcome of this research are the constraints that have been put on the age and style of deformation in the Cleveland Basin. E-W extension dominates the Cenozoic history of the Cleveland Basin. E-W extension occurs through the development of Meso-scale fault structures <10km in length and the reactivation of basin-scale structures such as the Peak Trough faults. The relationship between deformation, and fluid-flow and hence calcite mineralisation are complex with numerous complicated and highly variable calcite fills formed in fault and fracture structures. Localised oblique-slip faulting, in addition to, typical extensional structures have been documented at Port Mulgrave indicating the potential for more complicated deformation patterns at localised-scales of <1km.

### 6.4.1 Regional tectonics

The findings documented here have numerous implications for the understanding of the Cenozoic of the Cleveland Basin. Cenozoic E-W extensions documented supports previous assertions that uplift and exhumation of the Cleveland Basin occurred in the Late Cretaceous to Paleogene with little evidence of shortening related to orogenic inversion events. Uplift is thought have occurred due to tilting of Britain to the NW related to Atlantic opening and the establishment of the Iceland hotspot. Uplift and tilting related to Atlantic opening, and the E-W extension that occurred as a consequence, can explain the patterns of deformation and fluid-flow observed. There is no evidence that the Alpine and Pyrenean orogenies, although Figure 6.7 does show that they overlap in timing with the main period of extension and fluid-flow in the Cleveland Basin, had any large-scale influence on the tectonic history of the Cleveland Basin.

The Cleveland Basin is inferred to have been at shallow depths (<1-2km) during most of the Cenozoic with prior tilting leading to partial gravitational collapse down slope towards the Southern North Sea. The magnitude of collapse, shortening by folding and extension was only mild (magnitudes of <1%), and likely limited by the lack of sufficient thicknesses or dissolution of halokinetic Zechstein Evaporites underlying the onshore region of the Cleveland Basin. More extensive evidence for salt-related deformation is seen in offshore areas where the Zechstein sequences at depth are thicker due to halokinetic movement (Talbot et al., 1982).

### 6.4.2 Regional Fluid-flow

Utilising the regional model proposed in Section 6.3.9, it is possible to make additional deductions with regards to the Cenozoic fluid-flow regime of the Cleveland Basin. It is shown in Chapter 5 that isotopic and temperature variations in the data are best explained by interaction of hot fluid (80°C at an inferred depth of ~2km) with a highly $\delta^{18}O$ negative (-10‰) surface meteoric water at ~20°C. Since both fluids are evident in calcite mineralisation in Jurassic host-rocks at the same stratigraphic level it assumed that shallow circulating meteoric fluid mixed with deeply sourced basinal fluids. Some influence of connate waters in the host-rock is expected but is likely dominated by the other fluid components. This fluid interaction system is shown in Chapter 4 to be mainly associated with E-W extension with some post-kinematic mineralisation over a period of >20Myrs. Evidence from the Cleveland Dyke and previous AFTA work (Green, 1986; Bray et al., 1992) highlights the likelihood that deformation and calcite mineralisation post-dated at least initial uplift and exhumation of the Cleveland Basin. Section 6.3.3 also describes the evidence for elevated pore fluid pressures that influenced Cenozoic deformation and fluid-flow.

It is therefore suggested that widespread fracturing during gravity-driven extension, in addition to elevated pore fluid pressures could have led to the infiltration of warm fluids upwards, using faults and fractured zones as fluid conduits. These warm fluids would have migrated upwards into the shallowly buried (<1-2 km) Jurassic mudstones where variable mixing with downward-circulating meteoric fluids along with connate waters would have led to precipitation of calcite along actively moving faults and fractures that opened following local fault movement. Evidence of high pore fluid pressures means that a related pressure differential between low pressure shallow fluids and deep overpressured strata could have been the main driving mechanism for upward fluid movement. Evidence of overpressure greater than the principle vertical stress (Sv) associated with late-stage bedding veins (~21Ma) could imply that the surrounding fault and joint system were effectively sealed/cemented at this time. It is hypothesised that pulses of overpressure could have led to fault slip and the up-fault movement of overpressured fluids.

Further analysis is required to fingerprint the sources and pathways of fluid-flow further. Uncertainty inherent in the temperatures from clumped isotopes means that a model of mixing between just connate waters and meteoric waters without the need for input from deeper sourced fluids cannot be conclusively ruled out.

#### 6.4.2.1 Fracture and Faults as Fluid Conduits

The studied fault and fracture structures vary in size and the potential scale of hosted fluid-flow. Large centimetre sized crystals are associated with the Cayton Bay Fault and the float samples from near the Red Cliff Fault. These are most similar in style to the fluid-flow described by Roberts et al. (2020) for the Frontal Fault of the Flamborough Head Fault Zone, with anastomosing veins at the Cayton Bay Fault associated with a 2m wide zone of mineralisation. The Cayton Bay and Red Cliff faults are also the most southerly sampled in the basin (Fig 3.1), and are Red Cliff Fault samples are shown to be the most similar to the Flamborough Head Fault Zones in terms of fluid composition and age.

In contrast to these high-volume fluid-flow conduits, all other structures analysed have smaller calcite fills typically on average 2-3cm in thickness with cm- to mm-scale crystals. Instead of fluid-flow being focussed on a single structure, the distributed nature of the calcite mineralisation suggests it was spread out over much wider zones of fault related fracturing, within 10-50 metres of fault structures. This points to the absence of a singular conduit capable of transmitting fluid and hence fluid-flow through a more tortuous pathway.

Mudstone lithologies typically form low permeability lithologies in the subsurface, which effectively limits the vertical movement of fluids. Fracturing is one method of generating permeable pathways through an otherwise low permeability formation (Ingram & Urai, 1999). It is shown here that a highly variable array of extensional structures can be formed and work effectively as fluid conduits. In contrast to Flamborough Head (Roberts et al., 2020) where a large volume of fluid is isolated along the Frontal Fault system with an open fissure established, fluid-flow through the organic-rich Whitby Mudstone Formation is dominated by millimetre-scale to centimetre-scale structures with variable crack-fill, crack-seal and crack-seal-slip and vuggy porosity (Chapter 3 & 4). As faults slip, not only does mineralisation occur along the fault plane in veins and pull apart structures, but reactivation of pre-existing joints can occur, which can also act a vertical fluid conduits. Post-kinematic fills identified in Chapter 4 also indicate that fluid-flow persisted after local fault movement with fluids leading to mineralisation in remnant porosity and vugs.

### 6.4.3 Hydrocarbon and $CO_2$ storage

The Whitby Mudstone Formation represents an excellent analogue hydrocarbon seal and source rock interval with a thick (~105m) sequence of mud-rich lithologies (Powell, 2010). It is also locally organic-rich (the Jet Rock has an average Total Organic Carbon of 6.5% to a maximum of 18.2%) and is immature to early oil mature (Barnard & Cooper, 1983). Bitumen is preserved in a some extensional jogs associated with the extensional faults along the Port Mulgrave Fault Zone.

Early Jurassic organic-rich mudstones and similar Late Jurassic mudstones form important source and sealing lithologies in the Central and Northern North Sea (Ziegler, 1980; Barnard and Cooper, 1981; Cooper & Barnard; 1984). Cenozoic extension and linked fluid-flow may represent an analogue for later-stage hydrocarbon movement in other basins with fluid movement synchronous with uplift and or gravity-driven distributed extension. This hydrocarbon movement could be due to oil and/or gas expulsion from hydrocarbon mature source rocks (similar to the Whitby Mudstone Formation) or as seal breach where impermeable mudstones are acting as a local or regional hydrocarbon seals.

Evidence of Cenozoic fluid-flow in the Cleveland Basin suggests that uplift and exhumation of the basin was followed by prolonged phase of distributed extension and fluid migration. As detailed in Chapter 3, deformation is largely linked to fault structures which are mostly subseismic in scale, which could suggest that underlying onshore and shallow offshore hydrocarbon prospects in close proximity to N-S trending normal faults in the Southern North Sea may be at a high risk of seal breach. Cenozoic deformation, therefore, could provide an important control on the potential for future hydrocarbon exploration or $CO_2$ storage in the onshore and offshore Cleveland Basin and analogous exhumed basins.

## 6.5 Future Work

Future work could be undertaken to build on the results compiled in this research with a focus on further constraining and analysing Cenozoic extension and associated fluid-flow.

### 6.5.1 Borehole Analysis

Covid-19 related delays led to fairly limited wellbore core analysis with three wellbores logged of which only the Elm Tree Borehole is discussed herein as the other boreholes yielded little in the way of useful results. With more time and funding, the focus of wellbore sampling could be expanded to further onshore boreholes. In addition, the initial plan for this research was to run a second phase of wellbore logging and sampling focussed on offshore wellbores, but due to logistical and timing issues, the focus was kept on the onshore basin. Future work could target offshore boreholes (Fig 6.3; UK NDR 2022) that have penetrated and cored similar Liassic mudstones and look for similarly timed fluid-flow and deformation related to the offshore Peak Trough, or the more distal compressional structures indicated on BGS offshore mapping (Fig 6.3).

### 6.5.2 Fluid Inclusion Analysis

It was indicated in Section 5.1.2 that 10 samples were analysed for fluid inclusion work at NUI Galway's Geofluids Research Group. Future work could focus on additional analysis to find suitable inclusions for microthermometric and salinity analysis. This data along with potential strontium isotope analysis could be utilised in a similar manner to analyses in the Wessex Basin by Worden et al. (2015) and Faÿ-Gomord et al. (2018) to appraise the potential for deeper fluid sourcing from Triassic or deeper stratigraphy such as the Zechstein Evaporites. However, the failure of the original fluid inclusion work due to only poor preservation of fluid inclusions suggests that future fluid inclusion work could have a high chance of failure.

### 6.5.3 Further Isotopic Analyses

Clumped isotope results in this project were only generated a few months prior to thesis completion, which meant that the analysis was more limited than initially intended with statistical analysis via R programming language omitted. Future work could include a more thorough analysis with the development of comprehensive and expanded isotope mixing models for the Peak Trough and meso-scale faults. In addition to this, the stable isotope data would benefit from expansion towards under-populated structures including the bedding-parallel veins at Staithes and subvertical veins from Saltwick Nab and Sandsend. Issues relating to sample suitability and time constraints led to these populations being under-represented.

The results and analyses generated here suggest multiple avenues of future work with a few select examples suggested above. Future work and analyses will provide vital tests of the regional model, timing of uplift and inferred fluid-flow regime presented herein.

### 6.5.4 Burial History Modelling

Previous analyses by Williams (1986) and Emery (2016) have tried to constrain the burial history of the Cleveland Basin (Fig 6.), however evidence of the timing and extent of uplift, exhumation and Cenozoic extension discussed herein could be included into an updated burial history model of the Cleveland Basin. U-Pb calcite dates results associated with burial diagenetic phases have not been included here due to time constraints and as they record Early Toarcian to Cretaceous diagenesis and cementation unrelated to the larger story of

Cenozoic extension. These results will be further analysed for publication and could be used to further constrain the timing, temperature and depth of burial and diagenesis.

### 6.5.5 Relationship to the Durham Coast

As previously discussed in Section 6.3.6, Smith (1995) documented large-scale dissolution of the Zechstein Evaporites with associated collapse structures. Calcite veining is documented in associated with these collapse structures (Daniels, Pers. Comm.) and current work by Roberts and Holdsworth is focussed on analysing the absolute timing of this veining and deformation. The methodology applied herein of combined field characterisation, microscopy, U-Pb calcite geochronology and isotopic analyses will be utilised to investigate the timing of calcite veining and the relationship to the deformation and fluid-flow described herein.

Current work by Holdsworth and Roberts is now focusing on dating calcite mineralisation in the Permian carbonates to attempt to determine the age of dissolution and brecciation and future work could link this dissolution event to the narrative of Cenozoic extension documented herein.

# Chapter 7- Conclusions

## 7.1 Conclusions

The Lower Jurassic section of the Cleveland Basin has been demonstrated to have a complicated Cenozoic history of deformation and fluid-flow. The Cenozoic history of the Cleveland Basin was characterised by gravitationally-driven extension related to prior uplift and tilting of the basin as a consequence of Late Cretaceous to Early Paleogene mantle plume activity and North Atlantic opening.

- Extensive fieldwork, microstructural, U-Pb calcite geochronology and stable and clumped isotope analyses have been utilised to investigate a previously unconstrained period of deformation and fluid-flow in the onshore Cleveland Basin from ca. 45-20Ma with a peak of activity from 37-32Ma.
    - E-W extension is expressed through the formation of a series of N-S trending zones of normal faulting from and extensional reactivation of the regional-scale Peak Trough faults from ca. 39 to 20Ma following earlier dilational and cementation of pre-existing N-S trending subvertical joints from 45 to 39Ma.

- Field description has been presented for a series of regional to local scale faults from the onshore Cleveland Basin
    - Stress inversion demonstrates that the structures are typically consistent with E-W extension, with the exception of localised oblique-slip at Port Mulgrave, with evidence of synkinematic development of calcite fills.
    - Localised oblique-slip faulting at Port Mulgrave (ca. 39-20Ma) is consistent with Riedel shearing related to a zone of distributed dextral strike-slip interpreted to reflect a relay zone accommodating differential extension.
    - No clear evidence has been recorded of inversion of fault structures related to N-S compression and folding, which is inferred, therefore, to predate extension.
    - Regional extension is inferred to be of low magnitude (<1%) with deformation focussed on fault structures.

- Microstructural characterisation shows no evidence of large-scale calcite recrystallisation in samples described, and has been used to characterise samples in relation to host-structure kinematics i.e. pre-, syn- and post kinematic calcite fills.

- E-W extension has led to multiple phases of fluid-flow (ca. 45-21Ma) through the Whitby Mudstone Formation with fluid-flow associated with calcite mineralisation in a variety of regional to local fault and fracture structures.

- A regional model is presented to explain the prolonged E-W extension and associated fluid-flow with the subsequent exhumation of the Jurassic to the shallow sub-surface. Exhumation and tilting is caused by to Atlantic opening and the development of the proto-Iceland hotspot leading to partial gravitational collapse of the Cleveland Basin down slope towards the Southern North Sea.
    - N-S trending folds are formed due to an eastward migrating belt of compression related to tilting generated by Atlantic spreading and the Iceland hotspot.

- The Zechstein evaporites are inferred to play an important role facilitating thin-skinned deformation, acting as a detachment horizon.
    - A lack of a substantially thick evaporite section is thought to have limited collapse. The absence of sufficient halokinetic salt is thought to be related to initial depositional thickness or later dissolution similar to that documented along the Durham coastline.

- Cone-in-cone structures in association with oblique-slip faulting (ca. 39-33Ma) at Port Mulgrave, in combination with bedding-parallel veins (30-21Ma) at Staithes record evidence of overpressure in the Lower Jurassic mudstones although the mechanisms generating this pressure require further constraints.

- Clumped and stable isotopic analyses suggest a complex and tortuous fluid-flow system with significant spread of isotopic and temperature data indicating highly variable and isolated fluid pathways in the subsurface.
    - A model is proposed to explain variations in fluid-flow properties with mixing suggested between a shallow meteoric fluid (20°C) and a deeper sourced basinal fluid (~80°C).

    - Warm basinal fluids have utilised fault zones and associated fractures as fluid conduits explaining isotopic variation between hydraulically segregated fault zones.

- No evidence has been observed that the Alpine or Pyrenean orogenies have had a widespread effect on Cenozoic deformation in the Cleveland Basin with evidence from the Cleveland Dyke and Frontal Fault Zone supporting Late Cretaceous to Early Paleogene uplift and tilting of the Cleveland Basin.

# Bibliography

Adlan, Q., Davies, A.J. and John, C.M., 2020. Effects of oxygen plasma ashing treatment on carbonate clumped isotopes. *Rapid Communications in Mass Spectrometry*, *34*(14), p.e8802.

Alexander, J. and Gawthorpe, R.L., 1993. The complex nature of a Jurassic multistorey, alluvial sandstone body, Whitby, North Yorkshire. *Geological Society, London, Special Publications*, *73*(1), pp.123-142.

Alexander, J., 1986. Idealised flow models to predict alluvial sandstone body distribution in the Middle Jurassic Yorkshire Basin. *Marine and Petroleum Geology*, *3*(4), pp.298-305.

Allmendinger, R.W., Siron, C.R. and Scott, C.P., 2017. Structural data collection with mobile devices: Accuracy, redundancy, and best practices. *Journal of Structural Geology*, *102*, pp.98-112.

Anderson, E.M., 1951. The Dynamics of Faulting with Applications to Britain: Edinburgh. *Oliver and Boyd*.

Anderson, N.T., Kelson, J.R., Kele, S., Daëron, M., Bonifacie, M., Horita, J., Mackey, T.J., John, C.M., Kluge, T., Petschnig, P. and Jost, A.B., 2021. A unified clumped isotope thermometer calibration (0.5–1,100 C) using carbonate-based standardization. *Geophysical Research Letters*, *48*(7), p.e2020GL092069.

Ashman, I., 2017. Stratigraphic Variation in Fracture Densities in the Mudrock Dominated Succession of the Cleveland Basin, Northern England. *Department of Earth Science. Durham University.*

Attewell, P.B. and Taylor, R.K., 1971, September. Jointing in Robin Hood's Bay, North Yorkshire coast, England. In *International Journal of Rock Mechanics and Mining Sciences & Geomechanics Abstracts* (Vol. 8, No. 5, pp. 477-481). Pergamon.

Bankwitz, P. and Bankwitz, E., 1984. Die Symmetrie von Kluftoberflächen und ihre Nutzung für die Paläospannugsanalyse. Zeitschrift für geologische Wissenschaften, 12(3), pp.305-334.

b

Balson, P., Butcher, A., Holmes, R., Johnson, H., Lewis, M., Musson, R., Henni, D.P., Jones, S., Leppage, P. and Tuggey, G., 2001. North sea geology. British Geological Survey Technical Report, 8, p.48.

Barnard, P.C., PC, B. and BS, C., 1981. Oils and source rocks of the North Sea area.

Baroni, S., De Gironcoli, S., Dal Corso, A. and Giannozzi, P., 2001. Phonons and related crystal properties from density-functional perturbation theory. Reviews of modern Physics, 73(2), p.515.

Bergman, S.C., Huntington, K.W. and Crider, J.G., 2013. Tracing paleofluid sources using clumped isotope thermometry of diagenetic cements along the Moab Fault, Utah. *American Journal of Science*, *313*(5), pp.490-515.

Bernasconi, S.M., Daëron, M., Bergmann, K.D., Bonifacie, M., Meckler, A.N., Affek, H.P., Anderson, N., Bajnai, D., Barkan, E., Beverly, E. and Blamart, D., 2021. InterCarb: A community effort to improve interlaboratory standardization of the carbonate clumped isotope thermometer using carbonate standards. *Geochemistry, Geophysics, Geosystems*, *22*(5), p.e2020GC009588.

British Geological Survey materials, ©NERC 2021, https://mapapps.bgs.ac.uk/geologyofbritain/home.html

British Geological Survey materials, ©NERC 2022, https://mapapps.bgs.ac.uk/geologyofbritain/home.html

Black, M., 1928. “Washouts” in the Estuarine Series of Yorkshire. Geological Magazine, 65(7), pp.301-307.

Black, M., 1929. Drifted plant-beds of the Upper Estuarine Series of Yorkshire. *Quarterly Journal of the Geological Society*, *85*(1-4), pp.389-439.

Bons, P.D., Elburg, M.A. and Gomez-Rivas, E., 2012. A review of the formation of tectonic veins and their microstructures. *Journal of structural geology*, *43*, pp.33-62.

Bons, P.D., 2000. The formation of veins and their microstructures. *Journal of the Virtual Explorer*, *2*, p.12.

Bott, M.H.P., 1959. The mechanics of oblique slip faulting. Geological magazine, 96(2), pp.109-117.

Botz, R., Pokojski, H.D., Schmitt, M. and Thomm, M., 1996. Carbon isotope fractionation during bacterial methanogenesis by CO2 reduction. *Organic Geochemistry*, *25*(3-4), pp.255-262.

Bourg, I.C., 2015. Sealing shales versus brittle shales: a sharp threshold in the material properties and energy technology uses of fine-grained sedimentary rocks. *Environmental Science & Technology Letters*, *2*(10), pp.255-259.

Bray, R.J., Green, P.F. and Duddy, I.R., 1992. Thermal history reconstruction using apatite fission track analysis and vitrinite reflectance: a case study from the UK East Midlands and Southern North Sea. *Geological Society, London, Special Publications*, *67*(1), pp.3-25.

Brunstrom, R.G.W. and Walmsley, P.J., 1969. Permian evaporites in North Sea basin. *AAPG Bulletin*, *53*(4), pp.870-883.

Buckman, S.S., Fox-Strangeways, C. and Barrow, G., 1915. A palaeontological classification of the Jurassic rocks of the Whitby district; with a zonal table of Lias ammonites. *Fox-Strangways & Barrow (1915)*, pp.59-102.

Buckman, J.O., Corbett, P.W. and Mitchell, L., 2016. Charge contrast imaging (CCI): revealing enhanced diagenetic features of a coquina limestone. *Journal of Sedimentary Research*, *86*(6), pp.734-748.

Cameron, T.D.J., Bulat, J. and Mesdag, C.S., 1993. High resolution seismic profile through a Late Cenozoic delta complex in the southern North Sea. *Marine and Petroleum Geology*, *10*(6), pp.591-599.

Cartwright, J.A. and Jackson, M.P.A., 2008. Initiation of gravitational collapse of an evaporite basin margin: The Messinian saline giant, Levant Basin, eastern Mediterranean. *Geological Society of America Bulletin*, *120*(3-4), pp.399-413.

Catt, J.A., Gad, M.A., Le Riche, H.H. and Lord, A.R., 1971. Geochemistry, micropalaeontology and origin of the middle Lias ironstones in northeast Yorkshire (Great Britain). *Chemical Geology*, *8*(1), pp.61-76.

Cazenave, S., Chapoulie, R. and Villeneuve, G., 2003. Cathodoluminescence of synthetic and natural calcite: the effects of manganese and iron on orange emission. *Mineralogy and Petrology*, *78*(3), pp.243-253.

Chowns, T.M., 1968. *Environmental and diagenetic studies of the Cleveland ironstone formation of north east Yorkshire* (Doctoral dissertation, Newcastle University).

Cobbold, P.R. and Rodrigues, N., 2007. Seepage forces, important factors in the formation of horizontal hydraulic fractures and bedding-parallel fibrous veins (‘beef’and ‘cone-in-cone’). *Geofluids*, *7*(3), pp.313-322.

Cobbold, P.R., Zanella, A., Rodrigues, N. and Løseth, H., 2013. Bedding-parallel fibrous veins (beef and cone-in-cone): Worldwide occurrence and possible significance in terms of fluid overpressure, hydrocarbon generation and mineralization. *Marine and Petroleum Geology*, *43*, pp.1-20.

Cobbold, P.R., Zanella, A., Rodrigues, N. and Løseth, H., 2013. Bedding-parallel fibrous veins (beef and cone-in-cone): Worldwide occurrence and possible significance in terms of fluid overpressure, hydrocarbon generation and mineralization. *Marine and Petroleum Geology*, *43*, pp.1-20.

Coogan, L.A., Daëron, M. and Gillis, K.M., 2019. Seafloor weathering and the oxygen isotope ratio in seawater: Insight from whole-rock δ18O and carbonate δ18O and Δ47 from the Troodos ophiolite. *Earth and Planetary Science Letters*, *508*, pp.41-50.

Cooper, B.S. and Barnard, P.C., 1984. Source rocks and oils of the central and northern North Sea.

Cope, J.C., Guion, P.D., Sevastopulo, G.D. and Swan, A.R.H., 1992. Carboniferous. *Geological Society, London, Memoirs*, *13*(1), pp.67-86.

Cope, J.C., 1974. New information on the Kimmeridge Clay of Yorkshire. *Proceedings of the Geologists' Association*, *85*(2), pp.211-221.

Cope, J.C.W., 1994. A latest Cretaceous hotspot and the southeasterly tilt of Britain. *Journal of the Geological Society*, *151*(6), pp.905-908.

Coulomb, C.A., 1972. Essai sur une application des régles des maximis et minimis a quelques problèmes de statique relatifs a l'architecture, Mémoires par Divers Savants.

Cox, S.F. and Etheridge, M.A., 1983. Crack-seal fibre growth mechanisms and their significance in the development of oriented layer silicate microstructures. Tectonophysics, 92(1-3), pp.147-170.

Cox, S.F., 1987. Antitaxial crack-seal vein microstructures and their relationship to displacement paths. Journal of Structural Geology, 9(7), pp.779-787.

Cox, S.F. and Munroe, S.M., 2016. Breccia formation by particle fluidization in fault zones: implications for transitory, rupture-controlled fluid flow regimes in hydrothermal systems. American Journal of Science, 316(3), pp.241-278.

Craig, H., 1957. Isotopic standards for carbon and oxygen and correction factors for mass-spectrometric analysis of carbon dioxide. Geochimica et cosmochimica acta, 12(1-2), pp.133-149.

Cuthbert, S.J. and Buckman, J.O., 2005. Charge contrast imaging of fine-scale microstructure and compositional variation in garnet using the environmental scanning electron microscope. *American Mineralogist*, *90*(4), pp.701-707.

Daniels et al., 2017, personal communication of a draft paper entitled "Characterisation of fractures in shales: a case study of fractured Liassic mudstone from North Yorkshire, UK". version 10; 19/07/2016

Daniels, S.E., Tucker, M.E., Mawson, M.J., Holdsworth, R.E., Long, J.J., Gluyas, J.G. and Jones, R.R., 2020. Nature and origin of collapse breccias in the Zechstein of NE England: local observations with cross-border petroleum exploration and production significance, across the North Sea. Geological Society, London, Special Publications, 494.

De Paola, N., 2021, personal communications. Draft manuscript work based on the a MSci project by Roseanne Murray 18/11/2021.

De Souza, J.M.G., 2020. *Modeling of overpresure evolution during the gravitational collapse of the Amazon deep-sea fan, Foz do Amazonas Basin* (Doctoral dissertation, Sorbonne Université).

De Vera, J., Granado, P. and McClay, K., 2010. Structural evolution of the Orange Basin gravity-driven system, offshore Namibia. *Marine and Petroleum Geology*, *27*(1), pp.223-237.

Delvaux, D. and Sperner, B., 2003. New aspects of tectonic stress inversion with reference to the TENSOR program. *Geological Society, London, Special Publications*, *212*(1), pp.75-100.

Dewey, J.F. and Windley, B.F., 1988. Palaeocene-Oligocene tectonics of NW Europe. *Geological Society, London, Special Publications*, *39*(1), pp.25-31.

Dingle, R.V., 1971. A marine geological survey off the north-east coast of England (western North Sea). *Journal of the Geological Society*, *127*(4), pp.303-338.

Dixon, A.D.G., 1990. *Evolution of the Yorkshire, sole pit and east midland basin system, UK* (Doctoral dissertation, Durham University).

Doehne, E. and Carson, D., 2001. Charge Contrast Imaging (CCI) in the Environmental Scanning Electron Microscope: Optimizing Operating Parameters for Calcite. *Microscopy and Microanalysis*, *7*(S2), pp.780-781.

Douma, L., 2020. The elastic anisotropy and mechanical behaviour of the Whitby Mudstone.

Drake, H., Ivarsson, M., Heim, C., Snoeyenbos-West, O., Bengtson, S., Belivanova, V. and Whitehouse, M., 2021. Fossilized anaerobic and possibly methanogenesis-fueling fungi identified deep within the Siljan impact structure, Sweden. *Communications Earth & Environment*, *2*(1), pp.1-10.

Dunham, K.C., 1960. Syngenetic and diagenetic mineralization in Yorkshire. *Proceedings of the Yorkshire Geological Society*, *32*(3), pp.229-284.

Duval, B., Cramez, C. and Jackson, M.P.A., 1992. Raft tectonics in the Kwanza basin, Angola. *Marine and Petroleum Geology*, *9*(4), pp.389-404.

Egeberg, P.K. and Aagaard, P., 1989. Origin and evolution of formation waters from oil fields on the Norwegian shelf. *Applied Geochemistry*, *4*(2), pp.131-142.

Emery, A., 2016. Palaeopressure reconstruction to explain observed natural hydraulic fractures in the Cleveland Basin. *Marine and Petroleum Geology*, *77*, pp.535-552.

Engelder, T., Lacazette, A., Barton, N. and Stephansson, O., 1990. Natural hydraulic fracturing. *Rock joints*, pp.35-44.

Engelder, T., 1999. Transitional–tensile fracture propagation: a status report. *Journal of Structural Geology*, *21*(8-9), pp.1049-1055.

English, J.M., Finkbeiner, T., English, K.L. and Cherif, R.Y., 2017. State of stress in exhumed basins and implications for fluid flow: insights from the Illizi Basin, Algeria. *Geological Society, London, Special Publications*, *458*(1), pp.89-112.

Faÿ-Gomord, O., Allanic, C., Verbiest, M., Honlet, R., Champenois, F., Bonifacie, M., Chaduteau, C., Wouters, S., Muchez, P., Lasseur, E. and Swennen, R., 2018. Understanding fluid flow during tectonic reactivation: an example from the Flamborough Head Chalk Outcrop (UK). *Geofluids*, *2018*.

Fitch, F.J., Hooker, P.J., Miller, J.A. and Brereton, N.R., 1978. Glauconite dating of Palaeocene-Eocene rocks from East Kent and the time-scale of Palaeogene volcanism in the North Atlantic region. Journal of the Geological Society, 135(5), pp.499-512.

Fossen, H., 1992. The role of extensional tectonics in the Caledonides of south Norway. Journal of structural geology, 14(8-9), pp.1033-1046.

Fossen, H., 2016. Structural geology. Cambridge university press.

Fox-Strangways, C. and Woodward, H.B., 1892. The Jurassic Rocks of Britain.. (Vol. 1). HM Stationery Office.

Fox-Strangways, C. and Barrow, G., 1915. *The geology of the country between Whitby and Scarborough* (Vol. 35). HM Stationery Office.

Fraser, A.J. and Gawthorpe, R.L., 2003. An atlas of Carboniferous basin evolution in northern England.

Frenzel, M. and Woodcock, N.H., 2014. Cockade breccia: product of mineralisation along dilational faults. Journal of Structural Geology, 68, pp.194-206.

Gale, A.S. and Lovell, B., 2018. The Cretaceous–Paleogene unconformity in England: uplift and erosion related to the Iceland mantle plume. *Proceedings of the Geologists' Association*, *129*(3), pp.421-435.

Glennie, K.W., 1981. Sole Pit inversion tectonics. *Petroleum geology of the continental shelf of northwest Europe*, pp.110-120.

Glennie, K.W., 1984. Introduction to the petroleum geology of the North Sea.

Götze, J., 2002. Potential of cathodoluminescence (CL) microscopy and spectroscopy for the analysis of minerals and materials. *Analytical and bioanalytical chemistry*, *374*(4), pp.703-708.

Grant, R.J., Underhill, J.R., Hernández-Casado, J., Barker, S.M. and Jamieson, R.J., 2019. Upper Permian Zechstein Supergroup carbonate-evaporite platform palaeomorphology in the UK Southern North Sea. Marine and Petroleum Geology, 100, pp.484-518.

Grant, R.J., Booth, M.G., Underhill, J.R. and Bell, A., 2020. Structural evolution of the Breagh area: implications for carboniferous prospectivity of the Mid North Sea High, Southern North Sea. Petroleum Geoscience, 26(2), pp.174-203.

Green, P.F., 1986. On the thermo-tectonic evolution of Northern England: evidence from fission track analysis. *Geological Magazine*, *123*(5), pp.493-506.

Green, P.F., Duddy, I.R., Gleadow, A.J. and Lovering, J.F., 1989. Apatite fission-track analysis as a paleotemperature indicator for hydrocarbon exploration. In *Thermal history of sedimentary basins* (pp. 181-195). Springer, New York, NY.

Green, P.F. and Duddy, I.R., 2006. Interpretation of apatite (U–Th)/He ages and fission track ages from cratons. Earth and Planetary Science Letters, 244(3-4), pp.541-547.

Green, P.F., Westaway, R., Manning, D.A.C. and Younger, P.L., 2012. Cenozoic cooling and denudation in the North Pennines (northern England, UK) constrained by apatite fission-track analysis of cuttings from the Eastgate Borehole. Proceedings of the Geologists' Association, 123(3), pp.450-463.

Griffin, B.J., 1997. A new mechanism for the imaging of crystal structure in non-conductive materials: an application of charge-induced contrast in the environmental scanning electron microscope (ESEM). *Microscopy and Microanalysis*, *3*(S2), pp.1197-1198.

Griffin, B.J., 1998. Electrons, ions and cathodoluminescence in the environmental SEM. *Microscopy and Microanalysis*, *4*(S2), pp.290-291.

Griffin, B.J., 2000. Charge contrast imaging of material growth and defects in environmental scanning electron miscroscopy—linking electron emission and cathodoluminescence. Scanning, 22(4), pp.234-242.

Haarhoff, M.Q., Hughes, F., Heath-Clarke, M., Harrison, D., Taylor, C., Ware, D.L., Emms, G.G. and Mortimer, A., 2018. The history of hydrocarbon exploration and development in North Yorkshire. *Geological Society, London, Special Publications*, *465*(1), pp.119-136.

Habermann, D., Neuser, R.D. and Richter, D.K., 1998. Low limit of Mn2+-activated cathodoluminescence of calcite: state of the art. Sedimentary Geology, 116(1-2), pp.13-24.

Hama, L., Ruddle, R.A. and Paton, D., 2014. Geological Orientation Measurements using an iPad: Method Comparison. In *TPCG* (pp. 45-50).

Hardman, K., Holdsworth, R.E., Dempsey, E. and McCaffrey, K., 2020. Nature and significance of rift-related, near-surface fissure-fill networks in fractured carbonates below regional unconformities. *Journal of the Geological Society*, *177*(6), pp.1168-1185.

Hemingway, J.E. and Knox, R.O.B., 1973. Lithostratigraphical nomenclature of the Middle Jurassic strata of the Yorkshire Basin of north-east England. *Proceedings of the Yorkshire Geological Society*, *39*(4), pp.527-535.

Hemingway, J.E. and Riddler, G.P., 1982. Basin inversion in north Yorkshire. *Trans.-Inst. Min. Metall., Sect. B;(United Kingdom)*, *91*.

Hemingway, J.E., 1951. Cyclic sedimentation and the deposition of ironstone in the Yorkshire Lias. In *Proc. Yorks. geol. Soc.* (Vol. 28, pp. 67-74).

Hemingway, J.E., 1974. Jurassic. Pp. 161-223 in Rayner, D. H. & Hemingway, J. E. (editors): The geology and mineral resources of Yorkshire. Yorkshire Geol. Soc.

Hesselbo, S.P. and Jenkyns, H.C., 1998. British lower Jurassic sequence stratigraphy.

Hesselbo, S.P. and King, C., 2019. Stratigraphic Framework for the Yorkshire Lias, In Lord, A. (ed.). Fossils of the Lias of Yorkshire. Palaeontological Association, p. 30–40.

Hesthammer, J. and Fossen, H., 1999. Evolution and geometries of gravitational collapse structures with examples from the Statfjord Field, northern North Sea. *Marine and Petroleum Geology*, *16*(3), pp.259-281.

Hibsch, C., Jarrige, J.J., Cushing, E.M. and Mercier, J., 1995. Palaeostress analysis, a contribution to the understanding of basin tectonics and geodynamic evolution. Example of the Permian/Cenozoic tectonics of Great Britain and geodynamic implications in western Europe. *Tectonophysics*, *252*(1-4), pp.103-136.

Higgins, M.W., 1971. Cataclastic rocks.

Hill, C.A., Polyak, V.J., Asmerom, Y. and P. Provencio, P., 2016. Constraints on a Late Cretaceous uplift, denudation, and incision of the Grand Canyon region, southwestern Colorado Plateau, USA, from U-Pb dating of lacustrine limestone. Tectonics, 35(4), pp.896-906.

Hoefs, J. and Hoefs, J., 1997. Stable isotope geochemistry (Vol. 201). Berlin: Springer.

Holdsworth, R.E., Trice, R., Hardman, K., McCaffrey, K.J.W., Morton, A., Frei, D., Dempsey, E., Bird, A. and Rogers, S., 2020. The nature and age of basement host rocks and fissure fills in the Lancaster field fractured reservoir, West of Shetland. Journal of the Geological Society, 177(5), pp.1057-1073.

Holdsworth, R.E., McCaffrey, K.J.W., Dempsey, E., Roberts, N.M.W., Hardman, K., Morton, A., Feely, M., Hunt, J., Conway, A. and Robertson, A., 2019. Natural fracture propping and earthquake-induced oil migration in fractured basement reservoirs. *Geology*, *47*(8), pp.700-704.

Horstwood, M.S., Košler, J., Gehrels, G., Jackson, S.E., McLean, N.M., Paton, C., Pearson, N.J., Sircombe, K., Sylvester, P., Vermeesch, P. and Bowring, J.F., 2016. Community-derived standards for LA-ICP-MS U-(Th-) Pb geochronology–Uncertainty propagation, age interpretation and data reporting. *Geostandards and Geoanalytical Research*, *40*(3), pp.311-332.

Houben, M.E., Hardebol, N.J., Barnhoorn, A., Boersma, Q.D., Carone, A., Liu, Y., de Winter, D.A.M., Peach, C.J. and Drury, M.R., 2017. Fluid flow from matrix to fractures in Early Jurassic shales. International Journal of Coal Geology, 175, pp.26-39.

Howard, A.S., 1985. Lithostratigraphy of the Staithes sandstone and Cleveland Ironstone formations (Lower Jurassic) of north-east Yorkshire. *Proceedings of the Yorkshire Geological Society*, *45*(4), pp.261-275.

Howarth, M.K., 1955. Domerian of the Yorkshire coast. *Proceedings of the Yorkshire geological Society*, *30*(2), pp.147-175.

Howarth, M.K., 1962. The Jet Rock series and the Alum Shale series of the Yorkshire coast. *Proceedings of the Yorkshire Geological Society*, *33*(4), pp.381-422.

Huntington, K.W., Eiler, J.M., Affek, H.P., Guo, W., Bonifacie, M., Yeung, L.Y., Thiagarajan, N., Passey, B., Tripati, A., Daëron, M. and Came, R., 2009. Methods and limitations of 'clumped'CO2 isotope (Δ47) analysis by gas-source isotope ratio mass spectrometry. *Journal of Mass Spectrometry*, *44*(9), pp.1318-1329.

Huntington, K.W., Budd, D.A., Wernicke, B.P. and Eiler, J.M., 2011. Use of clumped-isotope thermometry to constrain the crystallization temperature of diagenetic calcite. *Journal of Sedimentary Research*, *81*(9), pp.656-669.

Hurford, A.J., 1977. A preliminary fission track dating survey of Caledonian "newer and last granites" from the Highlands of Scotland. *Scottish Journal of Geology*, *13*(4), pp.271-284.

Imber, J., Armstrong, H., Clancy, S., Daniels, S., Herringshaw, L., McCaffrey, K., Rodrigues, J., Trabucho-Alexandre, J. and Warren, C., 2014. Natural fractures in a United Kingdom shale reservoir analog, Cleveland Basin, northeast England. *AAPG Bulletin*, *98*(11), pp.2411-2437.

Imber, J., personal communications, unpublished field notebooks supplied by J Imber 01/10/2018.

Ingram, G.M. and Urai, J.L., 1999. Top-seal leakage through faults and fractures: the role of mudrock properties. *Geological Society, London, Special Publications*, *158*(1), pp.125-135.

Ivimey-Cook, H.C. and Powell, J.H., 1991. Late Triassic and early Jurassic biostratigraphy of the Felixkirk Borehole, North Yorkshire. *Proceedings of the Yorkshire Geological Society*, *48*(4), pp.367-374.

Japsen, P., 1997. Regional Neogene exhumation of Britain and the western North Sea. *Journal of the Geological Society*, *154*(2), pp.239-247.

Jeans, C.V., 1973. The Market Weighton Structure: tectonics, sedimentation and diagenesis during the Cretaceous. *Proceedings of the Yorkshire Geological Society*, *39*(3), pp.409-444.

Jeans, C.V., 1980. Early submarine lithification in the Red Chalk and Lower Chalk of eastern England: a bacterial control model and its implications. *Proceedings of the Yorkshire Geological Society*, *43*(2), pp.81-157.

Jochum, K.P., Weis, U., Stoll, B., Kuzmin, D., Yang, Q., Raczek, I., Jacob, D.E., Stracke, A., Birbaum, K., Frick, D.A. and Günther, D., 2011. Determination of reference values for NIST SRM 610–617 glasses following ISO guidelines. *Geostandards and Geoanalytical Research*, *35*(4), pp.397-429.

Jouzel, J., Froehlich, K. and Schotterer, U., 1997. Deuterium and oxygen-18 in present-day precipitation: data and modelling. *Hydrological Sciences Journal*, *42*(5), pp.747-763.

Kemp, S.J., Merriman, R.J. and Bouch, J.E., 2005. Clay mineral reaction progress–the maturity and burial history of the Lias Group of England and Wales. *Clay minerals*, *40*(1), pp.43-61.

Kent, P.E., 1974. Structural history. *The Geology and Mineral Resources of Yorkshire. Yorkshire Geological Society Occasional Publication*, *2*, pp.13-28.

Kent, P.E., 1980. Subsidence and uplift in East Yorkshire and Lincolnshire: a double inversion. *Proceedings of the Yorkshire Geological Society*, *42*(4), pp.505-524.

Kim, S.T. and O'Neil, J.R., 1997. Equilibrium and nonequilibrium oxygen isotope effects in synthetic carbonates. *Geochimica et cosmochimica acta*, *61*(16), pp.3461-3475.

Kim, Y.S., Peacock, D.C. and Sanderson, D.J., 2004. Fault damage zones. *Journal of structural geology*, *26*(3), pp.503-517.

Kley, J., 2018. Timing and spatial patterns of Cretaceous and Cenozoic inversion in the Southern Permian Basin. *Geological Society, London, Special Publications*, *469*(1), pp.19-31.

Knox, R.O.B., 1984. Lithostratigraphy and depositional history of the late Toarcian sequence at Ravenscar, Yorkshire. *Proceedings of the Yorkshire Geological Society*, *45*(1-2), pp.99-108.

Knox, R.O.B., 1991. Ryazanian to Barremian mineral stratigraphy of the Speeton Clay in the UK southern North Sea Basin. *Proceedings of the Yorkshire Geological Society*, *48*(3), pp.255-264.

Koehn, D. and Passchier, C.W., 2000. Shear sense indicators in striped bedding-veins. *Journal of Structural Geology*, *22*(8), pp.1141-1151.

Kulander, B.R., Barton, C.C. and Dean, S.L., 1979. *Application of fractography to core and outcrop fracture investigations* (No. METC/SP-79/3). Department of Energy, Morgantown, WV (USA). Morgantown Energy Research Centre.

Lake, S.D. and Karner, G.D., 1987. The structure and evolution of the Wessex Basin, southern England: an example of inversion tectonics. *Tectonophysics*, *137*(1-4), pp.347-378.

Leeder, M.R. and Nami, M., 1979. Sedimentary models for the non-marine Scalby Formation (Middle Jurassic) and evidence for late Bajocian/Bathonian uplift of the Yorkshire Basin. *Proceedings of the Yorkshire Geological Society*, *42*(3), pp.461-482.

Lee, M.R., 1990. *The sedimentology and diagenesis of the Raisby Formation (Z1 carbonate), northern England* (Doctoral dissertation, Newcastle University).

Lee, M.R., 1993. Formation and diagenesis of slope limestones within the Upper Permian (Zechstein) Raisby Formation, north-east England. *Proceedings of the Yorkshire Geological Society*, *49*(3), pp.215-227.

Leng, M.J. and Marshall, J.D., 2004. Palaeoclimate interpretation of stable isotope data from lake sediment archives. *Quaternary Science Reviews*, *23*(7-8), pp.811-831.

Lewis, C.L., Green, P.F., Carter, A. and Hurford, A.J., 1992. Elevated K/T palaeotemperatures throughout Nortwest England: three kilometres of Tertiary erosion?. *Earth and Planetary Science Letters*, *112*(1-4), pp.131-145.

Li, Q., Parrish, R.R., Horstwood, M.S.A. and McArthur, J.M., 2014. U–Pb dating of cements in Mesozoic ammonites. *Chemical Geology*, *376*, pp.76-83.

**Limans 1987**

Lodhia, B.H., Parent, A., Fraser, A.J., Nuemaier, M. and Hennissen, J.A., 2022. Thermal evolution and resources of the Bowland Basin (NW England) from apatite fission-track analyses and multidimensional basin modelling.

Lott, G.K. and Knox, R.W.O.B., 1994. Lithostratigraphical nomenclature of the UK North Sea, Volume 7. Post Triassic of the Southern North Sea.

Łuszczak, K., Persano, C. and Stuart, F.M., 2018. Early Cenozoic denudation of central west Britain in response to transient and permanent uplift above a mantle plume. *Tectonics*, *37*(3), pp.914-934.

MacDonald, J., Van Der Wal, J., Faithfull, J., Boyce, A., Roberts, N. and Winkelstern, I., 2020. Fingerprinting fluid source in calcite veins: combining LA-ICP-MS U-Pb calcite dating with trace elements and clumped isotope palaeothermometry.

Macdonald, R., Wilson, L., Thorpe, R.S. and Martin, A., 1988. Emplacement of the Cleveland dyke: evidence from geochemistry, mineralogy, and physical modelling. *Journal of Petrology*, *29*(3), pp.559-583.

Machel, H.G., 1985. Cathodoluminescence in calcite and dolomite and its chemical interpretation. *Geoscience Canada*.

Machel, H.G., 2000. Application of cathodoluminescence to carbonate diagenesis. In Cathodoluminescence in geosciences (pp. 271-301). Springer, Berlin, Heidelberg.

Marshall, J.D., 1992. Climatic and oceanographic isotopic signals from the carbonate rock record and their preservation. *Geological magazine*, *129*(2), pp.143-160.

McClay, K.R., 2013. *The mapping of geological structures*. John Wiley & Sons.

McCrea, J.M., 1950. On the isotopic chemistry of carbonates and a paleotemperature scale. *The Journal of Chemical Physics*, *18*(6), pp.849-857.

McGrath, A.G. and Davison, I., 1995. Damage zone geometry around fault tips. *Journal of Structural Geology*, *17*(7), pp.1011-1024.

McNamara, D.D., Lister, A. and Prior, D.J., 2016. Calcite sealing in a fractured geothermal reservoir: Insights from combined EBSD and chemistry mapping. *Journal of Volcanology and Geothermal Research*, *323*, pp.38-52.

Means, W.D. and Li, T., 2001. A laboratory simulation of fibrous veins: some first observations. *Journal of Structural Geology*, *23*(6-7), pp.857-863.

Megonigal, J.P., Hines, M.E. and Visscher, P.T., 2004. Anaerobic metabolism: linkages to trace gases. Biogeochemistry.

Milsom, J. and Rawson, P.F., 1989. The Peak Trough–a major control on the geology of the North Yorkshire coast. *Geological Magazine*, *126*(6), pp.699-705.

Mitchell, S.F., 1994. New data on the biostratigraphy of the Flamborough Chalk Formation (Santonian, Upper Cretaceous) between South Landing and Danes Dyke, North Yorkshire. *Proceedings of the Yorkshire Geological Society*, *50*(2), pp.113-118.

Mohr, O., 1914. *Abhandlungen aus dem Gebiete der technischen Mechanik*. W. Ernst & Sohn.

Morgans, H.S., Hesselbo, S.P. and Spicer, R.A., 1999. The seasonal climate of the Early-Middle Jurassic, Cleveland Basin, England. *Palaios*, pp.261-272.

Mortimore, R.N., 2019. Late Cretaceous to Miocene and Quaternary deformation history of the Chalk: Channels, slumps, faults, folds and glacitectonics. *Proceedings of the Geologists' Association*, *130*(1), pp.27-65.

Mortimore, R.N., Wood, C.J. and Gallois, R.W., 2001. *British upper cretaceous stratigraphy* (Vol. 23, pp. xx-558).

Narr, W. and Suppe, J., 1991. Joint spacing in sedimentary rocks. *Journal of Structural Geology*, *13*(9), pp.1037-1048.

Novakova, L. and Pavlis, T.L., 2017. Assessment of the precision of smart phones and tablets for measurement of planar orientations: A case study. *Journal of Structural Geology*, *97*, pp.93-103.

Nuriel, P., Wotzlaw, J.F., Ovtcharova, M., Vaks, A., Stremtan, C., Šala, M., Roberts, N.M. and Kylander-Clark, A.R., 2021. The use of ASH-15 flowstone as a matrix-matched reference material for laser-ablation U− Pb geochronology of calcite. *Geochronology*, *3*(1), pp.35-47.

Oliver, N.H. and Bons, P.D., 2001. Mechanisms of fluid flow and fluid–rock interaction in fossil metamorphic hydrothermal systems inferred from vein–wallrock patterns, geometry and microstructure. *Geofluids*, *1*(2), pp.137-162.

Parrish, R.R., Parrish, C.M. and Lasalle, S., 2018. Vein calcite dating reveals Pyrenean orogen as cause of Paleogene deformation in southern England. *Journal of the Geological Society*, *175*(3), pp.425-442.

Passchier, C.W. and Trouw, R.A., 2005. *Microtectonics*. Springer Science & Business Media.

Passey, B.H. and Henkes, G.A., 2012. Carbonate clumped isotope bond reordering and geospeedometry. Earth and Planetary Science Letters, 351, pp.223-236.

Peacock, D.C.P. and Sanderson, D.J., 1994. Strain and scaling of faults in the chalk at Flamborough Head, UK. *Journal of Structural Geology*, *16*(1), pp.97-107.

Petit, J.P., 1987. Criteria for the sense of movement on fault surfaces in brittle rocks. *Journal of structural Geology*, *9*(5-6), pp.597-608.

Pollard, D.D. and Aydin, A., 1988. Progress in understanding jointing over the past century. *Geological Society of America Bulletin*, *100*(8), pp.1181-1204.

Pollard, D.D., Segall, P.A.U.L. and Delaney, P.T., 1982. Formation and interpretation of dilatant echelon cracks. *Geological Society of America Bulletin*, *93*(12), pp.1291-1303.

Potts, G.J. and Reddy, S.M., 2000. Application of younging tables to the construction of relative deformation histories—1: fracture systems. *Journal of Structural Geology*, *22*(10), pp.1473-1490.

Powell, J.H., 1984. Lithostratigraphical nomenclature of the Lias Group in the Yorkshire Basin. *Proceedings of the Yorkshire Geological Society*, *45*(1-2), pp.51-57.

Powell, J.H., 1992. Gyrochorte burrows from the Scarborough Formation (Middle Jurassic) of the Cleveland Basin, and their sedimentological setting. *Proceedings of the Yorkshire Geological Society*, *49*(1), pp.41-47.

Powell, J.H., 2010. Jurassic sedimentation in the Cleveland Basin: a review. *Proceedings of the Yorkshire Geological Society*, *58*(1), pp.21-72.

Price, G.D. and Sellwood, B.W., 1997. "Warm" palaeotemperatures from high Late Jurassic palaeolatitudes (Falkland Plateau): Ecological, environmental or diagenetic controls?. *Palaeogeography, Palaeoclimatology, Palaeoecology*, *129*(3-4), pp.315-327.

Ramsay, J.G., Huber, M.I. and Lisle, R.J., 1983. The techniques of modern structural geology: Applications of continuum mechanics in structural geology (Vol. 3). Elsevier.

Rastall, R.H., 1905. The Blea Wyke beds and the Dogger in north-east Yorkshire. *Quarterly Journal of the Geological Society*, *61*(1-4), pp.441-460.

Rastall, R.H. and Hemingway, J.E., 1943. The Yorkshire Dogger: III. Upper Eskdale. *Geological Magazine*, *80*(6), pp.209-230.

Rawnsley, K.D., Rives, T., Petti, J.P., Hencher, S.R. and Lumsden, A.C., 1992. Joint development in perturbed stress fields near faults. *Journal of Structural Geology*, *14*(8-9), pp.939-951.

Rawson, P.F. and Wright, J.K., 1992. Geologists' Association Guide No. 34.

Richter, D.K., Götte, T., Götze, J. and Neuser, R.D., 2003. Progress in application of cathodoluminescence (CL) in sedimentary petrology. Mineralogy and Petrology, 79(3), pp.127-166.

Rives, T., Razack, M., Petit, J.P. and Rawnsley, K.D., 1992. Joint spacing: analogue and numerical simulations. *Journal of Structural Geology*, *14*(8-9), pp.925-937.

Roberts & Holdsworth (2022

Roberts, N.M. and Walker, R.J., 2016. U-Pb geochronology of calcite-mineralized faults: Absolute timing of rift-related fault events on the northeast Atlantic margin. *Geology*, *44*(7), pp.531-534.

Roberts, N.M., Rasbury, E.T., Parrish, R.R., Smith, C.J., Horstwood, M.S. and Condon, D.J., 2017. A calcite reference material for LA-ICP-MS U-Pb geochronology. *Geochemistry, Geophysics, Geosystems*, *18*(7), pp.2807-2814.

Roberts, N.M., Lee, J.K., Holdsworth, R.E., Jeans, C., Farrant, A.R. and Haslam, R., 2020. Near-surface Palaeocene fluid flow, mineralisation and faulting at Flamborough Head, UK: new field observations and U–Pb calcite dating constraints. *Solid Earth*, *11*(5), pp.1931-1945.

Robertson, E.C., 1982, August. Continuous formation of gouge and breccia during fault displacement. In *The 23rd US Symposium on Rock Mechanics (USRMS)*. OnePetro.

Robertson, K., Gauvin, R. and Finch, J., 2005. Application of charge contrast imaging in mineral characterization. *Minerals Engineering*, *18*(3), pp.343-352.

Sælen, G., Doyle, P. and Talbot, M.R., 1996. Stable-isotope analyses of belemnite rostra from the Whitby Mudstone Fm., England: surface water conditions during deposition of a marine black shale. *Palaios*, pp.97-117.

Sælen, G., Tyson, R.V., Telnæs, N. and Talbot, M.R., 2000. Contrasting watermass conditions during deposition of the Whitby Mudstone (Lower Jurassic) and Kimmeridge Clay (Upper Jurassic) formations, UK. *Palaeogeography, Palaeoclimatology, Palaeoecology*, *163*(3-4), pp.163-196.

Sagi, D.A., De Paola, N., McCaffrey, K.J.W. and Holdsworth, R.E., 2016. Fault and fracture patterns in low porosity chalk and their potential influence on sub-surface fluid flow—A case study from Flamborough Head, UK. *Tectonophysics*, *690*, pp.35-51.

Savalli, L. and Engelder, T., 2005. Mechanisms controlling rupture shape during subcritical growth of joints in layered rocks. *Geological Society of America Bulletin*, *117*(3-4), pp.436-449.

Savard, M.M., Veizer, J. and Hinton, R., 1995. Cathodoluminescene at low Fe and Mn concentrations; a SIMS study of zones in natural calcites. *Journal of Sedimentary Research*, *65*(1a), pp.208-213.

Sclater, J.G. and Christie, P.A., 1980. Continental stretching: An explanation of the post-mid-Cretaceous subsidence of the central North Sea basin. *Journal of Geophysical Research: Solid Earth*, *85*(B7), pp.3711-3739.

Sellwood, B.W. and Hallam, A., 1974. Bathonian volcanicity and North Sea rifting. *Nature*, *252*(5478), pp.27-28.

Sharp, Z., 2017. Principles of stable isotope geochemistry

Sibson, R.H., 1977. Fault rocks and fault mechanisms. *Journal of the Geological Society*, *133*(3), pp.191-213.

Sibson, R.H., 1986. Brecciation processes in fault zones: inferences from earthquake rupturing. *Pure and Applied Geophysics*, *124*(1), pp.159-175.

Sibson, R.H., 1996. Structural permeability of fluid-driven fault-fracture meshes. Journal of Structural Geology, 18(8), pp.1031-1042.

Sibson, R.H., 2000. Fluid involvement in normal faulting. Journal of Geodynamics, 29(3-5), pp.469-499.

Sibuet, J.C., Srivastava, S.P. and Spakman, W., 2004. Pyrenean orogeny and plate kinematics. *Journal of Geophysical Research: Solid Earth*, *109*(B8).

Silliphant, L.J., Engelder, T. and Gross, M.R., 2002. The state of stress in the limb of the Split Mountain anticline, Utah: constraints placed by transected joints. *Journal of Structural Geology*, *24*(1), pp.155-172.

Sippel, R.F., 1965. Simple device for luminescence petrography. *Review of Scientific Instruments*, *36*(11), pp.1556-1558.

Sippel, R.F. and Glover, E.D., 1965. Structures in carbonate rocks made visible by luminescence petrography. *Science*, *150*(3701), pp.1283-1287.

Smart, S., 2017, Kirby Misperton a wellsite km8 production well hydraulic fracture stimulation waste management plan (ref: te-epra-km8-hfs-wmp-05). https://consult.environment-agency.gov.uk/onshore-oil-and-gas/third-energy-kirby-misperton-information-page/supporting_documents/Waste%20Management%20Plan%20KM8.pdf

Smedley, P.L., Ward, R.S., Allen, G., Baptie, B., Daraktchieva, Z., Jones, D.G., Jordan, C.J., Purvis, R.M. and Cigna, F., 2015. Site selection strategy for environmental monitoring in connection with shale-gas exploration: Vale of Pickering, Yorkshire and Fylde, Lancashire.

Smith, D.B., 1995. The Permian marine rocks of England. In *Marine Permian of England* (pp. 1-11). Springer, Dordrecht.

Smith, D.B. and Taylor, J.C.M., 1989. A 'North-west Passage' to the southern Zechstein Basin of the UK North Sea. *Proceedings of the Yorkshire Geological Society*, *47*(4), pp.313-320.

Solomon, M. and Hill, P.A., 1962. Rib and Hackle Marks on Joint Faces at Renison Bell, Tasmania: A Preliminary Note. *The Journal of Geology*, *70*(4), pp.493-496.

Starmer, I.C., 1995. Deformation of the Upper Cretaceous Chalk at Selwicks Bay, Flamborough Head, Yorkshire: its significance in the structural evolution of north-east England and the North Sea Basin. *Proceedings of the Yorkshire Geological Society*, *50*(3), pp.213-228.

Starmer, I.C., 2008. The concentration of folding and faulting in the Chalk at Staple Newk (Scale Nab), near Flamborough, East Yorkshire. Proceedings of the Yorkshire Geological Society, 57(2), pp.95-106.

Starmer, I.C., 2013. Folding and faulting in the chalk at dykes end, Bridlington Bay, East Yorkshire, resulting from reactivations of the flamborough head fault zone. *Proceedings of the Yorkshire Geological Society*, *59*(3), pp.195-201.

Stewart, S.A. and Bailey, H.W., 1996. The Flamborough Tertiary outlier, UK southern North Sea. *Journal of the Geological Society*, *153*(1), pp.163-173.

Stewart, S.A. and Coward, M.P., 1995. Synthesis of salt tectonics in the southern North Sea, UK. *Marine and Petroleum Geology*, *12*(5), pp.457-475.

Stoneley, R., 1982. The structural development of the Wessex Basin. *Journal of the Geological Society*, *139*(4), pp.543-554.

Stolper, D.A. and Eiler, J.M., 2015. The kinetics of solid-state isotope-exchange reactions for clumped isotopes: A study of inorganic calcites and apatites from natural and experimental samples. *American Journal of Science*, *315*(5), pp.363-411.

Sumbler, M.G., 1999. The stratigraphy of the Chalk Group in Yorkshire and Lincolnshire.

Swart, P.K., Burns, S.J. and Leder, J.J., 1991. Fractionation of the stable isotopes of oxygen and carbon in carbon dioxide during the reaction of calcite with phosphoric acid as a function of temperature and technique. Chemical Geology: Isotope Geoscience section, 86(2), pp.89-96.

Taber, S., 1916. The origin of veins of the asbestiform minerals. Proceedings of the National Academy of Sciences of the United States of America, 2(12), p.659.

Taber, S., 1918. The origin of veinlets in the Silurian and Devonian strata of central New York. The Journal of Geology, 26(1), pp.56-73.

Talbot, C.J., Tully, C.P. and Woods, P.J.E., 1982. The structural geology of Boulby (potash) mine, Cleveland, United Kingdom. *Tectonophysics*, *85*(3-4), pp.167-204.

Tate, R. and Blake, J.F., 1876. *The Yorkshire Lias*. John van Voorst.

Taylor, W.L., Pollard, D.D. and Aydin, A., 1999. Fluid flow in discrete joint sets: Field observations and numerical simulations. *Journal of Geophysical Research: Solid Earth*, *104*(B12), pp.28983-29006.

Tipple, B.J., Meyers, S.R. and Pagani, M., 2010. Carbon isotope ratio of Cenozoic CO2: A comparative evaluation of available geochemical proxies. *Paleoceanography*, *25*(3).

Tucker, M.E., 1991. Sequence stratigraphy of carbonate-evaporite basins: models and application to the Upper Permian (Zechstein) of northeast England and adjoining North Sea. Journal of the Geological Society, 148(6), pp.1019-1036.

UK NDR 2022, UK National Data Respository (NDR), https://ndr.ogauthority.co.uk/

UKOGL, 2021, UK Onshore Geophysical Library, https://ukogl.org.uk/map/php/images.php?subfolder=regional\interpretations&filename=r003.gif

Underhill, J.R. and Partington, M.A., 1993, January. Jurassic thermal doming and deflation in the North Sea: implications of the sequence stratigraphic evidence. In *Geological Society, London, Petroleum Geology Conference Series* (Vol. 4, No. 1, pp. 337-345). Geological Society of London.

Underhill, J.R., 2009. Role of intrusion-induced salt mobility in controlling the formation of the enigmatic 'Silverpit Crater', UK Southern North Sea. *Petroleum Geoscience*, *15*(3), pp.197-216.

Urai, J.L. and Wong, S.W., 1994. Deformation mechanisms in experimentally deformed shales. In *Annales Geophysicae* (Vol. 12, p. C98).

Urai, J.L., 1995. Brittle and ductile deformation of mudrocks. *EOS November*, *7*(1995), p.F565.

Urey, H.C., 1947. The thermodynamic properties of isotopic substances. *Journal of the Chemical Society (Resumed)*, pp.562-581.

van Buchem, F.S. and Knox, R.W.O., 1999. Lower and Middle Liassic depositional sequences of Yorkshire (UK).

Van Buchem, F.S.P. and McCave, I.N., 1989. Cyclic sedimentation patterns in Lower Lias mudstones of Yorkshire (GB). *Terra Nova*, *1*(5), pp.461-467.

Veillard, C.M., John, C.M., Krevor, S. and Najorka, J., 2019. Rock-buffered recrystallization of Marion Plateau dolomites at low temperature evidenced by clumped isotope thermometry and X-ray diffraction analysis. *Geochimica et Cosmochimica Acta*, *252*, pp.190-212.

Vermeesch, P., 2018. IsoplotR: A free and open toolbox for geochronology. *Geoscience Frontiers*, *9*(5), pp.1479-1493.

Vernon, R., Ford, J., Watkinson, K., Haslam, R., Woods, M., Farrant, A., Burke, H., Davis, A., Lear, J., Tarnanas, H. and Wrathmell, E., 2020, May. Surface and subsurface fault mapping in the Yorkshire Wolds, UK. In *EGU General Assembly Conference Abstracts* (p. 7290).

Walker, R.J., Holdsworth, R.E., Imber, J. and Ellis, D., 2011. The development of cavities and clastic infills along fault-related fractures in Tertiary basalts on the NE Atlantic margin. *Journal of Structural Geology*, *33*(2), pp.92-106.

Wallace, R.E., 1951. Geometry of shearing stress and relation to faulting. *The Journal of geology*, *59*(2), pp.118-130.

Ward, R.S., Smedley, P.L., Allen, G., Baptie, B.J., Cave, M.R., Daraktchieva, Z., Fisher, R., Hawthorn, D., Jones, D.G., Lewis, A. and Lowry, D., 2018. Environmental baseline monitoring: Phase III final report (2017-2018).
Ward, R.S., Smedley, P.L., Allen, G., Baptie, B.J., Cave, M.R., Daraktchieva, Z., Fisher, R., Hawthorn, D., Jones, D.G., Lewis, A. and Lowry, D., 2018. Environmental baseline monitoring: Phase III final report (2017-2018).
Ward, R.S., Rivett, M.O., Smedley, P.L., Allen, G., Lewis, A., Purvis, R.M., Jordan, C.J., Taylor-Curran, H., Daraktchieva, Z., Baptie, B.J. and Horleston, A., 2020. Recommendations for Environmental Baseline Monitoring in areas of shale gas development.

Warren, A.R., Allen, L.A., Pang, H.M., Houk, R.S. and Janghorbani, M., 1994. Simultaneous measurement of ion ratios by inductively coupled plasma-mass spectrometry with a twin-quadrupole instrument. *Applied spectroscopy*, *48*(11), pp.1360-1366.

Watt, J., Young, N., Haigh, S., Kirkland, A. and Tilley, R.D., 2009. Synthesis and structural characterization of branched palladium nanostructures. *Advanced Materials*, *21*(22), pp.2288-2293.

White, N. and Lovell, B., 1997. Measuring the pulse of a plume with the sedimentary record. Nature, 387(6636), pp.888-891.

White, W.M., 2014. Isotope geochemistry. John Wiley & Sons.

Whitham, A.G., 1993. Facies and depositional processes in an Upper Jurassic to Lower Cretaceous pelagic sedimentary sequence, Antarctica. *Sedimentology*, *40*(2), pp.331-349.

Williams, P.F., 1986. Petroleum geochemistry of the Kimmeridge Clay of onshore southern and eastern England. *Marine and petroleum geology*, *3*(4), pp.258-281.

Williams, P.F. and Urai, J.L., 1989. Curved vein fibres: an alternative explanation. *Tectonophysics*, *158*(1-4), pp.311-333.

Woodcock, N.H., Omma, J.E. and Dickson, J.A.D., 2006. Chaotic breccia along the Dent Fault, NW England: implosion or collapse of a fault void?. Journal of the Geological Society, 163(3), pp.431-446.

Woodcock, N.H. and Strachan, R.A., 2009. Geological history of Britain and Ireland. John Wiley & Sons.

Woodhead, J.D. and Hergt, J.M., 2001. Strontium, neodymium and lead isotope analyses of NIST glass certified reference materials: SRM 610, 612, 614. *Geostandards Newsletter*, *25*(2-3), pp.261-266.

Woods, P.J.E., 1979. The geology of Boulby mine. Economic Geology, 74(2), pp.409-418.

Woods, M., personal communication between Mark Woods and Richard Haslam shared to Lee, J.K., via email 01/12/2021.

Worden, R.H., Benshatwan, M.S., Potts, G.J. and Elgarmadi, S.M., 2016. Basin-scale fluid movement patterns revealed by veins: Wessex Basin, UK. Geofluids, 16(1), pp.149-174.

Wright, J.K., 1978. The Callovian succession (excluding Cornbrash) in the western and northern parts of the Yorkshire Basin. Proceedings of the Geologists' Association, 89(4), pp.239-261.

Wright, J.K., 2009. The geology of the Corallian ridge (Upper Jurassic) between Gilling East and North Grimston, Howardian Hills, North Yorkshire. *Proceedings of the Yorkshire Geological Society*, *57*(3-4), pp.193-216.

Ziegler, P.A., 1980. Northwest European basin: geology and hydrocarbon provinces.

Ziegler, P.A., 1982. Faulting and graben formation in western and central Europe. *Philosophical Transactions of the Royal Society of London. Series A, Mathematical and Physical Sciences*, *305*(1489), pp.113-143.

Ziegler, P.A., 1987. Late Cretaceous and Cenozoic intra-plate compressional deformations in the Alpine foreland—a geodynamic model. *Tectonophysics*, *137*(1-4), pp.389-420.

Ziegler, P.A., 1989. Evolution of the North Atlantic--An Overview: Chapter 8: North Atlantic Perspectives.

Ziegler, P.A., 1990. *Geological atlas of western and central Europe* (Vol. 1). Geological Society Publishing House.